In the endeavor of exploiting the multifunctional properties of Ni-based Heusler alloys, the miniaturization of the active elements is consolidating as an effective approach to overcome their defective mechanical properties. Although the performance of microparticles, nanoparticles and powdered samples present unique advantages, in such regime, the control of internal strains, local stresses and point defects acquires a key relevance. Defects greatly influence both the magnetic properties and the martensitic transformation of Ni-based Heusler alloys. As the multifunctional properties are directly related with the characteristics of the martensitic transformation, the determination of the influence that defects have on the magnetic properties and on the martensitic transformation acquires a pivotal role for their development of practical devices and applications.

This thesis deals with the influence that defects have on the magnetic properties and on the martensitic transformation of Ni-Mn-Z (Z = Ga, Sn, In) and Ni-Fe-Ga alloys. In order to overcome the elusive nature of defects, a nuclear characterization approach has been selected for the consecution of this thesis. By means of positron annihilation lifetime spectroscopy and Mössbauer spectroscopy, the study is conducted at atomic scale level.

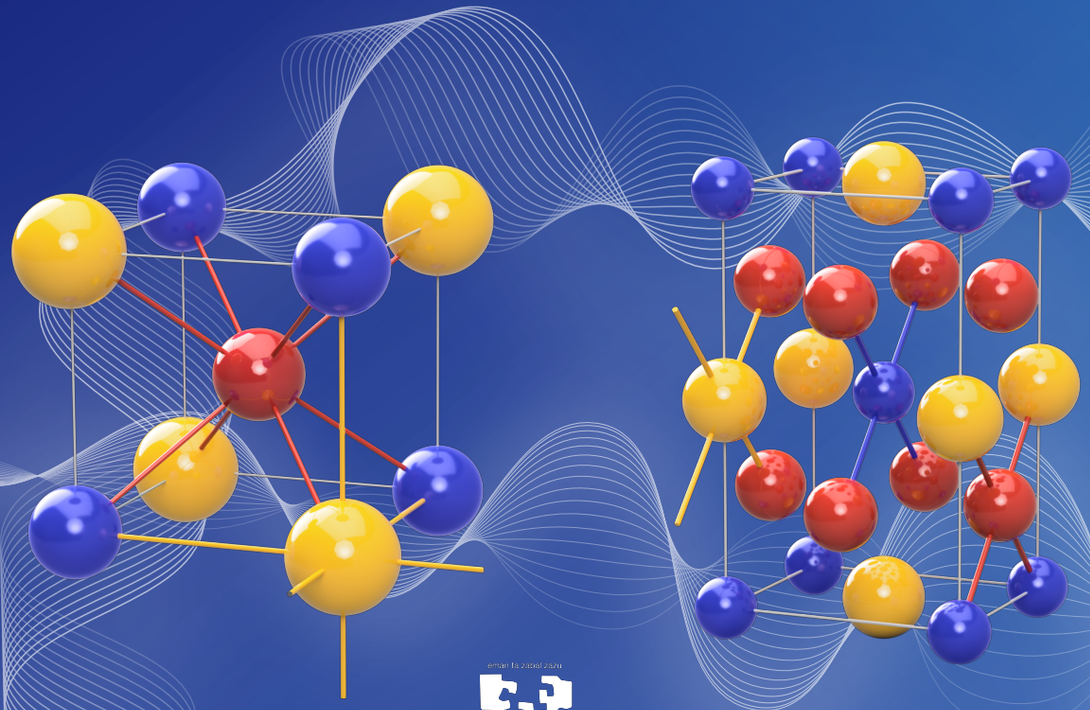

Universidad del País Vasco
Euskal Herriko Unibertsitatea

Influence of Structural Defects on the Properties of Ni-Based Heusler Alloys Iraultza Unzueta

Iraultza Unzueta Solozabal

Influence of Structural Defects on the Properties of Ni-Based Heusler Alloys

Influence of Microstructural Defects on the Martensitic Transformation and on the Magnetic Properties of Ni-based Heusler Alloys

ZTF-FCT
Zientzia eta Teknologia Fakultatea
Facultad de Ciencia y Tecnología

eman ta zabal zazu

Universidad del País Vasco
Euskal Herriko Unibertsitatea

Influence of Microstructural Defects on the Martensitic Transformation and on the Magnetic Properties of Ni-based Heusler Alloys

Iraultza Unzueta Solozabal

Supervised by
Prof. Fernando Plazaola

and

Prof. Jose Angel García

Electricity and Electronics Department
University of the Basque Country (UPV/EHU)

7 February 2019

This report is a PhD thesis developed during the period from January 2014 to December 2018 at MIMASPEC (Microstructural, Magnetic and Spectroscopic Characterization of Materials *with High-Tech and Biomedical Applications*) group, led by F. Plazaola and J. A. García (UPV-EHU). This thesis was funded by the Basque Government Grant PRE-2014-201 with a PhD fellowship and projects IT-1005-16 and IT-443-10, and by Spanish Ministry of Economy and Competitiveness MINECO under projects MAT2015-65165-C2-R (MINECO/FEDER) and MAT2012-37923-C02. The author thanks ILL and SpINS for beam time allocations and BCMaterials for their econonomical support.

An electronic version of this thesis can be found at https://addi.ehu.es/

Cover design by Mattin Urbieta.
This document was generated with the 2018 LaTeX distribution.
The LaTeX template is adapted from a template of Iagoba Apellaniz.
The bibliographic style was created by Sofía Martinez Garaot.

Nire amatxori...

Contents

Abstract

The thesis deals with the effect that microstructural defects have on the magnetic properties and martensitic transformation in Ni-Mn-Z (Z = Ga, In, Sn) and Ni-Fe-Ga alloys. For this purpose, along with the standard characterization techniques, two additional specific nuclear techniques have been employed; ^{119}Sn Mössbauer Spectroscopy and Positron Annihilation Lifetime Spectroscopy, PALS. For the consecution of this thesis one PALS spectrometer has been designed, built and optimized. For offline emission Mössbuauer experiments, a setup has been also built for measuring ion implanted samples. Finally, a high temperature annealing furnace has been designed and built to carry out the annealing of powdered samples under controllable atmosphere.

Regarding the effect that mechanically induced defects have on the properties of Ni-Mn-In alloys, it is shown that long ball milling times induce the disappearance of the long-range atomic order and the subsequent occurrence of the martensitic transformation, which ultimately leads to a frustrated magnetic system. The characterization of the obtained amorphous state reveals a canonical spin glass state of the ball-milled $Ni_{50}Mn_{34}In_{16}$ powders. The subsequent study of the crystallization dynamics reveals that the recovery takes place at two-stage crystallization processes. On heating, an abrupt crystallization process occurs around 500 K leading to a cubic B2 structure, evincing the suitability of ball milling and annealing procedures for reproducing the high-temperature B2 phase at much lower temperatures. On further

heating, and concurrently with a B2-$L2_1$ atomic ordering, a relaxation process takes place above 700 K, which gives rise to an anomalous two-step thermal expansion. Finally, the magnetocaloric effect is comparatively evaluated in both bulk and ball-milled powders. The relative cooling power linked to the magnetocaloric effect of the obtained nanoparticles makes them suitable for practical applications of magnetic refrigeration at nanoscale.

Taking into account the critical impact that ball milling has on the crystal structure of the synthesized nanoparticles, a more controllable mechanical distortion technique (hand-milling) have been used for Ni-Mn-Sn systems. In particular, the effect of combined mechanical and thermal treatments in a $Ni_{50}Mn_{35}Sn_{15}$ metamagnetic shape memory alloy is studied by means of ^{119}Sn-MS. Soft milled $Ni_{50}Mn_{35}Sn_{15}$ powdered samples are annealed at different temperatures producing different microstructural states that are correlated to the magneto-structural properties. These results evince that even by soft milling, a high average of internal strains, small grain sizes and a high density of defects are induced. Even though no atomic disorder is induced by milling, the anti-phase boundaries linked to dislocations promote the antiferromagnetic coupling of Mn atoms, resulting in a significant decrease in the saturation magnetization. The ^{119}Sn-MS results confirm the suitability of Mössbauer spectroscopy for linking the martensitic transformation with the microstructural state, becoming a practical tool to assess the microstructural characterization of the local strains and defect state. The recovery brought by annealing on the martensitic transformation is directly related to the intensity of the non-magnetic component revealed by ^{119}Sn-MS. Due to the high stability that the Ni-Mn-Sn systems show against the atomic disorder, this result opens an additional way to properly tune the multifunctional properties in the Ni-Mn-Sn systems.

The study of the effect that the presence of internal stresses and strains have on the martensitic transformation has been extended to other compositions, in essence to $Ni_{50}Mn_{37}Sn_{13}$ and to $Ni_{45}Co_5Mn_{37}Sn_{13}$. Specially, in $Ni_{45}Co_5Mn_{37}Sn_{13}$ samples, it is found that the mechanically-induced defects, far for worsening, improve the magnetocaloric response. The different exchange coupling between nearest-neighbors Mn atoms in the austenite and in the martensite phases makes the magnetization change at the martensitic transformation to be increased as a result of the presence of anti-phase boundaries linked to dislocations. The results of eMS measurements in samples implanted with ^{57}Mn and ^{119}In isotopes are also discussed.

Focusing on the effects of point defects on the martensitic transformation and magnetic properties of the studied Heusler alloys, a thorough PALS study has been performed in Ni-Mn-Z (Z = In, Sn). Indeed, PALS measurements in $Ni_{50}Mn_{50-x}Sn_x$ (x = 25, 20, 15, 13, 10) and $Ni_{50}Mn_{50-x}In_x$ (x = 25, 20, 16, 13) samples are complemented with DFT electron-positron theoretical calculations. The results confirm that the experimentally measured positron lifetime values correspond to teh contribution of positrons trapped at vacancies. In order to establish the parametrization of $\gamma(\mathbf{r})$ which best suits the experimental PALS results, a widely used five different parametrization of $\gamma(\mathbf{r})$ are analyzed within the LDA and GGA schemes. The results indicate that $\gamma(\mathbf{r})^{\mathrm{BN}}_{\mathrm{LDA}}$ parametrization is the one that best predicts PALS values

in the studied systems. Taking advantage of the existing PALS data in Ni-Mn-Ga systems, the accuracy of $\gamma(\mathbf{r})^{\mathrm{BN}}_{\mathrm{LDA}}$ parametrization is also tested and confirmed in Ni-Mn-Ga systems. Combining theory and experiments, V_{Ni} is identified as the type of vacancy trapping positrons in Ni-Mn-Z (Z = Ga, Sn, In) samples. The characteristic V_{Ni}-related positron lifetime ranges between 181 - 191 ps. These results show that, unlike what happens in Ni-Mn-Ga alloys, and regardless of the heat treatments, Ni-Mn-Sn and Ni-Mn-In alloys are characterized by a high C_v^{Ni} ($\geq$ 500 ppm).

Finally, $Ni_{55}Fe_{17}Ga_{28}$ alloys has been also investigated by PALS, where it is shown that in $Ni_{55}Fe_{17}Ga_{28}$ systems the evolution of vacancies and the T_{MT} evolve hand by hand. DSC measurements enable the tracking of T_{MT}, whereas PALS reveals its dependency on C_v. Thereby, the longstanding question whether the different T_{MT} evolution of samples quenched above or below $T_{L2_1\text{-}B2}$ rely on different vacancy dynamics, is demonstrated. Additionally, it is also shown that for Ni-Fe-Ga systems, $\gamma(\mathbf{r})^{\mathrm{BN}}_{\mathrm{LDA}}$ parametrization gives the most accurate positron lifetime values in electron-positron DFT calculations, which enables the identification of V_{Ni} as the most probable vacancy in the $Ni_{55}Fe_{17}Ga_{28}$ alloy. The investigation carried out in $Ni_{55}Fe_{17}Ga_{28}$ evinces the potential of vacancies for the fine tuning of T_{MT}, which enables shifts in T_{MT} up to $\approx$ 50 K.

Laburpena

TESI honetan mikroegiturako akatsek, $Ni_{50}Mn_{50-x}Z_x$ ($x = 25,\ 20,\ 16,\ 15,\ 13\ ,10$) eta Ni-Fe-Ga aleazioen transformazio martensitikoan eta propietate magnetikoetan duten eragina aztertzen da. Akatsen detekzioaren zailatsuna gainditzeko, ezaugarritze teknikak, bi teknika nuklear berezirekin osatu dira; positroi-deuseztapen bizidenboren espektroskopia (PALS) alde batetik, eta Mössbauer espektroskopia (MS) bestetik. Teknika nuklear hauek erabiliz, maila atomikoko ezaugarritze estruktural eta magnetikoa burutu da.

Material funtzionalek, kanpoko estimuluen funtziopean, erantzun jakinak ematen dituzten materialak dira. Propietate multifuntzional anitzak erakusten dituzten material funtzionalen ikerketa eta garapena geroz eta garrantzi handiagoa hartzen ari da azken urteotan, orohar, materialen zientziaren aurrerapenean erdietsi duten garrantzia dela eta. Testuinguru honetan, Heusler konposatuek berebiziko ospea hartu dute hainbat ikerketa eremu garaikidetan. Konposatu hauen egitura elektronikoaren malgutasuna dela eta, aplikazio potentzial anitzak ahalbideratzen dituzte erdieroale, supereroale eta material magneto-mekanikoen eremuetan, baita material termoelektriko zein espintronikarako materialen eremuetan ere.

Gaur egun, Heusler konposatu bezala ezagutzen den familiak 1000 konposatutik gora barnebiltzen ditu. Zenbait Heusler konposatuk ordea, transformazio martensitikoa deritzon fase-transformazioa jasaten dute. Fase-tranformazio hau da Heusler aleazioen propietate multifuntzionalen arrazoia. Heusler aleazio jakin hauek er-

akusten duten magnetoegiturako mihiztadura dela eta, egiturazko aldaketak maiz aldaketa magnetikoekin batera gertatzen dira. Mihiztadura honek egiturazko propietateen eta propietate magnetikoen aldibereko optimizazioa ahalbideratzen du, eta ondorioz, baita honekin loturiko propietate multifuntzionalena ere.

Hasiera batean Heusler aleazioen ikerketak ikuspuntu magnetiko zein estruktural batetik bideratu ziren arren, material hauen ikerketa gaur egun konposatu hauek erakusten dituzten propietate multifuntzionalen inguruan egiten da nagusiki. Horrela transformazio martensitikodun Heusler aleazioen ikerketak berebiziko garrantzia hartu du. Zehazki, magnetikoki eragindako forma-oroimen efektua dela eta, forma-oroimendun aleazio magnetiko bezala ezagutzen diren aleazioek arreta berezia piztu izan dute. Efektu hau bereziki esanguratsua egiten da Mn edo Fe dutenen konposatuen artean.

Ni_2(Mn,Fe)Z (Z = Ga Sn, In) Heusler aleazioen propietate multifuntzional anitzak direla eta, konposatu hauek geroz eta arreta handiagoa pizten ari dira materialen zientziaren komunitatean. Aleazio hauek magnetikoki eraginda lortzen diren esfortzu erraldoiak erakusten dituzte, baita magnetoerresistentzia efektua, efektu magnetokalorikoa, elkartruke-zehartua eta forma-oroimendun efektua ere. Guzti honen ondorioz, material hauen erabilera geroz eta gehiago hedatzen ari da espintronika, eguzki-zelula, energia batze zein hozte-magnetikoen teknologia-eremuetan.

Forma-oroimendun aleazio metamagnetikoek Ni-Mn-Z (Z = In, Sn, Sb) interes handia piztu dute azken urteotan. Aleazio hauen propietate metamagnetikoek, eremu bidez eragindako transformazio martensitikoa ahalbideratzen dute. Ni-Fe-Ga eta Ni-Mn-Ga aleazioetan ez bezala, forma-oroimendun aleazio metamagnetikoen kasuan, magnetikoki ezberdin ordenaturiko austenita eta martensita faseen artean gertatzen da. Ondorioz, aleazio hauek beste propietate multifuntzional batzuk erakusten dituzte, hala nola, eremu bidezko alderantzizko forma-oroimen efektua, efektu magnetokalorikoa, martensitaren harrapaketa-zinetikoa eta elkartuke-zehartu-aren efektua.

Propietate multifuntzional anitz hauek optimizatu ahal izateko, transformazio martensitikoa baldintzatzen duten parametroen kontrola edukitzea beharrezkoa da. Honetarako, transformazioaren tenperatura da gehien baldintzatzen duen parametroa, eta konposizioa da azken hau finkatzen duen parametrorik esanguratsuena. Tratamendu termiko, dopaketa eta beste hainbat metodoren bidez alda daitezke transformazioarekin lotutako ezaugarriak. Doiketa hauen helburu nagusia transformazio martensitikoarekin erlazioanatuta dauden propietate multifuntzionalak optimizatzea da. Nahiz eta aleazio hauek propietate interesgarri asko erakutsi, oso propietate mekaniko eskasak dituzte. Izatez, aleazio hauen hauskortasuna da aplikazio zein gailu praktikoen garapena oztopotzen duen faktorerik erabakigarriena. Azken hamarkadan, Ni-oinarridun Heusler aleazioetan oinarritutako elementu aktiboen garapenerako bidean, material hauen propietate mekanikoak hobetzea izan da helburu nagusiena.

Aleazio hauen totxo-laginen mugak gainditze bidean, zenbait bide ezberdin jorratu dira azken urteotan. Arrakastatsuenen artean, zinta, belaki zein film erako aleazioak erabiltzearenak aipa daitezke, baita forma-oroimendun partikulak matrize polimerikoetan txertatzearenak ere. Honen ondorioz, mikropartikulak eta nanopartikulak elementu aktibo gisa erabiltzearen planteamendua konponbide eraginkor bezala

finkatzen ari da. Eskala hauetan, akatsen, dislokazioen, hutsuneen, tokiko esfortzuen, tentsioen etab.-en kontrola ezibestekoa bilakatzen da. Hauek transformazio martensitikoan zuzenean eragiten dute. Horren harira, mikroegituraren gaineko kontrolak oraindik eta garrantzi handiagoa hartzen du hauts erako laginekin lotutako propietate multifuntzionalak doitzerako orduan. Laburbilduz, hauts erako mikropartikula eta nanopartikulen erabileraren bitartez, totxo-laginen propietate eskasak gaiditu daitezkela esan daiteke, baina mikro eta nano eskalan egonik, beste arazo berri batzuk kontuan hartu behar dira.

Akatsek, propietate magnetiko zein egiturazko propietateetan izan ditzaketen eragina zehaztera bidean ikerketa asko burutu diren arren, oso ikerketa gutxi burutu dira akatsek transformazio martensitikoan zein mikro eta nano eskalako partikulen propietateetan izan ditzaketen eraginaren azterketan. Ikerketa hauek guztiz beharrezkoak dira Ni-oinarridun Heusler aleazioen hauts-laginen portamoldea ulertzeko, noski. Partikula hauen aurretiazko ezaugarritze orokorrak ere berebiziko garrantzia hartzen du partikula hauen portamoldea aurresan ahal izateko. Ale-tamainak, barne tentsioek edota tokiko esfortzuek energia elastikoaren osagaian duten eragina dela eta, zuzenean eragiten die transformazio martensitikoari eta honen ezaugarriei. Konposizioaren eta mikroegituraren eraginaz gaindi, irispide luzeko ordena atomikoak Ni-Mn-Z (Z = Sn, In) eta Ni-Fe-Ga aleazioen transformazioa, transformazio-tenperatura eta propietate magnetikoak ere baldintzatzen ditu.

Hainbat ikerketen emaitzek erakusten duten bezala, Ni-Mn-Z (Z = In, Sn) aleazioen egiturazko ordena Z elementuaren independentea izan arren, egonkortasun ordena guztiz ezberdina da aleazio hauetan. Honek aleazio hauetan akatsen dinamikak duen garrantzia azaleratzen du. Izatez, Ni-Mn-Ga aleazioetan buru diren ikerketek aurreko hipotesia baieztatzen dute. Hala ere, akatsen izaera saiheskorra dela eta, hauek transformazio martensitikoan eta propietate magnetikoetan duten eragina ez da guztiz ondo ulertzen oraindik ere. Hutsune erako akatsen dinamika eta ordena atomikoaren mekanismoak guztiz lotuta daude. Biek irispide luzeko ordena atomikoan eragiten dute, eta ondorioz, transformazio martensitikoaren tenperaturan eta trantsizio-magnetikoari dagokion tenperaturan. Horrela, Ni-Mn-Sn, Ni-Mn-In eta Ni-Fe-Ga sistemetan behatutako ordenamendu prozesuen ezberdinek aukera ezin hobea eskeintzen dute hutsuneen dinamika eta ordena atomikoaren arteko erlazioa aztertzeko.

Laburbilduz, Ni-oinarridun Heusler aleazioen propietate multifuntzionalen abaintailak baliatze aldera, eragile-elementuen miniaturizazioak emaitza itxaropentsuak eman ditu orain arte. Izan ere, miniaturizazio hau, totxo-laginek erakusten dituzten propietate mekaniko eskasak gainditzeko ikuspuntu baliagarri bezala finkatzen ari da. Aurretik eztabaidatutakoaren harira, mikro eta nano eskalako akatsek propietate estruktural eta magnetikoetan duten eragina oso handia dela esan daiteke. Hutsuneek, tokiko tentsioek, esfortzuek eta mikroegituraren akatsek transformazio martensitikoan eta propietate magnetikoetan duten eraginaren ezaugarritzea ezinbestekoa da. Ezaugarritze honek, Ni-oinarridun Heusler aleazioak aplikazio eremu zabaletan erabili ahal izateko behar duten garapena ahalbidera dezake. Tesi honetan, akatsek $Ni_{50}Mn_{50-x}Z_x$ (x = 25, 20, 16, 15, 13 ,10) eta Ni-Fe-Ga aleazioen transformazio

martensitikoan eta propietate magnetikoetan duten eragina aztertu da.

Sarrerako atalean, azterturiko aleazioen ikuspegi orokor baten azalpena ematen da, aleazio hauen egiturazko propietateak, propietate magnetikoak eta tenperatura bereizgarriak erakutsiz, baita aleazio hauek horren interesgarri egiten dituzten propietate multifuntzionalak aipatuaz ere. Aleazio hauek gaur egungo egoeran dituzten abantaila eta desabantailak ere aipatzen dira. Azkenik, tesi honen helburuak finkatzen dira.

Bigarren atal batean, atal esperimentalean, tesi hau aurrera eramateko erabili diren ezaugarritze teknika ezberdinak erakusten dira. Lehenik eta behin, sintetizatze eta ezaugarritze-teknika arruntak azaltzen dira, hala nola, ekorketa diferentzialeko kalorimetria, ekorketako mikroskopio elektronikoa, neutroi difrakzioa, X-Izpien difrakzioa eta suberaketa teknikak. Ondoren, erabilitako bi teknika nuklearrak, positroi-deuseztapen bizidenboren espektroskopia eta Mössbauer espektroskopia, sakonki aztertzen dira, hauen printzipio fisikoetan arreta berezia jarriz. Tesi hau burutzeko egin diren muntaia-esperimentalak ere ageri dira atal honetan. Adibidez, hauts-laginak suberatzeko montatu den labe baten muntaiaren prozesua azaltzen da. Positroi neurketak burutu ahal izateko, PALS espektrometro baten muntaia eta optmizazioa ere azaltzen da. Amaitzeko, igorpenezko Mössbauer neurketak burutzeko garatu den espektrometro baten muntaia ere deskribatzen da atal honetan.

Hirugarren atalean, bolaz ehotako $Ni_{50}Mn_{34}In_{16}$ hauts-lagin nano eta mikrometrikoen egitura magnetikoa eta kristalizazio prozesua aztertzen da. Kapitulu honetan zehar plazaratuko den bezala, bolaz ehotako laginek, egitura kristalografiko amorfoaz gain, espin-beira kanonikoarekin bateragarri den egitura magnetikoa erakusten dute. Ondoren, laginak suberatu egin dira eta kristalizazio-prozesua aztertu da. Kristalizazio-prozesuaren hasieran, egitura amorfoa B2 erako kristal-egiturara eraldatzen da. Ehoketa eta suberaketa tratamendu egokiak konbinatuz, tenperatura altukoa den B2 fasea askoz ere tenperatura baxuagoetan lor daitekeela erakusten da. Bolaz ehotako $Ni_{50}Mn_{34}In_{16}$ laginek egitura amorfoa erakusten dute, eta ondorioz, lagin hauek ez dute transformazio martensitikorik jasaten. Neurketa magnetikoek, bestalde, ehotako laginen egitura magnetikoa espin-beirazko egiturarekin bateragarria dela adierazten dute. Jarraian, lagin hauen ordenamendua aztertzen da. Suberaketa-tenperatura igo ahala, erlaxazio-prozesu batekin batera B2-$L2_1$ ordenamendu-prozesua gertatzen da. Prozesu honekin lotuta, espantsio termiko anomalo bat gertatzen da. Bi prozesu hauek ahalbideratuta, transformazio martensitikoaren gertaera behatzen da bolaz ehotako hauts-laginetan. Bukatzeko, hasierako totxo-aleazioan eta bolaz ehotako hauts-laginetan efektu magnetokalorikoari lotutako hozte-ahalmen erlatiboaren balioak aztertzen dira, ehoketa eta suberaketa prozesuen konbinazio egokiak erabiliz, hozte-sistema magnetikokdun aplikazioetan erabiliak izan daitezkeen Ni-Mn-In nanopartikulak sintetizatzea posible dela erakutsiz.

Laugarren kapituluan, Ni-Mn-Sn sistemak aztertzen dira. Aurreko ataleko emaitzak kontutan hartuz, ehoketa era kontrolatuago batean egin da lagin hauetan. Tratamendu termomekanikoen bidez lortutako mikroegitura ezberdinak era sistematiko batean aztertzen dira. Ehotako laginak suberatu ahala, inklusio ez magnetikoekin eta

dislokazioekin lotutako tentsio-eremuak desargetu egiten dira, honek, asetasuneko-magnetizazioaren balio handitzen duelarik. Zehazki, Mn atomoen arteko mihiztadura ferromagnetikoa izatetik antiferromagnetikoa izatera pasatzen da anti-fase mugen inguruan. Hauek propietate magnetikoetan eta asetasuneko-magnetizazioan eragiten dute. Transformazio martensitikoa hedatzen den tenperatura-tarteak jasaten duen murrizketa, berreskurapen honen ondorio da. Atal honetan ikusiko den bezala, suberaketan zehar jasandako aldaketa hauek efektu magnetokalorikoa hobetzen dute. Azkenik, Ni-Mn-Sn sisteman burututako lan hau beste konposizio batzuetara hedatzen da, adibidez, Co-z dopatutako Ni-Mn-Sn laginera. Azken honetan ere, ehotako laginen efektu magnetokalorikoa aztertzen da. Lortutako emaitzek erakusten dutena da termomekanikoki eragindako mikroegituraren aldaketa dela Ni-Mn-Sn aleazioen propietate multifuntzionalak doitzeko modurik egokiena. Gainera, ehoketan zehar eragindako mikroegituraren distortsioa, ^{119}Sn-MS espektroek erakusten duten osagai ez-magnetikorekin erlazionatuta dagoela ikusten da. Emaitza honek, akatsek transformazio martensitikoan duten ekarpena kuantifikatzea ahalbideratzen du. Suberatutako laginekin alderatuz, ehotako Ni-Mn-Sn-Co aleazioetan lortzen den efektu magnetokalorikoak erakutsen du nola, akatsak, propietate multifuntzionalak kaltetzetik haratago, hauek doitzeko erabili daitezkeela.

Kapitulu honen amaieran, ISOLDE (CERN)-en eginiko igorpenezko Mössbauer neurketen emaitzak azaltzen dira. Ni-Mn-Z (Z = In, Sn) laginetan ^{119}Sn denez Mössbauer nukleo bakarra, aurreko atalean egindako azterketa ezin da Ni-Mn-Inko sistemetara hedatu. Arazo honi aurre egiteko, igorpenezko Mössbauer neurketak egin dira ISOLDE-n (CERN), aztergai diren laginak ioi erradiaktiboekin inplantatuz. Esperimentu hauek IS578 proiektuarn baitan burutu dira. Azterturiko laginetan ^{57}Mn eta ^{119}In ioiak inplantatu dira, ^{57}Fe eta ^{119}Sn igorpenezko Mössbauer neurketak burutuz.

Neurketa hauek erakusten dutena zera da, inplantazioaren ondorioz eragiten diren tokiko tentsio eta esfortzuek (inplantazio-kaltea) maila atomikoko magnetismoa sun-tsitzen dutela. Inplantazioarekin erlazionatutako kaltea gutxitzeko, lagin hauek suberatu egin behar dira. Inplantazio osteko suberaketa eta tratamendu termikoen bidez, zunda atomoaren inguruko distortsioa berreskuratu daiteke. ISOLDE-n burututako tenplaketa esperimentuen atariko emaitzek erakusten duten bezala, tenperatura altuan inplantatutako $Ni_{50}Mn_{25}Sn_{25}$ laginak nitrogeno likidora tenplatzen direnean osagai magnetiko handiago bat neurtzen da. Inplantatutako tenperatura altuetan, kaltearen berreskurapena ia bat-batekoa da, eta ondorioz, zunda atomoaren ingurunea askoz ere homogeneoagoa da. Hala ere, inplantaturiko ^{57}Mn eta ^{119}In ioien erdibizitza-denbora laburra dela eta (1.42 eta 2.4 minutu, hurrenez hurren), inplantazio osteko suberaketak egitea ez da posible, minutu gutxiren buruan laginen aktibitatea ia nulua bihurtzen delako. Arazo hau bizidenbora-luzeko ioi erradioaktiboen inplantazioak eginez konpondu daiteke, hala nola, ^{119m}Sn eta ^{57}Co ioiekin. Nukleo hauen erdibizitza denbora 293 eta 271 egunekoa da, hurrenez hurren. Horren ondorioz, posible da inplantazio osteko suberaketak burutzea laginaren aktibitatearen galera adierazgarririk izan gabe. ^{119m}Sn ioiekin inplantatutako Ni-Mn-Sn laginetatik ateratako behin-behineko ondorioek ikuspuntu honen baliogarritasuna

frogatzen dute.

Azken kapituluan, Ni-Mn-In, Ni-Mn-Sn eta Ni-Mn-Ga sistemen hutsuneak aztertzen dira PALS teknikaren bidez. Ni-Fe-Ga aleazioaren kasuan, hutsune-kontzentrazioaren eta transformazio martensitikoaren tenperaturaren arteko erlazioa ere aztertzen da. Neurketa esperimental guztiak Dentsitate-Funtzionalaren Teorian oinarritutako kalkulu teorikoekin alderatzen dira. Hasierako zatian DFT teoriaren zintzelada batzuk aipatzen dira. Positroiaren presentziak eragiten duen dentsitate elektronikoaren hazkundea modelizatzen duen hobekuntza-faktorearen parametrizazio ezberdinak ere aztertu dira. Zehazki, bost parametrizazio ezberdin aztertu dira Ni-Mn-In, Ni-Mn-Sn, eta Ni-Fe-Ga aleazioetan.

Kapitulu honetan ikusiko den bezala, neurketa esperimentalak hobekien aurresaten dituen hobekuntza-faktorearen parametrizazio egokiena Boronski-Nieminen-en parametrizazioa da. Parametrizazio honen balioak eta emaitza esperimentalak konbinatuz, aztertutako aleazioetan ageri den hutsune mota, Ni hutsunea dela frogatzen da. Haratago joanaz, literaturako Ni-Mn-Ga PALS emaitza esperimentalez baliatuz, eztabaida Ni-Mn-Ga sistemetara ere hedatzen da. Ni-Mn-Ga aleazioetan gertatu ez bezala, Ni-Mn-In eta Ni-Mn-Sn aleazioek oso hutsune-kontzentrazio altuak erakusten dituzte. Gainera, hutsuneen kontzentrazioa ez da Ni-Mn-Ga aleazioetan bezain erraz aldatzen eta tratamendu termikoen eragina ez da horren adierazgarria alezio hauetan. Ni-Fe-Ga aleazioaren kasuan, aldiz, transformazio martensitikoaren tenperaturaren aldaketaren eta hutsuneen eboluzioaren arteko erlazioa zuzena dela ikusten da. Tenplaketa eta suberaketa-tratamenduak erabiliz, transformazio martensitikoak jasaten duen aldaketa (50 K-erainokoa) hutsuneen kontzentrazioarekin erlazionatzen da zuzenean. Bestalde, B2 edo $L2_1$ fasetik tenplatutako Ni-Fe-Ga laginen hutsune-kontzentrazioaren dinamikak ezberdinak direla frogatzen da. Emaitza hauek, transformazio martensitikoaren tenperaturaren doikuntzan hutsuneek duten garrantzia frogatzen dute.

Emaitza hauekin lotuta, Hedayati *et al.*-ek lortutako emaitzak eztabaidatzen dira. Hauek, Ni-Mn-Sn aleazioen transformazio martensitikoa Sn atomoen hutsuneen kontzentrazioaren bidez alda daitekela baieztatzen dute, baina ez dute Sn atomoen hutsuneen inongo froga esperimetalik plazaratzen. Tesi honetan Ni-Mn-Sn aleazioetan agertzen diren hutsuneak Ni atomoaren hutsuneak direla frogatzen da. Bestalde, hutsune hauen kontzentrazioa oso handia dela frogatzen da, lagin hauei egiten zaien suberaketa-tratemendua edozein delarik ere. Horrela, tratamendu bidez hutsuneak kontrolatzearen atazak ez dirudi eraginkorra denik Ni-Mn-Sn laginetan.

Bukatzeko, azken kapituluan tesi honen helburu nagusiak azaltzen dira, kapitulu bakoitzaren kasurako lortutako emaitzak eta ondorioak laburbilduz.

Aknowledgments

"Eta mundu zabor honek ezin dastatu, zapore hori, zapore hori..."

- Doktors Klub, Papargorrixe

Lehenik eta behin, bost urte hauetan tesia aurrera eramaten lagundu didaten Jose Angel eta Fernando Plazaolari eman nahi dizkiet eskerrak, batez ere doktoretza egiteko aukera eman eta nigan konfidantza izatearren. Sekula ez dut ahaztuko eman didazuen aukera, horri esker bait nago gaur hemen. Eskerrik asko, benetan! Bestalde, ikerketa munduan emaniko lehen urrats hauetan eman didazuen laguntza ere eskertu nahi dizuet, baita ikerketa-eremutik kanpo erakutsi didazuen guztia ere. Mundu honetan murgiltzeko jakin behar denaren zati handi bat zuei esker ikasi dut.

Bigarrenik, eskerrak eman nahi dizkiet Aitziber Anakabe eta Nerea Otegiri ere, doktoretza egitearen zalantzak nituenean animoak eman eta saiatzeko esan zidatelako. Une horretan zin egin nion nire buruari, egunen batean tesiren bat egin eta bukatzen banuen, eskerretan agertuko zirela. Bestalde, hasiera batetik laborategian lagundu didaten David Merida, Estibaliz Legarra eta Eneko Axpe doktoreak (ea espaziotik noiz jeisten zaren....jajaja) ere eskertu nahi ditut, gaur egun laborategian dakidan dena zuek ereindako hazitik sortu delako. Zentzu honetan Jose Angeli ere esker bereziak eman nahi dizkiot, bere laguntza teknikoa izugarria izan baita!

También quiero agradecer a Iñaki Orue, Valentin Toyos y Jorge Feuchtwanger. El valor añadido que tiene el trabajo desinteresado que habéis hecho (y hacéis) no tiene precio. Debería haber una figura correspondiente a la labor que hacéis, qué pena que las instituciones no lo sepan valorar. Garitari ere eskerrak eman nahi dizkiot zalantza garrantzitsu asko argitzen lagundu didalako. Itzalean egonik ere asko lagundu didazu. Ezin Elektrizitate eta Elektronika departamentuari eskerrak eman gabe gelditu. Oso departamentu atsegina izateaz gain, beti egon zarete niri laguntzeko prest, eta benetan eskertzen dut hori. Familia txiki bat dirudi eta hasiera batetik sentitu naiz departamentuaren parte. Pilar, a ti también te doy las gracias, aunque a veces la burocracia nos haya vuelto un poco loco a los dos... a ver cuando me paso otra vez para que me pagues...que se yo...las facturas de casa?! jajaj!

Que decir sobre el tridente de UPNA, Vicente Sánchez-Alarcos, Vicente Recarte e Iñaki, siempre dispuestos a echar una mano...y no una mano cualquiera, no, una mano eficaz. Vuestro apoyo ha sido vital para la consecución de esta tesis. Desde la acogida que me habéis hecho en vuestro laboratorio para realizar las muestras, hasta los debates cieníficos que hemos tenido, que sin duda han sido claves para indagar en la parte científica del trabajo realizado. Sois muy buena gente y sabéis muchísimo. Os agradezco todo lo que me habéis aportado. No me quiero de olvidar de Javier López García (todavía nos queda faena que cerrar), Jesus (pisha), Silvia Larumbe y José Alberto Velamazán. Ciertamente vuestra contribución ha sido clave para la interpretación de los resultados.

Eskerrak eman nahi dizkiet Raúl Vera (ho aconseguirem), David Brizuela, Ibon Alonso, Iñaki Garay, Oscar Ecenarro, Ruth Lazkoz, Idoia, Asier Eiguren, Gabriel, Jon Sáenz eta Josu Martinez Perdiguero irakasleei ere, dozentziako lehen klaseak emateko aukera eskaintzearren. Esperientzia bikaina izan da, eta irakasgaiaren parte aktibo sentiarazi nauzue beti. Eskerrik asko! Eskerrak (eta animoak) Aritz Leonardori ere, lan izugarria egiten duzu gauza guzti horien ardura hartuz!!!

On the other hand, I would like to specially thank the eMS-collaboration. It's been a while since I met you all at CERN. Some people are not longer within the collaboration but I still considered them as members. In this sense, I would like to thank Torben for all the given support, both from scientific and personal point of view. It was a pleasure to share the live with you, Cristina and Sofía in Champ FFUSSY! I really miss these days ("lately, you've been living on the outside lane..."). Additionally, I would like to specially thank Haraldur Palle Gunnlausgsson, Roberto Mantovan, Karl Johnston, Deena Daido and Hilary, that along with senior members, are the main kernel of the collaboration. You make this collaboration to be possible. Additionally, many thanks to Juliana Schell for your constant disposition. It goes without seeing that I also have in mind the remaining members that I had the pleasure of metting; Sveinn and Yury (it was a nice walk in Alps), Aitana, Petko, Mehluli, Krish, Vanthini, Dimitri, Bing, Haflidi, Andrei, Radjeep, Kimara, Gerrard, Guido, Emil, Adelegh, Lino Guillerme, and many others that for sure I forget to mention. It was a pleasure to share with you the good and hard times, specially with the beloved Rubidium 0_o Looking forward to see you all again at WEMS2019 in Bilbao!

Arlo zientifikoa alde batera utzita, arlo pertsonalean ezinbestekoak izan diren

pertsonak aipatu nahi nituzke jarraian. Zentzu honetan, nola ez, GNT-tik hasi beharra daukat. Besarkada bero eta handi bat eman nahi diet bere sortzaile izan diren Joanes, Ekhi (ikaskide eta lagunak biak), Jokin (profesor en mejico), Asier (arraunien ia noz guezan galdetzen dotza Perez-ek ondiok) eta Julen Simon (Vol Damn! eta filosofia) kideei, baita gerora gehitzen joan diren eta inguruan ibili diren guztiei ere; Mattin (bukatu behingoz poster hori dedio), Iñigo (barru), Peio (hurrengokue zu, ikusikozu. Eurre), Jon (maitasunezko txalo bat zuretzat), Haritz (zeamako ure), Iagoba Apellaniz (ñaaaak) Ibai Aedo, Aitzol eta Julen Getari (nun lagaek txakolin botila?). Badakit honek betiko topikoa dirudiela baina benetan, oso garrantzitsuak izan zarete denbora guzti honetan. Espero dut betirako lagun talde bat izatea, "ez dadila haria eten".

Ezin aipatu gabe utzi goizetako kafe ordua posible egin duzuen guztiak; Luis Elcoro, Josu Igartua, Josu Ortega, Irene Urcelay, Raúl, Jon Sáenz, Estibaliz, Iñigo Etxebarria, Jon Urrestilla, Alan... Eskerrak Fisika Apikatua II eta Materia Kondentsatuko departamentuko irakasle eta kideei ere. Departamentukoa izan ez arren etxean bezala sentiarazi nauzuelako. Bestalde, unibertsitatean daramadan denboran zehar zuen jakintza irakasten ibili zareten irakasleak ere eskertu nahi ditut, zuek egindako lanagatik heldu naiz eta orain nagoen tokira.

Bestalde, bekadromotik igaro direnak aipatu nahi nituzke, oso momentu honak igaro ditut bertan. Egia da leiho bat edukiko bagenu ba beno, erosoagoa izango zela (borrkak aurrera darrai, ez etsi). Besarka bat denoi; Luca, Anabel, Jorge, Irati, Maite, Bea, Olaia, Edu, Eneko Garaio (pipertermia) eta beno...Chernenkoren troparen baitan etorri diren milioika eta milioka kideei ere :). Departamentu honetan ezagututako asko ere agurtu nahi nituzke, hala nola, Iván Aseguinolaza, Lulu, Estibaliz Asua, Raquel Justo, Inari, Libe, Popi, Mireia, Salazar, Josu Jugo, Nerea Zabala, Javi Etxanobe, Amparo Varona, Juan Mari Collantes, Alfredo, Manu, Patricia, Malu, Javi Alonso Massa ta Hamilton, Andoni, Katarina...eta aipatu gabe gelditzen direnak ere. Doktoretzan zehar ezagutu ditudan beste departamentu batzuetako doktoretza-ikasleak ere aipatu nahi ditut; Pablo (no olvidaré el momentazo en la antecima de Mont Blanc, abrazados, cuando vimos que lo que llevabamos planteando desde hace mucho tiempo, se iba a convertir en realidad. Fuiste un compañero de cordada excelente, amigo!), Borja, Laura, Santi (eskerrikasko Meteocielzer den erakustearren), Joao, Iker, Unai .... Bukatzeko, Asier Garateri be eskerrak emotie gureko neuke, *machine gun* irudixek etten laguntziarren.

Azkenik, Ane neskalagunari ere eman nahi dizkiot eskerrak. Bai, neskalaguna da bai, baina nik doktoretza bukatu izanaren merituaren zati bat berea ere bada, goizetan ohean "ardi zaharrak" bezala botata egotetik, eskutik heldu eta ni jaikitzera bultzatu nauelako. Ez dut uste unibertsitatera horren goiz helduko nintzatekeenik beragatik izango ez balitz. Amaitzeko, nire attetxo, arrebie, Antton eta Lur ere aipatu gure duaz. Batez be atte, zuk eta Amatxok hasi eta hezi doztezue, eta dana emon dozue nik guzti hau ein ahal izeteko. Oihantxu eta Antton, zuei be bai, familixako momentu zalletan hor egotiarren eta eukin dozuen dana emotiarren. Zuei seiroi eskeinite due lan hau, Maitte zattuet!

List of Publications

This thesis is supported on the following publications:

Chapter 2: Experimental Techniques

1. I. Unzueta, N. Zabala, V. Marín-Borrás, V. Munõz-Sanjosé, J. A. García, F. Plazaola
Observation of a Charge Delocalization from Se Vacancies in Bi_2Se_3: A Positron Annihilation Study of Native Defects,
Physical Review B **94**, 014117 (2016).

Chapter 3: Crystallization Dynamics of Disordered Ni-Mn-In Alloys

2. S. Larumbe, I. Unzueta, V. Sánchez-Alarcos, J. I. Pérez-Landazábal, V. Recarte, J. A. García, F. Plazaola
Low Temperature Magnetic Properties of a $Ni_{50}Mn_{34}In_{16}$ Ball-Milled Metamagnetic Shape Memory Alloy,
Journal of Non-Crystalline Solids **447** 16 (2016)

3. V. Sánchez-Alarcos, V. Recarte, J. I. Pérez-Landazábal, S. Larumbe, R. Caballero.Flores, I. Unzueta, J. A. García, F. Plazaola, J. A. Rodríguez-Velamazán

Mechanically Induced Disorder and Crystallization Process in Ni-Mn-In Ball-Milled Alloys,
Journal of Alloys and Compounds **689** 983 (2016)

Chapter 4: Effect of Internal Strains in the MT in Ni-Mn-Sn

4. I. Unzueta, J. López-García, V. Sánchez-Alarcos, V. Recarte, J. I. Pérez-Landazábal, J. A. Rodríguez-Velamazán, J. S. Garitaonandia, J. A. García, F. Plazaola
^{119}*Sn Mössbauer Spectroscopy for Assessing the Local Stress and Defect State Towards the Tuning of Ni-Mn-Sn Alloys*,
Applied Physics Letters **110**, 181908 (2017)

5. J. López-García, I. I. Unzueta,V. Sánchez-Alarcos, V. Recarte, J. I. Pérez-Landazábal, J. A. Rodríguez-Velamazán, J. A. García, F. Plazaola
Correlation Between Defects and Magneto-Structural Properties in Ni-Mn-Sn Metamagnetic Shape Memory Alloys,
Intermetallics **94**, 133 (2018)

6. I. Unzueta, J. López-García, V. Sánchez-Alarcos, V. Recarte, J. I. Pérez-Landazábal, J. A. Rodríguez-Velamazán, J. S. Garitaonandia, J. A. García, F. Plazaola
^{119}*Sn Mössbauer Spectroscopy in the Study of Metamagnetic Shape Memory Alloys*,
Hyperfine Interactions **239**, 34 (2018)

7. V. Sánchez-Alarcos, J. López-García, I. Unzueta, J. I. Pérez-Landazábal, V. Recarte, J. Beato-López, J. A. García, F. Plazaola, J. A. Rodríguez-Velamazán
Magnetocaloric Effect Enhancement Driven by Intrinsic Defects in a $Ni_{45}Co_5Mn_{35}Sn_{15}$ *Alloy*,
Journal of Alloys and Compounds **774**, 586 (2019)

Chapter 5: Vacancy Defects in Ni-Mn-Z and Ni-Fe-Ga Alloys

8. I. Unzueta, D. Alonso de R-Lorente, E. Cesari, V. Sánchez-Alarcos, V. Recarte, J. I. Pérez-Landazábal, J. A. García, F. Plazaola,
Experimental Observation of Vacancy Assisted Martensitic Transformation shift in Ni-Fe-Ga alloys,
Submitted to Physical Review Letters (Under Review)

9. I. Unzueta, V. Sánchez-Alarcos, V. Recarte, J. I. Pérez-Landazábal, N. Zabala, J. A. García, F. Plazaola
Identification of a Ni-Vacancy Defect in Ni-Mn-Z (Z = Ga, Sn, In): An experimental and DFT Positron-Annihilation Study,
Physical Review B **99**, 064108 (2019)

Other publications related to the work carried out during the thesis:

10. A. M. Gerami, K. Johnston, H. P. Gunnlaugsson, K. Nomura, R. Mantovan, H. Masenda, Y. A. Matveyev, T. E. Mølholt, M. Ncube, S. Shayestehaminzadeh, I. Unzueta, H. P. Gislason, P. B. Krastev, G. Langouche, D. Naidoo, S. Olafsson, ISOLDE Collaboration,
^{57}*Fe Emission Mössbauer Spectroscopy Following Dilute Implantation* ^{57}*Mn into* In_2O_3,
Hyperfine Interactions **237** 75 (2016).

11. P. B. Krastev, H. P. Gunnlaugsson, K. Nomura, V. Adoons, A. M. Gerami , K. Johnston, M. Ncube, R. Mantovan, H. Masenda, Y. A. Matveyev, T. E. Mølholt, I. Unzueta, K. Bharuth-Ram, H. Gislason, G. Langouche, D. Naidoo, S. Olafsson, ISOLDE Collaboration,
^{57}*Fe Emission Mössbauer Study on* $Gd_3Ga_5O_{12}$ *Implanted with Dilute* ^{57}*Mn*,
Hyperfine Interactions **237** 37 (2016).

12. T. E. Mølholt, H. P. Gunnlaugsson, K. Johnston, R. Mantovan, J. Röder, V. Adoons, A. M. Gerami, H. Masenda, Y. A. Matveyev, M. Ncube, I. Unzueta, K. Bharuth-Ram, H. P. Gislason, P. B. Krastev, G. Langouche, D. Naidoo, S. Olafsson, A. Zenkevich, ISOLDE Collaboration,
Charge States and Lattice Sites of Dilute Implanted Sn in ZnO,
Journal of Physics: Condensed Matter **29** 15 (2017)

13. B. Qia, H. P. Gunnlaugsson, A. M. Gerami, H. P. Gislason, S. Olafsson, F. Magnusa, T. E. Mølholt, H. Masenda, Aitana Tarazaga Martín-Luengo, A. Bonanni, P. B. Krastev, V. Masondo, I. Unzueta, K. Bharuth-Ram, K. Johnston, D. Naidoo, J. Schell, P. Schaaf, ISOLDE Collaboration,
^{57}*Fe Mössbauer Study of Epitaxial TiN Thin Film Grown on Mg (100) by Magnetron Sputtering*,
Applied Surface Science **464** 682 (2019)

List of Figures

List of Tables

List of Abbreviations

$\overline{\tau}$	Average Positron Lifetime
AF	Antiferromagnetic
APB	AntiPhase Boundaries
AQ	As-Quenched
DSC	Differential Scanning Calorimetry
eMS	Emission Mössbauer Spectroscopy
FC	Field Cooling
FH	Field Heating
FM	Ferromagnetic
FWHM	Full Width at Half Maximum
$\mathbf{I}_s$	Intensity of the Singlet Component
MCE	MagnetoCaloric Effect
MS	Mössbauer Spectroscopy

PPAD Parallel Plate Avalanche Detector

PALS Positron Annihilation Lifetime Spectroscopy

PM Paramagnetic

PND Powder Neutron Diffraction

RKKY Ruderman-Kittel-Kasuya-Yosida

SEM Scanning Electron Microscope

^{119}**Sn-MS** ^{119}Sn Mössbauer Spectroscopy

TEM Transmission Electron Microscopy

$\mathbf{T_i}$ Maximum Isochronal Annealing Temperature

$\mathbf{T_{MT}}$ MT Temperature

XRD X-Ray Diffraction

ZFC Zero Field Cooling

1 Introduction

FUNCTIONAL materials, also known as active or smart materials, represent a set of advanced compounds and composites in which a technologically interesting property undergoes a substantial change in response to an external stimuli [1]. These materials present a plethora of properties and functionalities such as ferroelectricity, thermoelectricity, piezoelectricity and shape memory effect among the most relevant. These functional properties, in turn, lead to potential applications in energy storage technologies, in magneto and electrostrictive materials for sensors and actuators, in the field of phase transforming materials, and also in modern functional coatings and films [2, 3, 4]. Due to the increasing demand of materials exhibiting plural functionalities, the development of novel active materials represent a fast growing field due to the pivotal role they acquire for the advance of materials science.

In the quest of materials exhibiting a wide range of multifunctional properties, the so-called Heusler compounds are consolidating as promising candidates in many of contemporary research fields. Owing to their extremely flexible electronic structure [5], Heusler compounds exhibit a wide spectrum of potential applications, ranging from magnetic and magneto-mechanical materials, semiconductors, superconductors and thermoelectric materials, up to compounds for spintronic applications [6, 7]. Indeed, since the discovery of half-metallic ferromagnetism in Ni-Mn-Sb and also, both, shape memory effect and large magnetic field-induced strain in Ni_2MnGa [8],

Heusler alloys are receiving an increasing interest within the experimental and theoretical framework [9].

1.1 Structure of Heusler Alloys

Heusler alloys were discovered in 1903, when Fritz Heusler realized that Cu_2MnAl behaves like a ferromagnet even though none of its constituent elements are FM in their pure state [10]. Currently, the so-called Heusler compounds comprise a vast collection of more than 1000 compounds. In a nutshell, these compounds are a ternary, magnetic and intermetallic compounds defined by the generic X_2YZ formula (full-heusler)[1], where X and Y are transition metals, and Z belongs to IIIA (13), IVA (14) or VA (15) groups of the periodic table [5].

As shown in Fig. 1.1, the Heusler structure consists in four interpenetrating face centered cubic sublattices where atoms are placed at A(0,0,0), B(1/2,1/2,1/2), C(1/4,1/4,1/4) and D(3/4,3/4,3/4) position, resulting in a $L2_1$ crystal structure, (space group $Fm\bar{3}m$ N° 225). In stoichiometric fully ordered Heusler alloy, A, B, C and D positions are occupied by Z, Y, X and X elements respectively. In other words,

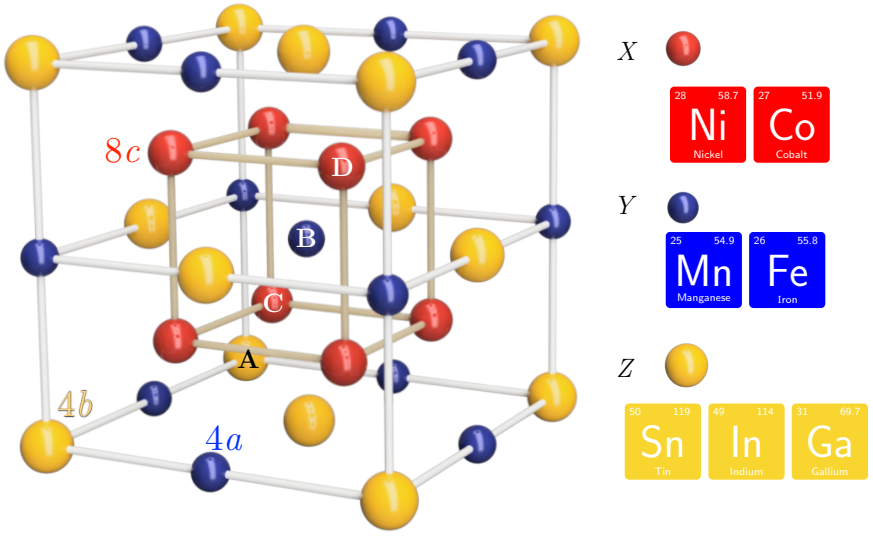

Figure 1.1: The $L2_1$ crystal structure of X_2YZ Heusler alloys. The type X, Y and Z elements employed during this thesis are Ni, Co, Mn, Fe, Sn, In and Ga.

[1]The intermetallic ternary compounds with the generic XYZ expression are known as half-Heusler alloys

X atoms occupy the $8c$ Wyckoff positions (C and D), and Y and Z are located at $4a$ (B) and $4b$ (A) Wyckoff positions, respectively. However, a fully ordered Heusler compound is not always attainable, and in practice there is always some degree of chemical disorder present in Heusler alloys. For example, when X remains unaltered and the disorder occurs between Y and Z positions, the structure changes from the $L2_1$ to a B2 structure ($Pm\overline{3}m$ space group N^o 221). Moreover, if the constituent atoms are randomly occupying X, Y and Z positions, Heusler alloys exhibit an additional crystal structure, which is A2 (space group Im$\overline{3}$m N^o 229) [11]. B2 and A2 phases are high-temperature phases.

In addition to the high-temperature phases described above, several Heusler compounds undergo the so-called martensitic transformation (MT). As a result, an additional structural phase is observed at lower temperatures. Indeed, the occurrence of such phase transition is the primary mechanism which gives rise to the wide range of multifunctional properties that Heusler alloys exhibit. Owing to the magnetostructural coupling, structural modifications are generally related to substantial changes on magnetic properties. This interplay between structure and magnetism allows their concurrent tuning, enabling an optimization of the multifunctional properties as well.

1.2 Martensitic Transformation in Heusler Alloys

The MT is a solid-state first order phase transformation, which takes place between a highly symmetric cubic structure (also referred as austenite) and a low symmetric martensite phase. Being a first order phase transition, both, parent and martensite phases coexist during the transformation, and unlike in order-disorder transitions, the MT takes place via dominant shear mechanism. The MT is defined as a lattice deformation involving shear deformation, which results in non-diffusional cooperative movement of the atoms in the crystal [12]. In essence, during the MT there is no long-range displacement of atoms. The driving force of the MT is rooted on electronic properties and its microscopic origin is associated with the Jahn-Teller splitting mechanism [13, 14]. However, most of the theoretical explanations concerning the underlying mechanism of the MT are phenomenological studies based on the free energy.

For simplicity, let's suppose that the Gibbs free energy[2] of the martensite and austenite phases, G^M and G^A respectively, are decreasing linear functions of temperature [15]. As shown in Fig. 1.2, in the intersection of these two curves a thermodynamic equilibrium state is achieved, and the difference between the Gibbs energy of the austenite and martensite phases is null. This point, T_0, is often called the equilibrium temperature. As it is illustrated in Fig. 1.2, for temperatures $T < T_0$ the

[2] $\Delta G = \Delta H - T\Delta S$ where ΔH is the enthalpy change and ΔS the entropy change.

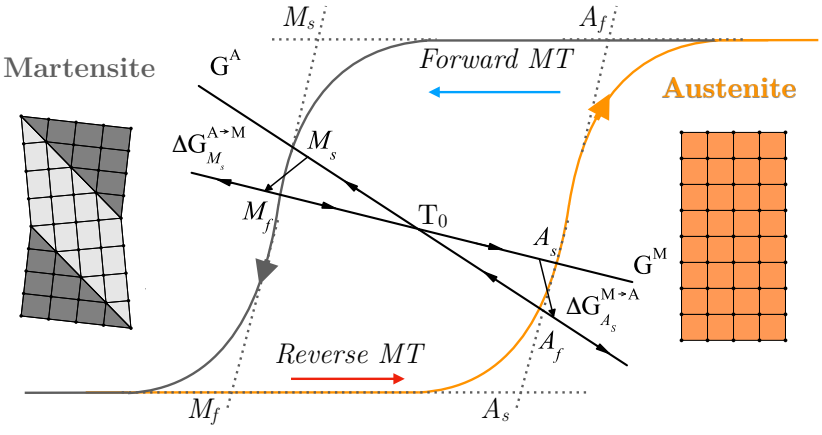

Figure 1.2: Illustration of the hysteresis loop between the direct and forward MT. The grey and orange curves indicate cooling and heating directions respectively. Austenite start and finish temperatures are defined as A_s and A_f, while martensite start and finish temperatures are labelled as M_s and M_f.

martensite phase is more favorable than the austenite phase, while for $T > T_0$, the austenite phase is thermodynamically favored. Thus, depending on the temperature and on the existing driving forces ($\Delta G^{M\to A}_{A_s}$ and $\Delta G^{A\to M}_{M_s}$), the austenite phase can transform to the martensite phase and *vice versa*.

One characteristic feature of MT is the hysteresis that the transformation exhibits. Due to that, the temperature dependence of several physical magnitudes such as, resistivity, magnetization, electrical conductivity, transformation related heat-flow etc. display the same qualitative behavior, which is illustrated in Fig. 1.2. Upon cooling, the high temperature austenite phase undergoes the MT at M_s (martensite start temperature). During the transformation, both martensite and austenite phases coexist until at M_f (martensite finish temperature), all the sample is transformed to the martensite phase. The MT that takes place during cooling is called as the forward MT. On the other hand, during the reverse MT (i. e., on heating) the martensite starts transforming to austenite at A_s (austenite start temperature). The process if fulfilled after A_f temperature (austenite finish temperature), when all the sample is transformed to the austenite phase. As a result, the width of the hysteresis is given by the difference between A_f and M_s. As pointed out before, the characteristic temperatures can be determined by analyzing the evolution of several physical magnitudes, which exhibit a substantial change during the MT.

Magnetic measurements and Differential Scanning Calorimetry (DSC) measurements represent the most widely used techniques for the determination and the characterization of the MT in martensitic Heusler compounds. On the one hand, by means of DSC measurements the characteristic temperatures, i. e., magnetic transition temperature T_c and MT temperature T_{MT}, can be directly obtained. In Fig. 1.3 (left), the typical DSC response to the MT is depicted. The two largest endothermic and exothermic peaks are related to the enthalpy of the structural transition

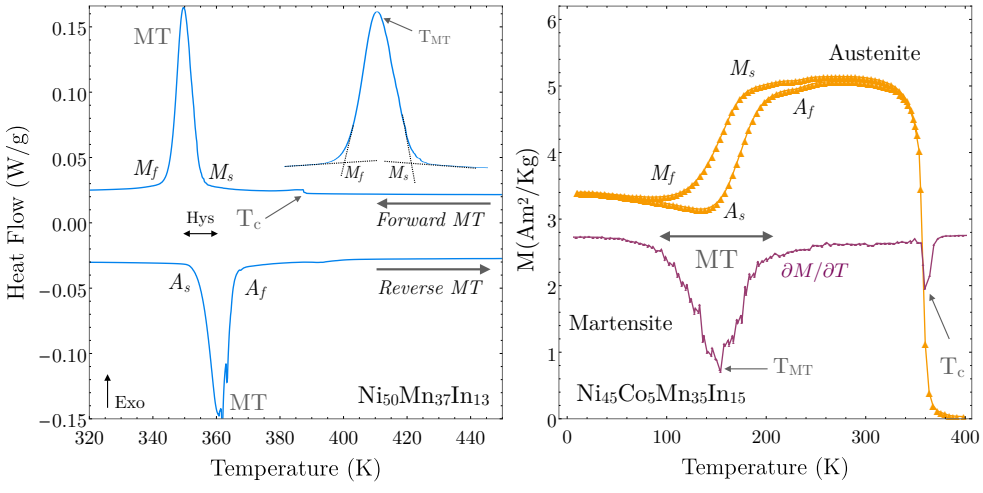

Figure 1.3: Characteristic features that DSC and $M(T)$ measurements present during the MT. (left) The exothermic and endothermic peaks that DSC shows on cooling and on heating determines the T_{MT} and T_c. (right) Regarding the $M(T)$ curves, T_c and T_{MT} characteristic temperatures are calculated from the peaks of the $\partial M/\partial T$ curve.

(MT). In the present case, the exothermic peak is related to the direct MT, whereas the endothermic peak indicates the reverse MT. Regarding the determination of the T_{MT}, the most commonly used method is the intersection method. The intersections of the tangent lines drawn at the start and at the end of the transformation peaks are accepted as the transformation temperatures, see Fig. 1.3. The λ type shoulder, which is noticed by a change of the baseline height around 390 K, is related to the T_c ferromagnetic-paramagnetic (FM-PM) or Curie's magnetic transition.

As previously said, magnetic measurements are also used to characterize the MT, even more when MT takes place at such low temperatures that DSC cannot operate. Regarding magnetic measurements, the $M(T)$ thermomagnetization curves corresponding to a standard ZFC-FC-FH sequence are shown in Fig. 1.3 (right). The purpose of this sequence is to characterize the structural and magnetic transitions that may take place in the scanned temperature range. Prior to the $M(T)$ measurement, the sample is prepared in a Zero-Field-Cooled state (ZFC). Starting from a PM state, the sample is cooled down to the lowest temperature possible ($\approx$ 5 K) in the absence of magnetic fields. Afterwards, a relatively low external magnetic field (e. g., 0.01 T) is applied, and the sample is heated while measuring the corresponding magnetization. Subsequently, the sample is again cooled down but without removing the applied magnetic field (field-cooled (FC)). Finally, a last heating cycle is performed without removing the magnetic field, where the magnetization is measured as the temperature increases (FH). In this way, the occurrence of the MT can be detected due to the fact that any hysteresis in the FC-FH sequence is expected to be associated with a structural transition [16]. Indeed, the hysteric behavior of the mag-

netization between 100-200 K depicted in Fig. 1.3 is the fingerprint of the occurrence of the MT. Moreover, and as it will be seen in Chapter 3, the splitting between the ZFC and FC curves below FM transition temperatures reveals the coexistence of AF exchange interactions [16]. On the other hand, the sudden drop of the magnetization at ≈ 390 K reveals a magnetic transition at T_c.

Although the initial studies on Heusler compounds were focused from the structural and magnetic point of view, the research on Heusler compounds has been directed to the multifunctional properties they exhibit. Due to the complex interplay between the crystal structure and the magnetism, the martensitic Heusler alloys are particularly interesting for fundamental investigations. In particular, the so-called magnetic shape memory alloys have attracted a great interest because they exhibit the magnetic shape memory effect. This effect takes place specially when the Y species are Mn and Fe, being other transition elements also possible [16].

In this regard, Ni_2(Mn,Fe)Z (Z = Ga Sn, In) Heusler alloys are subject of intense research due to the wide range of multifunctional properties they exhibit, such as large magnetic-field-induced strain [8, 17], magnetorresitivity [18, 19], the magnetocaloric effect [20, 21, 22, 23], exchange bias [24, 25] and the shape-memory effect [26], consolidating as potential candidates for applications in spintronics, solar cells, energy harvesting applications and solid-state refrigeration technologies [27].

1.3 Ni-Fe-Ga and Ni-Mn-Z (Z =Sn, In) Heusler Alloys

In the so-called ferromagnetic shape memory alloys, the MT is a reversible process. By means of a field-induced reorientation of the martensitic variants, it is possible to develop magnetically induced strain [29] and shape memory effect. Indeed, this reorientation of the variants is driven by the motion of twin boundaries. Since the discovery of large magnetic-field-induced strains up to 10% in Ni_2MnGa single crystals [8, 17], Ni-based Heusler alloys have been subject of intense research. However, the defective mechanical properties and the brittleness of Ni-Mn-Ga system, by far the most studied up to now, have promoted the research on other ferromagnetic shape memory alloy systems (e. g., Co-Ni-Ga and Co-Ni-Al among others), which exhibit better mechanical properties and enhanced actuation. In particular, Oikawa *et al.* [30] realized that the toughness and the mechanical properties of Ni-Mn-Ga systems can be drastically improved through the replacement of the Mn constituent by Fe.

As a result, Ni-Fe-Ga systems are attracting an increasing interest due to their enhanced mechanical properties and deformation behavior they exhibit [31, 32, 33]. Recently, a giant reversible elastocaloric effect has been reported in Ni-Fe-Ga alloys near room temperature [34]. The improved ductility performance in bulky off-stoichiometric samples makes Ni-Fe-Ga system a promising alternative to the classic

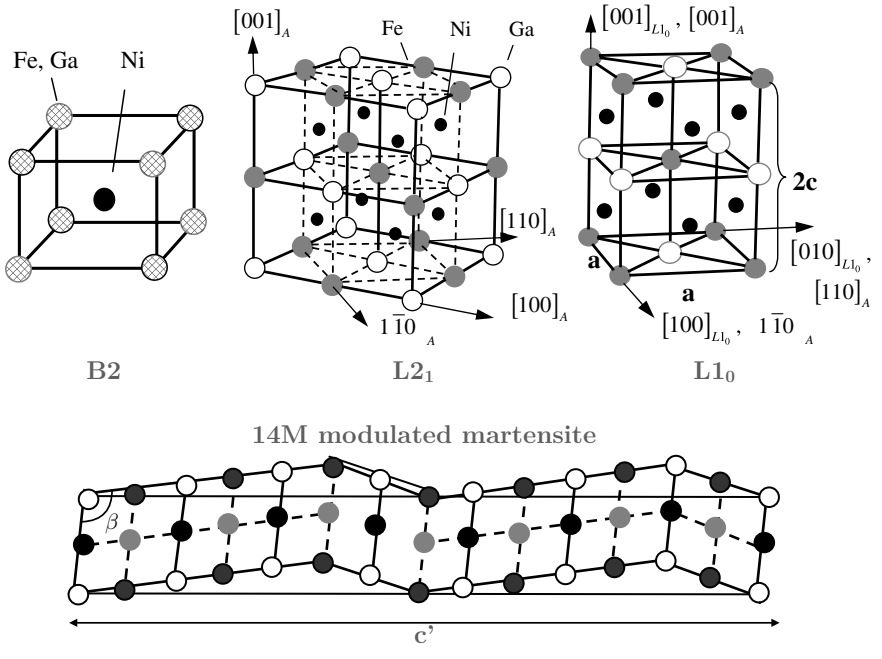

Figure 1.4: B2, $L2_1$ austenite and tetragonal $L1_0$ crystal structures of Ni-Fe-Ga alloys. The structure in the bottom shows the 14M modulated martensite structure composed by a monoclinic unit cell [28].

Ni-Mn-Ga alloys [35]. Moreover, the modulated martensite of Ni-Fe-Ga systems also facilitates obtaining large magnetic field induced strains [36]. Compared with Ni-Mn-Ga systems, in Ni-Fe-Ga alloys T_{MT} can be easily increased by slight variations in its compositions. Indeed, the composition can be tuned to get T_{MT} near room temperature [30] while T_c can be increased up to 430 K [37].

Fig. 1.4 shows several crystal structures of Ni-Fe-Ga alloys. When Ni atoms (X site) remain ordered, but a full disorder occurs between Fe and Ga atoms (Y and Z sites respectively, according to Fig. 1.1) a B2 structure is obtained, which in turn, is a high temperature phase that the parent NiGa system exhibits. A proper doping of Fe in Ni-rich NiGa alloys enables the crystallization of the $L2_1$ structure at lower temperatures. The ordering transition from B2 to $L2_1$, which naturally depends strongly on composition, takes place at $T_{L2_1\text{-}B2} \approx 900$ K. In addition to the crystallization of $L2_1$ structure, Fe doping also enables the occurrence of MT, which takes place in a wide range of temperatures depending on composition. As depicted in Fig. 1.4, in $L2_1$ structure Ni atoms are located in $8c$ positions and Fe and Ga atoms in $4a$ and $4b$ ones respectively (see Fig. 1.1). The transition from $L2_1$ to the martensite phase results in a low temperature tetragonal $L1_0$ phase. However, it is also possible to obtain a modulated martensite phases and inter-martensitic transitions through 10M (5 modulation period, not shown here) and 14M (7 modulation period) structures.

The 14M martensitic structure is shown in the bottom of Fig. 1.4, which is composed of a unit cell with monoclinic crystal structure [28].

Fe doping in NiGa parent phase, along with enabling the occurrence of MT, is also the responsible of the ferromagnetic nature that $L2_1$ phase exhibits. The magnetism in Ni-Fe-Ga systems is mediated by indirect-exchange interactions between Fe-Fe atoms trough conduction electrons [38, 39]. In fact, the exchange interactions between intra-lattice atoms show oscillating behavior, signifying the existence of indirect exchange through Ruderman-Kittel-Kasuya-Yosida (RKKY) interactions [33]. Thus, Fe atoms play an important role in the improvement of the magnetization. In this context, inter-lattice interactions between Fe atoms are comparatively stronger than intralattice interactions. As a result, the magnetic behavior is dictated by inter-lattice Fe-Fe interactions. Unlike in Ni-Mn-Ga alloys, where the dominant AF behavior is observed in Mn-Mn inter-lattice interactions, in Ni-Fe-Ga systems the exchange parameters are dominated by FM interaction [33]. For example, in off-stoichiometric conditions, the magnetic moment related to Fe atoms located at Ni positions ($1.99\mu_B$), is lower compared with the related moment of a Fe atom in a stoichiometric alloy ($2.9\mu_B$, but still positive). However, the exceeded Fe atom carries a magnetic moment value of $3\mu_B$ when it is located at Ga positions [33].

In ferromagnetic shape memory alloys, such as Ni-Mn-Ga and Ni-Fe-Ga systems, the MT takes place between similarly ordered magnetic phases. As pointed out before, the magnetic actuation occurs by variant reorientation in a ferromagnetic martensite phase. However, in order to observe the magnetic shape memory effect, the magnetic driving force should be high enough to allow the motion of phase fronts or variants. Thus, the low magnetization discrepancy ΔM of the MT of Ni-Mn-Ga and Ni-Fe-Ga systems, which is the difference between austenite and martensite phases, presents the main drawback for exhibiting the field induced MT. Due to the similar magnetic nature of the parent and martensite phases, the field induced phase transformation in Ni-Mn-Ga and in Ni-Fe-Ga systems is often hindered [40]. It only takes place under special conditions; at temperatures close to A_s or when a certain phase is observed before a modulated phase [41]. In this connection, the so-called metamagnetic shape memory alloys Ni-Mn-Z (Z = In, Sn, Sb) have attracted a considerable attention since, due to their metamagnetic character, they are able to exhibit magnetic field-induced phase transformation. The metamagnetic behavior that these alloys exhibit refers to the sudden transition they experience from a low magnetization state to a high magnetization state during MT (and *vice versa*).

Despite the case of Ni-Fe-Ga and Ni-Mn-Ga [42], in the so-called metamagnetic shape memory alloys the MT may take place between a ferromagnetic austenite phase and a weak magnetic or paramagnetic martensite phase [26]. The change in interatomic distances caused by the MT alters the magnetic exchange interaction. As a result, the magnetic properties, and even the type of the magnetic ordering of the resulting structural phase, is different with respect to the magnetism of the parent phase [15]. This magnetization discrepancy ΔM between the austenite and martensite phases creates a Zeeman energy term, which is the main source, or the driving force for field induced phase transformations. Owing to the metamagnetic na-

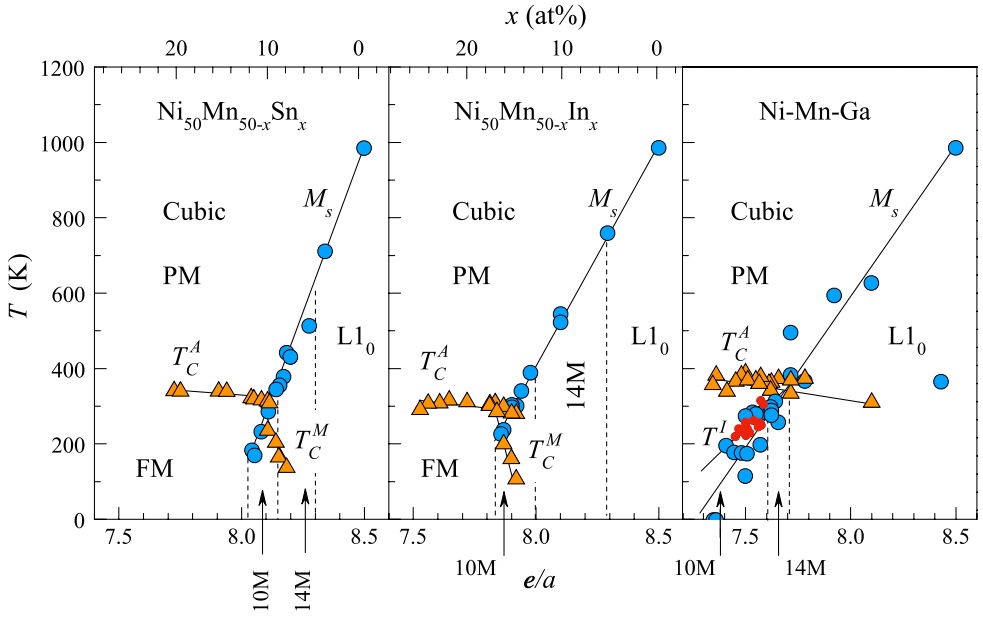

Figure 1.5: Structural and magnetic phase diagram for Ni-Mn-Sn, Ni-Mn-In and Ni-Mn-Ga systems. Triangles indicate T_c while T_{MT} are indicated with circles. The small red circles in Ni-Mn-Ga systems correspond to premartensitic transition temperatures. This picture is adapted from Ref. [20].

ture of the MT, the metamagnetic alloys show additional multifunctional effects such as the inverse magnetic field induced shape-change [43], the inverse magnetocaloric effect [22, 23], kinetic arrest of the martensite [19] and exchange bias effect [24, 25].

The structural phases that metamagnetic alloys display are very similar to those described for Ni-Fe-Ga systems. In the metamagnetic shape memory alloys, the cubic austenitic phase shows the $L2_1$ Heusler crystal structure (space group $Fm\bar{3}m$). According to the crystal structure shown in Fig. 1.1, in stoichiometric Ni-Mn-Z (Z = Sn, In, Sb) compounds, Ni, Mn and Z atoms occupies $8c$, $4a$ and $4b$ positions, respectively. However, unlike what happens in Ni-Mn-Ga and Ni-Fe-Ga systems, the stoichiometric metamagnetic compounds do not exhibit MT since the structural stability of the austenite and martensite phases depends strongly on composition. As shown in Fig. 1.5, the MT starts happening for Sn and In content below 15-16% [44, 16]. Additionally, the structure of the martensite also depends on composition, and several martensite structures appear ranging from 10M and 14M modulated monoclinic martensite [44] and orthorhombic martensite [45, 46]. At low Z contents, the high temperature austenite phase transforms to $L1_0$ tetragonal structure (space group P4/mmm, N° 123), which is the structure of the NiMn compound [20].

Due to the magnetostructural coupling that Ni-Mn-Z (Z = Sn, In, Sb) systems exhibit, the phase transformation is often accompanied with a substantial change of magnetic properties. Although these compounds be metals, the magnetic moments

in these alloys are mainly confined to Mn atoms, carrying a value $\approx 4\mu_B$. The $3d$ electrons belonging to different Mn atoms do not overlap considerably and as described for Ni-Fe-Ga systems, the FM is thought to arise from the indirect exchange interaction through the conduction electrons by means of RKKY interaction. As a result, a successful approach for classifying the metamagnetic alloys is to relate the relevant structural and magnetic parameters with the valence electron concentration e/a. As shown in Fig. 1.5, the e/a ratio varies while the composition changes. In fact, both, T_c and T_{MT} are linear functions of e/a.

The change of interatomic distances during the MT affects directly the magnetic properties of Ni-Mn based Heusler alloys. The cell contraction linked to the MT changes the Mn-Mn distances [15], and due to the RKKY exchange interaction, the coupling between Mn atoms is also modified. What is more, depending on the element Z, both, the lattice parameters and the available conduction electron concentration change, which ultimately affects the intensity of the exchange interaction. Although in stoichiometric conditions the coupling between Mn-Mn atoms is FM, in off-stoichiometric $Ni_{50}Mn_{50-x}Z_x$ ($x = 25,\ 20,\ 16,\ 15,\ 13$,10) compounds, the exceeded Mn atoms tend to occupy the natural position of Z, (i. e., $4b$ positions) [44, 16]. As a result, the reduced distance between the Mn atoms located in $4a$ and $4b$ position may induce an AF Mn-Mn coupling, which decreases the overall magnetism in off-stoichiometric compounds.

1.4 Tuning the Martensitic Transformation

As previously pointed out, all the multifunctional properties that Ni-based Heusler alloys present are directly linked with the occurrence of the MT, Fig. 1.6. Thus, a good control of the parameters that govern phase stability and MT is necessary to optimize the materials design for the improvement of their functional properties. Naturally, this task requires an accurate control of T_{MT} and of the characteristics of MT as well. The temperature at which MT takes place determines the range where the multifunctional properties can be exploited, and therefore, T_{MT} is the most relevant parameter from the application development point of view. For instance, practical household refrigerators require a T_{MT} lying close to RT.

In this regard, the composition presents the main factor affecting the T_{MT} [26, 16, 44, 24]. As shown in Fig. 1.5, slight compositional changes lead to shifts of tens of Kelvins on both, T_{MT} and T_c. Then, by a proper selection of the composition of Ni-based Heusler alloys, T_c and MT temperatures can be tuned according to the required specification. As previously pointed out, the stoichiometric Ni-Mn-In and Ni-Mn-Sn alloys do not exhibit MT, (T_c is ≈ 350 K). When Z is substituted for Mn (keeping Ni at 50%), the T_c decreases. In fact, in $Ni_{50}Mn_{50-x}Z_x$ ($x = 25,\ 20,\ 16,\ 15,\ 13$,10) metamagnetic alloys, the T_{MT} increases when Z atoms are substituted by Mn atoms,

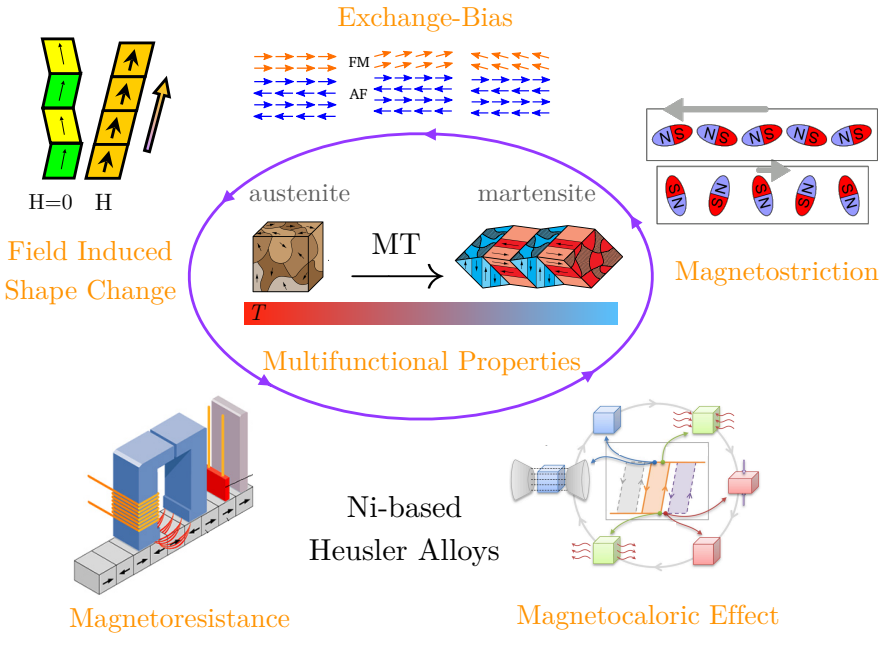

Figure 1.6: The occurrence of the martensitic transformation is on the basis of all the multifunctional properties that Ni-based Heusler exhibit. The proper characterization and the tuning of the MT temperature, as well as the transformation characteristics, is the crux of the matter for optimizing the wide range of the multifunctional properties they exhibit.

while T_c decreases on further increase of Mn content.

When Sn and In concentration reaches $\approx 15\%$, these compounds start exhibiting the MT. For instance, the $Ni_{50}Mn_{35}Sn_{15}$ alloy has T_{MT}= 220 K. In this regard, among $Ni_{50}Mn_{50-x}Z_x$ (x = 25, 20, 16, 15, 13 ,10) systems, $Ni_{50}Mn_{37}Sn_{13}$, $Ni_{50}Mn_{40}Sn_{10}$ and $Ni_{50}Mn_{37}In_{13}$ are the most widely studied samples because they present a T_{MT} that lies slightly above RT. Although the T_{MT} of the $Ni_{50}Mn_{34}In_{16}$ compound lies below RT, this alloy is subject of intense research due to a large inverse MCE related to the MT it exhibits. In addition, owing to PM-FM transition that $Ni_{50}Mn_{34}In_{16}$ alloys present, it gives rise to a fairly large conventional MCE around RT [47].

However, an excessive substitution of Mn in $Ni_{50}Mn_{50-x}Z_x$ (samples far away from stoichiometry) decreases the magnetism due to the AF coupling of Mn-Mn atoms [16]. In order to enhance the magnetic properties of the off-stoichiometric samples, often 3-5% of Ni atoms are substituted for another transition element like Co, which increases the T_c and the magnetism of the austenite phase while reducing T_{MT} [48]. In fact, by Co-doping the magnetism of the martensite phase can be greatly suppressed giving rise to an almost PM martensite phase. As a result of the enhanced ΔM between austenite and martensite phases in Ni-Co-Mn-In alloys, they exhibit a large inverse MCE [27]. In this sense, doping is stablished as an effective

way to tune the characteristic temperatures and the related properties of Ni-based Heusler alloys.

Finally, heat treatments present an effective way to tune the magnetostructural properties of these alloys. The configurational order of the constituent elements of Ni-based Heusler alloys have a great impact in both magnetic properties and MT characteristics. The modification of the lattice site occupancy in the crystal lattice and its subsequent electronic structure modification can be easily performed by means of standard thermal treatments [49]. Standard quenching experiments from B2 phase to $L2_1$ phase allow to retain a portion of the lower atomic order of B2 structure, leading to shifts of tens of Kelvins in both T_c and T_{MT}. Additionally, the metastable phase obtained through quenching can be tuned by means of annealing treatments. In this way, in $Ni_{50}Mn_{50-x}Z_x$ systems the increase on the atomic order increases both T_c and T_{MT}, while in Ni-Fe-Ga systems, T_{MT} is shifted to lower temperatures for larger degree of atomic order.

1.4.1 Drawbacks of Ni-Based Heusler Alloys

As previously pointed out, the T_{MT}, the magnetic properties and the MT of Ni-based Heusler alloys can be tailored by compositional modification, by doping, by different heat-treatments, etc. These approaches are intended to enable a proper tuning of the multifunctional properties thought the tuning of MT and its characteristics. However, despite the promising features that Ni-based Heusler alloys exhibit, they show very poor mechanical properties and their brittleness and fragility present the main drawbacks for their development towards practical devices and applications. As a result, during the last decade, many efforts have been put forward on tailoring the mechanical properties of these systems, which is the crux of the matter for the development of functional elements based on Ni-based Heusler compounds.

In order to surpass the limitations of the bulk material, several alternatives have been investigated during the last years, such as the use of alloys in form of ribbons [50], foams [51] or films [52], as well as embedding shape memory particles in a polymer matrix [53, 54]. As a result, the use of microparticles and powdered samples as active elements is consolidating as an effective approach to overcome the defective mechanical properties [55, 56, 57, 58]. Moreover, it has been recently proposed that below a critical size, shape memory alloy nanoparticles show non-hysteretic behavior [59], becoming a promising alternative procedure to improve simultaneously the mechanical behavior and the related multifunctionalities.

Although the performance of powdered Ni-based Heusler alloys has unique advantages, in such regime, the control of defects, local stresses, internal strains, dislocations etc., acquires a key relevance since they influence directly the MT [60, 61, 62]. Thus, the control of the microstructure becomes even more fundamental in order to enhance the multifunctional properties of micro-particles and films. Recent works also demonstrate that by controlling the microstructure it is possible to properly tune the MT and the related multifunctional properties [63, 64, 65]. In summary, it can be said that powdered samples solve virtually the main drawback that bulk

samples present. However, but it turns out that it gives rise to another issues that must take into consideration in systems tending micro and nano scale.

In recent years, several attempts have been carried out in order to determine the effect that defects have on structural transitions and magnetic properties in different shape memory alloys (Ni-Mn-Ga, Ni-Mn-In and Ni-Mn-Sn) which have been prepared by different methods, such as ball milling or laser ablation [66, 67, 68, 69, 70]. Nevertheless, up to know, much less work have been devoted to the analysis of the MT and the related magnetic properties at reducing sizes tending to micro and nanoscale. This, acquires a key relevance for a proper performance in compounds comprehending Ni-based Heulser alloys based powdered samples. Additionally, a previous thorough characterization of the micro- and nano-particle powders is needed in order to properly tune their performance in such regime.

The grain size and the state of internal-stresses are known to be two parameters highly influencing the characteristics of the MT through the variation of the elastic energy term [61]. It is well known that the presence of residual stress and strains increase the thermal hysteresis and the irreversibility of the MT [71]. Internal stresses or local stresses are retained when samples are cycled through the phase transformation [72], being one of the main causes for the degradation of the MT, the deformation behavior, and the shape memory effect [73]. As a consequence, the defects and the stresses that are usually induced during the synthesis of micro-nano-particles and powdered samples (ball-milling, laser ablation, electric explosion of wire) may inhibit the MT [74] and influence the FM interactions as well [75, 64]. In summary, the control of the microstructural defects that are often linked to the synthesis process, present one of the main issues that must be considered specially in the micro- and nano-regime.

Apart from the composition and the microstructural state, the degree of long-range atomic order is known to strongly affect the T_{MT}, MT characteristics and magnetic properties of Ni-Mn-Z (Z = Sn, In) alloys [49, 63, 15, 76, 77, 78]. For instance, in the case of Ni-Mn-Ga and Ni-Mn-In samples, Sanchez-Alarcos *et al.* [76] demonstrated that T_c, T_{MT} and magnetization changes with quenching temperature when it is increased from 1000 K to 1200 K. At that high temperatures, Ni-Mn-Z and Ni-Fe-Ga alloys present the B2 structure (see Fig. 1.4) and during the quenching, a certain degree of B2 structure is retained within the samples [63]. Additionally, during the quenching vacancies are also trapped and all together contribute to the modification of the atomic order degree.

The atomic order variation induced by quenching and by subsequent annealing treatments has profound effects on the characteristic temperatures of aforementioned alloys, enabling shifts of T_{MT} up to $\Delta T_{MT} \approx 100$ K [49]. As a result, by proper quenching an annealing treatments it is possible to tune the characteristic temperatures, which is driven through the recovery of the long-range atomic order taking place during annealing. However, the null effect of quenching on the structural and magnetic properties in Ni-Mn-Sn system is proved to be related to the negligible $L2_1$ atomic disorder achieved with high-temperature annealing [63]. In fact, a surprising absence of $L2_1$-B2 ordering transition reflects the extraordinary stability of the L21

structure in these alloys.

Therefore, even though the structural order in Ni-Mn-Z (Z = In, Sn) alloys is the same, independently of Z, the stability order presented by the alloys is completely different, which indicates the importance of defect dynamics in the behavior of these alloys. In fact, preliminary studies in Ni-Mn-Ga [79, 80] show the large role played by vacancy type defects in their behavior. However, due to the elusive nature of vacancies, the influence of point defects on the martensitic transformation and the defects recovery kinetics are not still understood. Vacancy type defects dynamics and atomic ordering mechanism are strongly correlated, which ultimately affects the long-range atomic order and the T_c and T_{MT}. Thus, the huge differences reported between Ni-Mn-Sn, Ni-Mn-In and Ni-Fe-Ga systems concerning the ordering process gives rise to a good opportunity to understand the still unknown interplay between vacancy dynamics and atomic ordering.

In conclusion, in the endeavor of exploiting the multifunctional properties that are related to the occurrence of the MT in the Ni-based Heusler Alloys, the miniaturization of the active elements is consolidating as an effective approach to overcome the non-desired mechanical properties that bulk alloys present. However, as discussed above, in the micro and nano-regime, microstructural defects and the microstructural state have a great impact on the macroscopic structural and magnetic properties. Thus, the characterization of defects, the local stresses and the effect of strains are crucial to gain insight into the influence of such defects in the MT for a proper tuning of the structural and magnetic properties of Ni-Mn based Heusler alloys for more extensive applications [58, 81].

1.5 Objectives and Structure of the Thesis

The main objective of this thesis is to uncover how the microstructural defects affect the magnetic properties, the MT and the related multifunctional properties in $Ni_{50}Mn_{50-x}Z_x$ (x = 25, 20, 16, 15, 13 , 10, Z = Ga, Sn, In) and Ni-Fe-Ga alloys. The promising trend of miniaturization of the active elements that the field of Ni-based Heusler compounds is experiencing, requires a deep understanding of the role that defects and microstructural states play on the MT and the related mutifunctional properties. In order to overcome the elusive nature of defects, a nuclear characterization approach has been selected in this thesis, which has been carried out using both Mössbauer spectroscopy (MS) and Positron Annihilation Lifetime Spectroscopy (PALS). Along with standard characterization techniques (XRD, DSC, SEM, etc.), the use of the nuclear techniques is intended to have a closer look of the defects at atomic scale level.

Due to the magnetostructural coupling that the investigated alloys exhibit, MS provides the required sensitivity needed for their concurrent characterization at atomic

scale level. Due to the enhanced sensitivity of the hyperfine interactions, MS brings a unique site specific characterization of the atomic scale magnetism and local structure surrounding the probe atom. Regarding the characterization of point defects, PALS is one of the most powerful techniques for the advance characterization of defects in metal and semiconductors. Actually, its unique sensitivity allows the direct detection of vacancies, which combined with proper thermal treatments enables the determination of vacancy dynamics and their influence in the atomic ordering. In order to carry out the objectives of the thesis, the research have been organized as follows:

- Initially, the Chapter 2 gathers all the experimental techniques that have been employed for the consecution of the thesis. First, the standard characterization techniques such as XRD, PND, SEM, etc. are briefly presented. Later on, the theoretical basis and operational principles underlaying PALS and Mössbauer spectroscopies are thoroughly presented. Additionally, several setups that have been built and optimized for the consecution of the thesis, which are explained in detail. Finally, the chapter concludes with a review of the samples that have been synthesized for this thesis.

- Chapter 3 is devoted to study how mechanically induced defects affect the magnetic properties of a $Ni_{50}Mn_{34}In_{16}$ sample. As ball-milling is one of the cheapest way to produce nano-structured samples, this is the technique that has been employed for obtaining micro and nanoparticles of $Ni_{50}Mn_{34}In_{16}$. In this chapter, the obtained powdered samples are investigated using a wide range of characterization techniques. Initially, the nature of the obtained powder is analyzed and complemented with a thorough magnetic characterization. Subsequently, the crystallization process of the ball-milled alloys is investigated in depth and the different stages of the crystallization process are identified. Finally, a comparative study of the MCE between the bulk and powdered samples is carried out to determine the suitability of ball-milling and subsequent annealing treatments for tailoring the multifunctional properties of $Ni_{50}Mn_{34}In_{16}$ alloy.

- Taking into account the results of Chapter 3, in Chapter 4 the study is extended to Ni-Mn-Sn samples. However, in this case, the ball milling procedure is replaced by a more controllable approach and the powdered samples are obtained by soft-milling. Taking into account that the high stability of $L2_1$ structure of Ni-Mn-Sn systems precludes the modification of T_{MT} and T_c by means of standard treatments, the main objective of this chapter is to investigate an additional way to modify the MT characteristics for Ni-Mn-Sn systems. The effect of local stresses and strains induced during the milling is measured by ^{119}Sn-MS, which enables to track the evolution of the width of the MT. The microstructural state is directly related to the macroscopic magnetic and structural evolution that samples shows upon annealing. Moreover, the influence of defects is comparatively investigated in $Ni_{50}Mn_{37}In_{13}$ and $Ni_{45}Co_5Mn_{37}In_{13}$

samples. Finally, the contribution of the microstructural defects to the MCE is evaluated in the $Ni_{45}Co_5Mn_{37}In_{13}$ alloy.

- Chapter 5 deals with the determination of point defects (i. e, vacancies) present in Ni-Mn-Z and Ni-Fe-Ga alloys. Additionally, this chapter is devoted to determine the role that vacancies have on the shift of the MT. Initially, the vacancy dynamics is studied by PALS in a wide compositional range of Ni-Mn-Sn and Ni-Mn-In alloys. Moreover, the experimental results are complemented with theoretical electron-positron calculations. Taking advantage of the existing PALS results in the literature, the study is extended to Ni-Mn-Ga system as well. Moreover, by combining the experimental and theoretical results, the type and the concentration of the actual vacancy-type defect present in Ni-Mn-Z (Z = Ga, Sn, In) alloys is discussed and determined. Finally, PALS investigation is moved to Ni-Fe-Ga alloy, where T_{MT} shows a strong dependence on quenching and annealing treatments. In this last part, the vacancy dynamics is connected with the ordering process and the shift that the T_{MT} exhibit upon annealing the quenched $Ni_{55}Fe_{17}Ga_{28}$ samples.

- In Chapter 6 the main results and conclusion arisen from the thesis are briefly summarized.

2 Experimental Techniques

The characterization of the influence that microstructural defects have on the magnetic properties and on the MT of Ni-based Heusler alloys have been carried out using a wide-range of experimental techniques. This chapter details the procedures followed for the synthesis, preparation and for the proper characterization of the samples investigated throughout this thesis.

All the Ni-Mn-Z (Z = In, Sn) samples have been synthesized by means of arc-melting method, while $Ni_{55}Fe_{17}Ga_{28}$ alloy has been cast by an induction melting furnace. For PND and Mössbauer studies, some of the synthesized samples have been further prepared in a powder form by means of different milling techniques. Regarding the bulk samples directed to positron studies, they have been tuned by several heat treatments, such as quenching and isochronal annealing treatments. Due to the magnetostructural coupling that the investigated samples exhibit, the characterization has been focused from the magnetic and structural point of view.

The description of the employed techniques is divided in two parts. First, the standard characterization techniques, such as, DSC, magnetic measurements, SEM etc, are briefly summarized. Later on, the non-standard PALS and Mössbauer spectroscopy techniques are explored more thoroughly, where a more detailed theoretical basis and the development of the experimental setups are presented. Finally, the initial characterization results of all the studied samples are summarized.

2.1 Sample Preparation

All samples belonging to Ni-Mn-Z (Z = In, Sn) systems have been synthesized in the Materials Laboratory of the Department of Physics of the Public University of Navarra (UPNA), in collaboration with the group of V. Sánchez-Alarcos, J. I. Pérez-Landazábal and V. Recarte. On the other hand, the polycrystalline $Ni_{55}Fe_{17}Ga_{28}$ samples were synthesized by the group of E. Cesari, in the Department of Physics of the Universitat de les Illes Balears UBI in Spain.

2.1.1 Arc Melting Furnace

Ni-Mn-Z (Z =In, Sn) polycrystalline samples have been synthesized using an Edmund Bühler MAM-1 arc melting furnace shown in Fig. 2.1 (left). The high purity elements of Ni, Mn, Sn and In, provided by Goodfellow, are mixed in the crucible shown in Fig. 2.1 (right).

This set-up allows the synthesis of samples up to 15-20g. Even though the synthesis of bigger samples is not strictly impossible, the control and the quality of the obtained ingots is reduced for larger masses. Thus, the desired final mass of the ingot m_T is a factor that has to be taken into account in advance, and the masses of the constituent elements (along with the stoichiometry), have to be weighted according to m_T. Let's take a generic expression for a sample of $Ni_\alpha Mn_\beta Z_\gamma$. According to this stoichiometry, the mass of Ni is given by

$$m_{\mathrm{Ni}} = \frac{\alpha M_{\mathrm{Ni}}}{\alpha M_{\mathrm{Ni}} + \beta M_{\mathrm{Mn}} + \gamma M_{\mathrm{Z}}} \cdot m_T \tag{2.1}$$

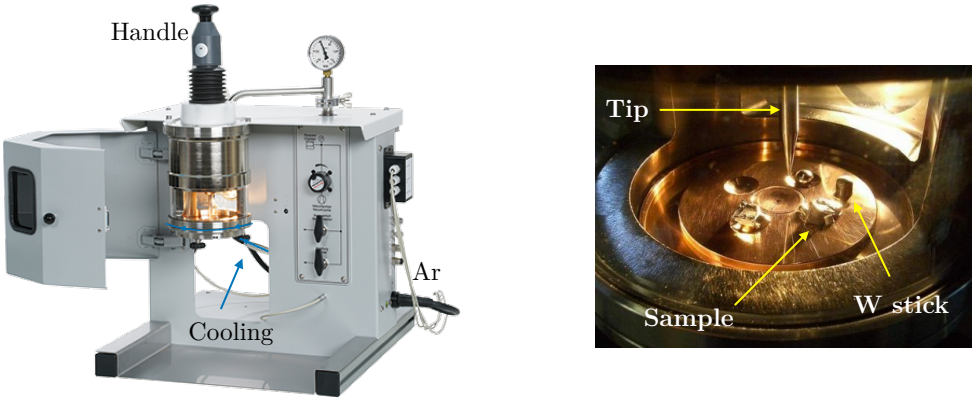

Figure 2.1: Left, a picture of Edmund Bühler MAM-1 equipment. Right, a detailed view of the crucible is shown. *Credit: MSE Supplies LLC and ETH Zurich/LMPT respectively.*

where M_{Ni}, M_{Mn} and M_{Z} are the atomic masses of Ni, Mn and Z elements respectively. The masses of the remaining elements are calculated following the same procedure. Right masses of the constituent elements are located in the crucible and the chamber is purged 3-4 times using an Ar gas flow. After the final purgue, the chamber is kept at 1.5 bar under protective Ar atmosphere. This atmosphere, apart for preventing the oxidation of the elements (specially Mn), provides the required conditions for the electrical discharge to happen.

The electrical discharge takes place by inducing a voltage difference between a tip and a stick attached to the crucible. This high voltage is provided by a transformer. While the tip approaches the Wolframium stick, eventually the arc discharge takes place. The position of the arc is easily adjusted with the crucible by means of a handle. Then, the arc can be located where the elements are placed, hitting them right from above. During this process, temperatures up to 4000 K ensure the fusion of all constituents, resulting in a droplet containing a mixture of all melted elements. The crucible is refrigerated underneath by a constant water current that avoids its overheating. Finally, the high voltage is turned off and the arc is vanished while the droplet solidifies within few seconds. This process is repeated up to eight times to ensure the homogeneity of the synthesized ingot.

2.1.2 Preparation of Powder Samples

Starting from the initial ingots, the powdered samples have been obtained by milling the as-cast ingots by means of three different methods shown in Fig. 2.2. The first approach consists in using an agate mortar. The fragility and the brittleness of the Ni-Mn-Z (Z = In, Sn) samples make them easy to break in small pieces. By means of an agate mortar, the size of the obtained pieces can be reduced below the mm. The samples milled in the agate mortar are not significantly amorphized, which ensures a good grade of crystallinity of the obtained microparticles.

With the aim of further decrease the size of the particles, a more energetic milling

Figure 2.2: From left to right, an agate mortar, a planetary ball mill PM400 and Emax mill. *Credit: Retsch*

has been performed using the planetary Ball Mill PM400 of Fig. 2.2. This planetary ball mill is equipped with 4 jars of Tungsten carbide (WC) of 10 ml volume each. WC balls of 10 mm in diameter are added within the jars for the grinding. In the present case, the initial as-crushed[3] samples are mixed with the grinding balls. The maximum velocity that can be achieved is 300 rpm. Due to the lack of refrigeration, the milling sequence is interrupted from time to time to avoid overheating of the sample. The sample is ball-milled during 10 mins, and afterwards the milling is stopped for another 10 mins. Even though the maximum velocity of the planetary Ball Mill PM400 is moderate, long effective-milling periods ($\approx$ 40 h) can lead to the amorphization of the samples (as will be shown in Chapter 3).

Finally, with the main purpose of obtaining Ni-Mn based nanoparticles, a third approach has been used. By means of the Emax mill shown in Fig. 2.2, the powders are subjected to high-energy ball milling. The equipment is able to reach velocities up to 1600 rpm, in which the powder can be downsized $<$ 100 nm. However, due to the highly energetic milling the samples get amorphized, which barely show any crystallinity degree. As a consequence, the recovery of the structure requires high temperature annealing, which presents a handicap due to the low bulk-surface ratio of the obtained powders.

2.1.3 Heat Treatments

2.1.3.1 Homogenization of as-cast ingots

Although the synthesized ingots are remelted several times within the arc-melting furnace, the solidification process of the ingot is not homogeneous. Due to the refrigerating system, the temperature of the crucible is much lower than the temperature of the melted mixture and the solidification turns out to be directional; from the bottom to the top, and from the edges to the center of the droplet. As a result, further post-synthesis annealing treatments are needed to homogenize the sample. Noticeably, the melting point of the ingot has to be taken into account when selecting the proper annealing temperature.

Among Ni-Mn-Z (Z = In, Sn) systems, Ni-Mn-In samples present the lowest melting point, around $1200 - 1300$ K. The melting point depends on the stoichiometry of the samples and the as-cast Ni-Mn-In ingots have been homogenized at 1173 K during 24 h. Regarding Ni-Mn-Sn samples, and contrary to what happens in Ni-Mn-In systems, the inhomogeneous rapid solidification of the ingot may lead to a dendritic structure [82]. Because the melting point of these structures is higher than the surrounding bulk of Ni-Mn-Sn alloy, a further annealing of 4 h at 1273 K have been performed in order to remove these spurious inhomogeneities. In the case of Ni-Fe-Ga alloys, the samples have been encapsulated in a quartz ampoule and homogenized during 24 h at 1423 K in Ar atmosphere.

[3] In order to increase the effectiveness of the ball milling, the ingots are previously crushed by a hammer by which small particles $\approx$ mm in size are obtained as starting powder samples.

2.1.3.2 Quenching

Quenching is the rapid cooling of samples from high-temperature to low temperature (iced water in this thesis), which is intended to achieve certain properties like harder structure, obtention of out-of-equilibrium phases, etc. In the framework of this thesis, the quenching procedure has been used for: *i*) inducing structural disorder in the samples and subsequently investigate how the magnetic properties are modified throughout the recovery process and *ii*) to modify the vacancy structure of samples quenched from the high-temperature B2 phase to $L2_1$ phase.

The quenching is performed in a vertically suited furnace. The furnace consists in an oven, a temperature controller, a quartz tube, an Ar gas supply, a rough pump and a hasp that holds the sample within the quartz tube. Initially, the sample is hanging from the hasp and it is carefully located in the middle part of the oven. The system is sealed by a set of vacuum fittings and clamps. Afterwards, the quartz tube is purged several times using the rough pump. In each purge, the quartz tube is refilled with Ar gas for removing the remaining air molecules. Finally, the quartz tube is filled with Ar gas up to 800 mbar.

Before quenching, the sample is heated at the desired quenching temperature and kept during 30 min in order to ensure a proper thermalization. In the present case, all the studied samples have been quenched from 1173 K. Due to the expansion that the Ar gas experiences at 1173 K, the pressure within the annealing chamber (where the sample is located) increases from the initial 800 mbar up to 950 mbar. The low pressure difference between the outside and the inside of the chamber allows an easy removal of the blank flange placed at the bottom of the quartz tube. Simultaneously, the hasp that holds up the sample is released and the sample drops into a recipient located underneath the quenching furnace, which contains iced water.

2.1.3.3 Isothermal and Isochronal Annealing

Annealing treatments are one of the most extensively employed treatments in material science for the proper characterization of thermally activated processes. Among the different existing annealing treatments, in this thesis two types have been used. As shown by the green curve in Fig. 2.3(a), in the so-called isothermal annealing, the samples are heated up to a certain temperature at a fast heating rate. Afterwards, the sample is kept at this temperature during a specific time and the evolution of the magnitude of interest is analyzed as a function of the temperature T and time t.

On the other hand, in the so-called isochronal annealing treatments, heating and cooling are performed at a controlled rate. The schematic illustration of isochronal annealing cycles used in this thesis is shown in Fig. 2.3(a). The sample is heated at a constant heating rate from room temperature up to a maximum temperature T_i. As mentioned later, the standard heating rate used in DSC measurements is 10 K/min. For the sake of comparison, during the present thesis the heating rate employed during all isochronal annealing cycles has been fixed to 10 K/min. Once

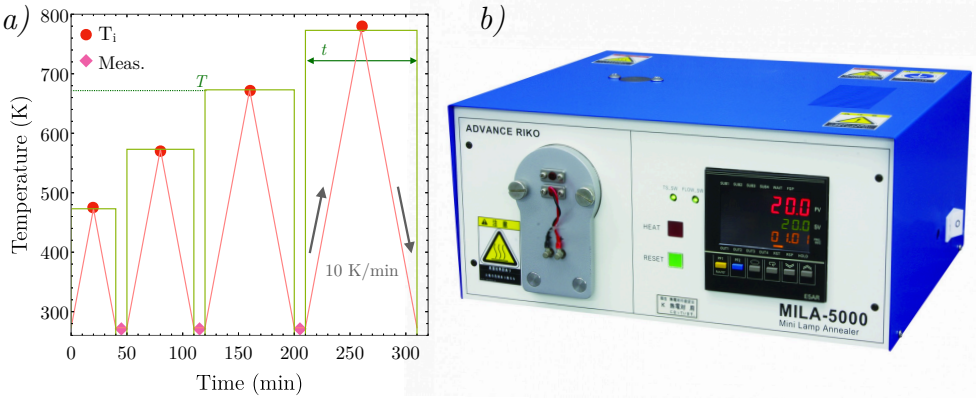

Figure 2.3: (a) Schematic representation of isothermal (green) and isochronal annealing (red) heat treatments. (b) Picture of Mila-5000 furnace employed to carry out the heat treatments.

the temperature reaches T_i, the sample is cooled down to the starting temperature at the same 10 K/min rate. After each cycle, a certain measurement is often taken (e.g., PALS, Mössbauer etc.) by which the effect of the isochronal annealing in a certain magnitude (e.g., vacancy concentration, non-magnetic component etc.) is investigated as a function of T_i.

In order to perform such heat-treatments, the control of the heating and cooling rate acquires a key relevance. Both isothermal and isochronal annealing treatments have been carried out using the Mila-5000 furnace shown of Fig. 2.3(b). This furnace provides an accuracy of 0.2 K on both heating and cooling ramps. Moreover, the furnace is equipped with a turbomolecular pumping station and constant Ar, N and He gas circulating system, which provides different annealing conditions such as; a high vacuum annealing or a controllable atmosphere annealing to prevent the oxidation of samples.

2.2 Development and Optimization of an Annealing Furnace

As pointed out in Sec. 2.1.2, the annealing of powdered samples requires a precise control of the annealing atmosphere. Due to the high surface-bulk ratio of the powders, the oxidation of the samples present the main issue to deal with, specially when the samples are annealed at high temperature. Moreover, in the present case where the powdered Ni-Mn-Z (Z = In, Sn) samples contain a substantial portion of Mn, the oxidation becomes of great concern. Due to the low vapor pressure of the constituent elements (specially Sn, In and Mn), the high temperature annealing under

ultra-high vacuum results in evaporation of the elements with its subsequent compositional change. On the other hand, the high temperature annealing performed in conventional furnaces with ordinary sealing systems results in a complete oxidation of Ni-Mn-Z (Z = In, Sn) powders. Thus, with the aim of facilitating a proper high temperature annealing of Ni-Mn-Z (Z = Ga, In, Sn) powders, a high temperature annealing furnace has been designed, built and optimized.

2.2.1 Furnace Specifications

The annealing furnace must consist of an oven that allows the annealing chamber (a tube) to be housed inside. Additionally, this tube should be able to host the powdered sample subjected to annealing and also to allow the incorporation of a controllable atmosphere. As the annealing chamber must have a good stability at high temperatures, a tube of Khantal APM^{TM} has been acquired from *Sandvic*, which is a dispersion strengthened ferritic iron-chromium-aluminium (FeCrAl) alloy, suitable up to 1520 K. The annealing temperature for Ni-Mn-Z (Z = In, Sn) powders never will exceed 1120 K, so the stability of the tube is guaranteed throughout annealing.

The coupling of Khantal APM^{TM} tube to the rest of the furnace has been done by

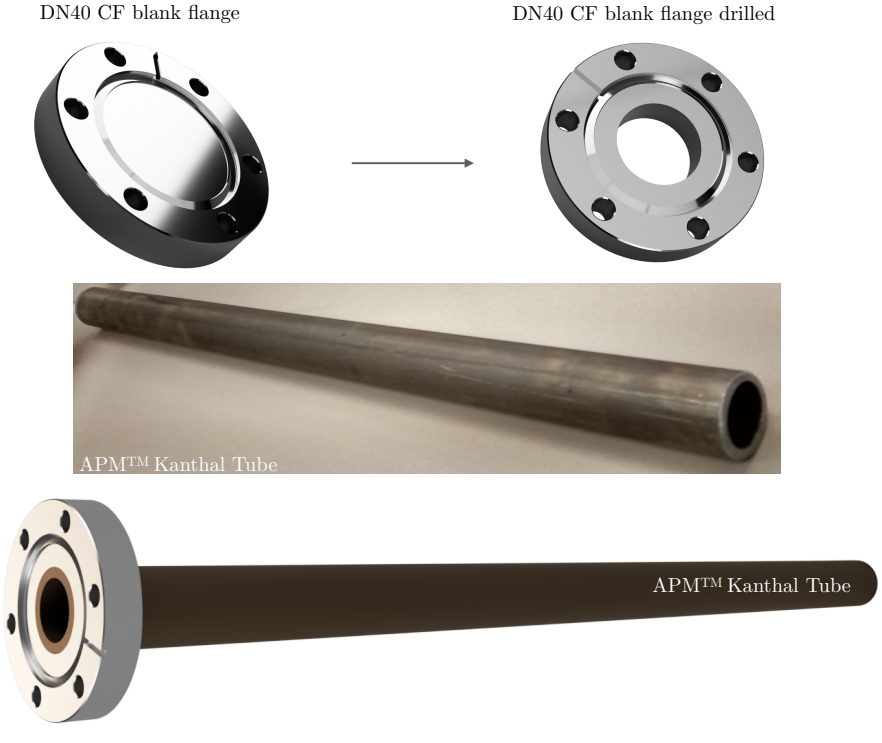

Figure 2.4: APM Khantal^{TM} tube and the coupling with DN40 CF flange.

welding the tube to a DN40 CF flange. The procedure is shown in Fig. 2.4. Initially, the 40 DN CF flange has been drilled in order to match the outer diameter of the Khantal APM^{TM} tube. Then, the flange has been welded to one end, and the other end of the tube has been sealed using a piece of the same Khantal APM^{TM} alloy. The DN40 CF flange is attached to a DN25 ISO-K reducer using a cooper gasket. This system ensures a coupling with leak rates $< 10^{-9}$ mbar l/s.

Regarding the requirement of the annealing atmosphere, a slightly reductive inert gas has been used for the treatments. Indeed, Ar + H_2 mixture gas has been selected for this purpose. In this way, the spurious oxygen that may be present will react first with H_2, avoiding the oxidation of the constituent elements of the powdered samples.

On the other hand, the sample mounting/removal and the incorporation of the desired atmosphere should be handleable and user-friendly. The attachment between the annealing chamber and the remaining part of the setup (pumping, pressure read-out and gas incorporation system) has been done by a conventional clampleable KF flanges and O-rings. The actual picture of the setup, as well as the diagram are shown in Fig. 2.5. All the systems lying on the left-hand side of the detachable flange can

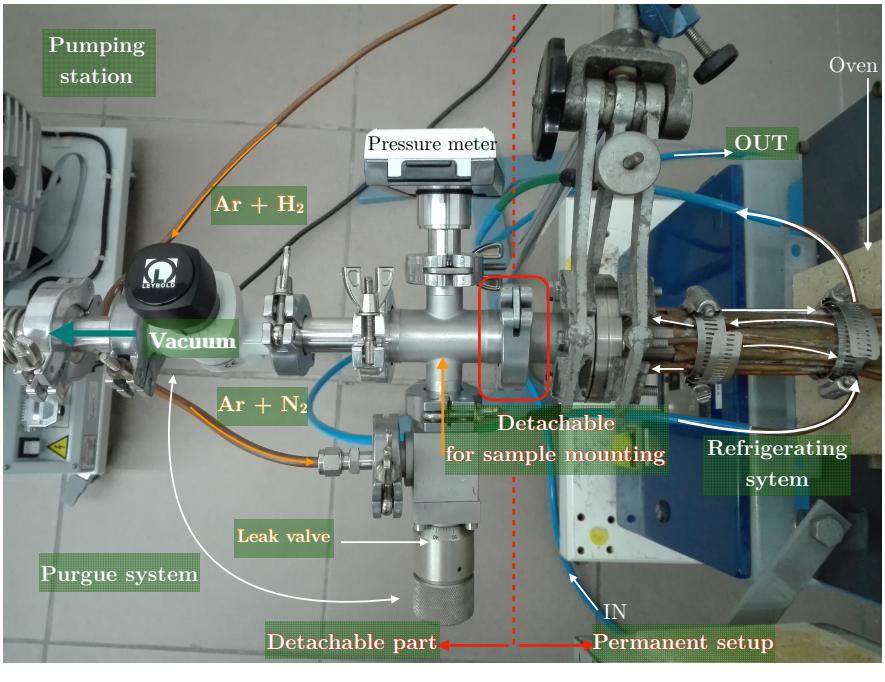

Figure 2.5: Picture and diagram of the furnace and fittings. The oven is located in the right-hand side of the annealing chamber and the pumping station on the left-hand side. The Khantal APM^{TM} is wrapped with a cooper foil to ensure a good thermal contact with the refrigeration system that surrounds the tube. The DN40 CF flange is connected to a reducer piece, which in turn, is connected to a T piece. This T piece allows the reading of the pressure, the incorporation of the gas and the pumping of the system by means of two different valves.

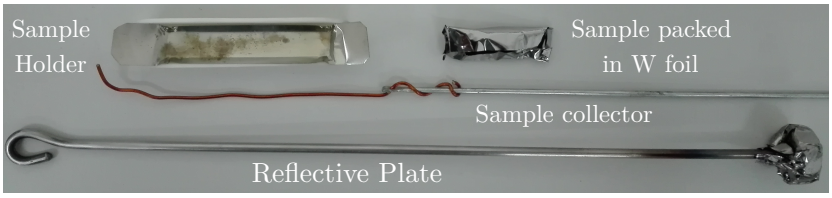

Figure 2.6: The sample is wrapped in a Tungsten (W) foil and the pack is located in an alumina crucible. The sample holder is incorporated and removed from the tube using a stick. The reflective plate placed after the sample prevents the overheating of the outer part of the tube due to the thermal radiation.

be moved independently to the annealing chamber and the oven, allowing an easy mounting and removal of samples.

Regarding the temperature that the Khantal APM^{TM} tube reaches during the annealing, it has to make sure that the temperature at the detachable part does not exceed the level from which the O-ring starts outgassing. For this purpose, a refrigeration systems consisting on a cooper tube filled with constant water flow has been attached to the part of the tube hanging outside the oven, see Fig. 2.5. Additionally, in order to minimize the heat transfer due to the radiation, a reflective metallic piece consisting on the same material of the tube has been placed, see Fig. 2.6.

Before incorporating the desired atmosphere to the chamber, the tube has to be purged several times. With this purpose an nEXT Edwards Turbo Pumping Station has been used. Using the backing pump of the pumping station and the Ar + H_2 gas, the chamber is purged and filled with the gas several times by combining the two valves of Fig. 2.5. This procedure is repeated up to five times to ensure the proper removal of impurities. Later on, the chamber is pumped using the turbomolecular pump until a vacuum $\approx 10^{-7}$ mbar is obtained. Finally, the chamber is filled with the gas mixture at a desired pressure, ranging from 200 - 600 mbar.

A pressure reader from ambient pressure down to 10^{-4} mbar has been added in order to monitor the pressure of the chamber. Additionally, the display provides real time values, which can be used to detect possible leaks. As shown in the inset of Fig. 2.7, a Digital Thermovac TM101 DN16 KF has been acquired from Leybold.

As pointed out before, the outgassing of the constituent elements in Ni-Mn-Z (Z = In, Sn) is avoided by using a slightly reductive atmosphere at a certain pressure. After several tests, the optimal pressure has been found to be $\approx 200 - 600$ mbar. However, during the annealing, the gas is heated and the pressure within the chamber increases. If the pressure inside the tube exceeds or reaches pressure values close to the ambient one, the vacuum fittings lost their effectiveness and the sealing of the setup may be compromised. The maximum pressure reached during the annealing must be in a range that allows an adequate performance of the vacuum fittings (in depression, which in turn, facilitates the sealing of the fittings). Thus, the maximum pressure achieved during the annealing has been estimated as a function of the initial pressure and the annealing temperature.

Let's consider that Ar + H_2 gas behaves as an ideal gas described by the well-

known ideal-gas equation $PV = nRT$. The volume, pressure and the temperature at the initial stage (i. e., room temperature) are labeled as P_i, V_i and T_i. The initial temperature T_i is room temperature, ≈ 300 K. If the value of the pressure, volume and the temperature of the gas at the maximum temperature achieved during the annealing are P', V' and T', during the heat treatment the relation

$$\frac{P_i V_i}{T_i} = \frac{P' V'}{T'} \tag{2.2}$$

is satisfied as n remains constant. However, the volume of the chamber which is heated is not the entire volume but rather a third part of the tube (the rest is refrigerated outside the oven). Due to the refrigeration system attached at one end of the tube, the temperature in this extreme is considered to be the same during the annealing. Accordingly, the equation (2.2) becomes into

$$\frac{P_i V_i}{T_i} = P' \left(\frac{2V_i}{3T_i} + \frac{V_i}{3T'} \right) \tag{2.3}$$

$$P_i \cancel{V_i} = \frac{2P' \cancel{V_i}}{3} + \frac{P' T_i \cancel{V_i}}{3T'} \tag{2.4}$$

As a result, the maximum P' pressure reached at the maximum temperature T' is given by

$$P' = \frac{3P_i T'}{2T' + T_i} \tag{2.5}$$

Fig. 2.7 shows the Eq. (2.5) for different maximum annealing temperatures T'. Additionally, experimental P' values are also plotted, indicating the good agreement between Eq. (2.5) and the actual performance of the furnace.

The overview of the whole setup (FUPOG[4]) is shown in Fig. 2.8. The furnace is vertically placed so that the annealing chamber lies horizontal. The tube is secured using two clamps preventing it from leaning on the walls of the oven. The pumping system containing both backing and turbo pumps is attached directly by a set of vacuum fittings and valves (for more detail see Fig. 2.5). The Ar + H_2 containing bottle is put apart for safety reasons and the annealing chamber is gas filled by means of a leak valve, which allows a well-calibrated gas incorporation.

Finally, the furnace has been tested several times by annealing samples during few hours and up to 24 h at temperatures of 1173 K. The obtained powder sample did not show any appreciable oxidation during the annealing, indicating an optimal performance of the furnace.

[4]Feuchtwanger-Unzueta-Pérez-Orue-García Furnace.

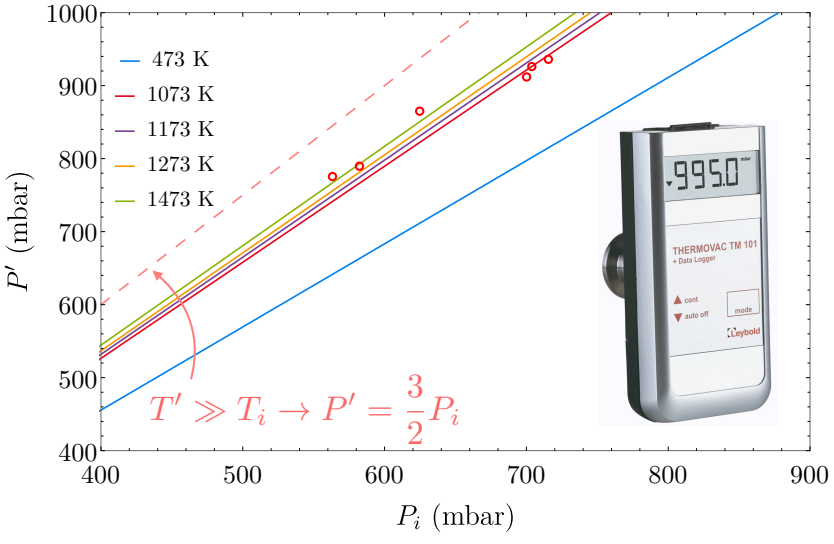

Figure 2.7: $P'(P_i)$ plot according to Eq. (2.5). For increasing temperatures, the final pressure approaches the limit where $P' = 3P_i/2$

Figure 2.8: Picture of the high temperature annealing furnace FUPOG.

2.3 Standard Characterization Techniques

The synthesized samples have been characterized and studied by several techniques, which have been divided in two sections. On the one hand, there are the standard characterization techniques such as DSC, SEM, magnetic measurements etc., and in the other hand, the specific characterization techniques, such as PALS and Mössbauer spectroscopy.

2.3.1 Differential Scanning Calorimetry DSC

Differential Scanning Calorimetry (DSC) is a thermoanalitic characterization technique in which the difference in the amount of heat required to increase the temperature of a sample and a reference-sample is measured as a function of temperature. Normally, the temperature increases linearly as a function of time, where both the sample and the reference are kept at the same temperature. In the framework of this thesis, the heating and cooling rate has been fixed to 10 K/min. If during the thermal cycle the sample undergoes a phase transition or a chemical reaction (e. g., oxidation), the amount of heat needed to keep constant the temperature of both the sample and the reference varies. By tracking this deviation it is possible to detect phase transitions and chemical reactions taking place during the heating/cooling, as well as determine the characteristic temperatures of such processes and their corresponding enthalpy.

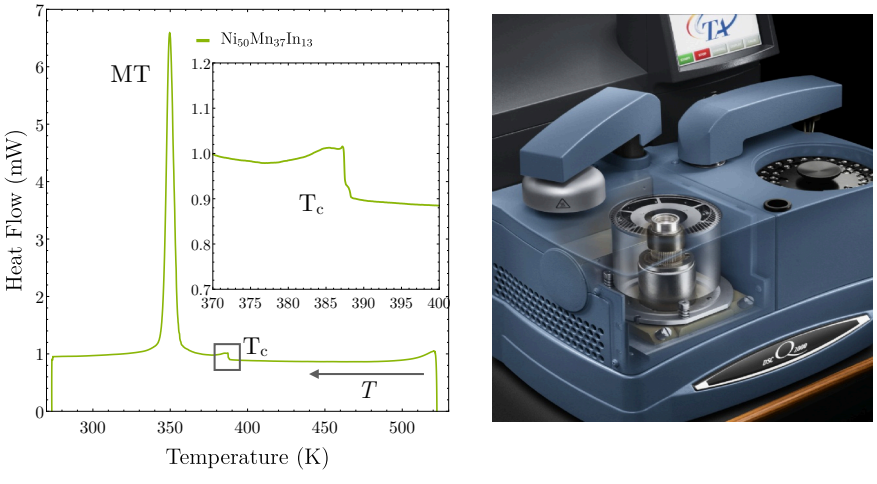

Figure 2.9: Left, a standard DSC thermogram where the change of the heat flow corresponding to the MT and magnetic transition can be observed. The inset shows the T_c transition in more detail. Right, the picture of the TA Q2000 DSC setup.

For example, the fusion of a sample (e. g., ice - water phase transition) requires more heat flowing to the sample to keep the temperature of both the reference and the sample at the same value. As the heat is absorbed by the sample, this endothermic process is reflected as a sharp peak in the heat-flow. Likewise, if the sample undergoes an exothermic process (e. g., crystallization), the amount of heat needed to increase the temperature of the sample to fit the temperature of the reference sample is lower. Indeed, as the sample emanates heat during the crystallization process, it results in a exothermic peak where less heat flow is needed to keep the sample at the same temperature compared with the reference.

The DSC characterization has been used to check both T_c and T_{MT}, as well as for characterizing the features of the DSC peak related to the MT. A typical DSC thermogram of a sample exhibiting both MT and Curie's transition is shown in Fig. 2.9 (left). In fact, a great exothermic peak is observed at 350 K during cooling, which is related to the occurrence of the MT. On the other hand, the cut of the base-line observed at 385 K (λ type) is related to the magnetic transition at T_c.

DSC measurements have been carried out in a TA Q2000 equipment shown in Fig. 2.9 (right). The sample is mounted in an Al crucible and an empty Al crucible is used as reference. By comparing the heat needed to keep both samples at the same temperature, the transition events are detected. In the framework of this thesis, DSC measurements have been carried out in the 100 - 673 K temperature range.

2.3.2 Electron Microscopy and Energy Dispersive Analysis

An electron microscope is a type of microscope that, unlike the conventional optical microscopes produces images by means of focused electron beams. Since the resolution depends on the wavelength of the radiation used to investigate the sample, one of the main advantages of electronic microscopes is the enhanced resolution they can

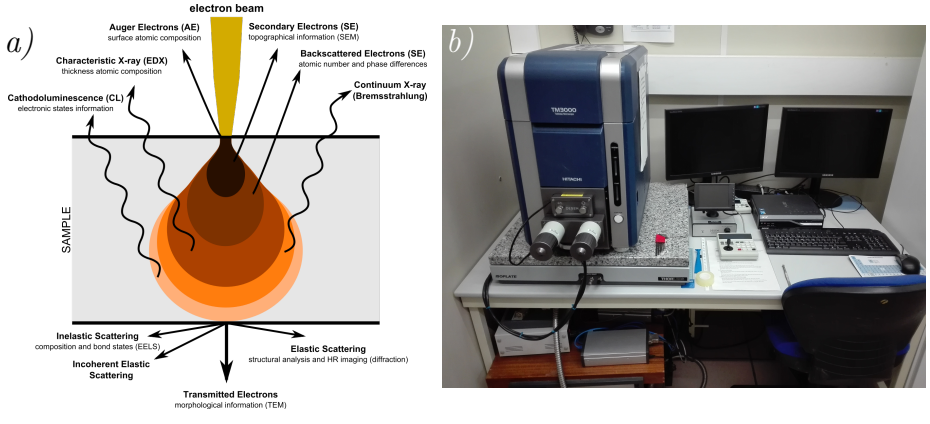

Figure 2.10: (a) Interaction of highly energetic electrons with matter and the related processes. (b) Picture of the desktop SEM equipment employed for characterizing samples.

achieve compared to optical ones.

The development of electronic microscopes began thanks to the discovery of the potential applications offered by the wavelength of electrons. According to the Broglie hypothesis, all matter, not jut light, has a wave-like nature [83], where the related λ is proportional to the momentum p of the particle $\lambda = h/p$, being h the Planck's constant. Despite the wavelength of the visible light is bounded between 400 - 700 nm, the wavelength of electrons can be easily tuned taking into account that a wavelength of a matter particle depends directly on its corresponding kinetic energy.

In electron microscopes, electrons are accelerated using high-voltages V. As a result, the electrostatic potential energy eV turns into kinetic energy $1/2m_e v^2$ so,

$$\lambda = \frac{h}{m_e v} = \frac{h}{m_e}\frac{1}{\sqrt{\frac{2eV}{m_e}}} = \sqrt{\frac{h^2}{2m_e V e}} = \frac{1.23}{\sqrt{V}} \tag{2.6}$$

where m_e is the electron mass. According to the last equation, the wavelength of the electrons, and as a consequence, the resolution of the equipment can be easily tuned by selecting the value of V.

The incident electrons are created in a purpose-specific filament (an electron-gun of LaB_6, W, etc.) and are accelerated using a high voltage stage typically ranging between 40-400 keV. Afterwards, the beam of electrons is focused by means of several electromagnetic lens, by which the imaging characteristics are defined. Once the beam is handled and focused, electrons interact with the sample to be analyzed. Fig. 2.10(a) shows the diverse processes that take place when energetic electrons interact with matter. Each type of process reveals a unique information. For example, secondary electrons and backscattered electrons, which are produced within the interaction volume, are mostly used for imaging purposes. The emission of backscattered and secondary electrons depends strongly on the incident angle and the roughness of the sample. By probing the specimen with a focused electron beam that is scanned across a rectangular area of the specimen, (Scanning Electron Microscope, SEM), high-quality pictures of the surface of the sample can be obtained.

The emission of secondary electrons, auger and backscattering electrons are also accompanied with emission of X-Rays. Apart from the continuous X-Rays emission, characteristic X-rays are also emitted, which uniquely depend on the nature of the reemitting atom. As a result, by means of Energy Dispersive X-Rays Analysis (EDX), it is possible to obtain compositional information of the sample. On the other hand and for very thin samples ($\approx$ nm) it is also possible to analyze electrons transmitted through the sample (Transmission Electron Microscopy TEM), which enables a higher spacial resolution. During this thesis, for both, compositional and topographic purposes a Hitachi TM3000 Desktop SEM setup has been used, Fig. 2.10(b). A further electron microscopy characterization has been carried out using a Hitachi H600 100 keV TEM setup and a Jeol JSM-5610LV SEM.

2.3.3 Magnetic Characterization: SQUID and VSM

The magnetic characterization of the samples have been carried out in the Advanced Research Facility SGIKER of the University of the Basque Country UPV/EHU and in the Materials Laboratory of the Department of Physics of the Public University of Navarra (UPNA). The magnetization characterization has been carried out using a Superconducting Quantum Interference Device (SQUID) and a vibrating-sample magnetometer (VSM).

SQUID magnetometer is a very sensitive device intended to measure the magnetic moments and magnetic fields, capable to detect fields as low as 10^{-14} T. This experimental set up is one of the most relevant applications of the superconductivity and the measurement principle of the SQUID is based on the so-called Josephson effect [84]. This effect takes place when a non-superconducting material is placed between two superconductors (Josephson junction). The SQUID magnetometer consists of a ring or loop of a superconducting material disrupted by two Josephson junctions. These junctions act as barriers that electrons have to tunnel across. The current in the loop depends on the characteristics of the junctions and on the magnetic flux Φ crossing it. The current J is defined as

$$J \propto \sin\phi \cos\left(\frac{e\Phi}{h}\right) + \frac{2V}{R}, \tag{2.7}$$

where V is the potential difference, R the resistance of the junction and ϕ the phase difference of the wave-functions describing the quantum behavior of the Cooper pairs responsible of the superconductivity between the ends of each junction. Thus, slight changes on the magnetic flux induces a changes in the measured current J. However, because the superconducting ring is not big enough to host a sample holder,

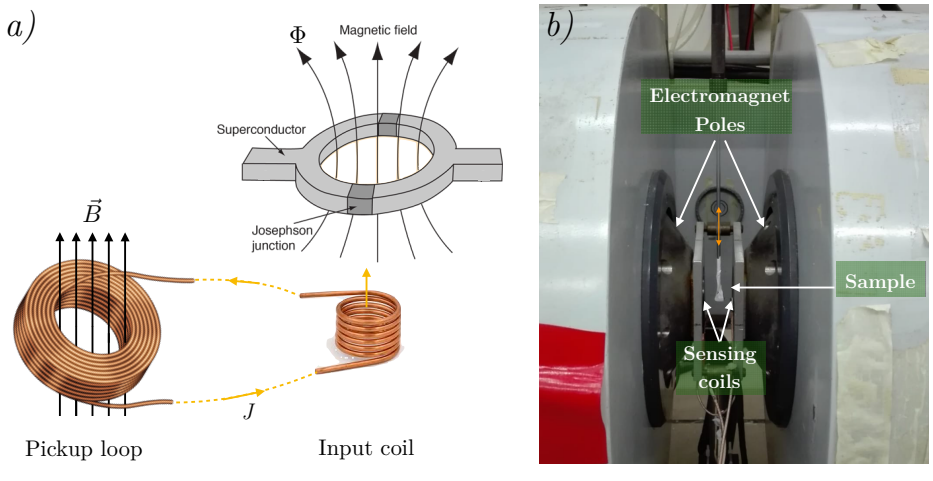

Figure 2.11: Schematic representation of (a) a superconducting quantum interference device (SQUID) and (b) a vibrating sample magnetometer (VSM).

the magnetic field **B** to be measured is collected by another superconducting pick-up coil, see Fig. 2.11(a). The supercurrent induced in the pick-up loop is then transferred to the so-called input coil. The flux created by the latter coil is measured by the SQUID. In order to obtain the magnetic moment related to the measured flux, the magnetometer is calibrated using a Pd reference sample. During this thesis, a MPMS-2 SQUID VSM setup from Quantum Design has been used. The accessible temperatures for measurements range from 1.7 K up to 400 K with a maximum applied magnetic field of 7 T.

For the high temperature magnetic characterization of the samples, a Vibrating Sample Magnetometer (VSM) equipment has been used [85, 86], which enables to measure $M(T)$ and $M(H)$ cycles in a temperature range from 77 K up to 673 K with a maximum applied magnetic field of 1.8 T. In a VSM, a magnetic material is placed vibrating within a uniform magnetic field, which can be generated by an electromagnet or superconducting magnet, see Fig. 2.11(b). According to the Faraday law, the variation of the flux induced by the vibration of the magnetic sample, induces an electromotive force, which is captured by suitably placed sensing coils. The V_{vsm} voltage induced in the VSM sensing coils is given by

$$V_{vsm} = A\nu G(z)m \tag{2.8}$$

where A is the vibration amplitude, ν the vibration frequency and m the magnetic moment of the sample. $G(z)$ is a sensitivity function of the V_{vsm}, which takes into account the position of the sample respect to the sensing coils. Thus, the induced V_{vsm} voltage is proportional to the magnetic moment.

2.3.4 Diffraction Experiments: X-Ray and Neutron Diffraction

The influence of milling on the magnetostructural properties of Ni-Mn-In and Ni-Mn-Sn powder samples has been analyzed by means of two diffraction techniques, X-Ray Diffraction (XRD) and Powder Neutron Diffraction (PND). With the use of these diffraction techniques, the aim is to study the evolution of the atomic-order degree as a function of annealing, as well as to analyze the crystallinity of the milled samples.

The XRD is based on the constructive and destructive interference of X-Rays. The constituent atoms of the analyzed samples are irradiated using an external X-Ray source, in the present case, a Cu Kα radiation of $\lambda = 1.5418$ Å. The incident X-Rays are absorbed and reemitted as a point-like sources, which depending on the difference of the X-Ray's path, results in a destructive or constructive interference pattern. This condition is given by the Bragg law [87]:

$$2d_{\mathrm{hkl}} \sin\theta = n\lambda \tag{2.9}$$

where d_{hkl} is the interplanar spacing defined by the Miller's h, k, l indexes, λ the wavelength of the incident X-ray, θ the Bragg's angle and n the number of the reflexion order. The X-Rays measurements have been carried out in a Siemens X-Ray Diffractometer D5000 suited in a reflexion geometry (also known as Bragg-Brentano

configuration). In this configuration, both, X-ray source and the detector are placed forming a 2θ angle. During the measurements the source and the detector are moved simultaneously keeping the 2θ geometry. The handleable configuration of the setup and its suitability for the study of the different state of the samples is ideal for performing XRD on powdered samples.

Due to the magnetostructural coupling that Ni-based Heusler alloys exhibit, the structural changes are often accompanied with magnetic changes and vice versa. Thus, the XRD measurements have been complemented by an additional diffraction experiment, i. e., PND. This technique is capable to analyze both structural and magnetic structure at the same time. Although the employed wavelength of the neutron is similar to that of X-Rays[5], the neutron posses an intrinsic magnetic moment, which in addition to the structural characterization, is sensitive to the magnetic structure.

When a neutron enters a solid, it interacts with the nuclei and electrons of constituent atoms. The neutron interaction with nuclei is driven by the strong nuclear force, which results in a spherically symmetric scattering event. As the interaction length of the strong nuclear force is $\propto 10^{-15}$ m, the structural resolution of neutrons is better than the XRD technique. Moreover, contrary to what happens in XRD, the cross section of the strong nuclear interaction does not depend on the angle, and the intensity of neutron reflections does not decrease as a function of the angle.

On the other hand, due to the intrinsic magnetic moment, the neutron interacts also with all electrons of the sample. Anyway, while the contribution of the paired electrons is zero, the contribution of the neutron scattering related to the unpaired electrons is the one which prevails. As a result, by neutron diffraction the magnetic structure can be additionally characterized. However, as occurs in XRD, the intensity of the magnetic contribution decreases while increasing the scattering angle.

The neutron diffractogram varies depending on the magnetic state of the studied sample. Regarding Ni-Mn-Z (Z = In, Sn) samples, they mostly exhibit ferromagnetism and paramagnetism. As a result, the magnetic contribution is superimposed to the structural contribution (ferromagnetism) or to the background noise (paramagnetism)[6]. This effect is shown in Fig. 2.12, which is an example of how the magnetic contribution is overlapped with the structural peaks in a $Ni_{50}Mn_{35}Sn_{15}$ sample. Both, annealed and milled samples of Fig. 2.12 are measured at the ferromagnetic state (270 K, green line) and at paramagnetic state (400 K, blue line). The difference in the intensity is the magnetic contribution to the spectra, which as will be shown in Chapter 4, enables the quantification of the FM and AF coupling of Mn atoms. The structural and magnetic parameters are obtained by fitting the diffraction spectra. However, the fitting of the experimental XRD and PND spectra is often hindered by an excessive overlap of peaks related to different reflexions. This

[5]According to Eq. (2.6), the wavelength of neutrons can be tuned by changing their kinetic energy. However, for resolution purposes, in the diffraction techniques a wavelength of the same order of magnitude of the investigated physical system is used.

[6]In general the magnetic and structural contributions are not the same. In addition to the structural diffraction peaks, additional peaks related to the magnetic structure can appear.

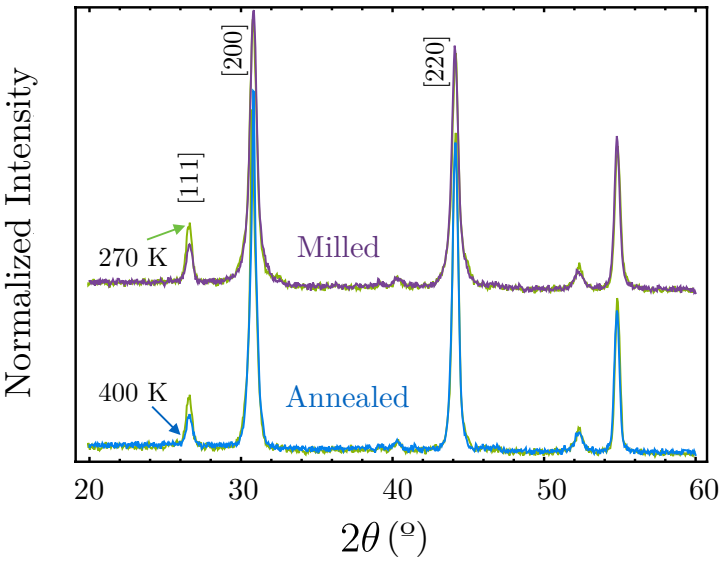

Figure 2.12: Example of powder neutron diffraction spectra in the ferromagnetic and the paramagnetic state of $Ni_{50}Mn_{35}Sn_{15}$ sample. The different magnetic contribution of FM and PM state is observed in the different intensity of the 111 peak (blue and green).

limitation can be overcome by Rietveld Method [88, 89]. During the Rietveld refinement, the structural parameters, background coefficients and the parameters related to the spectra are fitted by means of the least squared approximation until a good agreement between the experimental and simulated spectra is obtained.

In order to correlate the microstructural parameters with the magnetic properties in the Ni-Mn-Z (Z = In, Sn) alloys, special attention has been paid to three parameters extracted from the Rietveld analysis. The evolution of atomic-order degree in the milled and annealed samples has been analyzed by checking the occupation of the corresponding sites of the austenite and martensite phases. Additionally, the integrated intensity of the austenite [111] reflection (the peak is indicated in Fig. 2.12) also provides information about the $L2_1$atomic order, which is exclusively linked to that type of order [63].

The presence of local stresses and strains has been tracked by analyzing the width of XRD and PND peaks of the spectra. Although in a perfectly arranged infinite atomic lattice the diffraction peaks would have a Dirac's δ shape, the diffraction peaks of experimental spectra always present a certain width which arises from different factors. On the one hand, the resolution of the equipment contributes to the widening of the peaks. This contribution however can be easily subtracted after a proper calibration of the setup. On the other hand, the crystallite sizes and the presence of local stresses and strains also contribute to the width of the peaks. The peak width varies inversely with the crystalline size, and as the crystallite size gets smaller, the peaks get broader. On the other hand, slight microstructural distortions also

contribute to the width of the peaks. Due to the presence of local stresses, strains, defects and lattice imperfections, it may occur that the same planes in principle are not oriented in the same way, resulting in broadening of the peaks. Thus, the size of the particles, as well as their internal stresses and strain state have been analyzed by tracking the width of the XRD and PND peaks.

PND experiments have been carried out in the Laue-Langevin Institute (ILL, Grenoble, France) in D1B and D2 instruments. Neutrons are created by a ^{235}U nuclear fission process in a reactor that is placed in the center of the facility. The proper wavelength of neutrons are selected by means of a monochromator. Due to the high intensity of the neutrons, it is possible to obtain a diffractogram in few minutes, becoming suitable for *in-situ* characterization of crystallization and/or recovery processes. In this thesis, neutron wavelengths of 1.23 Å and 1.33 Å have been employed.

2.4 Mössbauer Spectroscopy

Mössbauer spectroscopy is a nuclear technique, which provides a unique structural and magnetic information probed at atomic scale. This technique is based on the Mössbauer effect, which in turn, is based on the resonant absorption phenomena discovered by R. L. Mössbauer in 1957 [90], awarded with the Nobel Prize in physics in 1961. The easy implementation of a Mössbauer spectrometer has turned it into a technique that has been widely used since its discovery. In contrast, the relationship between the Mössbauer and the macroscopic properties of solids is usually a matter of controversy. Therefore, in the following section, the foundations of the Mössbauer effect are explained in more detail.

2.4.1 Resonant absorption

The Mössbauer effect is based on the nuclear recoilless resonant absorption effect. The resonant absorption process starts when an atom or nucleus in an excited state E_e, emits a γ ray when it decays to its ground state E_g. If a nucleus of the same species absorbs this γ ray, it will be promoted to an excited state. This process is called resonant absorption. So, due to the quantification of the energy levels, the absorption only takes place when the energy of the absorbed γ ray and the energy of the excited state match.

When a nucleus emits a γ ray, it experiences a recoil effect according to the momentum conservation law. As a result, the E_γ energy of the γ ray emitted by a nucleus satisfies

$$E_\gamma = E_0 + E_R + E_D \tag{2.10}$$

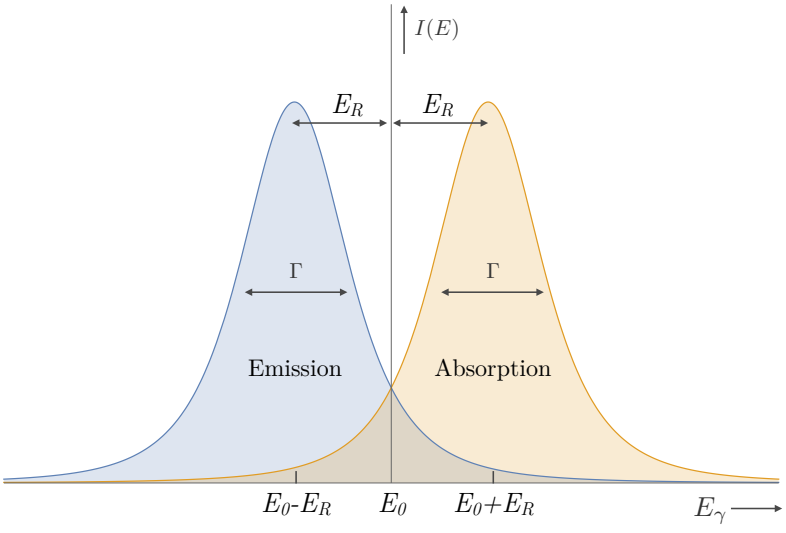

Figure 2.13: Statistic distribution of the emission and the absorption during a nuclear resonant absorption process

where $E_0 = E_e - E_g$, E_R the recoil energy and E_D the energy due to the Doppler effect, which comprehends the energy term arisen from thermal fluctuations (i. e., vibrations) of nuclei at a certain temperature. For a free nucleus at $T = 0$ K, the recoil energy is determined by the momentum conservation principle

$$E_R = \frac{E_0^2}{2Mc^2} \tag{2.11}$$

where c is the speed of light in vacuum and M the rest mass of the nucleus. For example, in the case of ^{57}Fe, $E_R = 1.95 \cdot 10^{-3}$ eV [91]. Thus, the γ ray emitted during the de-excitation process does not inherit the energy difference between the exited and the ground state, but a lower energy due to the fact that part of its energy is transmitted to the recoil atom. As a result, the energy distribution of the emitted γ ray of Eq. (2.10) is shifted by the $-E_R$ value. In the same way, the energy needed to excite a nucleus from its ground state to the excited state requires an extra $+E_R$ energy.

As shown in Fig. 2.13, the resonant absorption takes place when emission and absorption distributions overlap. This overlapping depends also in the characteristic width (Γ) of the emission and absorption distributions. According to the Heisenberg uncertainty principle, the lifetime of an excited state is the inverse of the energy E_0. In the case of ^{57}Fe, the lifetime of the excited state is $\approx 10^{-7}$s, which implies $\Gamma_{\text{Fe}} \approx 10^{-9}$ eV. Taking into account that the recoil energy of ^{57}Fe is about 10^{-3}, the offset between emission and absorption profiles is $\propto 10^6$. In essence, the resonant absorption does not take place in free nuclei.

The Γ of emission and absorption lines can be enhanced by thermal effects. Nuclei

at $T \neq 0$ temperature experience vibrations, that is a thermal energy that broadens the characteristic emission and absorption lines. The doppler effect, which is proportional to the relative velocity v of the emitter and the absorber, can be used to broad the characteristic lines. The broadening derived from the Doppler shift is given by

$$\Delta E_D = \frac{E_0 v}{c}. \tag{2.12}$$

By means of the Doppler effect, the difference of $2E_R$ can be diminished by ΔE_D, eventually allowing the overlapping between the emission and absorption profiles, and therefore, the resonant absorption.

However, when a nucleus of identical isotope of the γ rays emitting source is host in a solid, the recoil energy is absorbed by creating collective lattice excitations (phonons). In fact, the recoil energy and the characteristic energy scale of phonons are of the same order of magnitude $\approx meV$. However, if the recoil energy is not enough to excite the lowest energy phonon, then this recoil energy is transferred to the entire crystal. As the mass of a solid is about 10^{30} times bigger than the atom mass, a recoilless absorption takes place. Recoilless nuclei are denominated Mössbauer nucleus. As a result, the emission and absorption lines shown in Fig. 2.13 become strongly overlapped as $E_R = 0$, allowing the resonant absorption phenomena to take place.

2.4.2 Measuring the Mössbauer Effect

Although resonant absorption happens in solids, the nuclear levels are sensitive to the environment surrounding the nucleus. Despite the electromagnetic interaction between nuclei and lattice is rather weak compared with the interactions responsible for the nuclear structure (by a factor 10^{-10}), it shifts the nuclear energy levels in such a way that may destroy the resonance absorption. Indeed, the order of magnitude of these interactions is $\approx 10^{-6}$ eV, 3 orders of magnitude larger than Γ. This implies that the resonant absorption may vanish as a result of the surrounding environment of the probe atom, which is really sensitive to slight chemical and structural modifications. The interactions between the nucleus and its surrounding environment are known as hyperfine interactions.

Thus, by analyzing hyperfine interactions with a proper theoretical framework, it is possible to gather the structural information of the environment surrounding the host probe atom, and as a consequence, the structural and magnetic properties of a sample at atomic level. Indeed, this is the main idea behind Mössbauer spectrometry. As pointed out before, the shifts on the nuclear energy levels caused by the environment of the probe atoms can diminish the resonant absorption phenomena. However, in line with the effect described in Eq. (2.12), the energy shift on the nuclear levels can be scanned by means of the Doppler effect. The energy of the emitted γ ray is increased/decreased by means of a vibrating transducer, which vibrates at velocity v. The energy E'_γ of the emitted γ, in ray respect to the absorber is given by

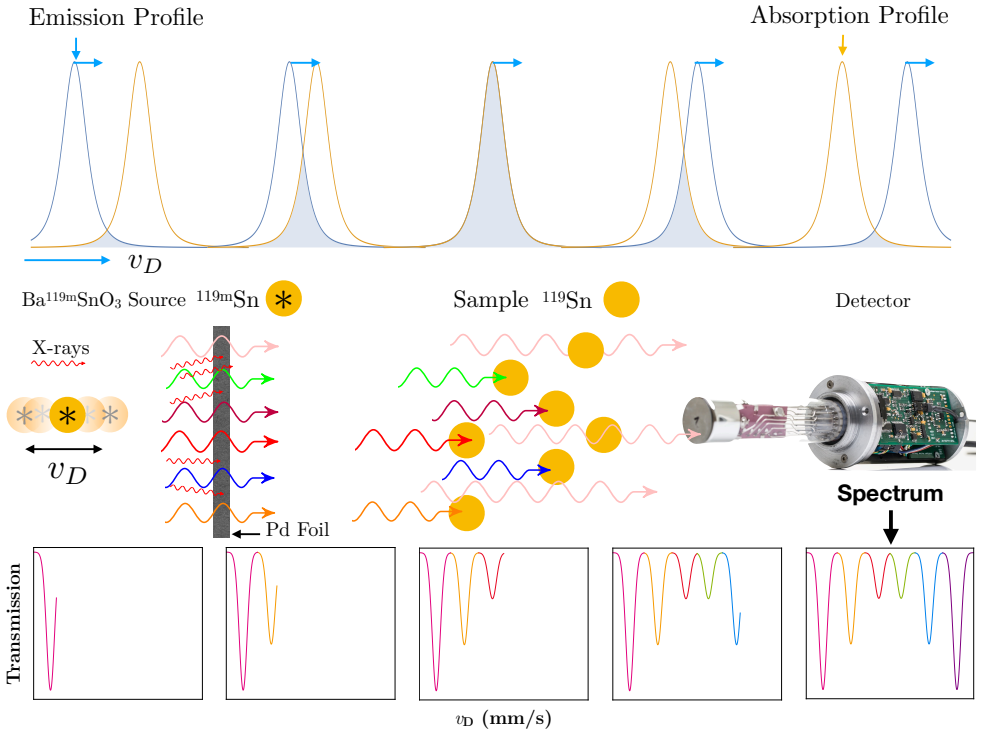

Figure 2.14: Schematic temporal sequence of transmission Mössbauer measurement. The γ ray energy emitted by the source is Doppler shifted in order to scan the hyperfine energy levels. In the case of ^{119}Sn-MS, a Pd foil is placed between the source and the sample to reduce the background noise.

$$E'_\gamma = \left(1 \pm \frac{v}{c}\right) E_0 \tag{2.13}$$

Thus, the E_0 energy of the γ ray corresponding to the energy difference of the excited and ground state of the emitting nucleus, is shifted in such a quantity that allows to scan the energy scale of hyperfine interactions. In fact, $v = 1$ mm/s equals to 10^{-6} eV, which is of the same order of magnitude of the hyperfine interactions. In this manner, the resonant absorption that has been previously destroyed due to the hyperfine interactions is restored by adding an extra energy to the γ ray by means of the Doppler effect.

A Mössbauer measurement consists in detecting the resonant absorption of a suitable stable Mössbauer nucleus host in the investigated sample [92]. In transmission Mössbauer experiments carried out during the thesis, the radioactive source is host in a $Ca^{119m}SnO_3$ matrix, and the absorber is the stable Sn atom of the investigated Ni-Mn-Sn and Ni-Co-Mn-Sn alloys. In the transmission geometry, the sample (absorber) is placed between the Mössbauer source and a detector. If the resonant absorption takes place, then the amount of γ rays transmitted through the sample

decreases. Thus, by monitoring the decrease of the counts at resonant velocities, a Mössbauer spectrum is obtained. The γ ray with variable energy, which scans the hyperfine interactions, is obtained by inducing a relative velocity between the source and absorber by means of a transducer. The transducer vibrates with velocities of mm/s, thus modulating the γ ray energy by the Doppler effect.

The overlap between the emission and absorption profiles is shown in Fig. 2.14. In the transmission geometry, a source of $Ca^{119m}SnO_3$ is moved from higher $+v$ to lower $(-v)$ velocities. As the absorber (sample) is stationary, the energy of the γ rays of the source is Doppler shifted, enabling the resonant absorption to happen. This absorption, is illustrated in Fig. 2.14 by the overlap of both, absorption and emission profiles. In order to avoid excessive background noise, in the case of $Ca^{119m}SnO_3$ source a 50μm thick Pd foil is placed between the source and the sample which stops the characteristic X-Rays emitted during the ^{119m}Sn decay process. As a result, the detector gives a count-rate as a function of the velocity scan of the source, which vibrates with constant velocity and triangle waveform by means of a transducer. Finally, the counts collected as a function of the velocity are plotted in a Multichannel Analyzer (MCA) by which the Mössbauer spectrum is displayed.

2.4.3 Hyperfine Interactions

2.4.2.1 Isomer Shift δ

The isomer shift δ, also denominated chemical shift, comprehends two different contributions. On the one hand, the shift arises because of the non-zero volume of the nucleus and due to the different nuclear volume (radius) of the ground and excited states. The probability of finding s electrons within the finite volume of the nucleus has a non-zero value, and the variation of the nuclear size affects the interaction energy between the nucleus and s electrons, giving rise to δ shifts. Additionally, the different electron density between s electrons surrounding the γ ray emitting Mössbauer nucleus and the absorber probe atoms also contributes to δ.

The s electron charge density at the nuclei ($|\Psi_s(0)|^2$) depends on the surrounding environment of the probe atom. Thus, its contribution to isomer shift is different for emitter and absorber nucleus. The Doppler velocity v_δ needed to scan the isomer shift hyperfine interaction is given by

$$v_\delta = \left(\frac{4\pi c}{5E_\gamma}\right) Ze^2 \left[|\Psi_s(0)|_A^2 - |\Psi_s(0)|_E^2\right] \left(\frac{\delta R}{R}\right) R^2 \tag{2.14}$$

where δR is the radius difference between the excited and ground state, Z the atomic charge and E_γ the characteristic transition energy of the nucleus. $|\Psi_s(0)|_A^2$ - $|\Psi_s(0)|_E^2$ is the difference between s electron charge density in the absorber and emitter nuclei, which means that isomer shift is essentially a measure of the difference in the chemical environment of the probe atom respect to the host of the emitter nucleus.

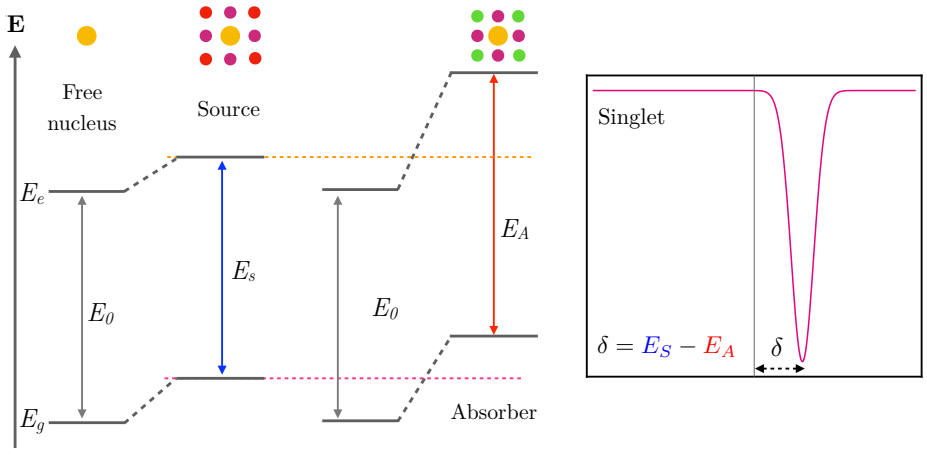

Figure 2.15: The effect of isomer shift δ on nuclear energy levels. The resonant absorption related to this effect gives a single absorption line (peak), which is known as a singlet.

The different electronic environment between the source and absorber results in a shift of the necessary Doppler velocity to attain the absorption resonance as depicted in Fig. 2.15. The single absorption or emission peak is known as singlet.

2.4.2.2 Quadrupole Splitting Δ

When considering the electric monopole interaction and the resulting isomer shift, it is implicitly assumed that the nuclear charge distribution is spherical [91]. However, if the nucleus does not have a spherically symmetric charge distribution (e. g., nuclei in states with nuclear angular momentum $I > 1/2$) it will possess an electric nuclear quadrupole moment Q. When the nuclear quadrupole moment interacts with an asymmetric electronic charge distribution, the electric quadruple interaction gives rise to a Δ splitting of nuclear energy levels as depicted in Fig. 2.16. This splitting comes from the different alignments of the quadrupole moment with respect to the principal axis of the electric field gradient. If a suitable coordinate system is chosen, the electric field gradient can be represented by three principal axes, V_{xx}, V_{yy} and V_{zz} where $V_{xx} + V_{yy} + V_{zz} = 0$. As a result, only two independent parameters are needed to describe the electric field gradient. Usually, an asymmetry parameter η is defined as

$$\eta = \left(\frac{V_{xx} - V_{yy}}{V_{zz}} \right), \tag{2.15}$$

where $0 < \eta < 1$, so that the electric field gradient is defined by V_{zz} and η. The eigenvalues of the split states E_Δ due to the quadrupole interaction are

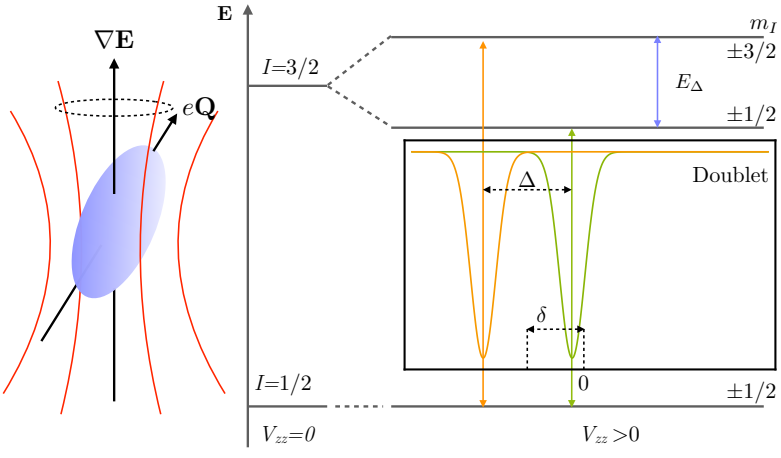

Figure 2.16: The electric quadrupole interaction, which is visualized by the precession of the quadrupole moment vector about the field gradient, splits the degenerate $I = 3/2$ level in two substates with $m_I = \pm 3/2, \pm 1/2$. This interaction gives rise to two transition lines with equal intensity which are separated by E_Δ, often called as doublets.

$$E_\Delta = \frac{eQ_{zz}}{4I(2I-1)}(3m^2 - I(I-1))\left(1 + \frac{\eta^2}{3}\right)^{1/2} \tag{2.16}$$

where $m = I, I-1, \ldots, -|I|$ and e the electron charge. The energy difference between the two sublevels is given by,

$$\Delta = \frac{eQV_{zz}}{2}\left(1 + \frac{\eta^2}{3}\right)^{1/2}. \tag{2.17}$$

As illustrated in Fig. 2.16, in the Mössbauer spectrum the splitting results in a quadrupole doublet component. The quadrupole splitting is a measure of the site symmetry in a crystal and retrieves information about chemical binding and whether the surrounding crystal structure is cubic ($V_{zz} = 0$) or not ($V_{zz} \neq 0$).

2.4.2.3 Magnetic Hyperfine Splitting B_{hf}

The interaction between the nuclear magnetic dipole moment μ and the magnetic field $\mathbf{B}$ at the nucleus produced by the surrounding electrons or ions is called magnetic hyperfine interaction [91], i. e., Zeeman effect. The magnetic field experienced by the nucleus can arise from an external source, from the atom itself and from its neighboring unpaired electrons. The energy of the nuclear Zeeman effect is

$$\mathcal{H}_m = -\vec{\mu}\cdot\mathbf{B} = -g_n\mu_N\mathbf{I}\cdot\mathbf{B} \tag{2.18}$$

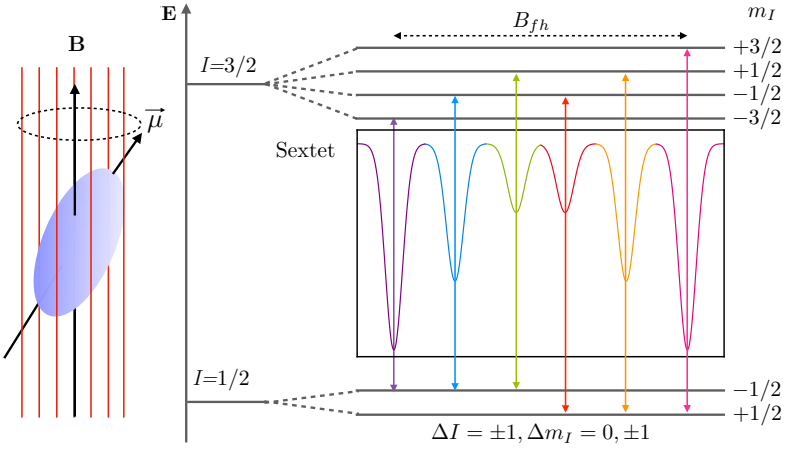

Figure 2.17: The effect of magnetic splitting on nuclear energy levels in the absence of quadrupole splitting. The magnitude of splitting is proportional to the total magnetic field at the nucleus.

where g_n is the Landé factor and $\mu_N = e\hbar/2M$ the nuclear magneton, being M the mass of the nucleus. The presence of a magnetic field leads to a complete removal of the degeneracy of the nuclear levels. The $I = 1/2$ ground state is split in two sublevels, while the excited state $I = 3/2$ splits in four sublevels as depicted in Fig. 2.17. Considering $\mathcal{H}_m$ as a perturbation term of the nuclear levels, the splitting of energy is proportional to m and it is given by

$$E_m = -g_n \mu_N m B \tag{2.19}$$

The selection rule of $\Delta m = 0, \pm 1$ and $\Delta I = 0$ allows six possible transitions, giving rise to a spectrum splitting into six lines, also known as a sextet pattern. In principle, the relative intensities of the absorption peaks depends on the direction of the hyperfine magnetic field with respect to the direction of the incident photons ($\vec{\gamma}$). However, in polycrystalline powdered samples, the hyperfine field is randomly oriented in respect to $\vec{\gamma}$, resulting in a relation between the peaks of 3:2:1:1:2:3.

This magnetic or Zeeman splitting is a combination of a constant nuclear term and a variable magnetic term, influenced by the electronic structure. The effective magnetic field $\mathbf{B_{eff}}$ at the nucleus has several terms associated with it. A general expression is [93, 94]

$$\mathbf{B_{eff}} = \mathbf{B}_{loc} + \mathbf{B}_{hf} \tag{2.20}$$

$$= \left(\mathbf{B}_{ext} - D\mathbf{M} + \frac{4\pi}{3}\mathbf{M}\right) + (\mathbf{B_S} + \mathbf{B_L} + \mathbf{B_D}) \tag{2.21}$$

where $\mathbf{B}_{ext}$ is the applied external field, $D\mathbf{M}$ is the demagnetizing field, $4/3\pi\mathbf{M}$ the so called Lorentz field, $\mathbf{B_S}$ the Fermi contact term, $\mathbf{B_L}$ the orbital magnetic term

and $\mathbf{B_D}$ the dipolar term. These last three terms, configure the so-called hyperfine field $\mathbf{B}_{hf}$. The demagnetizing field and the Lorentz field are usually negligible compared to the other terms [95]. Regarding $\mathbf{B_D}$, the dipolar field is produced by the total spin magnetic moments of the valence electrons, while $\mathbf{B_L}$ is the field due to the orbital motions of the unpaired electrons [95]. As will be shown below, in the samples studied during this thesis the dominating term is $\mathbf{B_S}$, the Fermi contact term.

2.4.2.4 ^{119}Sn Mössbauer Spectroscopy

Among the 18 practicable Mössbauer nucleus, the most common isotope used in Mössbauer spectroscopy is ^{57}Fe, which has a relative natural abundance of 2.2%. However, the resonance of ^{119}Sn, which was discovered months after the original paper of ^{57}Fe [90], is the next widely used Mössbauer isotope in material science, with a relative natural abundance of 8.58%. In turn, in the framework of this thesis it acquires a key relevance as ^{119}Sn-MS ensures the study of the chemical environment of Sn nucleus in Ni-Mn-Sn alloys. The decay scheme of the radioactive ^{119m}Sn atom, which is used as the source of Mössbauer experiments is shown in Fig. 2.18. The relevant parameters of ^{119}Sn isotope are gathered in Table 2.1.

The parent nuclide used for performing transmission ^{119}Sn-MS experiments is ^{119m}Sn, which can be produced by high-flux neutron irradiation of ^{118}Sn. As depicted in Fig. 2.18, the 23.87 keV state is populated by the isomeric γ transition from ^{119m}Sn (half-life of 293 days). Although the high recoil free fraction of the 23.9 keV γ ray allows the measurements well above room temperature, the energy resolution of the ^{119}Sn resonance is about five times worse than that of ^{57}Fe. In this thesis, the Ca^{119m}SnO$_3$ source acquired from Eurostandard CZ has been used to perform transmission ^{119}Sn-MS experiments. Due to the cubic symmetry of the Ca^{119m}SnO$_3$ matrix, it shows a narrow emission line width. In order to avoid the parasite background radiation, a 50μm Pd foil is placed between the source and the absorber (sample).

The Sn atom, not being a transition element, does not posses an intrinsic hyperfine field at the nucleus created by open orbitals of its own electron shell. As a result, often the isomer shift and quadrupole splitting are only resolved. However, in certain circumstances, the Zeeman effect related to the magnetic hyperfine interaction can be observed in ^{119}Sn-MS. The hyperfine field in such cases is a so called *transferred hyperfine field*. The so-called transferred hyperfine field is produced through

$E^* - E_g$	I_g	I^*	g	g^*	$t_{1/2}$	Abundance
23.9 keV	$1/2^+$	$3/2^+$	1.047	0.658	17.75 ns	% 8.58

Table 2.1: From left to right, the transition energy ($E^* - E_g$), the nuclear spins of the ground (I_g) and excited states (I^*), the g-factor for the ground and excited states (g and g^*, respectively), the half-life of the Mössbuer state and the natural abundance of the ^{119}Sn Mössbauer nuclide.

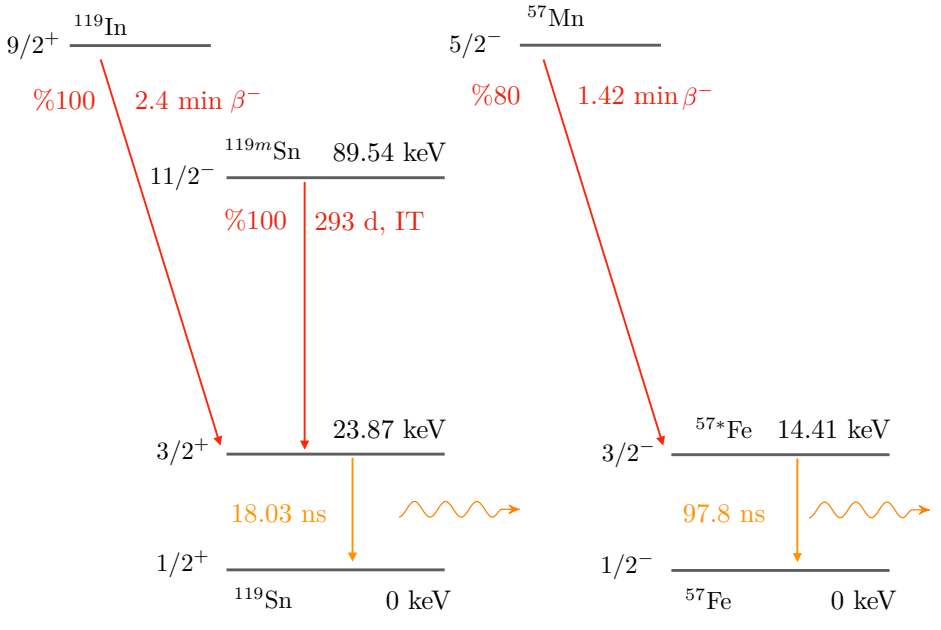

Figure 2.18: Decay scheme of ^{119}In, ^{119m}Sn (Isomeric Transition) and ^{57}Mn nuclei [96].

spin polarization of the closed s shells of the diamagnetic ion by direct exchange interactions with neighboring magnetically ordered spins and/or by the presence of polarized conduction electrons in the nuclei [95, 97]. In metals, the main contribution is expected to come from the polarization of conduction electrons by the moments of the surrounding magnetic ions. Thus, in the systems studied during this thesis, the dominating term is the Fermi contact term $\mathbf{B_S}$, which is given by [95]

$$\mathbf{B_S} = -\frac{2\mu_0}{3}\mu_B \sum_n \left(|\Psi_{ns\uparrow}(0)|^2 - |\Psi_{ns\downarrow}(0)|^2\right)^2 \tag{2.22}$$

where μ_B is the Bohr magneton and $|\Psi_{ns\uparrow}(0)|^2 - |\Psi_{ns\downarrow}(0)|^2$ the spin-up and spin-down densities at the nucleus [91]. In the case of Ni-Mn-Sn alloys, the magnetic moment of Mn atoms polarize the conduction electrons of ^{119}Sn atom, giving rise the Zeeman splitting and the corresponding sextet spectrum. This polarization is transmitted to the s-electron shells of the Sn atom by indirect exchange interaction leading to a Fermi contact field. Additionally, other contributions like the overlap of d-electrons of magnetic ions with the $4s$ electrons of Sn can play a role as well [95].

As will be shown in Sec. 4, ^{119}Sn-MS measurements have been focused on Ni-Mn-Sn and in Ni-Mn-Sn-Co alloys, both of them containing ^{119}Sn Mössbauer nucleus. However, in samples that do not contain any Mössbauer active elements as Ni-Mn-In samples, the Mössbauer studies have been carried out by specific ion-implantation at ISOLDE. As Ni, Mn, and In atoms are not Mössbauer active atoms, Ni-Mn-In

samples have been implanted with ^{57}Mn and ^{119}In nuclei, which decay to ^{57*}Fe and ^{119m}Sn states, thus enabling Mössbauer measurements in these materials. The decay schemes of these implanted isotopes are shown in Fig. 2.18.

2.4.4 Emission Mössbauer Spectroscopy at ISOLDE (CERN)

The eMS measurements have been carried out at ISOLDE (Isotope Separator On-Line-DEvice) facility as part of *Mössbauer Collaboration at ISOLDE/CERN* team. ISOLDE is located at CERN, on the border between Swiss and France and close to Geneva. ISOLDE, is part of other experimental facilities conforming CERN like LHC, ATLAS, SPS, etc. ISOLDE delivers a large variety of radioactive ion beams for many different experiments in the fields of nuclear and atomic physics, solid-state physics, materials science and life sciences.

The layout of the ISOLDE facility is shown in Fig. 2.19. The radioactive ion beam is produced by irradiating a fixed target material with high energetic protons. Initially, protons are created and accelerated up to 50 MeV in a linear accelerator. Afterwards, protons are introduced in the Proton Synchrotron Booster which contains four superimposed rings with radius of 25 m where the protons are accelerated up to 1.4 GeV. Finally the radioactive ions are produced using a 1.4 GeV proton-induced nuclear fission in a uranium carbide UC_2 target, which is placed in the target zone by robots.

During the implantation of the protons, the target is kept at 2000 K in order to facilitate the diffusion of the fission fragments to the surface. These fission fragments (i. e., radioactive atoms) are desorbed and ionized with elemental selective multi-

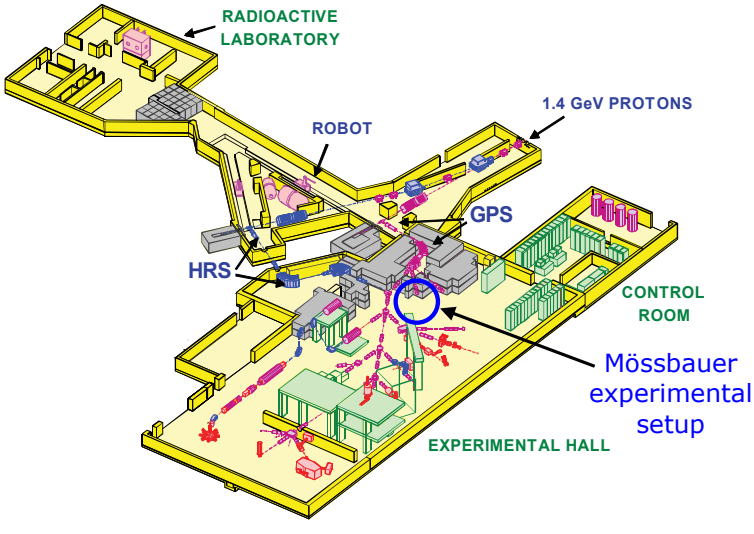

Figure 2.19: The disposal of the ISOLDE facility at CERN. 1.4 GeV protons are directed to the target, from which the radioactive ions are obtained.

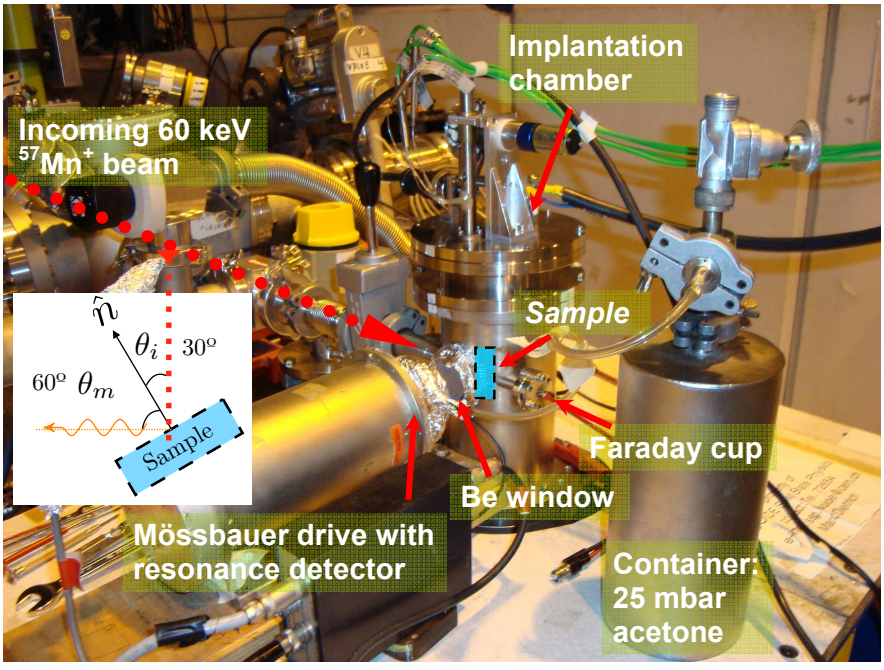

Figure 2.20: Picture of the high vacuum implantation chamber used to carry out eMS experiments at ISOLDE (CERN). Samples are mounted in different lids so that the radioactive beam is implanted in the sample. Mössbauer spectra are recorded using a avalanche parallel plate detector, which is filled with acetone gas. Figure adapted from T. S. Molhølt thesis [98].

photon laser ionization processes [99, 100]. The lasers are used for a isotope-selective ionization as well as to increase the yield respect to other isotopic contaminants resulting from the uncontrolled fission of the target material. Fe and Sn emission Mössbuaer experiments have been carried out by ^{57}Mn and ^{119}In radioactive ion implantation, respectively (see Fig. 2.18). The ionized $^{57}Mn^{+}$ and $^{119}In^{+}$ isotopes are then accelerated at 40-60 keV, and by means of magnetic fields pure $^{57}Mn^{+}$ and $^{119}In^{+}$ beams can be obtained. The radioactive beam is then directed to the eMS experimental setup, which is placed in one of the endings of the General Purpose Separator (GPS) beam (see Fig. 2.19). Prior to the beginning of the beamtime, the beam-settings (mass, lasers, deflector settings) as well as the alignment of the implantation chamber are optimized for the experiments. With the beam intensity available at ISOLDE/CERN ($\approx 10^8$ ions/s) spectra of good statistics are obtained within few minutes.

The picture of the implantation chamber and the setup used for carrying out the eMS experiments is shown in Fig. 2.20. In order to take advantage of the high yield provided by ISOLDE, and to make sure that the samples are in line with the beam, the chamber has to be precisely aligned respect to the incoming beam-line. The chamber is aligned using lasers and the alignment is checked with a Faraday

Cup which is mounted behind the sample position on the implantation chamber. By means of stable ^{40}K beam, the transmission is measured in the Faraday cup and compared with the transmission obtained in a stage prior to the implantation chamber[7].

Once the chamber is properly aligned, it is pumped by successive rough and turbo-molecular pumps stages to keep the chamber at $\approx 10^{-6}$ mbar. After that, the setup is connected to the beam-line vacuum by soft bellows to eliminate the spurious vibrations that could affect the Mössbauer measurements. At this stage, the chamber is connected directly with the beam-line where the radioactive beam comes from. In order not to vent the target, the beam-line must be always at ultra-high vacuum conditions. As the implantation chamber is repeatedly opened during the beam-time for loading the samples, several valves ensures the good vacuum in the beam line when the chamber is opened.

As depicted in Fig. 2.20, the ion implantation is performed at an incident angle $\theta_i = 30^o$and measured at $\theta_m = 60^o$, $(\theta_i + \theta_m = 90^o)$ both relative to the sample surface normal $\hat{n}$. The constant acceleration Mössbauer drive with the resonance detector is placed outside the implantation chamber at 90^o relative to the beam direction. In order to remove the high energetic electrons emitted during the β^- decay, a Be window is placed on the UHV window of the implantation chamber. This Be filter blocks effectively electrons, allowing γ ray transmission related to the Mössbauer transitions up to 90%. Unlike in the transmission configuration, in eMS the sample acts as a source since the radioactive ions are implanted within the sample. For safety and handleability reasons, the radioactive sample is kept stationary while the detector, which in the current setup acts as the absorber, is moved with the Mössbauer drive.

In order to perform eMS measurements under diverse experimental conditions, a multipurpose implantation chamber has been employed. The employed lids are shown in Fig. 2.21. The high temperature eMS measurements series have been conducted using a four position lid. A moveable sample holder allows to change the position of the sample without breaking the vacuum, reducing the time spent on removing and mounting lids, thus saving the limited time of the competitive beamtime allocation. A heating lamp coupled to the lid enables to collect eMS measurements in the 300 - 800 K temperature range.

Further measurements have been carried out using another lid labelled as *rotation lid*. This lids enables the rotation of the sample during the measurements allowing the determination of the angular dependence of the collected spectrum. Initially, an online measurement (implanting and measuring) is taken during four minutes at $\theta_i = 30^o (\theta_m = 60^o)$. After this time, the beam is switched off and the lid is rotated, so the $\hat{n}$ of the sample is faced parallel to the detector ($\theta_i = 90^o$, see Fig. 2.20). At this position, the decay radiation is measured during other four minutes. The whole process is repeated several times to improve the statistics. This *rotation lid* also allows to perform angular dependence by attaching NdFeB or a set of SmCo

[7]In the stable beam procedure, the beam is transmitted through a hole in an empty position of the four position lid shown further below.

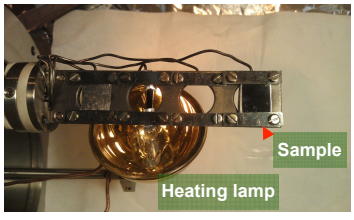

4 Position hot lid: 300 K - 800K

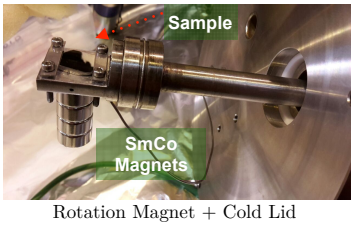

Rotation Magnet + Cold Lid
B_{ext} =0.6 T, 300 K - 77 K

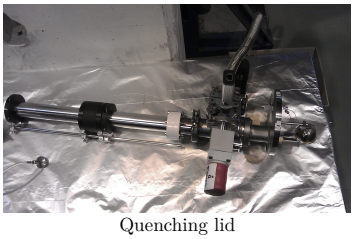

Quenching lid

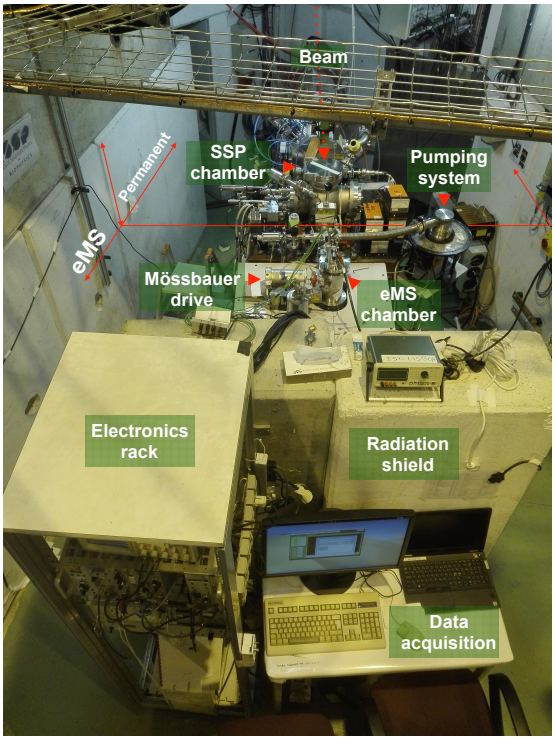

Figure 2.21: Left, the picture of the 4 position hot lid, the rotation magnet lid, cold lid and the quenching lid. Right, the top view of the whole setup for carrying out the eMS measurements.

permanent magnets on the back of the sample. The applied field direction is parallel to $\hat{n}$ with field strength of $B_{ext} = 0.6$ T.

The low temperature measurements have been conducted using another sample holder, labelled as *cold lid*. The temperature is controlled by sucking liquid N_2 through a cold finger that cools down the sample. The measurement temperature, which ranges between 90 -300 K is controlled by a k-type thermocouple. Finally, the samples have been also subjected to quenching experiments. As will be shown in Sec. 4, the implantation damage induced during the ion implantation is negligible at high enough temperatures. However, at low temperatures, the implantation damage can dominate the spectrum hindering the information. In order to investigate the low temperature properties and overcome the implantation damage, quenching experiments have been carried out. The sample is implanted at temperatures well above room temperature (e. g., 700 K) where no implantation damage is induced due to the ultra-fast recovery of the lattice [98]. Afterwards, the sample is quenched into liquid N_2, reaching 90 K temperature almost instantaneously. Once the sample is cooled down, an off-line eMS measurement is performed by collecting the decay radiation of the probe atom located within the sample.

In this connection, post-implantation annealing treatments could also help to remove the implantation damage and perform eMS measurements in other laboratories. However, due to the short lifetime of the implanted ions, the activity of the sample does not allow post-implantation annealing treatments. The half-life of the ^{57}Mn atom is 1.5 min whereas the one of ^{119}In is 2.1 min. Such a short lifetime implies that the the activity decays in matter of minutes. After 45 mins, it can be considered that samples are not radioactive anymore.

However, by implantating long-lived isotopes, such as ^{119m}Sn (see Fig. 2.18), it is possible to collect the decay radiation in a more extended period[8]. In fact, during the interval that the sample is radioactive, the implanted samples can be subjected to annealing treatments to eliminate the implantation damage. The emission spectrum of the implanted sample can be measured off-line in a supervised lab equipped with an off-line eMS spectrometer.

2.4.5 Setting up for an Off-Line eMS Spectrometer

For an off-line eMS measurements, samples are first implanted with the desired long-lived isotope, in the present case, ^{119m}Sn. In principle, a sample of $\approx 3\mu$Ci (0.1 MBq) is enough for having an useful source for off-line measurements during a year (for ^{119m}Sn [98]). The implantations are performed at the solid state physics chamber (SSP, see Fig. 2.21), and bearing in mind the fluence of the beam, it is implanted during a certain period to obtain the desired activity. As the beam spot area is ≈ 0.3 cm^2, the implanted samples are usually small.

The radioactive ions are directly implanted into the sample, and as a result, in the off-line setup the sample acts as the source of the γ rays. Thus, a detector with a proper absorber is required for measuring the emission spectrum. For this purpose, a resonance detector is employed, where the conversion electrons originated from the decay of the Mössbauer state at an absorber/detector plate are collected. The γ rays of the Mössbauer transition emanated from the implanted samples are absorbed by the detector, which in turn, consists in a plate containing the right isotope to enable the resonant absorption (e. g., stable ^{119}Sn). When the stable nucleus located at the detector absorbs the γ ray by the recoilless resonant absorption, the nucleus is promoted to an excited state which eventually decays back to its ground state. In this transition, along with the corresponding γ ray, conversion electrons are also produced. Thus, by detecting the conversion electrons resulted from the de-excitation process of ^{119}Sn nucleus, the absorption events (i. e., the emission events of the radioactive sample) can be detected.

However, the detection of conversion electrons is not sufficient to produce a large enough signal. Thus, the resonance detector is provided by a parallel plate avalanche detector (PPAD), see Fig. 2.22. A PPAD consists in two conductive parallel plates where a bias voltage is applied to create a homogenous electric field. One of the conductive plates is made of the resonance absorber material (absorber) and the whole detector is filled with gas (in the present case acetone). As the scope of the

[8]The implantations are performed in the solid state physics (SSP) chamber.

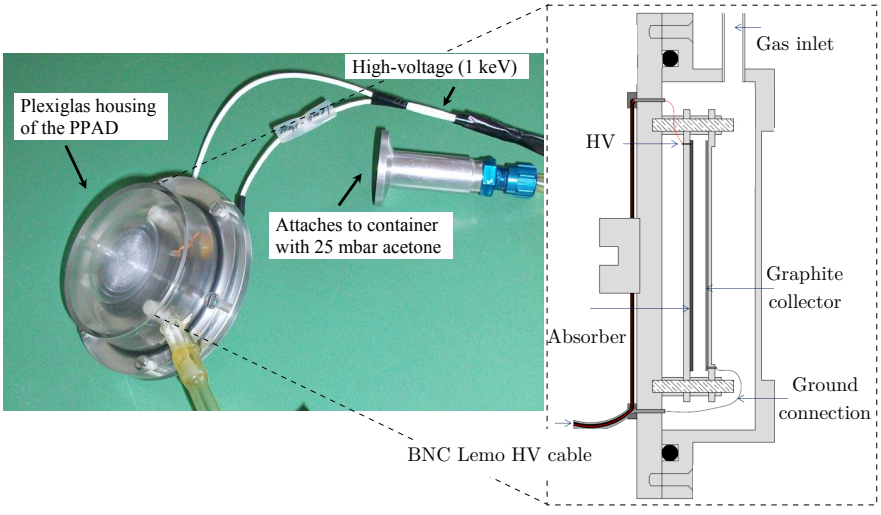

Figure 2.22: From left to right, the picture of the resonance parallel plate avalanche detector and the cross-sectional view. Pictures are adapted from the thesis of and T.E. Molhølt [98] and H. Masenda [101].

detector is to amplify the signal by producing an avalanche of electrons, the pressure of the detector is set according to the desired breakdown voltage, which in turn, depends on the pressure and the gap between the absorber and the collector plate (Paschen law [102]). The detector is filled to 25 mbar pressure of acetone gas [101]. As the breakdown voltage depends strongly on the pressure and the nature of the gas, an acetone gas reservoir is coupled to the detector to keep the optimal conditions over time. Thus, when a γ ray coming from the sample is absorbed by the detector, the conversion electrons are accelerated from the absorber to the cathode (collector), and a pulse of the proportional cascade induced by the conversion electrons is detected. The PPAD has a resolution time of 10^{-9} s and an excellent signal to noise ratio, becoming suitable for off-line Mössbauer measurements.

The diagram of the whole off-line Mössbauer spectrometer is shown in Fig. 2.23. Unlike in the online eMS measurements (at ISOLDE), the implanted sample is placed in the Mössbauer drive. As the implanted samples are usually small, it is easier to move the sample rather than the detector. The drive is connected to a Mössbauer Drive Unit 500, which incorporates a digital function generator within it. The detector, is pumped and filled with the acetone gas several times and eventually kept at 25 mbar. Then, the PPAD is connected to the Model 2006 Proportional Counter Preamplifier by means of Lemo-BNC special wires to power up the detector and to amplify the signal collected by PPAD. The signal is connected to an oscilloscope in order to see the height of pulses, which are kept below 30 mV. The amplitude of the pulses can be tuned by modifying the bias voltage given by the HV Model Ortec 556. Additionally, the signal is subsequently amplified and introduced in the Single Channel Analyzer SCA 103.

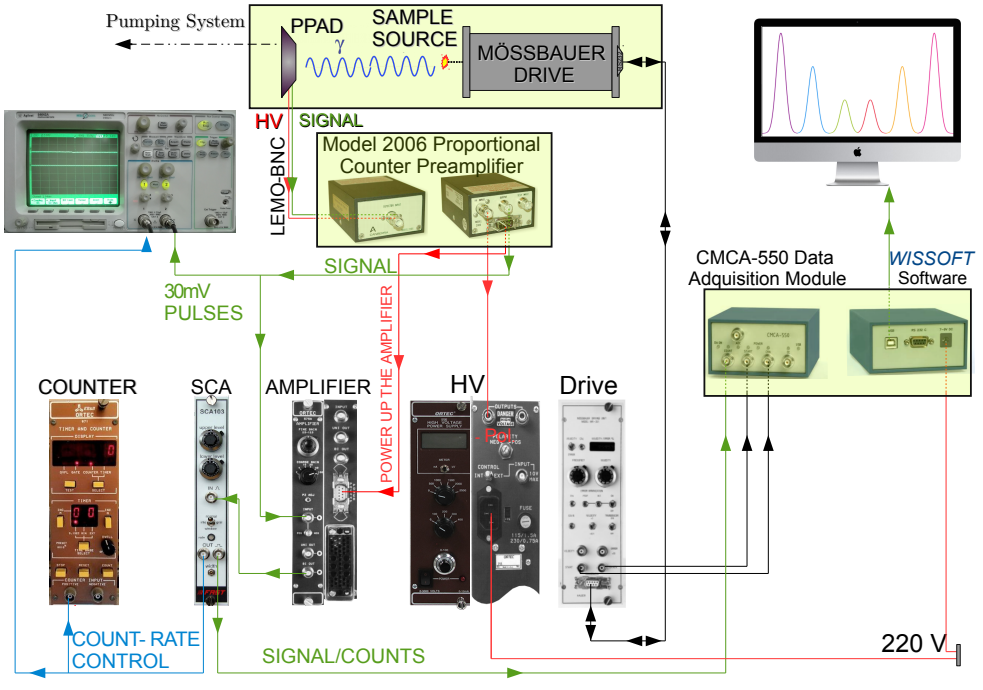

Figure 2.23: Schematic diagram of the electronics of the off-line eMS spectrometer.

The output of the SCA is connected to the Ortec 971 Timer and Counter Module. Monitoring the shape of the pulses and the count-rate is crucial to detect misbehavings or possible leaks of the detector, which give rise to non-desired sparking events. On the other hand, the signal of the SCA is read by the CMCA-550 Data Acquisition Module. This module also takes the start and the channel advance signal from the Mössbauer Drive Unit. These three inputs are digitally managed in a built in Multi Channel Analyzer (MCA) CMCA-550 data acquisition module. Finally, the module is connected to a computer to display the emission Mössbauer spectrum. An actual picture of the whole setup is shown in Fig. 2.24.

Transmission ^{119}Sn-MS measurements have been carried out using a Mössbauer spectrometer coupled with a 12 K closed cycle refrigerator system and a vibration isolation stand. This setup allows to collect spectra in the 15-315 K temperature range. Further measurements have been additionally conducted in a second Mössbauer spectrometer, where a liquid nitrogen cryostat has been used for ^{119}Sn-MS measurements in the 77-400 K temperature range. The analysis of the experimental ^{119}Sn-MS spectra have been performed using the NORMOS [103] and VINDA [104] programs.

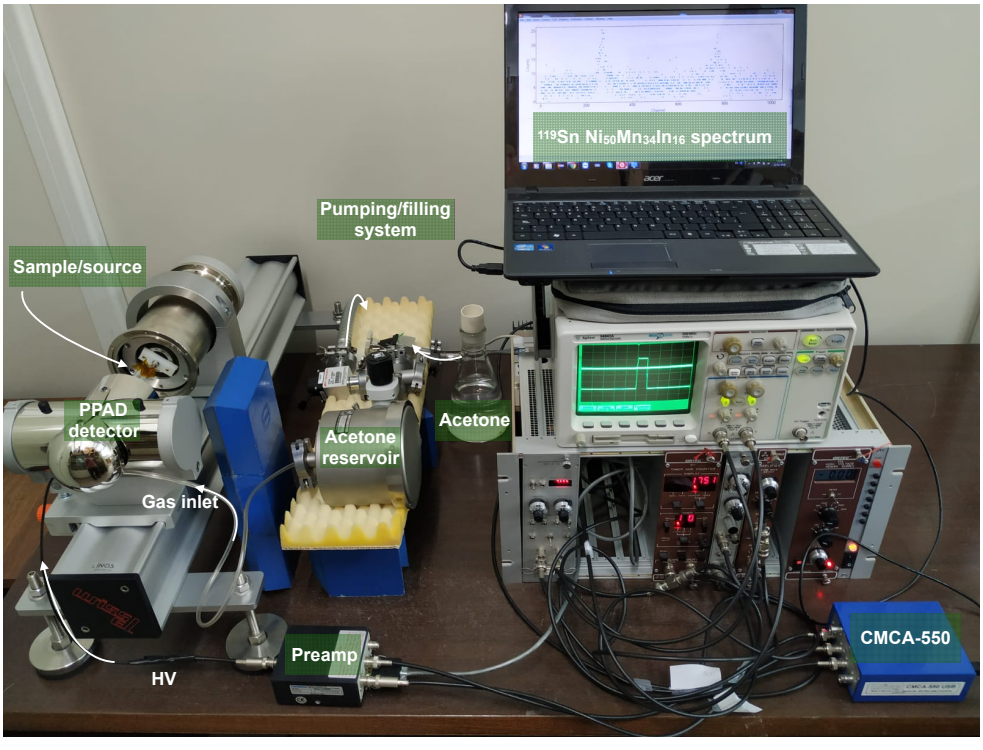

Figure 2.24: Picture of the set up for off-line eMS measurements developed in the Nuclear Techniques Laboratory at the UPV/EHU with the advice of H. P. Gunnlaugsson.

2.5 Positron Annihilation Lifetime Spectroscopy (PALS)

PALS is a nondestructive spectroscopy, which is intended to study defects in solids [105]. The technique is based on the fact that positrons (e^+) entering the solid annihilate with surrounding electrons. The lifetime of positrons depends strongly on the electronic density of the solid, where larger electron density implies faster annihilation rate of the positron and vice versa. Crystal imperfections such as vacancies and dislocations act as trapping centers for positrons in metals and semiconductors [106]. The electron density that the positron feels when it is trapped in such imperfections varies compared with the electron density of the perfect solid. As a result, the probability of the positron to "find" an electron varies and the lifetime of the positron differs the positron lifetime in the undefected lattice. Thus, the positron lifetime gives direct information of the presence and the nature of defects.

The electron-positron annihilation can take place through the emission of one,

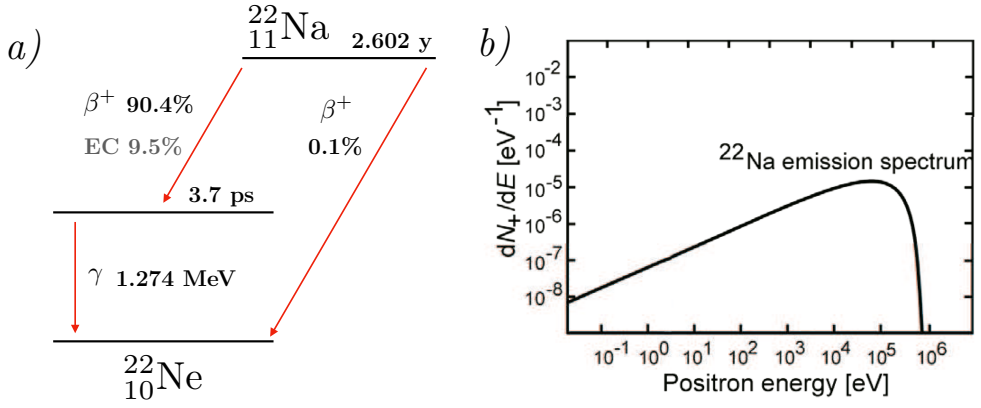

Figure 2.25: (a) Decay scheme of ^{22}Na isotope. According to Eq. (2.23), in 90.4% of decays are followed by an emission of a positron, an electron neutrino and a gamma ray of 1.274 MeV. The probability of the direct transition to the ground state of ^{22}Ne following a β^+ decay can be considered as negligible. (b) Positron emission spectrum where dN_+/dE is the number of positrons per energy channel. The maximum energy of emitted positrons is $E_{max} \approx 0.57$ MeV [106].

two, three or more light quanta[9]. In solids, the most probable disintegration channel is via two γ rays [107] and the probability of annihilation at three photons is very small, around 0.3%[10].

2.5.1 Positron Sources

The most common way to obtain positrons for PALS is by means of radioactive isotopes, which exhibit β^+ *decay*. Among the most suitable isotopes (e. g., ^{64}Cu, ^{58}Co, ^{68}Ge), ^{22}Na isotope is the most widely used because of its relative long half-life (2.6 years) and the high efficiency of positron production. When a ^{22}Na isotope experiences β^+ decay, one proton transmutes into a neutron with a simultaneous emission of a e^+, an electronic neutrino ν_e and a γ ray

$$^{22}\mathrm{Na} = {}^{22}\mathrm{Ne} + e^+ + \nu_e + \gamma \tag{2.23}$$

As shown in Fig. 2.25, 90.4% of ^{22}Na isotope decays into an excited state of ^{22}Ne, in which along with an electron neutrino ν_e, a positron is emitted. Afterwards, the excited state of ^{22}Ne decays to its ground state via emitting a γ ray of 1.27 MeV. Although the electron capture process and the direct transition to the ground state are also possible, these events are less than 10% of the total events. As a result, the

[9] Although the production of a γ ray would in principle violate the conservation of energy and momentum, according to the quantum field theory this process is allowed as an intermediate quantum state for sufficiently short times in which the violation of the conservation of energy can be accommodated to the Heisenberg uncertainty principle.

[10] Annihilations to more than three photons are also possible. However, these events are less likely for increasing number of photons due to the magnitude of the fine structure constant α.

efficiency of positron production of ^{22}Na is very high. As it will be shown later, the emission of the 1.27 MeV γ ray is crucial in order to identify the birth of the positron.

2.5.2 Penetration Length

The energy of positrons emitted by a radioactive source has a characteristic distribution. In the case of ^{22}Na, as shown in Fig. 2.25, the maximum energy of positrons emitted during the decay is 0.57 MeV. Depending on the energy of the emitted positrons, they will penetrate in the material accordingly. The implantation profile of positrons, $P_+(z)$ is described by

$$P_+(z) = \alpha_+ e^{-\alpha_+ z} \tag{2.24}$$

where z is the penetration length and α_+ the absorption coefficient. The inverse of the absorption coefficient $R_+ = \alpha_+^{-1}$ defines an average implantation profile of the positrons, which depends on the maximum energy of positrons and on the density ρ of the solid [108],

$$\alpha_+ = R_+^{-1} = a \frac{\rho[\mathrm{g/cm^3}]}{E_{max}^b[\mathrm{MeV}]} \mathrm{cm}^{-1} \tag{2.25}$$

where $a = 17$ and $b = 1.43$ are empiric constants[11]. The penetration range of Eq. 2.25 defines the minimum thickness of the material for PALS measurements in order to ensure that most of implanted positrons are annihilated within the sample. From the experimental point of view, this penetration length also dictates the depth of the sample that would be scanned by positrons[12].

2.5.3 Thermalization and Diffusion

When a positron enters a solid, it loses energy until reaches thermal equilibrium. Independently of the origin of the positron (isotope sources or mono-energetic slow positron beams), the kinetic energy of positrons is much larger than the thermal energy of the solid [106]. As a result, this energy difference is dissipated in the crystal by several mechanisms, such as, core ionization processes [109], plasmon excitations [110], excitation of conduction electrons in metals, excitation of electron-hole pairs in semiconductors, and finally, via scattering of phonons at sub-electronvolt energies [109].

For the most energetic positrons, the energy-lost rate is large, $\approx$ MeV/ps for positrons between 100 keV and 1 MeV kinetic energy. However, the energy-lost rate depends on the kinetic energy of positrons and both magnitudes evolves over time. The thermalization time in which positrons acquire the thermal equilibrium within

[11] The empirical constants are deduced from transmission experiments.

[12] For monitoring defects as a function of depth, slow-positron-beam techniques are used, in which the energy of the positrons are moderated in order to adjust the depth profile.

the solid is $\approx 10^{-12}$-10^{-13} s, much lower than the average lifetime of positrons in solids[13] [108].

Thermalization is followed by diffusion through the solid, where positrons behave as charged particles. Due to the positive charge of e^+, they are repelled by the nuclei and the position probability density is found to be the largest in interstitial sites [106]. During diffusion, positrons can be scattered by longitudinal acoustic phonons [111, 112] and by optical phonons [113]. In addition, due to a finite lifetime that positrons exhibit in a defect free solid, τ_b, the positron L_+ diffusion length is limited in such way that

$$L_+ = \sqrt{\tau_b D_+} \quad \text{with} \quad D_+ = \tau_r \frac{k_B T}{m^*} \tag{2.26}$$

where τ_r is the relaxation time of the dominant scattering process and m^* the positron effective mass[14]. For example, the length that e^+ scan during its lifetime at 300 K is ≈ 5000Å [115]. During the diffusion process the positron may get trapped at defects before annihilation takes place, which reduces the effective diffusion length.

The positron annihilation rate λ, i. e., the inverse of the positron lifetime τ, is given by the overlap of the positron density $n_+(\mathbf{r})$ and the electron density of the solid $n_-(\mathbf{r})$ as

$$\lambda = \frac{1}{\tau} = \pi c r_0^2 \int n_+(\mathbf{r}) n_-(\mathbf{r}) \gamma(\mathbf{r}) \mathrm{d}\mathbf{r}, \tag{2.27}$$

where c is the speed of light in vacuum, r_0 the classical electron radius and $\gamma(\mathbf{r})$ the so-called enhancement factor that comprises the enhanced electron density due to the positron Coulomb attraction.

2.5.4 Positron Trapping at Defects

In a defect-free lattice, the positron annihilates from the delocalized state (i. e., Bloch state) at an average rate λ_b or with a characteristic lifetime τ_b. However, solids have imperfections in their lattice, such as vacancies or dislocations that may act as positron traps. The trapping occurs when a positron turns from the Bloch state into a localized state within a defect (i.e. the positron wave function is localized at the defect). The κ_d trapping rate of a defect is proportional to the defect concentration C_d as $\kappa_d = \mu_d C_d$ [116]. The μ_d parameter is the specific trapping coefficient of the defect and it depends on the type of defect and on the surrounding lattice [105, 117].

Defects characterized with considerable open-volume, such as vacancies, present the most effective trapping centers for positrons in metals. Due to the lack of the ion, the repulsion sensed by positrons is lowered and such defects act as attractive potential wells for positrons [115]. The ground state of the positron localized at such

[13] It is noteworthy to mention that the thermalization also depends on the solid temperature. The lower the temperature of the solid in which the positron is implanted, the larger is the thermalization time.

[14] The effective positron mass m^* is larger than the rest mass of the free positron due to the phonon scattering, screening of positrons by electrons and the effect of the periodic lattice [114].

defect is generally deep, with a binding energy larger than 1 eV [117]. Moreover, vacancies are characterized by an open volume with an electron density lower than the one corresponding to the perfect lattice, and according to Eq. (2.27), positrons trapped at vacancies exhibit longer lifetimes.

2.5.5 Interpretation of PALS spectra

As pointed out before, the delocalized positrons can be annihilated from the delocalized Bloch state at a λ_b rate (with a characteristic τ_b lifetime), or instead, get trapped in a defect and annihilate from the localized state at a λ rate (with a characteristic τ lifetime).

Let us consider $n_b(t)$ as the number of positrons present in the delocalized state at instant t with a characteristic λ_b annihilation rate. For a total k type of defects trapping positrons, each one is characterized by an specific annihilation and trapping rate, λ_i and κ_i, respectively. Additionally, due to the thermal energy (k_BT) that may overcome the binding energy of the positron to the defect, some positrons may detrap from defects at δ_i detrapping-rate at high-enough temperatures[15]. If the total amount of positrons that are trapped in defects at instant t is $n_i(t)$, then the kinetic equations governing the evolution of these two states are given by

$$\frac{dn_b(t)}{dt} = -\left(\lambda_b + \sum_{i=1}^{k} \kappa_i\right) n_b(t) + \sum_{i=1}^{k} \delta_i n_i(t) \tag{2.28}$$

and

$$\frac{dn_i(t)}{dt} = \kappa_i n_b(t) - (\lambda_i + \delta_i)\, n_i. \tag{2.29}$$

These two kinetic equations describe the trapping and the annihilation process of positrons in a solid. It is noteworthy to mention that the thermalization time (≈ 1 ps) is much smaller than the positron lifetime. Considering that at $t = 0$ all positrons N_0 present in the solid are in the delocalized state, then the initial conditions are $n_b(0) = N_0$ and $n_i(0) = 0$. As a result, the solution to Eq. (2.28) and to Eq. (2.29) is,

$$D(t) = \sum_{i=1}^{k+1} I_i e^{-t/\tau_i} \tag{2.30}$$

The previous expression defines the probability of a positron to remain alive at time t. As shown by Eq. (2.30), the probability decreases following an exponential law. Apart from the characteristic τ_b constant (referring to positron annihilation from the delocalized state), each type of defect is characterized with a characteristic constant τ_i, which depends on the nature of the defect and the surrounding environment [106]. Additionally, the sum of all intensities must be one $\sum_{i_1}^{k+1} I_i = 1$. Thus,

[15] As it will be see, due to the high binding energy of positron to the defects, this effect is negligible in metals.

the positron lifetime spectra $\mathcal{F}(t)$, is the time derivate of $D(t)$ and it represents the probability of a positron to be annihilated at instant t [106]

$$\mathcal{F}(t) \equiv \left| \frac{dD(t)}{dt} \right| = \sum_{i=1}^{k+1} \frac{I_i}{\tau_i} e^{-t/\tau_i}. \tag{2.31}$$

Taking into account that at $t = 0$, the variation of the number of positrons present in the solid only depends on the annihilation rate λ_b of the delocalized state, the previous expression results in

$$\left| \frac{dD(0)}{dt} \right| = \lambda_b = \sum_{i=1}^{k+1} \frac{I_i}{\tau_i}. \tag{2.32}$$

If no positron traps are present in the solid (undefected solid), $k = 0$ and then τ_i of Eq. (2.32) corresponds to τ_b. In such scenario, the experimental PALS spectrum reveals a single component with a characteristic lifetime τ_b related to the electron density of the sample. However, if one or more type of defects are present in the solid, then $\overline{\tau}$ present the statistically strongest parameter, which is defined as

$$\overline{\tau} = \int_0^\infty t \left(\frac{dD(t)}{dt} \right) dt = \sum_{i=1}^{k+1} I_i \tau_i \tag{2.33}$$

Eq. (2.33) shows the average positron lifetime $\overline{\tau}$. Along with τ_b component, the contribution of the other type of defects present in the solid appear mixed in a single $\overline{\tau}$ component. Thus, in order to extract different components contributing to $\overline{\tau}$ and eventually, the characteristic lifetimes related to each type of defects, experimentally measured $\overline{\tau}$ lifetime must be decomposed.

The positron evolution throughout implantation described in the previous sections are summarized in Fig. 2.26. Subsequent to the ^{22}Na decay, and along with the emission of the positrons, a 1.27 Mev γ ray is emitted. The detection of this γ ray marks the birth of the positron and it is often called START photon. As previously pointed out, the emission and thermalization of positrons is much more shorter (≈ 1 ps) than the positron lifetime in solids (100 - 500) ps. Thus, the detection of the γ photon represents the $t = 0$ of the positron lifetime.

After the thermalization process, the positron is diffused through the solid until it annihilates with a surrounding electron. In the $e - e^+$ annihilation, the rest mass of each particle turns into energy according to $E = m_0c^2$, which results in the emission of two gamma rays of 511 keV. The detection of a 511 keV γ ray determines the end of the positron lifetime (STOP photon). Thus, the lifetime of the positron is obtained by measuring the time interval between the detection of the START and STOP γ quanta.

It is noteworthy to mention that the previous scheme is only applicable if there is only one positron in the solid at a time. If this condition is not fulfilled, different start and stop signals related to different creation and annihilation events can be mixed, resulting in a biased lifetime measurement. However, the amount of positrons

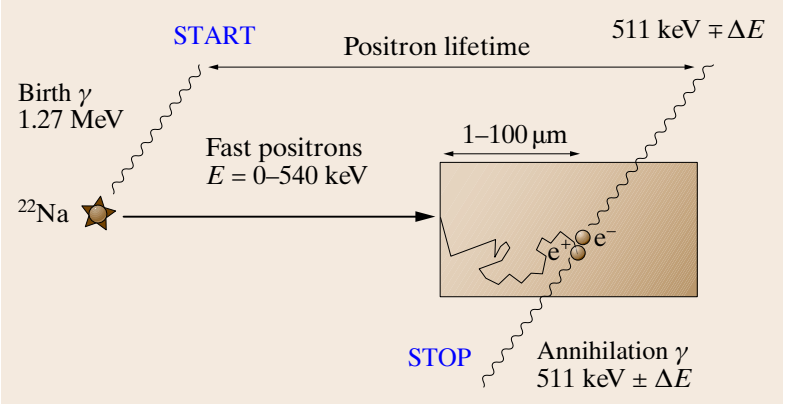

Figure 2.26: Illustration of the birth and the annihilation of the positron throughout its lifetime. The initial 1.27 MeV γ ray acts as a start signal of the atomic clock. After the annihilation of the positron with a surrounding electron, the detection of one of the 511 keV γ rays marks the end of the positron lifetime. Schematic obtained from Ref. [115].

entering the solid is controlled by the activity of the ^{22}Na source. In the present thesis, ^{22}Na sources of 20 μCi have been used, where for a given time, the $1e^+$/sample condition is fulfilled.

2.5.6 Trapping Models: *One-trap* Model

When a single type of open-volume defect is present in the solid (in the present case a vacancy type defect is considered), positrons may annihilate from the delocalized state at an average λ_b rate, or, if the concentration of vacancies is sufficiently high, a certain fraction of positrons may be trapped at such defects. If the probability of a positron of being thermally detrapped from the vacancy is negligible, then positrons trapped at vacancies may annihilate from the localized state at an average rate λ_v (i. e., $\lambda_b > \lambda_v$ and therefore $\tau_b < \tau_v$). Vacancies act as deep traps for positrons in metals with characteristic binding energies higher than 1 eV and the detrapping phenomena can be considered negligible. Then, according to the Eq. (2.28) and Eq. (2.29), the kinetic equations governing the positron physics when a single vacancy type defect is present in the solid, are given by the following two equations:

$$\frac{dn_b(t)}{dt} = -(\lambda_b + \kappa_v)n_b(t) \tag{2.34}$$

$$\frac{dn_v(t)}{dt} = -\lambda_v n_v(t) + \kappa_v n_b(t). \tag{2.35}$$

Considering that no positron trapping takes place during the thermalization process, the initial conditions are given by $n_b(0) = N_0, n_d(0) = 0$ constraints, where N_0 is the total number of positrons at $t = 0$. The solution of the previous two equations is the positron lifetime spectrum of Eq. (2.30) in which $k = 1$,

$$D(t) = I_1 e^{-t/\tau_1} + I_2 e^{-t/\tau_2} \tag{2.36}$$

where

$$\tau_1 = \frac{1}{\lambda_b + \kappa_v}, \quad \tau_2 = \lambda_v^{-1} \tag{2.37}$$

$$I_1 = 1 - I_2, \quad I_2 = \frac{\kappa_v}{\lambda_b - \lambda_v + \kappa_v}. \tag{2.38}$$

Rather than the positron annihilation rate λ, it is more common to use the characteristics lifetimes τ. However, it is important to notice that in general, the lifetimes obtained from Eq. (2.36) and from the positron lifetime spectrum of Eq. (2.31) are not directly related to the bulk and defect-related positron lifetimes. As shown in Eq. (2.37), due to the weight of κ_v, τ_1 is often called as the reduced-positron lifetime. However, τ_2 depends only in the annihilation rate of the present vacancy. By redefining $\tau_v = \lambda_v^{-1}$ and $\tau_b = \lambda_b^{-1}$, and taking into account that the trapping rate is proportional to the vacancy concentration C_v, from Eqs. (2.37) and (2.38), the relation between the characteristic positron lifetime and C_v can be obtained by means of

$$\kappa_v = \mu_v C_v = I_2 \left(\frac{1}{\tau_1} - \frac{1}{\tau_2} \right) = \frac{I_2}{I_1} \left(\frac{1}{\tau_b} - \frac{1}{\tau_v} \right). \tag{2.39}$$

Additionally, according to the definition of $\overline{\tau}$ of Eq. (2.33) and combining with the previous equation, the so-called *one-trap model* is obtained

$$\overline{\tau} = \tau_b \frac{1 + \kappa_v \tau_v}{1 + \kappa_v \tau_b} \qquad \kappa_v = \mu_v C_v = \frac{1}{\tau_b} \frac{\overline{\tau} - \tau_b}{\tau_v - \overline{\tau}} \tag{2.40}$$

where μ_v is the specific trapping coefficient of the vacancy, which depends on the type of defect and also on the surrounding lattice [117].

2.5.7 Basics of PALS Measurements

Fig. 2.27 shows the diagram of a PALS spectrometer along with details of the sample-source sandwich arrangement (SA).

Samples are placed in a collinear geometry between two photomultiplier (PM) tubes. Each photomultiplier is optimized for detecting a specific energy window of the γ ray, allowing a selective detection of either the birth 1.27 MeV γ ray in the START channel, or the 511 keV γ ray of the positron annihilation in the STOP channel. When ^{22}Na decays, the 1.27 MeV γ ray emitted at the positron birth is detected on the START channel. This gamma ray is properly detected combining the photomultiplier with a plastic scintillator (SC) located right between the SA and PM. The corresponding energy window is selected in the SCA of the DCFD module. When the positron gets annihilated, a 511 keV γ ray is detected in an analoge way in the STOP channel.

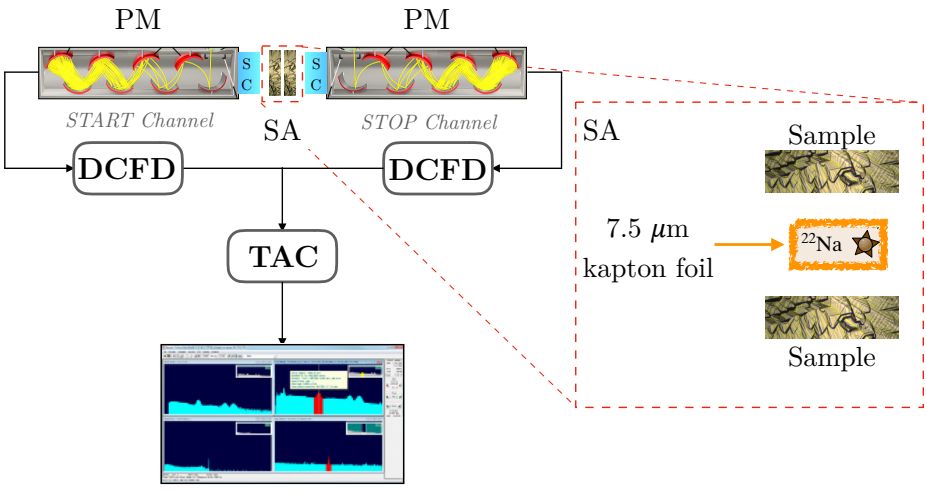

Figure 2.27: Diagram of a fast-fast coincidence positron lifetime spectrometer along with a schematic representation of the sample-source sandwich arrangement.

After a proper electric handling of the signal (explained further below), PALS spectra are collected and visualized by the MCA. As shown in Fig. 2.28, an histogram is obtained, which by means of standard computer programs based on Gauss-Newton non-linear fitting routines (e. g., LIFSPECFIT or POSITRONFIT [118]), the different positron lifetimes can be subtracted from the experimental spectrum.

The spectrum shown in Fig. 2.28 presents a typical PALS spectrum. In general, PALS spectra are composed, at least, by three different components, which in the present case have been labeled as $\overline{\tau}$, τ_{SL} and τ_{SK}. However, among the three components, $\overline{\tau}$ is the only one giving sample's information. $\overline{\tau}$ comprehends the different contributions of positron annihilated from both bulk and defects as defined in Eq. 2.33. The othe two τ_{SL} and τ_{SK} comprise the so-called source contribution. As shown in the inset of Fig. 2.27, the ^{22}Na source is wrapped in a 7.5μm Kapton© foil. Thus, some positrons are annihilated in the Kapton© foil, and their contribution has to be subtracted from the experimental PALS spectrum. The characteristic positron lifetime in Kapton© has a very well-known value of 382 ps [119, 120][16]. The second contribution of the source component, τ_{SL}, is related to positronium formation at the interface source-sample. Its characteristic positron lifetime is typically around 1500 ps [121, 122]. As a result, and prior to spectra decomposition, these two source components have to be subtracted to obtain the raw PALS spectrum of the sample, shown in Fig. 2.29.

[16] Although the foil is only 7.5μm thick, due to backscattering of positrons from the samples, the contribution of positrons annihilating in Kapton© has to be taken into account [121].

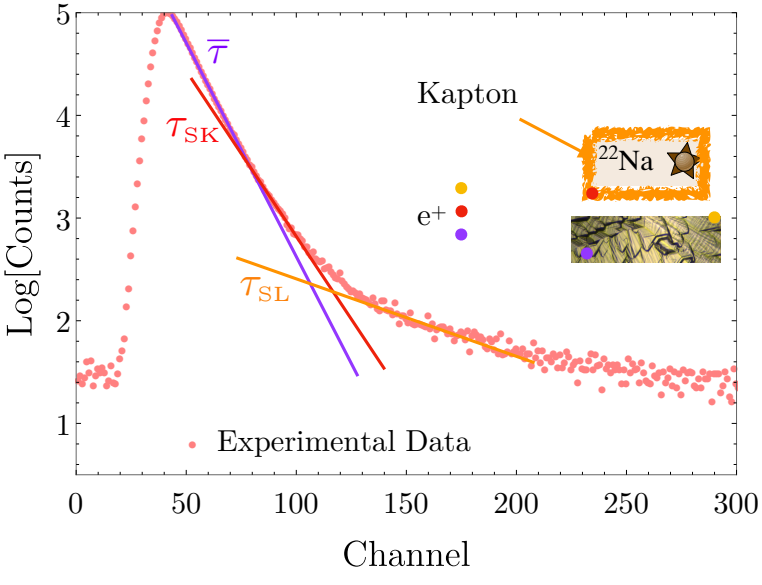

Figure 2.28: Example of an experimental PALS spectrum, in which the different contributions are displayed. $\overline{\tau}$ is related to the positron annihilated from the sample, whereas τ_{SL} and τ_{SK} represent the source component.

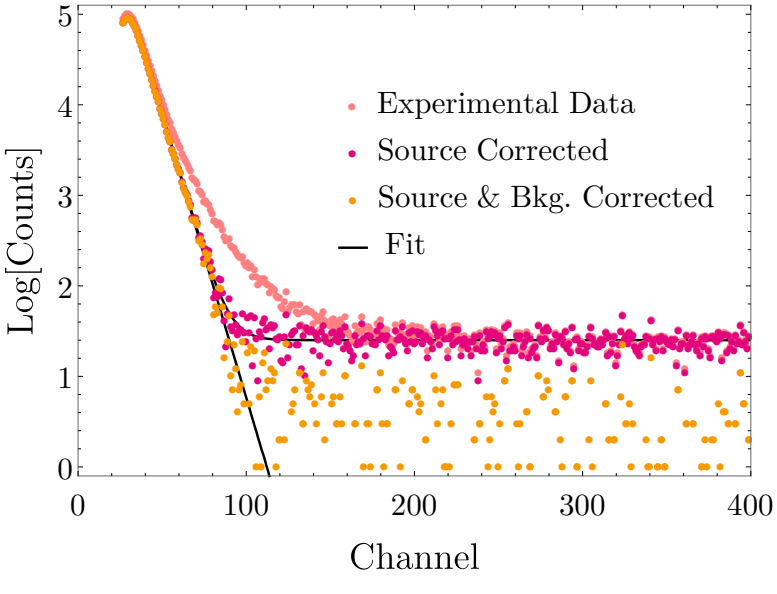

Figure 2.29: Source and background corrected PALS spectrum.

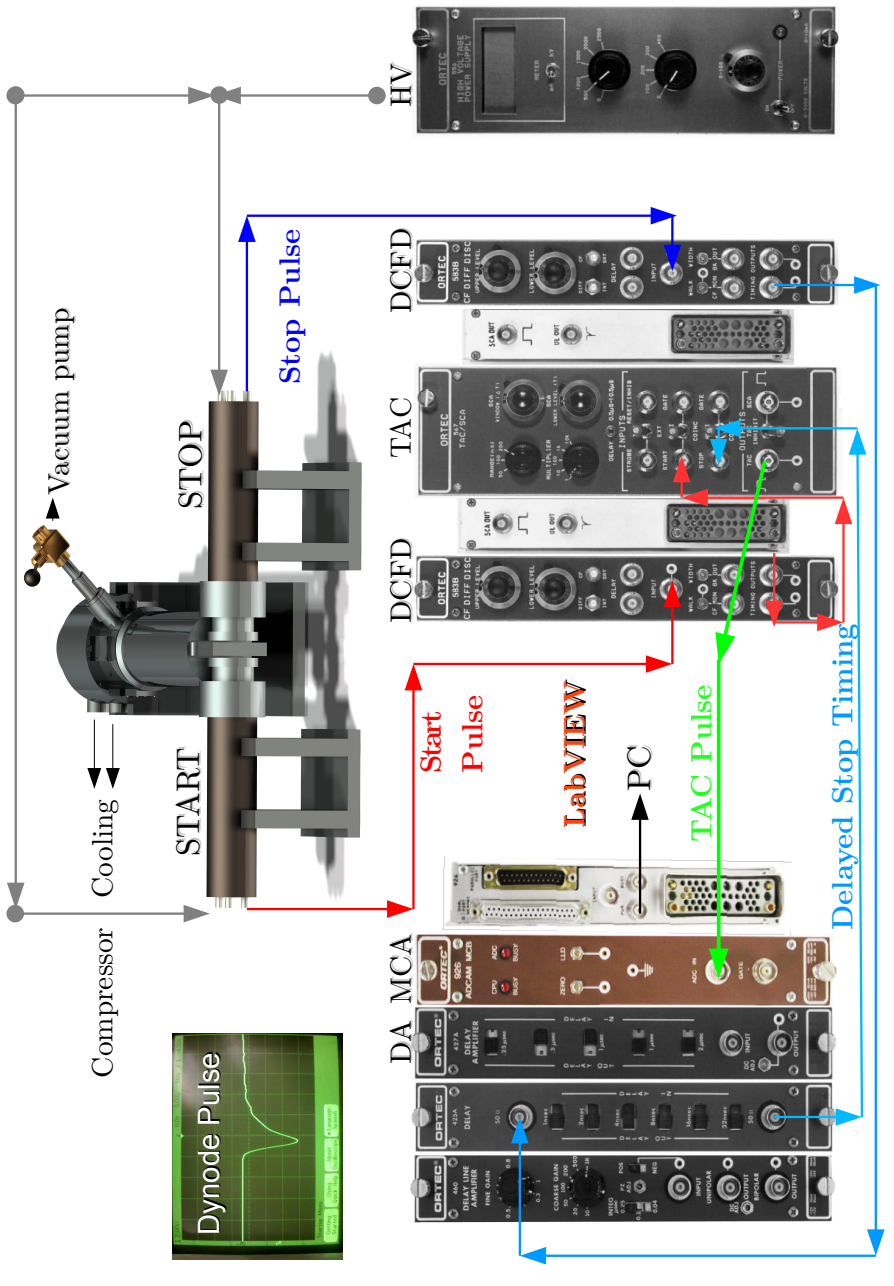

Figure 2.30: Diagram and configuration of the electronics of the PALS spectrometer

2.5.8 Development and Optimization of a PALS Spectrometer

In order to characterize different type of materials, a fast-fast PALS spectrometer has been developed and optimized specifically to carried out the measurements of the thesis. Additionally, taking into account future prospects, it has been designed to operate in 10 K - 350 K temperature range. As a result, the implementation of the spectrometer requires an ultra-high vacuum system, a temperature controller, a handleable cryostat allowing the measurements at low temperatures and a friendly sample loading/removal system along with a control program. The schematics of the built setup is illustrated in Fig. 2.30.

Detectors Photomultipliers and Scintillators

As explained in Sec. 2.5.7, the START 1.27 MeV and the STOP 511 keV γ rays are detected by combining photomultiplier tubes with plastic scintillator. The plastic scintillators BC-422 from Saint Gobain Company are directly attached to the H1949-50 Hamamatsu photomultiplier windows. The coupling is performed by using an optical grease which balances the refraction indexes of photomultipliers and the scintillators. A sectional view of the PM and the coupling with the plastic scintillators is shown in Fig. 2.31.

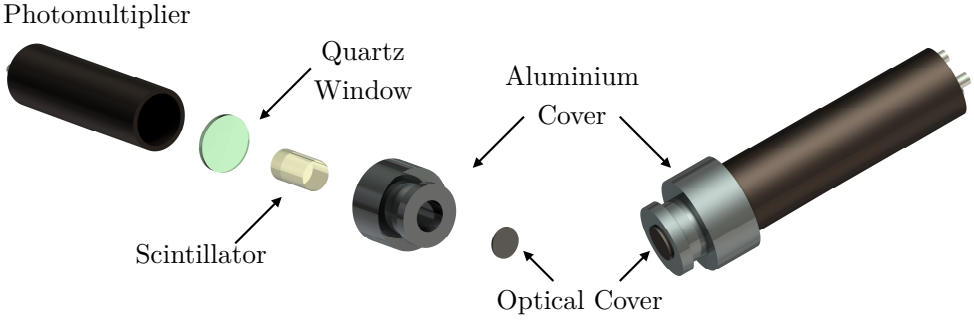

Figure 2.31: Sectional view of the γ ray detecting photomultiplier tube coupled with the plastic scintillator. In order to avoid the environmental spurious light, the first stage of the detector is covered with an aluminum shield and optically sealed. This initial stage is the one that detects the γ radiation of the positron birth and annihilation.

The BC-422 scintillator is a polyvinyltoluene plastic, which in turn, is doped with benzofenol impurities that enhances its performance. The energy of the incoming γ ray is absorbed by the scintillator. The absorbed energy is practically instantaneously emitted in the form of a light pulse with a narrow wavelength ranging between 380 - 400 nm. The intensity of the pulse is related to the energy that the scintillator has absorbed from the incident γ ray. The generated pulse of light (violet) is collected in the H1949-50 photomultiplier. A photocathode located at the first stage emits electrons after the photons coming from the scintillator strike it. The electrons created in this event are accelerated by a bias HV in successive steps through a set of

dynodes until a handleable electric pulse is created at the end of the photomultiplier. In order to make the detection faster, the pulse, which is directed to the DCFD system, is collected from the second dynode stage (fast-fast coincidence)[17]. The bias HV voltage is supplied by Ortec 556 High Voltage Power Supply Module (0-2000 V).

Electronic Modules

The necessary electronic modules has been obtained from Ortec company. The performances of each module are listed below:

- **ORTEC 583B Differential Constant Fraction Discriminator (DCFD):** These two modules (one for each channel) are responsible for i) selecting the proper pulses according with the birth and the annihilation of the positron, and ii) for defining the time $t = 0$ of the pulses. The DCFD of START channel must select pulses related to the detection of 1.27 MeV γ rays. The DCFD of the STOP channel, selects pulses related to the 511 keV γ rays. For this purpose, a energy window can be tuned accordingly, so that the pulses lying within the window will be selected. After the detection of the pulse, this module generates a timing signal.

  Initially, the accepted pulse is multiplied by a factor which is subsequently delayed and inverted. The resulting signal is superimposed with the original pulse, and as a result of this operation, the final pulse cuts the abscise. This cut is defined as the $t = 0$, which is independent of the pulse shape. Additionally, the cut with the abscise is independent of the pulse height (voltage), which means that the determination of $t = 0$ is the same regardless of the energy of the detected pulses. Moreover, this module also provides a $0.5\mu s$ width gate signal which is used to optimize the energy window.

- **ORTEC 425A Nanosecond Delay:** This module provides well-defined delays in the signal coming from the STOP channel (according to Fig. 2.30, the delayed is introduced in the STOP signal). By means of this module, the calibration of time/channel of the MCA can be obtained.

- **ORTEC 567 Time To Amplitude Converter, TAC/SCA:** The output timing pulses coming from DCFD modules are collected by the TAC module. Once the pulse corresponding to the START is collected, TAC generates an square analog pulse, which linearly increases in voltage until the STOP signal is detected. As a result, the height of the generated square pulse is proportional to the time interval between START and STOP signals.

- **ORTEC 926 Analog To Digital Converter (MCA):** This MCA module collects the output signals from the TAC module and assigns a specific channel depending on the height of the pulses. As a result the obtained histogram

[17] If the signal is collected from the last stage of dynodes, the configuration is labelled as slow-slow. Additionally, slow-fast and fast-slow coincidence setups are also possible.

displays the amount of counts as a function of the time interval between START and STOP signal, i. e., the positron lifetime spectrum. This histogram is the PALS spectrum. The module is connected to the computer by means of a specific graphic card for visualizing the spectra.

- **ORTEC 460 Delay Line Amplifier and ORTEC 427A Delay Amplifier:** These two modules, along with DCFD modules, are used for selecting the START and STOP pulses and to check the energy window, as the signal of the dynodes has to be amplified for a proper visualization. Additionally, these modules enable the determination of the equipment resolution.

Low Temperature Cryostat and Peripherals

The developed PALS spectrometer has been equipped with a low temperature cryostat due to the fact that in many materials such as semiconductors, the evolution of the positron lifetime as a function of temperature provides valuable information of defects. Thus, the spectrometer has been designed to operate in the 10 - 350 K range. In order to reach these temperatures, a closed-loop helium gas circulating compressor with an incorporated cooler has been acquired (HC-4E Indoor Water-Cooled Compressor). The system is attached directly to the cryostat. Additionally, during the measurement the cryostat has to be under high vacuum conditions $\approx 10^{-7}$ mbar. With this purpose, an oil-free vacuum station has been acquired, consisting in a rough pump and a turbomolecular pump, i. e., EXPT Pumping Station of the Edwards company.

The cryostat is covered with a rigid vacuum housing. Additionally, the sample holder is equipped with a radiation chamber which minimizes the heat transfer (in form of radiation) towards the sample. It is important to notice that the distance

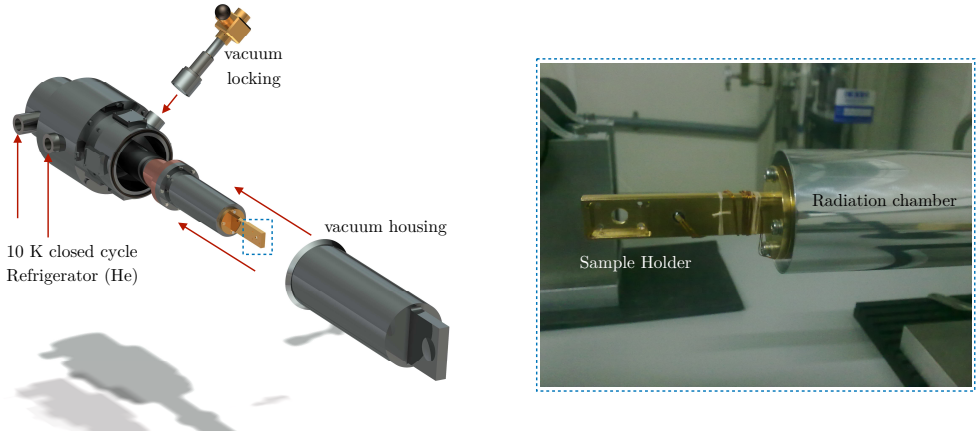

Figure 2.32: Left, scheme of the cryostat and the sample holder and how the vacuum housing is attached to the cryostat. Right, a more detailed view of the sample holder.

between the sample and the window of the photomultiplier must be minimized in order to maximize the detection rate. The larger the distance to the photomultiplier window, the longer will take the PALS spectrum collection. The vacuum housing is designed to minimize this distance. Moreover, this housing must have two windows that allows the transmission of γ rays. The configuration of the described features are illustrated in Fig. 2.32, which has been provided by Janis Cryosindustries according to previous specifications.

As it is shown in Fig. 2.32, a temperature sensor is placed close to the sample, which provides a real time temperature of the sample holder. The temperature control is carried out by a Cryogenic Temperature Controller of Lakeshore Model 335 with a precision of 0.2 K. Finally, the whole measurement process is synchronized by a program based on LabView, which enables the specification of temperature series, precision, PDI control, the maximum count-rate, etc.

Optimization and Calibration of the Spectrometer

As previously pointed out, in a fast-fast spectrometer the detection signals are collected from the second dynodes of the START and STOP channel photomultipliers. However, the energy spectrum that each photomultiplier detects is a continuous spectrum, in which several events are also collected (e. g., Compton scattering). Thus, each detector and the corresponding electronics has to be optimized for the identification of a specific event. In order to display the energy spectrum that the photomultiplier detects, the output of the second dynode is connected to a preamplifier. Finally, the output is connected to the MCA module for its visualization.

Fig. 2.33 shows the histogram of the energy spectrum collected in each PM. Although the fast speed of the detector, the energy resolution is rather low. Even though, the resolution is high enough to identify START and STOP signals. From left to right, the green colored peaks represent the histogram channel of the 511 keV and 1.27 MeV γ rays, respectively. Thus, in order to tune the energy window, the output of the dynodes is directed to DCFD, where the upper and lower level values of the window are adjusted using knobs. The selection of the energy window ΔE determines the resolution of the spectrometer. The narrower ΔE, the better the resolution. However, a very narrow window also implies longer collection times for obtaining a proper statistics in the lifetime spectrum.

Once the spectrometer is properly optimized, the resolution is measured and the channel-time parameter is callibrated. The resolution of the equipment is given by the FWHM value. The quantification of the FWHM is performed by using a ^{60}Co radioactive source. Although the disintegration of the ^{60}Co is different to ^{22}Na, ^{60}Co also emits γ rays. The detection of these γ rays can be considered as simultaneous in both START and STOP detectors. If the resolution of the spectrometer would be infinite, the spectrum of ^{60}Co would resemble a $\delta(t)$. However, the detectors have a limited resolution function, which resembles more to a Gaussian distribution. The obtained spectra is fitted to a Gaussian by which the FWHM is obtained.

At this stage the FWHM is only given in channels. Thus, a further calibration is

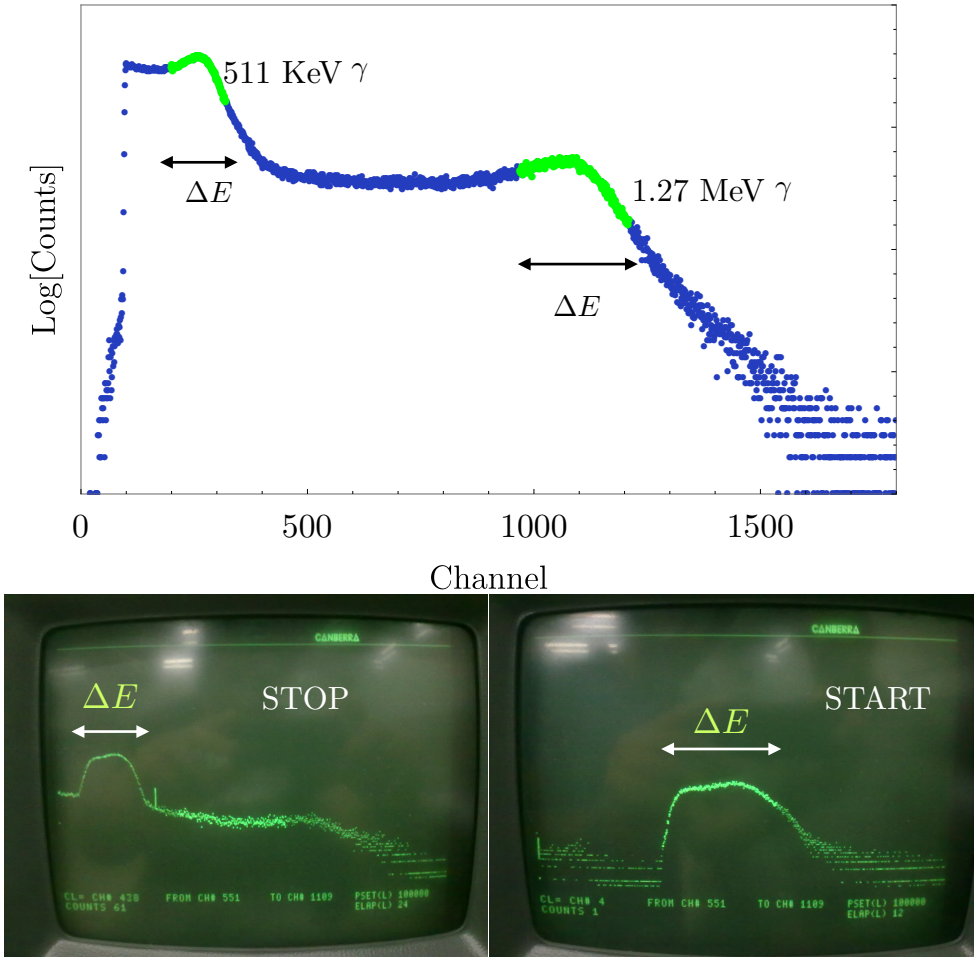

Figure 2.33: The histogram of the energy spectrum obtained by each photomultiplier. The green peak on the left-hand side corresponds to the energy window of 511 keV γ rays, and the peak in the right (more energetic) to 1.27 MeV γ rays.

needed by which a time interval is associated to each channel of the MCA. This is performed using a Nanosecond Delay Module. By means of this module, a calibrated delay is introduced in the STOP channel. As a result, the obtained Gaussian peak of ^{60}Co is shifted to increasing channels. By applying several delays and measuring the position of the Gaussian function, a direct relationship between the channel number and the delay time can be obtained. In Fig. 2.34 the relation between channel and delay time is plotted for delays of 2, 6, 14, 24 and 30 ns. The lineal regression obtained was

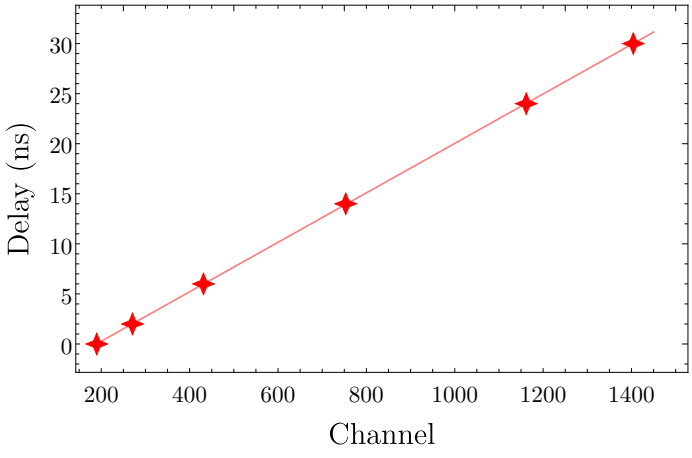

Figure 2.34: Channel-time calibration of the optimized PALS spectrometer.

$$y = -(4.66 \pm 0.02) + (0.02470 \pm 0.00003) \quad \text{ns/ channel.} \tag{2.41}$$

Once the ns/channel value is obtained, the resolution of the equipment can be calculated by multiplying it by the number of channels at FWHM. The obtained resolution of the spectrometer has been determined to be 252 ps. Finally, in order to check the accuracy of the spectrometer, a reference sample with a well-known positron lifetime is measured at room temperature. For this purpose, an Al sample has been used. As this Al reference samples has no defects (at least in the sensitivity range of the technique), the expected measured positron lifetime should be similar to its well-know bulk lifetime value of 165 ps. A measured $\overline{\tau}$ value of 164 ps for Al, which is in good agreement with the experimental reports [123], confirms the optimal performance of the spectrometer.

The whole performance of the equipment (pumping station, close-cycle refrigeration systems, controlling program etc...) has been tested by measuring a Bi_2Se_3 sample from 10 K up to 325 K [124]. Bi_2Se_3 is a narrow band-gap semiconductor and in contrary to metals, the temperature evolution of the $\overline{\tau}$ could reveal variations of the charge state of vacancies. Indeed, PALS experiments in Bi_2Se_3 results in a strong temperature dependence, by which the presence of shallow positron traps and a charge delocalization of selenium vacancies is detected. Additionally, by combining the experimental and theoretical simulations of the positron lifetime, the proper Se vacancy responsible of the n-type conductivity of the sample is determined [125][18].

[18]For further details see "I. Unzueta, N. Zabala, V. Marín-Borrás, V. Muñoz-Sanjosé, J. A. García and F. Plazaola *Observation of a Charge Delocalization from Se Vacancies in Bi_2Se_3: A Positron Annihilation Study of Native Defects* Physical Review B, **94**, 014117 (2016)".

2.6 Summary of Synthesized Samples

In order to carry out the objectives of the thesis (defined in the Sec. 1.5), several samples covering a wide compositional range have been employed. Regarding the metamagnetic systems, the study has been focused in $Ni_{50}Mn_{50-x}In_x$ (x = 25, 20, 16, 13) and in $Ni_{50}Mn_{50-x}Sn_x$ (x = 25, 20, 16, 13, 10) samples. Although the $x = 25$ and $x = 20$ samples do not exhibit the MT, they have been added in order to complete full compositional series. Specially, the $x = 25$ samples have been used as reference samples in order to help the interpretation of PALS and Mösbauer results in off-stoichiometric samples. All the samples synthesized during the whole period of the thesis, are described below:

- $Ni_{50}Mn_{50-x}In_x$ (x = 25, 20, 16, 13) and $Ni_{50}Mn_{50-x}Sn_x$ (x = 25, 20, 16, 13, 10) samples for ball milling studies. Although all the samples have been ball-milled (specially the x = 25 ones), the obtained results do not lead to any sample-dependent conclusion. However, the most interesting results have been obtained in the $Ni_{50}Mn_{34}In_{16}$. Apart from exhibiting the MT, the ball-milled sample exhibits an intricate magnetic structure at low temperatures. Additionally, the existing lack in the literature regarding the crystallization process of the ball-milled $Ni_{50}Mn_{34}In_{16}$ nanoparticles, makes this study of broad interest. As a result, the Chapter 3 gathers the effect that the ball milling has on the magnetostructural properties of $Ni_{50}Mn_{34}In_{16}$ alloys. Moreover, the crystallization dynamics are also studied in detail.

- $Ni_{50}Mn_{50-x}In_x$ (x = 25, 20, 16, 13) and $Ni_{50}Mn_{50-x}Sn_x$ (x = 25, 20, 16, 13, 10) samples for positron annihilation studies. The vacancy states of these two batches have been studied by combining experimental and theoretical PALS result. The composition-dependent study enables a proper identification of the most favorable defect present in Ni-Mn-Sn, Ni-Mn-In and Ni-Mn-Ga systems. The results are developed in Chapter 5, which is devoted to the study of the influence that vacancies have on the MT.

- An additional set of $Ni_{50}Mn_{50-x}Sn_x$ (x = 25, 20, 16, 13, 10) samples for Mössbauer studies. Taking into account the amorphization that ball milling induces, in $Ni_{50}Mn_{50-x}Sn_x$ (x = 25, 20, 16, 13, 10) samples, a more controllable approach has been used. In fact, the samples have been hand milled (or soft milled) in order to get a good crystallinity. Although all the Ni-Mn-Sn samples have been subjected to soft milling and the subsequent analysis, only the results of $Ni_{50}Mn_{35}Sn_{15}$ and $Ni_{50}Mn_{37}Sn_{13}$ are presented in the thesis. This is mainly because these samples are the ones that best exhibit the existing relation between the atomic scale structural parameters and the MT. The results obtained from this study are developed in Chapter 4.

- $Ni_{45}Co_5Mn_{50-x}In_x$ ($x = 16, 13$) and $Ni_{45}Co_5Mn_{50-x}Sn_x$ ($x = 15, 13$) samples for assessing the influence of Co-doping. Among these samples, only the results of the quaternary $Ni_{45}Co_5Mn_{37}Sn_{13}$ alloy are shown explicitly. In fact, the comparative study performed with the ternary $Ni_{50}Mn_{35}Sn_{15}$ and $Ni_{50}Mn_{37}In_{13}$, has enable to determine the enhanced MCE that the quaternary alloys exhibit in a slightly distorted powdered sample. The results are shown in Chapter 4.
- Regarding $Ni_{55}Fe_{17}Ga_{28}$ samples, a polycrystalline and a single-crystal samples have been investigated throughout the thesis. However, as the vacancy dynamics measured in both samples were almost identical, only the results obtained in the polycrystalline $Ni_{55}Fe_{17}Ga_{28}$ sample are shown in this report. The PALS investigation on $Ni_{55}Fe_{17}Ga_{28}$ alloy was intended to uncover how the vacancies may influence the MT and T_{MT}. The $Ni_{55}Fe_{17}Ga_{28}$ composition was selected due to the strong dependence that the T_{MT} shows to quenching and annealing treatments, which in principle, could be mediated by diffusion of vacancies.

		Characteristic Temperatures		
Chapter	Composition	Label	T_{MT}(K)	T_c(K)
Chapter 3	$Ni_{50}Mn_{34}In_{16}$	In_{16}-10h, In_{16}-40h	241	300
Chapter 4	$Ni_{50}Mn_{35}Sn_{15}$	Sn15	209	320
	$Ni_{50}Mn_{37}Sn_{13}$	Sn13	320	$\approx T_{MT}$
	$Ni_{45}Co_5Mn_{37}Sn_{13}$	Sn13Co	160	370
	$Ni_{50}Mn_{25}In_{25}$	(—)	(—)	325
	$Ni_{50}Mn_{35}Sn_{15}$	(—)	280	300
Chapter 5	$Ni_{50}Mn_{25}Sn_{25}$	Sn_{25}	(—)	340
	$Ni_{50}Mn_{30}Sn_{20}$	Sn_{20}	(—)	335
	$Ni_{50}Mn_{35}Sn_{15}$	Sn_{15}	223	313
	$Ni_{50}Mn_{37}Sn_{13}$	Sn_{13}	310	$\approx T_{MT}$
	$Ni_{50}Mn_{40}Sn_{10}$	Sn_{10}	373	$\approx T_{MT}$
	$Ni_{50}Mn_{25}In_{25}$	In_{25}	(—)	320
	$Ni_{50}Mn_{30}In_{20}$	In_{20}	(—)	320
	$Ni_{50}Mn_{34}In_{16}$	In_{16}	225	300
	$Ni_{50}Mn_{37}In_{13}$	In_{13}	360	380
	$Ni_{50}Mn_{40}In_{10}$	In_{10}	(—)	(—)
	$Ni_{55}Fe_{17}Ga_{28}$	(—)	300	$\approx T_{MT}$

Table 2.2: Composition and characteristic T_{MT} and T_c temperatures obtained from the initial characterization measurements of all the studied samples.

After their synthesis, all the above mentioned samples have been characterized using DSC and magnetic measurement. Some of these measurements are shown in Fig. 2.35 and Fig. 2.36, and the characteristic temperatures are gathered in Table 2.2.

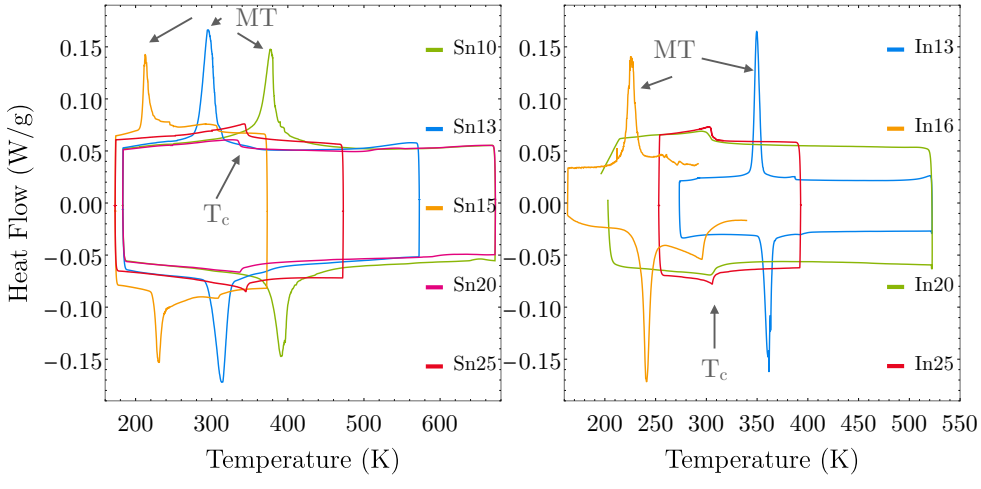

Figure 2.35: Left, DSC of $Ni_{50}Mn_{50-x}Sn_x$ ($x = 25, 20, 15, 13, 10$). Right, DSC of $Ni_{50}Mn_{50-x}In_x$ ($x = 25, 20, 16, 13$) samples.

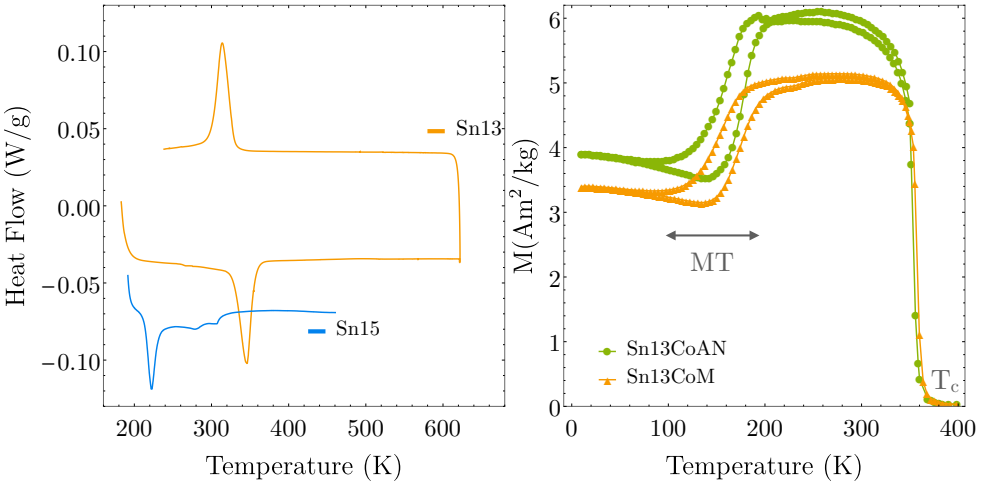

Figure 2.36: DSC measurements of $Ni_{50}Mn_{35}Sn_{15}$ and $Ni_{50}Mn_{37}Sn_{13}$ samples, along with the $M(T)$ of $Ni_{45}Co_5Mn_{37}In_{13}$ sample.

3 Crystallization Dynamics of Disordered Ni-Mn-In Alloys

Owing to the defective mechanical properties that Ni-based Heusler alloys exhibit, the use of microparticles as microactuator elements is consolidating as an effective approach in order to overcome the brittleness and fragility that bulk samples exhibit. As previously pointed out in Sec. 1.4.1, due to the synthesis process of powdered samples, the resulting micro and nanoparticles often exhibit partially disordered structures and defects. These defects have a great impact in both structural and magnetic properties, which can hinder the multifunctional properties of the obtained particles. In recent years, several attempts have been carried out in order to determine the effect of defects on the characteristics of the structural transition and magnetic properties in different shape memory alloys (Ni-Mn-Ga, Ni-Mn-In and Ni-Mn-Sn), which have been prepared by different methods such as laser ablation, melt spinning and ball milling [66, 67, 68, 69, 70].

In this sense, ball milling technique is one of the simplest and cheapest methods to produce nanostructured materials. Indeed, the reduction of particle size trought ball milling can be used to optimize the MCE in different magnetic systems, either by increasing the temperature range [126] or by reducing the hysteretic losses linked to

the MT [127]. However, together with the grain size reduction, ball milling produces a huge amount of defects (i. e., vacancies, dislocations, chemical disorder, strains ...) in the ball-milled samples.

The effect of ball milling on the magnetostructural properties has been previously studied in Ni-Mn-Ga [67, 68] systems. It has been already reported that the decrease of the size in Ni-Mn-Ga particles prepared by ball milling leads to a distortion of the structure. This distortion affects in such a way that, in order to induce $L2_1$ phase crystallization and observe the expected MT, it is necessary to anneal the sample at high temperatures (1073 K). Nevertheless, low temperature annealing (< 573 K) only allows the crystallization process to a disordered BCC structure [68]. Likewise, nanoparticles of Ni-Mn-Sn have been also obtained by ball milling [75, 74], but as in Ni-Mn-Ga powders, the atomic disorder and lattice strains inhibit the MT. Again, the $L2_1$ phase is obtained only after heating up to high temperatures (1223 K) [128].

On the contrary, the use of ball milling in the quest for functional nanoparticles has been scarcely studied in Ni-Mn-In alloys [129, 130]. In this latter case, a magnetic transition from paramagnetic-like to spin-glass state is suggested to occur at low temperatures as a consequence of the induced defects. The structural disorder induced by ball milling arises as a critical factor for the appearance of spin glass behavior in different magnetic oxides [131, 132, 133, 134], nanosized particles [135] or metallic alloys [136, 137, 138].

Spin glasses are described as systems that merge structural and magnetic disorder, giving rise to a magnetic frustration and short-range order (competition between FM and AF exchange interactions). A freezing temperature T_f is defined, below which the spins are randomly oriented. Generally, it can be distinguished between canonical and cluster spin glasses. Canonical spin glasses are characterized by the existence of randomly oriented isolated magnetic moments. On the other hand, the cluster spin glasses are composed of collective disordered spins in different regions of the material, which are dispersed in the metallic matrix with RKKY indirect exchange interactions [138]. The difference between both types of spin glasses relays on the different interaction and dynamic behavior.

Thus, a proper analysis of the milled powder samples may therefore provide a valuable information concerning the influence of those defects on both MT and magnetic properties. In fact, a complete study on the correlation between microstructure and magnetostructural properties in Ni-Mn-In nanoparticles is still absent. Up to now, most of the studies on ball milling have been carried out in Ni-Mn-Sn system, where the main objective has been to modify their highly stable $L2_1$ atomic order degree. Thus, the following chapter is devoted to the study of the evolution of both the MT and the magnetic properties (as a function of microstructural state) in ball-milled Ni-Mn-In nanometric particles. The ball milling procedure allows to reduce the particle size and also to introduce defects. With the characterization of defects and their influence in the relevant properties of Ni-Mn-In samples, it is intended to gain control on the microstructural parameters that govern the phase transformation and magnetic properties at micro and nano regime.

As will be shown, ball-milled samples display an amorphous structure with a

frustrated magnetic state compatible with a canonical spin glass. Afterwards, the ball-milled powdered samples are annealed, by which the subsequent crystallization process is investigated. The crystallization process taking place on heating, results in a B2 structure, which implies a reproduction of the high-temperature phase at much lower temperatures. With further annealing, above 700 K, a relaxation process occurs, which concurs with a B2-$L2_1$ atomic ordering process. In fact, it is observed that this ordering gives rise to an anomalous two-step thermal expansion. The combined effect of both processes makes possible the occurrence of the MT. Finally, the relative cooling power linked to the magnetocaloric effect is comparatively evaluated in the ball-milled and bulk samples.

3.1 Sample preparation and Experimental Details

Among the synthesized $Ni_{50}Mn_{50-x}In_x$ ($x = 25,\ 20,\ 16,\ 13$) alloys, the characterization of the ball-milled samples have been carried out in a $Ni_{50}Mn_{34}In_{16}$ sample. On the one hand, the $x = 25$ and $x = 20$ samples do not exhibit the MT, so they have been discarded at this stage. Although the T_{MT} of the $Ni_{50}Mn_{34}In_{16}$ compound lies below room temperature, this compound is nowadays subject of intense research due to a large inverse MCE it exhibits related to the MT. Additionally, owing to the existence of a PM-FM transition, it exhibits a fairly large conventional MCE around room temperature [47]. As the objective is to track the evolution of a certain multifunctional property as a function of the microstructural state (and defects present within), the larger ΔM that $x = 16$ exhibit in comparison to $x = 13$ sample, enables a better determination of the MCE.

A $Ni_{50}Mn_{34}In_{16}$ alloy is prepared from high purity elements by means of arc melting method[19]. After the homogenization at 1073 K during 15 h, the alloy is crushed in order to obtain the initial powder to subject it to a ball milling process. In order to avoid oxidation, the sample is milled during 5 min (effective-milling time) and then stopped for 10 min to prevent overheating of both the sample and grinding jars. The $Ni_{50}Mn_{34}In_{16}$ sample has been ball-milled under a protective Ar atmosphere during different effective milling times; 10 h and 40 h at room temperature. From now on, the 10 h and 40 h ball-milled $Ni_{50}Mn_{34}In_{16}$ samples are labeled as In_{16}-10h and In_{16}-40h, respectively.

Ball milling was performed at 300 rpm in a Retsch PM4 with a ball:powder ratio of 7:1, using 7 balls of 5 mm diameter. Both, jars and balls were of tungsten carbide (WC). The final chemical composition was determined by Energy Dispersive Scattering (EDS) with a Jeol JSM-5610LV SEM, by which the stoichiometry of the samples after 10 h and 40 h milling times was confirmed to be identical to the nominal

[19] For more details see Sec. 2.1.1.

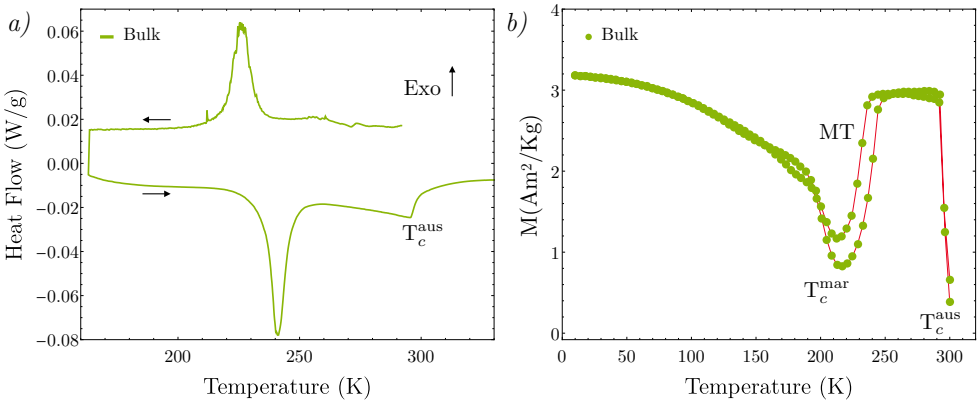

Figure 3.1: (a) DSC thermogram performed on cooling/heating the reference bulk $Ni_{50}Mn_{34}In_{16}$ sample at 10 K/min. (b) Temperature dependence of magnetization for the bulk reference alloy at 0.01 T.

composition $Ni_{50}Mn_{34}In_{16}$.

The structural transformations and the recovery processes of In_{16}-10h and In_{16}-40h samples has been characterized by DSC with a heating rate of 10 K/min under nitrogen atmosphere (flow of 50 mL/min). In order to analyze the crystallographic structure of the ball-milled sample, room temperature XRD patterns are measured with a model Siemens D5000 diffractometer, using a step of 0.02°. The magnetic characterization (magnetization and susceptibility measurements) is performed by SQUID magnetometry in a QD MPMS XL-7 setup.

The shape and size of the particles have been observed and characterized by conventional transmission electron microscopy (Hitachi H600 100 kV TEM). The evolution of crystal structure, long-range atomic order, crystallite size and microstrains were determined from in-situ PND measurements performed on the high-flux D1B two-axis diffractometer, at the Institute Laue-Langevin (Grenoble, France). The diffraction patterns have been measured on heating from room temperature up to 1173 K at 1 K/min using a neutron wavelength of 1.28 Å. Finally, the structure was refined by the Rietveld method using FullProf package programs [139].

Fig. 3.1(a) shows the DSC thermogram performed on cooling/heating of the reference bulk alloy between 165 K and 350 K. The occurrence of a first-order MT, which takes place below room temperature, is evidenced by the presence of exothermic and endothermic peaks corresponding to the forward and reverse MT. Along with it, a second-order magnetic transition taking place in the austenite phase can be also inferred from the baseline inflection observed above the MT, around 300 K. This non-hysteretic λ-type shoulder is linked to the ferromagnetic to paramagnetic transition at T_c.

The MT temperatures, taken as the temperature of the peak maximum, are T_{MT}^{f} = 226 K and T_{MT}^{r} = 241 K, which implies a thermal hysteresis of ΔT = 15 K for the T_{MT}. Additionally, the complete sequence of magnetostructural transitions has

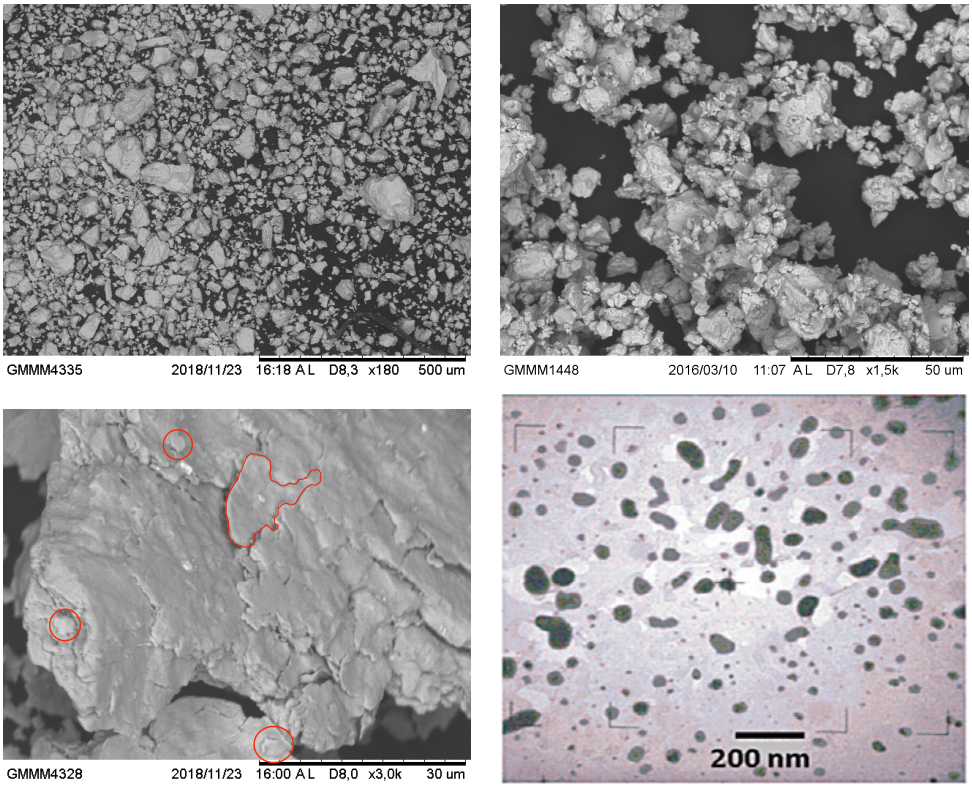

Figure 3.2: SEM micrographs revealing the actual particle size of the as-crushed $Ni_{50}Mn_{34}In_{16}$ sample (upper-left corner), the In_{16}-10h sample (upper-right corner) and a closer look of a particle, which evinces the conglomerated nature of the particles revealed by SEM. The picture of the lower-right corner shows the TEM micrograph displaying the spheroidal nature of the obtained nanoparticles of the In_{16}-40h sample.

been determined from the low-field (0.01 T) magnetization versus temperature curve $M(T)$, shown in Fig. 3.1(b). The magnetization increases on cooling below 300 K, due to the ferromagnetic ordering of the austenite phase at the Curie temperature, T_c^{aus}, and then, it suddenly decreases on further cooling to the almost paramagnetic martensite. The subsequent increase of magnetization at lower temperatures is linked to the magnetic ordering of the low-temperature phase at T_c^{mar}.

Once the initial ingot is characterized, and with the aim of introducing defects and obtain nanoparticles, the bulk alloy has been subjected to high energy ball milling. As described above, in the experimental part, the ingot initially has been crushed in order to reduce the size of the powder and to increase the effectiveness of the ball milling procedure. The SEM micrograph, shown in the upper-left corner of Fig. 3.2, shows the as-crushed $Ni_{50}Mn_{34}In_{16}$ sample. It is composed of particles that exhibit a large dispersion in size, but generally smaller than 1 mm. The initial wide distribution of the as-crushed samples is rapidly homogenized with the milling time

increase. For instance, the micrograph of the In_{16}-10h sample, shown in the upper-right corner of Fig. 3.2, reveals a narrower distribution of particles along with the notorious reduction in size.

For higher grinding times, it is observed that the size of particles reaches a plateau or a saturation level, below which no substantial changes in size are observed regardless of the milling time. However, as shown in the lower-left corner of Fig. 3.2, the particles revealed by SEM micrographs are, in turn, made of smaller particles. In order to obtain a closer perspective, the In_{16}-40h sample has been observed by TEM. The particle size revealed by TEM is drastically different from the one exhibited by SEM. As it can be seen in the lower-right corner of Fig. 3.2, the milled powder mainly consists of spheroidal nanometric particles with an average size of tens of nm. Additionally, bigger clusters can be also observed. As a result, it can be concluded that the obtained powder is actually composed by nanoparticles. However, these nanoparticles get conglomerated forming bigger clusters as it is observed by SEM.

3.2 Structural Analysis of the Ball-Milled Samples

In order to ascertain the effect of the ball milling in the structural properties, the obtained milled powders have been analyzed by DSC measurements. Fig. 3.3 shows the thermograms obtained on heating the amorphous powders up to 700 K, at a 1 K/min rate for both In_{16}-10h and In_{16}-40h samples.

DSC curves undoubtedly indicate that no transformation is detected, neither below nor around room temperature, and just three exothermic peaks are observed in both cases on heating above 350 K; one *S*-shaped broad shoulder and two intense P_1 and P_2 peaks. Indeed, the narrow exothermic peak P_1 is overlapped with a much broader peak P_2 between 500 K and 600 K.

The first *S*-shaped shoulder is commonly related to a glass transition temperature in different amorphous metallic alloys [140], although in some ball-milled systems is covered up by an exothermic peak related to the crystallization process. The temperature associated with this first transition remains nearly constant for both samples, whereas the P_1 and P_2 peaks shift to higher temperatures with increasing the milling time. Nevertheless, the enthalpy of the whole double-peak ($\Delta H \approx 70$ J/g) is similar to that obtained for the crystallization process in similar alloys [141]. As a result, the same origin could be attributed to both peaks, which would be related to the exothermic peak of the crystallization process.

The kinetics of the associated processes has been analyzed using the well-known *Kissinger's* [142] method, from which the activation energy of a thermally activated process can be obtained from the variation of the DSC peak temperature (T_P) as a function of the heating rate ϕ:

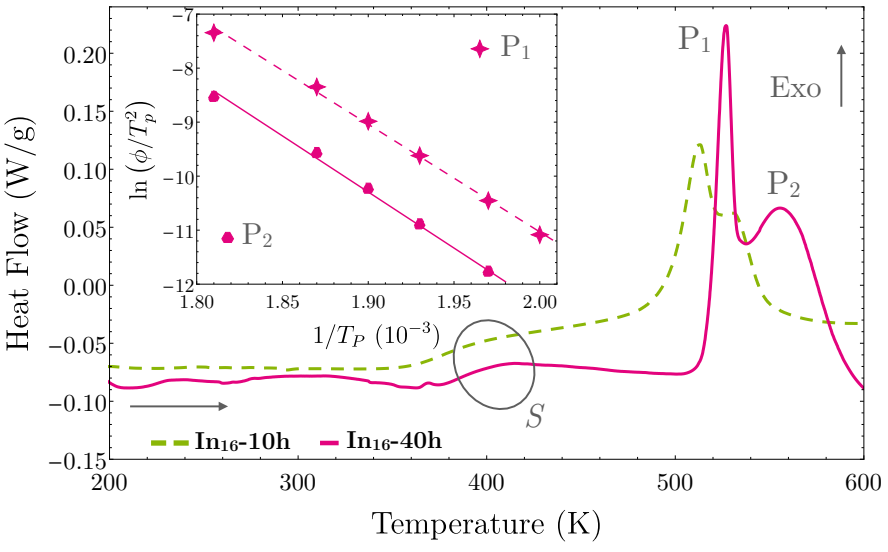

Figure 3.3: DSC thermograms on the powder In_{16}-10h and In_{16}-40h $Ni_{50}Mn_{34}In_{16}$ ball-milled samples. The inset shows the Kissinger's fittings of $\mathrm{Ln}\left(\phi/T_P^2\right)$ vs $1/T_P$ for P_1 and P_2 peaks for the In_{16}-40h sample.

$$\ln \frac{\phi}{T_P^2} = \frac{-E_a}{k_B T} + \beta, \tag{3.1}$$

where k_B is the Boltzmann constant, E_a is the activation energy and β is a constant. The activation energies, determined from the linear fit of $\ln(\phi/T_P^2)$ vs $1/T_P$, are $E_a = 1.7$ eV and $E_a = 1.8$ eV for the P_1 and P_2 peaks, respectively (see the inset in Fig. 3.3). The similarity between both values, which are also in agreement with those obtained for the crystallization process in ball-milled amorphous Fe_2MnGe alloys [141], reinforces the idea of a similar origin of both exothermic peaks. In order to determine the structure of the ball-milled alloys, as well as to ascertain the possible structural processes linked to the exothermic peaks observed in the thermograms, XRD measurements have been carried out.

In line with the DSC measurements, XRD spectra of In_{16}-10h and In_{16}-40h samples do not show any well-defined Bragg reflections, which evinces the achievement of an amorphous phase as a result of the structural distortion caused by the ball milling process. As the structure is highly altered by mechanical treatments, both samples do not show the MT. Thus, in order to analyze the recovery process, as well as to asses the origin of the two P_1 and P_2 peaks observed by DSC, the In_{16}-40h sample has been annealed at $T_1 = 538$ K and $T_2 = 630$ K (where $T_{P_1} < T_1 < T_{P_2}$ and $T_2 > T_{P_2}$).

Once the ball-milled sample is heated up to above the P_1 peak temperature (538 K), some Bragg reflections appear in the diffractogram, indicating an initial crystallization stage to the cubic B2 structure, see Fig. 3.4. On further heating above

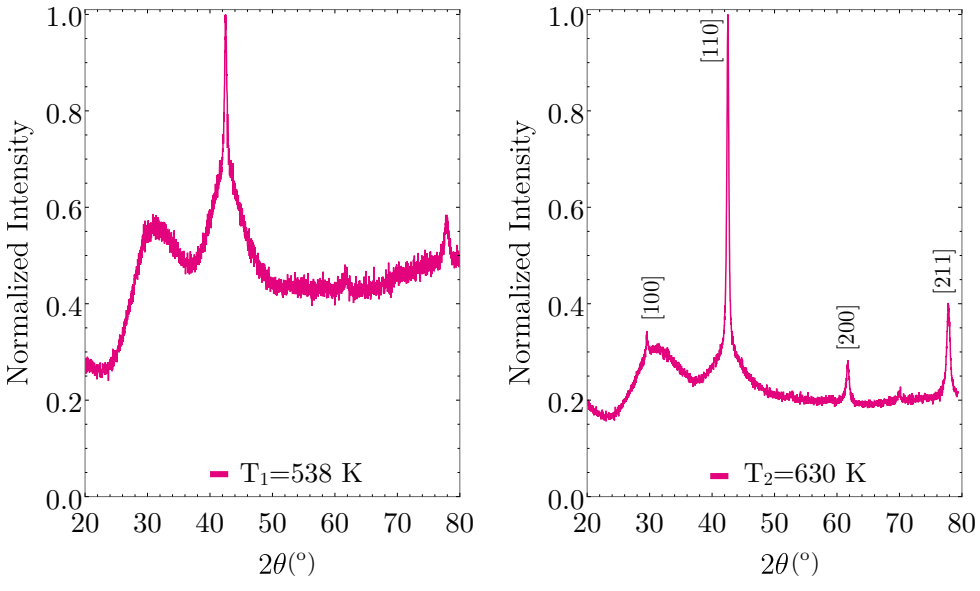

Figure 3.4: XRD patterns for the In_{16}-40h $Ni_{50}Mn_{34}In_{16}$ ball-milled sample after the annealing at 538 K (after P_1 peak) and 630 K (after P_2 peak).

the P_2 peak temperature (630 K), no other structural transformation takes place and just an increase of the intensity of the B2 diffraction peaks is observed. Therefore, the two exothermic peaks detected in the DSC curves could be related to a two-stage crystallization process from the amorphous state to a cubic B2 structure[20]. Subsequent DSC measurements performed in the heat-treated samples confirmed that such B2 structure does not undergo martensitic transformation (as expected). As it will be inferred from magnetic studies presented further below, an annealing treatment above 1173 K is needed to achieve the austenite $L2_1$ Heusler structure.

3.3 Magnetic Properties of the Ball-Milled Alloys

The initial characterization of both the In_{16}-10h and In_{16}-40h ball-milled powders reveal the absence of MT due to the achieved amorphous state. Taking into account that in a similar Ni-Mn-In allo it has been proposed that the amorphous state may be linked to a possible spin glass behavior [129], the evolution of the magnetism brought by the crystallization process has been analyzed in a more detail. In this

[20] As a consequence of the low contrast of X-ray scattering lengths of Ni, Mn and In, the degree of long-range atomic order could not be evaluated from the diffractograms.

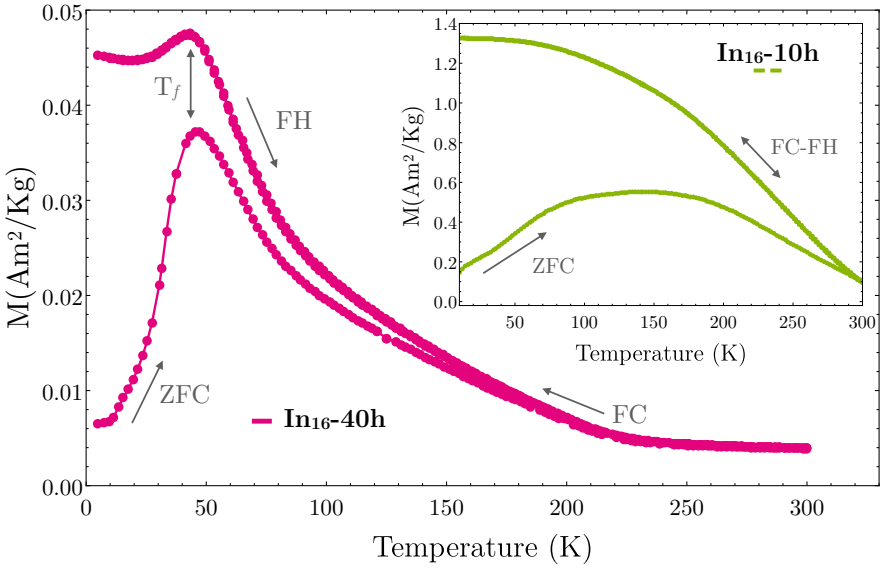

Figure 3.5: Zero Field Cooled/Field Cooled/Field Heating (ZFC/FC/FH) curves measured at 0.01 T for the In_{16}-10h and In_{16}-40h $Ni_{50}Mn_{34}In_{16}$ ball-milled samples.

sense, magnetization and susceptibility measurements have been performed on In_{16}-10h and In_{16}-40h samples.

Regarding the thermomagnetization curves, the ZFC/FC/FH curves at 0.01 T are shown in Fig. 3.5. As expected, the magnetization of the amorphous phase decreases as the milling time increases and the low temperature magnetization of the In_{16}-10h sample is greater compared with the In_{16}-40h sample. However, with respect to the temperature dependence of magnetization, the two samples exhibit distinct features. Aside the ZFC curve, any hysteresis in the FC-FH sequence is associated with structural transitions [16]. As observed in both In_{16}-10h and In_{16}-40h samples, both FC and FH curves are identical, pointing out the lack of any structural transition throughout the measured temperature range. In essence, due to the amorphization, none of the samples exhibit the MT.

On the other hand, the broad peak in the ZFC curve for the sample with lower milling time (In_{16}-10h) could be probably ascribed to a distribution of spin-glass states correlated to a certain inhomogeneity with different amorphization degrees. The In_{16}-40h ball-milled sample shown in Fig. 3.5, in turn, shows a clear spin glass behavior at low temperatures, with the characteristic sharp drop of the magnetization in the ZFC curve bellow 50 K [135]. As the splitting of the ZFC and FC curves below a magnetic transition temperature is expected to be associated with coexisting AF exchange, freezing or blocking phenomena [16], the behavior that ZFC-FC curves exhibit is a fingerprint of frustrated magnetic systems. The quality of the peak or the splitting is much more clear in In_{16}-40h sample compared with the one obtained

for In_{16}-10h sample, revealing a more homogeneous amorphization of the In_{16}-40h ball-milled powder.

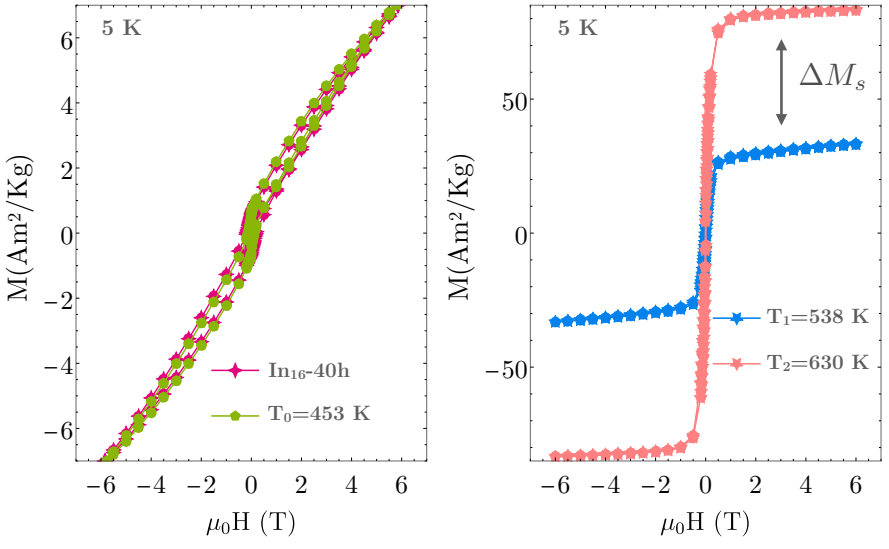

Figure 3.6: Hysteresis loops at 5 K for the In_{16}-40h $Ni_{50}Mn_{34}In_{16}$ ball-milled sample, and after annealing it at $T_0 = 453$ K (where $T_0 < T_{P_1}$, just above S-shaped peak), T_1 and at T_2 temperatures.

For a more detailed magnetic characterization, $M(H)$ cycles have been carried out in the ball-milled In_{16}-40h sample[21] after annealing it at $T_0 = 453$ K ($T_0 < T_{P_1}$, just above S-shaped peak), and at T_1 and T_2 temperatures. In a nutshell, $M(H)$ cycles corroborate the proposed spin-glass behavior. The hysteresis loops measured at 5 K in both the ball-milled state and after annealing at 453 K, 538 K and 630 K are shown in Fig. 3.6. The ball-milled In_{16}-40h sample is characterized by a high coercivity ($\approx$ 0.2 T) magnetic state, by a high magnetic anisotropy (non-saturated system) and by a low magnetization (8 Am^2/Kg by applying 6 T), distinctive of frustrated system (i. e., spin glass system) [134]. While no significant variation is observed on heating above S shoulder, a clear decrease in coercivity and a high increase in magnetization (ΔM_s) occur on annealing at the corresponding temperatures related to P_1 and P_2 peaks, above which a well-developed ferromagnetic state can be inferred.

In particular, the high field magnetization (at 6 T) increases to 33 Am^2/Kg and 83 Am^2/Kg after the annealing at 538 K and at 630 K, respectively. This fact is in accordance with the proposed two-stage crystallization process. Fig. 3.7 (left) shows the temperature dependence of the magnetization at low applied fields (0.01 T) for the In_{16}-40h sample annealed at 538 K and at 630 K temperatures. First, it is interesting to highlight that no MT is detected in none of the annealed In_{16}-40h sample. On the other hand, the evolution of $M(T)$ is almost the same after both

[21] Due to the better resolution of P_1 and P_2 peaks and the more homogeneous amorphization, from now on the study has been focused in the In_{16}-40h sample.

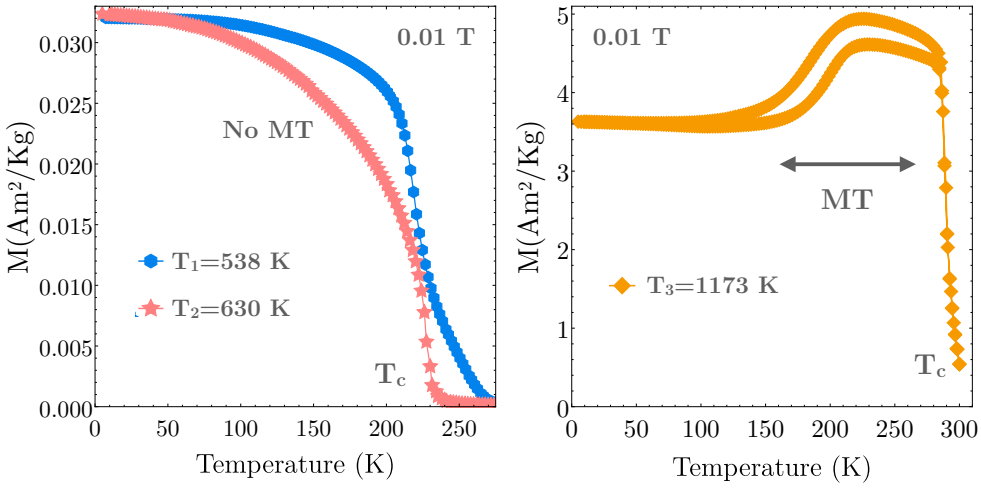

Figure 3.7: Left, $M(T)$ curves for the In_{16}-40h $Ni_{50}Mn_{34}In_{16}$ ball-milled sample measured after annealing at 538 K, 630 K and 1173 K temperatures, measured at 0.01 T. The annealing above the P_1 and P_2 crystallization process does not recover the MT in the In_{16}-40h sample. Right, $M(T)$ (0.01 T) of the In_{16}-40h sample annealed at $T_3 = 1173$ K, which shows the recover of the structural transition.

heating treatments: the samples are paramagnetic at high temperatures and become magnetically ordered on cooling below 250 K. This transition temperature is quite lower than the T_c^{aus} of the bulk sample, see Fig. 3.1. This behavior, in agreement with a higher atomic disorder of the B2 structure, results in a higher contribution of AF coupling between Mn atoms and therefore, a lower T_c^{aus} [49].

Furthermore, an annealing treatment at $T_3 = 1173$ K is undertaken in order to determine the occurrence of $L2_1$ structure crystallization process [128]. The occurrence of MT in the In_{16}-40h ball-milled sample is just observed once heated above 900 K, that is, once the B2-$L2_1$ atomic ordering and the microstructural relaxation process have been fulfilled. As an example, Fig. 3.7 (right) shows the $M(T)$ for the In_{16}-40h sample heated up to 1173 K (measured at 0.01 T). The global behavior of the magnetization is practically the same of the bulk sample (see Fig. 3.1), where a sudden increase corresponding to the PM-FM transition and a hysteretic drop linked to the MT are observed around 220 K and 300 K, respectively. This accordance between the ball-milled powder and the reference bulk sample remarks the constancy of the composition after the annealing[22].

Up to know, the initial structural and magnetic characterization indicate that the ball milling procedure amorphizes the $Ni_{50}Mn_{34}In_{16}$ sample in such a way that inhibits the MT. In addition, the magnetic characterization reveals that the obtained amorphous phase is compatible with a spin-glass state.

[22] As will be shown further, in Sec. 3.5.1 the small differences can be attributed to a slight oxidation process during the annealing, which is shown in Fig. 3.10.

3.4 Determination of the Spin-Glass State

The nature of the obtained amorphous powders have been analyzed in further detail by AC susceptibility measurements. Fig. 3.8 shows the real part of the AC susceptibility at different frequencies within the 0.02 – 200 Hz range.

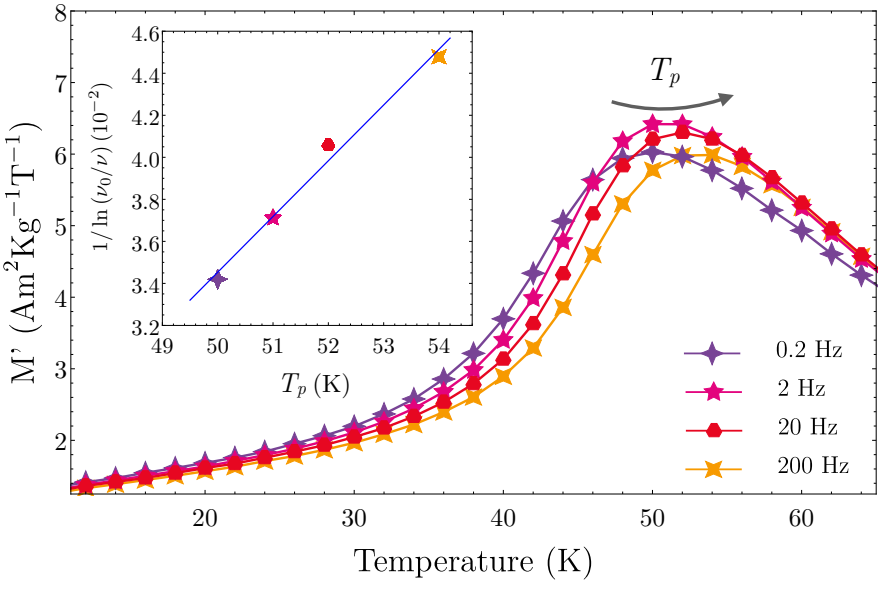

Figure 3.8: Temperature dependence of the real part of the susceptibility at different ν frequencies (0.2, 2, 20, 200 Hz) for In_{16}-40h $Ni_{50}Mn_{34}In_{16}$ sample. The inset shows the linear fitting to the Vogel-Fulcher law of Eq. (3.3)

It is well known that in the vicinity of the freezing or blocking temperature T_f, spin glass systems exhibit an AC frequency dependence characterized by a shift in the observed maximum (ΔT_p in the measured frequency interval) to higher temperatures when frequency ($\omega = 2\pi\nu$) increases. In this context, a c parameter is defined

$$c = \frac{\Delta T_p}{T_p \Delta \mathrm{Log}_{10}\omega} \tag{3.2}$$

which quantifies the interaction strength between the nanoparticles. The lower values of c, the greater are the magnetic interactions [131]. In this regard, and depending on the value of c parameter, three different regimes are defined; a non-interacting superparamagnetic regime ($c > 0.3$), a medium interaction regime ($0.05 < c < 0.13$) or an interacting spin glass regime ($0.005 < c < 0.05$). The ball-milled sample displayed a value of $c = 0.02$, and according to the previous classification it

is within the limit established for interacting spin glass systems. In contrast to what happens with the imaginary part, the magnitude of the real part of the susceptibility decreases since the magnetic moments cannot follow the magnetic field.

In the interacting spin glass systems, the frequency dependence of the T_f is well described by the Vogel-Fulscher law, which is defined by the following equation [134, 143]:

$$\nu = \nu_o \exp\left(\frac{-E_a}{k_B(T_p - T_0)}\right) \tag{3.3}$$

where ν is the frequency, ν_0 a characteristic frequency and T_0 a parameter that measures the interaction strength due to dipolar and exchange interactions between the clusters or magnetic moments. The fitting to this exponential law, shown in the inset in Fig. 3.8, leads to $T_0 = 47$ K, $\nu_0 = 6.4105$ Hz and $E_a/k_B = 40$ K. Taking into account that for systems with negligible magnetic interactions $T_0 = 0$ [138], the high value of T_0 indicates strong magnetic interactions between the magnetic moments in the In_{16}-40h sample. The coefficient $(T_p - T_0)/T_p$, where T_p is the maximum temperature of the ZFC curve, is a parameter usually employed as an indication of a slow frequency dependence in canonical spin glasses (< 0.1) or high dependence in cluster spin glasses (> 0.5) [133, 144]. Furthermore, the value of the characteristic frequency $\tau_0 = \nu_0^{-1}$ for the different systems is also indicative of each type of spin glasses. Thus, τ_0 values above $10^{-4}s$ are related to canonical systems, whereas for τ_0 values below $10^{-7}s$ are related to cluster spin glasses [144]. In the present case, the obtained parameters are $(T_p - T_0)/T_p = 0.04$ and $\tau_0 = 10^{-5}s$, so a canonical spin glass seems to be the most feasible explanation for describing the magnetic system of the obtained ball-milled $Ni_{50}Mn_{34}In_{16}$ sample.

In order to confirm the nature of the disordered system, several ZFC/FC curves have been measured at different applied magnetic fields ranging from 0.01 T up to 4 T. These curves are shown in Fig. 3.9. On the one hand it is observed that when the applied magnetic field increases, the maximum temperature of the ZFC curve T_p shifts towards lower temperatures. This shift can be attributed to a change in the energy barrier between the spin glass state and the high temperature magnetic state. According to that, at a critical magnetic field H_0, the irreversibility in ZFC/FC curves is vanished since the magnetic anisotropy of the frustrated state is overcome. Almeida and Thouless' law [145] describes the line between the magnetic state at low temperatures and the corresponding state at high temperatures through the dependence of this energy barrier at different magnetic fields:

$$H = H_0\left(1 - \frac{T_p}{T_f}\right)^{3/2}. \tag{3.4}$$

In the inset of Fig. 3.9 the fitting is represented with an estimated T_f value of 35 K and a critical magnetic field of $\mu_0 H = 8$ T, confirming the existence of magnetic interactions, which indeed, are in agreement with the high T_0 obtained from the Vogel-Fulcher law fitting (see the inset of Fig. 3.8).

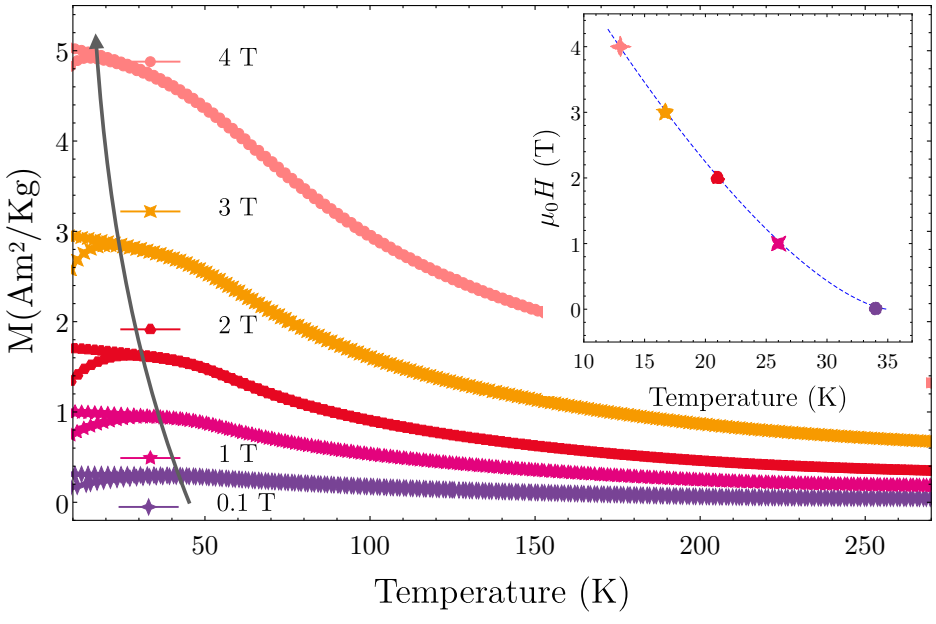

Figure 3.9: ZFC/FC curves measured at different applied magnetic fields ranging from 0.1 T to 4 T for In_{16}-40h $Ni_{50}Mn_{34}In_{16}$ ball-milled sample. The inset shows the fitting of the experimental data to the Almeida-Thouless law of Eq. (3.4).

Summarizing, the ball-milled $Ni_{50}Mn_{34}In_{16}$ powders do not show any MT. Moreover, the powder samples exhibit a low magnetization values and the obtained magnetic structure for the In_{16}-40h sample is in agreement with a spin-glass behavior. The frequency dependence of the freezing temperature, $T_f(\nu)$, perfectly fits to the Vogel-Fulcher law, which confirms the spin-glass state of the amorphized sample. Additionally, the dependence that the shift of T_p shows to the applied magnetic field fits to the Almeida and Thouless' law, by which also the canonical spin-glass nature of the In_{16}-40h sample is confirmed. However, although the In_{16}-40h sample is annealed above the two P_1 and P_2 crystallization peaks, the obtained ball-milled samples do not exhibit the MT. In fact, the recovery and the crystallization process that allows the powdered samples to exhibit the MT, takes place at much higher temperatures than the ones corresponding to P_1 and P_2 crystallization peaks.

3.5 Study of the Crystallization Dynamics

Fig. 3.7 evinces that the In_{16}-40h amorphous sample have to be annealed at temperatures up to 1173 K in order to exhibit the MT. In the endeavor of exploit-

ing the multifunctional properties of Ni-Mn based nanoparticles, the occurrence of the MT acquires a key relevance, so the magnetostructural recovery of the In_{16}-40h $Ni_{50}Mn_{34}In_{16}$ nanoparticles has been studied in depth.

3.5.1 Neutron Diffraction Study

The microstructural evolution and the recovery processes taking place on heating the amorphous In_{16}-40h sample have been analyzed by means of *in-situ* PND experiments. Fig. 3.10 shows the thermodiffractograms obtained on heating from room temperature up to 1220 K at a 1 K/min heating constant rate.

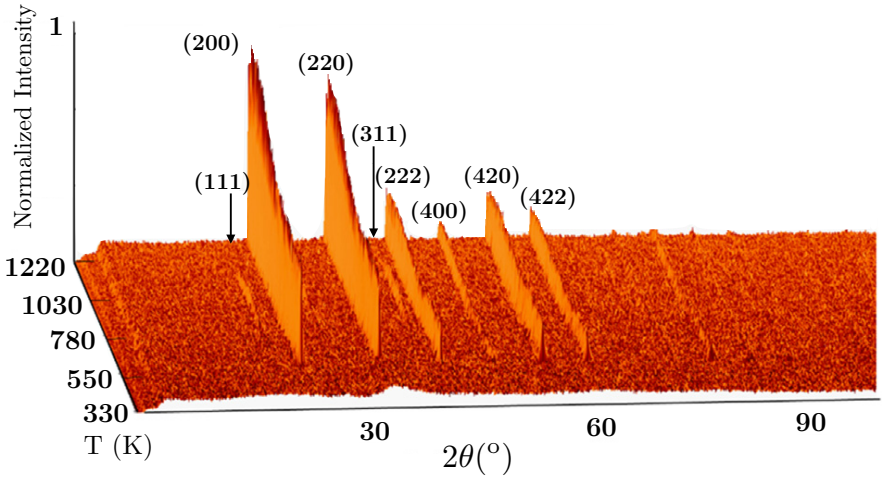

Figure 3.10: *In-situ* neutron powder thermodiffractograms of In_{16}-40h $Ni_{50}Mn_{34}In_{16}$ samplle on heating from 330 K up to 1220 K, measured at 1 K/min heating rate.

It can be seen that the amorphous structure remains stable up to 500-550 K. At this temperature a sharp crystallization process takes place, which is evinced by the sudden appearance of Bragg reflections. As pointed out before, the occurrence of this process does indeed confirm the amorphous-like state of the ball-milled In_{16}-40h sample. The temperature range of this crystallization process is in agreement with the sharp crystallization process revealed by DSC measurements of Fig. 3.3.

As previously revealed by XRD measurements, PND confirms that the sample crystallizes to a disordered B2 cubic structure with nearest-neighbors long-range atomic order. On heating around 700 K, the appearance of $L2_1$ superstructure reflections (those in which the h, k, l indices are all odd, according to the corresponding unit cell structure factor) indicates the occurrence of an ordering process from B2 to a $L2_1$ cubic structure with next-nearest-neighbors long-range atomic order. A similar B2-$L2_1$ ordering process is observed on heating bulk Ni-Mn-In alloys that have been previously quenched from high temperatures. In that case, in turn, the ordering temperature (which indeed depends on the degree of disorder retained by quench-

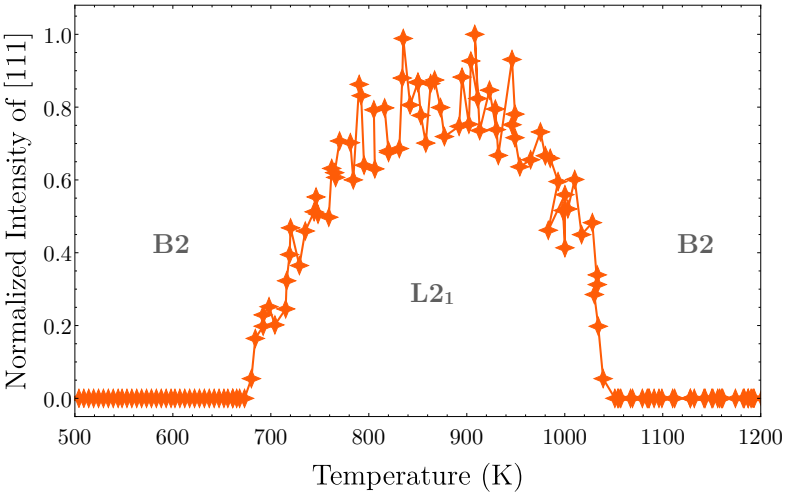

Figure 3.11: Integrated intensity of the (111) reflection peak as a function of the temperature for the In_{16}-40h $Ni_{50}Mn_{34}In_{16}$ sample. The $L2_1$ atomic order starts emerging at $\approx$ 700 K. Above 1050 K, the sample shows the B2 structure.

ing) typically lies between 500 K and 600 K [49, 15]. Back to In_{16}-40h sample, on further heating above 900 K, the intensity of the $L2_1$ reflections gradually decreases until it completely vanishes as a consequence of the $L2_1$-B2 order-disorder transition. This transition takes place at 1050 K [49, 15]. The temperature dependence of the integrated intensity of the [111] reflection is shown in Fig. 3.11, which illustrates the evolution of long-range atomic order of the nanometric particles as a function of temperature. The two consecutive ordering processes are clearly recognizable from the appearance and subsequent disappearance of the superstructure reflection.

The microstructural relaxation can be also explored by analyzing the width of the Bragg peaks of the diffraction patterns. In this respect, the Integral Breadth Method [146] is widely used to determine the microstructural effects from the analysis of the shape of the diffraction peaks. This method allows to obtain separately the crystallite size and microstrain contributions to the full-width at half maximum (FWHM) of the diffraction peaks. These peaks are ffitted to a Thompson-Cox-Hasting pseudo-Voigt profile function [88].

The profile instrumental resolution function used for the analysis of the diffraction patterns has been obtained from the room temperature diffractogram performed on a $Na_2Ca_3Al_2F_{14}$ sample (typical calibration compound). As an example, Fig. 3.12 shows the diffractograms and the respective fits by Rietveld method obtained for the B2 structure at three different temperatures. It can be seen that the broadening of the reflections decreases significantly (and simultaneously the integrated intensity

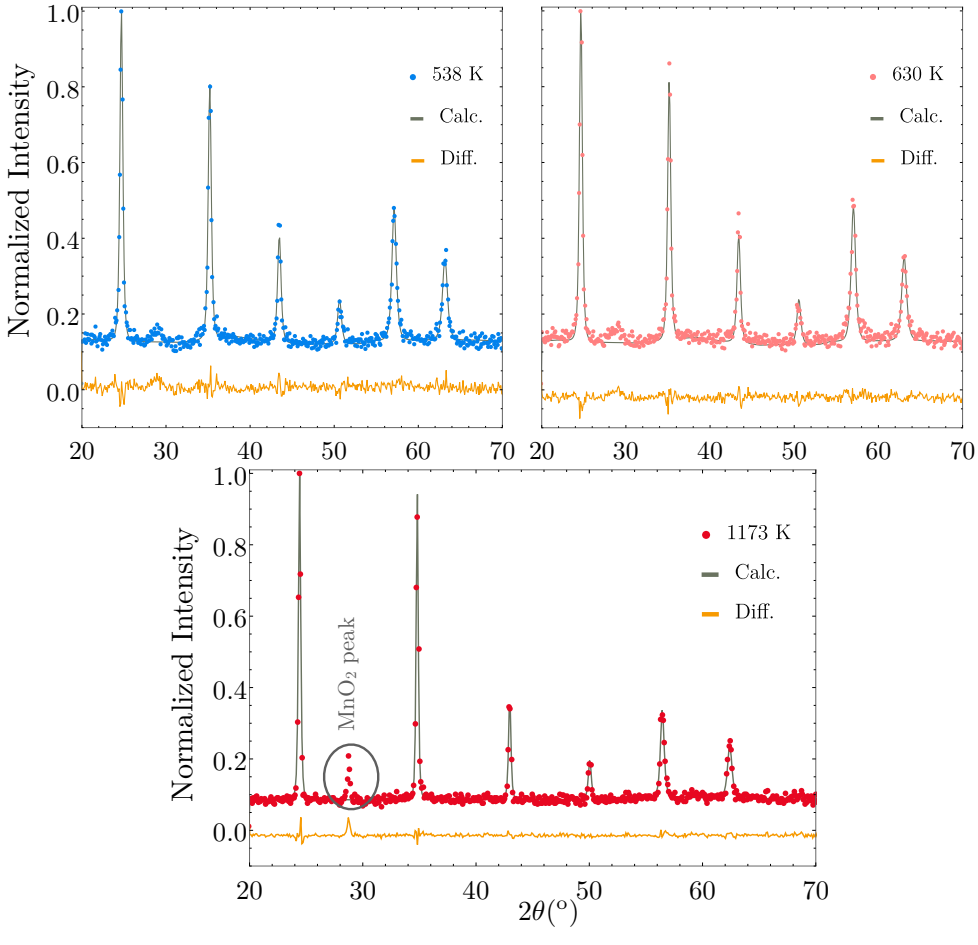

Figure 3.12: Measured PND patterns (dots), calculated profile (line) and difference between experimental and calculated profiles for the ball-milled In_{16}-40h $Ni_{50}Mn_{34}In_{16}$ sample, measured at 538 K, 630 K, and 1173 K. The 538 K and 630 K temperatures correspond to temperatures above P_1 and P_2 peaks respectively (see Fig. 3.3).

increases) on heating up to 1173 K, pointing out a relaxation of the microstructure. It is also worth noting the presence of small additional peaks, especially the one at $2\theta \approx 29^{\circ}$. This peak can be ascribed to the appearance of a small amount of manganese oxide. In any case, just a very small mass fraction of the alleged oxide is inferred from the relative intensity of the peaks, so no significant effect is expected neither on the magnetic properties nor on the alloy composition.

The temperature evolution of both microstrain and crystallite size is shown in Fig. 3.13. The main microstructural relaxation takes place between 700 K and 800 K, where the microstrains abruptly decrease from 0.35% to 0.1%. This is precisely

the temperature range in which the B2-$L2_1$ ordering process takes place (Fig. 3.11). Taking into account that atomic ordering implies atomic diffusion (as long as it is mediated by vacancies [79]), the observed relaxation points to vacancy elimination and/or vacancy-assisted dislocation annihilation as the main recovery process. On the other hand, the crystallite size increases exponentially with the increasing temperature. i. e., from 20 nm at room temperature (in agreement with TEM observations) to 150 nm at 1100 K, approximately.

As expected, the higher growth rate is reached above 800 K, just after the recovery process that the microstrain drop evinces, is fulfilled. Likewise, it is interesting to note that the temperature dependence of the lattice parameter depicted in Fig. 3.13, shows a marked change in slope between 700 K and 800 K. This process takes place concurrently with both the B2-$L2_1$ ordering and the relaxation processes, thus giving rise to an anomalous two-step thermal expansion.

Due to the magnetostructural coupling these alloys exhibit, the recovery of the

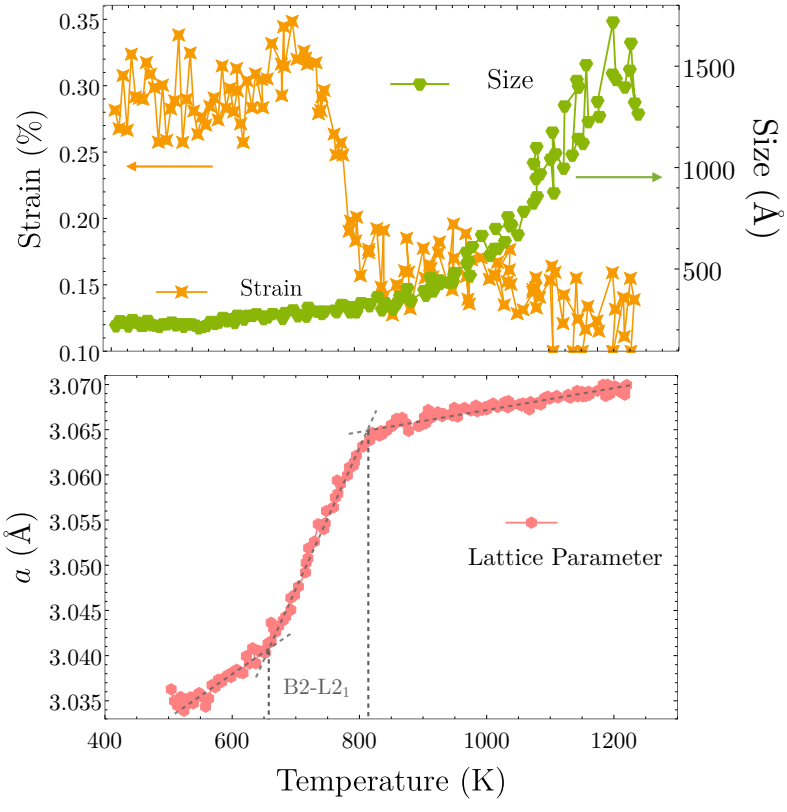

Figure 3.13: Evolution of the microstructural parameters of the In_{16}-40h $Ni_{50}Mn_{34}In_{16}$ sample. The upper figure shows the microstrain and crystalline size as a function of temperature. The figure below shows the evolution of the lattice parameter on terms of the B2 structure as a function of the annealing temperature.

microstructure is accompanied with an enhancement of the magnetic properties. Previously, in Sec. 3.3, it has been observed that the magnetization is recovered when the In_{16}-40h $Ni_{50}Mn_{34}In_{16}$ ball-milled sample is annealed at increasing temperatures.

3.5.2 Magnetism Recovery Upon Crystallization

In order to analyze the evolution of magnetic properties linked with P_1 and P_2 crystallization process, In_{16}-40h sample has been annealed at both 538 K and 630 K. Afterwards, isofield magnetization measurements taken at different temperatures around the magnetic transition T_c have been performed. This temperature is defined as the sudden drop that the thermomagnetization curves exhibit in Fig. 3.7 (left), which lies around 240 K. Fig. 3.14 shows the magnetic-field dependence of magnetization taken between 175 K and 275 K for applied magnetic fields up to 6 T. For the sample heated up to 630 K (Fig. 3.14, right), the evolution of the $M(H)$ curves corresponds to a typical PM-FM transition; at high temperatures (above T_c) the magnetization increases linearly with the applied magnetic field, whereas below T_c, the magnetization shows a sharp increase at low fields and a further slow increase at high fields. Additionally, below T_c the magnetization reaches almost the magnetization saturation value ($\approx$ 75 Am^2/Kg).

In the sample heated up to 538 K, Fig. 3.14 (left), in turn, magnetization does not approach the saturation value in the ferromagnetic region, which could be indicative of magnetic disorder, magnetic inhomogeneity or AF clusters. The presence of short-range correlations and the characteristics of the magnetic transition have been studied through the analysis of the critical exponents, which have been determined from the magnetization data according to the modified Arrott plots method. This method is

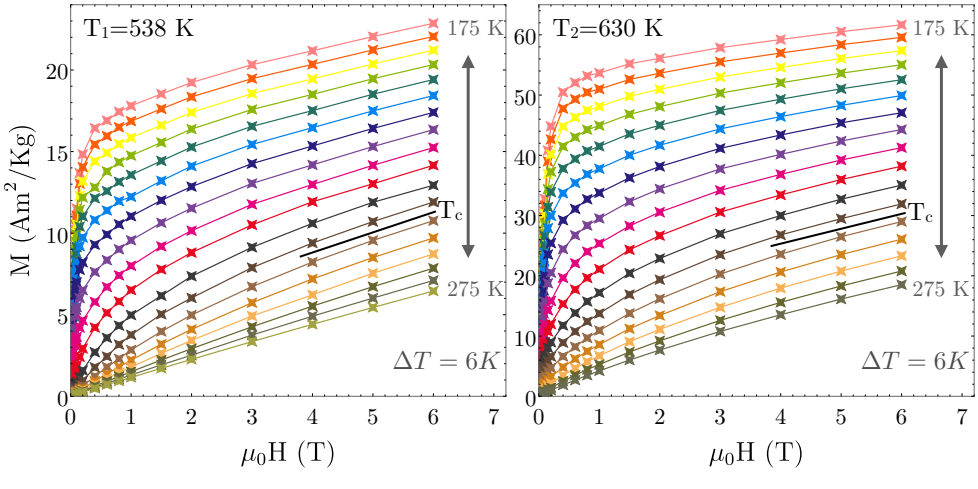

Figure 3.14: Isofield magnetization measurements carried out between 175 K and 275 K for In_{16}-40h $Ni_{50}Mn_{34}In_{16}$ ball-milled sample after annealed at 538 K (left) and 630 K (right).

based on the Arrott-Noakes equation of state [147],

$$\left(\frac{H}{M}\right)^{1/\gamma} = a\epsilon + bM^{1/\beta} \tag{3.5}$$

where $\epsilon = (T - T_c)/T_c$ is the reduced temperature, a, b are constants and γ and β are the critical exponents that characterize the second-order magnetic transition near T_c. γ and β are associated to the spontaneous magnetization M_s and the initial susceptibility χ_0 respectively trought

$$M_s(T) = M_0\,(-\epsilon)^{\beta} \qquad \epsilon < 0 \tag{3.6}$$

and

$$\chi_0^{-1}(T) = \left(\frac{H_0}{M_0}\right)\epsilon^{\gamma} \qquad \epsilon > 0 \tag{3.7}$$

expressions [148]. M_0 and (H_0/M_0) are the critical amplitudes. From the Arrott-Noakes Eq. (3.5), the plot of $M^{1/\beta}$ versus $(H/M)^{1/\gamma}$ at different temperatures around T_c, consists in straight lines that lay parallel to each other for high fields. The line crossing the coordinate origin corresponding to T_c. Starting from initial trial values $\beta = 0.5$ and $\gamma = 1.0$, $M_s(T)$ and χ_0^{-1} data are obtained from the intersection of the linear extrapolation of the straight lines with the $M^{1/\beta}$ and $(H/M)^{1/\gamma}$ axis, respectively. These data are fitted to equations Eq. (3.6) and Eq. (3.7), and the obtained parameters are then used for the next $M^{1/\beta}$ versus $(H/M)^{1/\gamma}$ plot, repeating the process iteratively until β and γ values converge.

The critical exponents obtained from the last iterative step are shown in Fig. 3.15 (a,b). The obtained values are $\beta = 0.5$, $\gamma = 1.26$, and $T_c = 219$ K after heating above P_1 and $\beta = 0.47$, $\gamma = 1.27$ and $T_c = 233$ K and after heating above P_2 peak[23]. Likewise, the critical exponents have been also determined by the Kouvel-Fisher Method [149], from the linear relations

$$M_s\left[\frac{dM_s}{dT}\right]^{-1} = \frac{(T - T_c)}{\beta} \tag{3.8}$$

$$\chi_0^{-1}\left[\frac{d\chi_0^{-1}}{dT}\right]^{-1} = \frac{(T - T_c)}{\gamma} \tag{3.9}$$

Fig. 3.15(c,d) show the plot of both Eq. (3.8) and Eq. (3.9) as a function of temperature. The critical exponents obtained from the linear fits are $\beta = 0.46$, $\gamma = 1.21$ and $T_c = 219$ K after heating above P_1 and $\beta = 0.47$, $\gamma = 1.21$ and $T_c = 233$ K after heating above P_2, almost the same than those achieved from modified Arrot plots. It is important to notice that the fitted value of T_c increases 14 K after heating above the second peak, which is in agreement with the higher magnetization that the sample shows at high fields, and consistent with the above

[23] See Fig. 3.3 for P_1 and P_2 peaks.

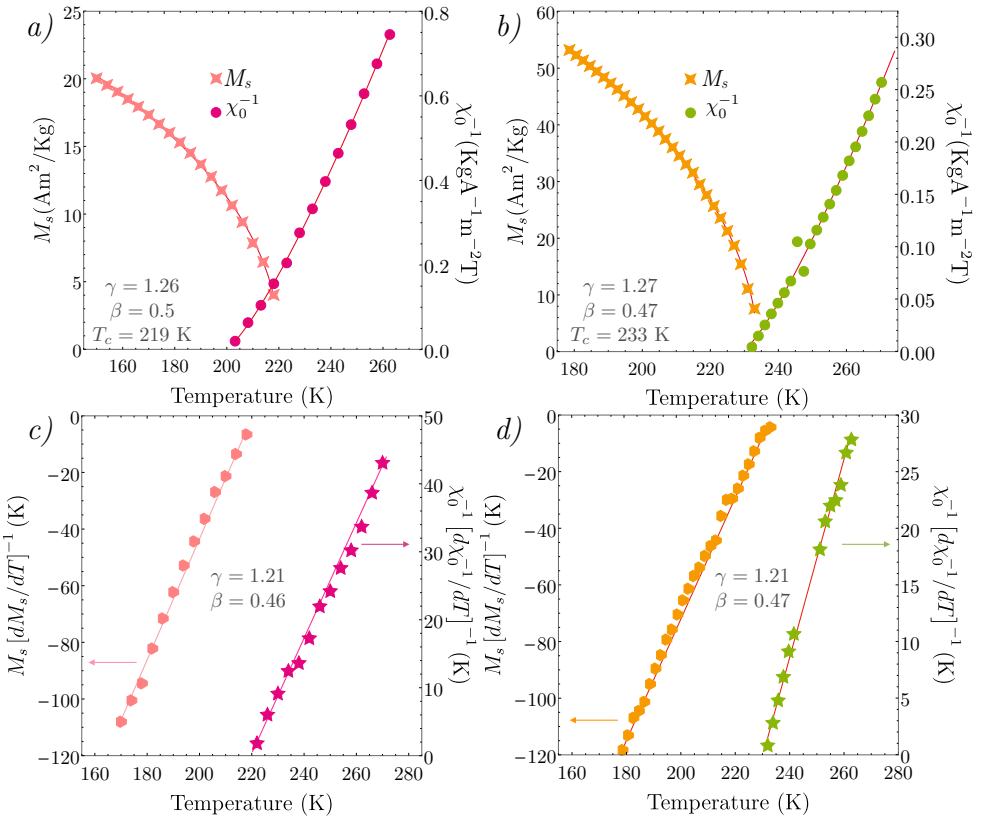

Figure 3.15: Temperature dependence of spontaneous magnetization M_s, the inverse of the initial susceptibility χ_0^{-1} together with their fitting to the Eq. (3.6) and Eq. (3.7), for (a) the In_{16}-40h $Ni_{50}Mn_{34}In_{16}$ ball-milled sample heated up to 538 K and (b) heated up to 638 K. In (c) and (d) the Kouvel-Fisher fitting plots for the In_{16}-40h $Ni_{50}Mn_{34}In_{16}$ ball-milled sample heated up to 538 K and (b) heated up to 638 K are respectively shown.

mentioned slight increase of the B2 order parameter. In both cases, the obtained β values are close to that predicted by the mean-field theory ($\beta = 0.5$) whereas γ values agree with that proposed by 3D Ising Model ($\gamma = 1.24$) [149]. These values point out the competing long and short range magnetic couplings in the B2 structure.

Nevertheless, the corresponding critical exponents show no difference at all after both annealing treatments, and therefore the same nature can be attributed to the magnetic transition in both cases. The observed ΔM difference between the high field magnetization values shown in Fig. 3.6 could be then due to the above mentioned B2 atomic order variations and, mainly, to the fact that the crystallization process is not concluded at 538 K (the P_1 peak is truncated as a consequence of the overlapping with P_2 peak and some amorphous fraction may still persists). In any case, no significant structural nor magnetic variation is observed linked to the P_2 peak.

3.6 Evaluation of the Magnetocaloric Effect

In Sec. 3.3 it has been shown that the MT is only recovered once the sample is heated above 1173 K, in essence, once the B2-$L2_1$ atomic ordering and the microstructural relaxation processes have been fulfilled. As shown in Fig. 3.7 (right), the $M(T)$ evolution of the ball-milled In_{16}-40h sample treated up to 1173 K is practically the same compared with the reference bulk sample shown in Fig. 3.1. Nevertheless, the MT on the annealed powder spreads over a bit higher temperature range, due to the higher storage of the strain energy linked to the reduced particle size. In order to compare the capabilty of the ball-milled powders for practical applications, the magnetocaloric effect associated to the MT in both bulk and in the annealed particles of In_{16}-40h sample has been measured.

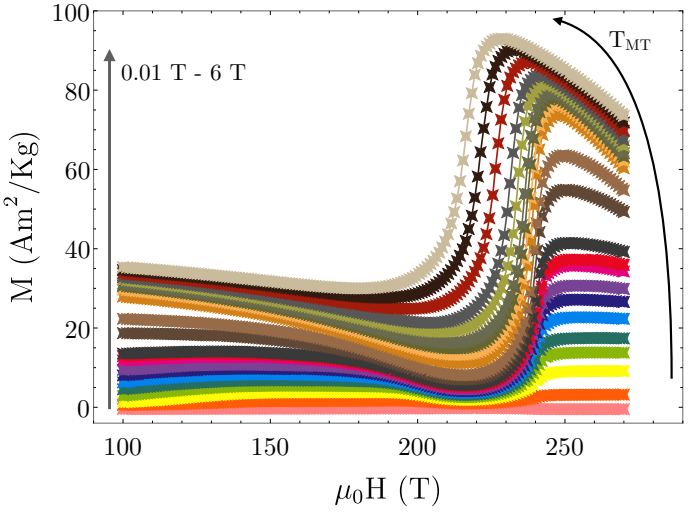

Figure 3.16: $M(T)$ curves for different applied magnetic fields ranging from 0.01 T up to 6 T for In_{16}-40h $Ni_{50}Mn_{34}In_{16}$ ball-milled sample. For higher magnetic fields, the T_{MT} is shifted to lower temperatures.

To evaluate the MCE, initially the magnetization curves at different applied field are measured for both bulk and In_{16}-40h sample. The $M(T)$ curves taken at different applied magnetic fields for In_{16}-40h sample are shown Fig. 3.16 (not shown for bulk sample). In both cases, the magnetization drop associated to the MT (ΔM) occurs at lower temperatures on increasing the applied magnetic field. The shift of the T_{MT} as a function of the applied field $\mu_0 H$ is expected to follow the well-known *Clausius-Clapeyron* equation,

$$\frac{dT_{MT}}{dH} = -\mu_0 \frac{\Delta M}{\Delta S} \tag{3.10}$$

where ΔS is the entropy change at T_{MT}. The different exchange interactions in each structural phase promote a discontinuity in the magnetic entropy at the T_{MT}. Thus, the application of a magnetic field at temperatures close to MT may result in the induction of the MT, and therefore, in a magnetically induced entropy change; i. e., a MCE. The entropy change in isothermal conditions can be calculated by numerical integration of the derivative of the magnetization with respect to temperature following the expression [150]

$$\Delta S_{\text{iso}} = S(T,H) - S(T,0) = \int_0^H \left(\frac{\partial M}{\partial T}\right)_H dH \tag{3.11}$$

Then, the MCE associated to the MT is estimated from the magnetization curves at different applied magnetic fields through Eq. (3.11). The obtained MCE values for the bulk sample, as a function of both temperature and applied magnetic field, are shown in Fig. 3.17 (left). A positive peak, that is the inverse MCE effect is observed linked to the MT, which increases with the increasing magnetic field up to a maximum value of $\Delta S = 12$ J/KgK at 6 T. The obtained MCE value is in agreement with previous reports [151].

Regarding the ball-milled In_{16}-40h sample, Fig. 3.17 (right) shows that the inverse MCE associated to the MT is also observed together with a direct MCE linked to second-order magnetic transition. The maximum positive entropy change, achieved for the higher applied field (6 T), is $\Delta S = 2$ J/KgK. Even though this value is considerately lower than the MCE obtained in the reference bulk sample, the broad temperature range covered by the MT in the ball-milled sample results in a broad associated entropy peak ($\Delta T = 75$ K), thus giving rise to a quite large relative cooling power.

The relative cooling power is defined as $\Delta S \cdot \Delta T$, which is the main performance

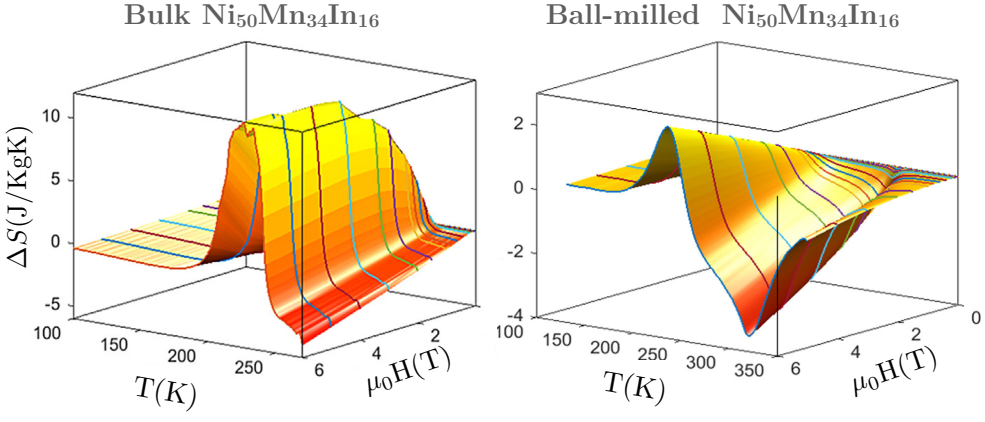

Figure 3.17: Left, Magnetically-induced entropy change or the evaluation of the MCE in the bulk $Ni_{50}Mn_{34}In_{16}$. Right, evaluation of the MCE for In_{16}-40h $Ni_{50}Mn_{34}In_{16}$ ball-milled sample as a function of temperature and the applied magnetic field.

metric to rank magnetocaloric materials. This parameter quantifies the magnitude of the heat extracted in a thermodynamic cycle [152]. In particular, a relative cooling power value of 150 J/Kg is obtained in the ball-milled particles, which is comparable to those values found in similar bulk alloys [153]. This results implies that, by means of ball milling and adequate thermal treatments, functional Ni-Mn-In metamagnetic shape memory powders (around 150 nm after the annealing at 1173 K) can be obtained for practical applications of magnetic refrigeration at nanoscale.

4 Effect of Internal Strains in the MT in Ni-Mn-Sn

In the previous chapter, the effect that mechanically induced defects have on both magnetic and structural properties has been analyzed in micro/nano powdered Ni-Mn-In samples. However, due to the critical impact that the ball milling process has in the crystallinity of the ball-milled alloys, a more detailed study on the effect that the presence of local-stresses and strains have on the MT could not be carried out. The ball-milled samples have to be heated up to 1173 K in order to recover the MT. Thus, to prevent the amorphization of the structure, the ball milling procedure has been replaced by a more controlled mechanical treatment which preserves the structure and the occurrence of the MT in the obtained powdered samples.

As previously mentioned in the introduction, the characteristic temperatures of Ni-Mn-In and Ni-Fe-Ga systems can be easily tuned by means of standard heat treatments. However, the extraordinary high stability of the $L2_1$ long range atomic order that Ni-Mn-Sn alloys (and Ni-Mn-Sb) exhibit, precludes the variation of atomic order by means of conventional thermal treatments[63]. As a result, the tuning of the MT features becomes unfeasible by means of standard thermal treatments, which in turn, is the most widely used approach to the control of both T_{MT} and T_c. Therefore,

the modification of the microstructural properties and defects configuration could be, along with composition, the only way to properly tune the functional properties in Ni-Mn-Sn systems.

In a recent work, Mañosa *et. al*[154] have demonstrated that the presence of thermal hysteresis, far from worsening, can be used to enhance the multifunctional properties (in this case the MCE) of Ni-Mn-In Heusler alloys. Despite the conventional idea that the inherent hysteresis of magnetostructural phase-change materials must be minimized to maximize the reversible magnetocaloric effect, Mañosa *et. al* show the way to take advantage of the thermal hysteresis in order to enhance the MCE. It is well known that in Ni-Mn-Sn alloys, the T_{MT} remains almost unaltered under the presence of local stresses and strains (in line with the great stability of $L2_1$), while the width of the MT is greatly broadened[155, 156]. Local stresses and strains induced during soft-milling may be the responsible of the observed broadening of the MT, which in turn, could enhance the MCE in Ni-Mn-Sn systems. Moreover, stress annealing has a significant influence on FM exchange interactions, exchange bias and on MCE in Ni-Mn-Sn systems[75, 74].

All in all, this chapter is devoted to investigate an additional way to further modify the MT characteristics in an otherwise hardly tunable Ni-Mn-Sn system. The main objective is to induce a controlled microstructural distortion and to investigate how the defects can be used to modify the MT characterisitics. To do so, a Ni-Mn-Sn sample has been subjected to soft-milling using an agate mortar. With the aim of evaluating the effect that internal-stresses, defects and strains have on the MT of Ni-Mn-Sn systems, the standard techniques (e. g., DSC, PN and magnetic measurements) for MT characterization have been complemented with ^{119}Sn Mössbauer Spectroscopy (^{119}Sn-MS). Mössbauer spectroscopy is a powerful technique for both structural and magnetic characterization at atomic level. Indeed, due to the magnetostructural coupling that these alloys exhibit, ^{119}Sn-MS acquires a key relevance in the microstructural study of Ni-Mn-Sn alloys. Although several works can be found in which ^{57}Fe-MS has been used in Fe doped Ni-Mn-Sn alloys[75, 157, 158, 159], ^{119}Sn-MS, which makes doping unnecessary and therefore helps to ensure chemical environment of Sn atoms, has been scarcely employed[160]. Thus, ^{119}Sn-MS may result a powerful tool to shed light on the relation between nanoscale properties and the MT features in Ni-Mn-Sn systems.

Additionally, the different microstructural states caused by the thermomechanical treatments are systematically studied and quantitatively correlated to the magnetostructural properties of a Ni-Mn-Sn alloy. The kinetics, i.e. the thermoelastic balance, of the MT and both, the local and the average magnetism can be directly related to the evolution of internal strains. Upon annealing, the density of non-magnetic inclusions (defects) and the stress field created by dislocations decrease, thus leading to an increase in the saturation magnetization and a decrease in the MT temperature range. Moreover, it is observed that the coupling between Mn atoms is altered in the vicinity of anti-phase boundaries (APB), resulting in a significant decrease of the saturation magnetization. As will be shown, these changes optimize the magnetocaloric response of the alloy. Even though the milling and the post-annealing

processes do not produce any variation of transition temperatures and atomic order, the induced microstructural distortions affect greatly the interval in which the MT takes place. Finally, the work developed in a ternary Ni-Mn-Sn compound is extended in composition to a Co-doped quaternary alloy, in which the effect that the milling has on the MCE is comparatively evaluated.

The obtained results confirm that, once the transition temperature has been fixed by composition, the modification of the microstructure through thermomechanical treatments appears as the best way to tune the functional properties of these alloys. The recovery of the microstructural distortions induced by milling is directly related to the intensity of the non-magnetic component revealed by ^{119}Sn-MS, which opens the possibility of tracking the whole contribution of defects and the local stresses on the MT in Ni-Mn-Sn alloys. Last but not least, the comparison of the MCE evaluated in the disordered and annealed Ni-Mn-Sn-Co samples shows that the presence of defects, far for worsening, enhances the MCE.

4.1 Experimental Details

The evaluation of the effect that internal strains, defects and local stresses have on the MT has been conducted in three different Ni-Mn-Sn samples. Thus, samples not showing MT have been discarded (i. e., $Ni_{50}Mn_{25}Sn_{25}$ and $Ni_{50}Mn_{30}Sn_{20}$). Initially a $Ni_{50}Mn_{35}Sn_{15}$ sample has been selected to carry out the investigation. This sample has a T_{MT}= 220 K and a T_c= 310 K, which implies that the austenite phase is FM in a wide temperature range. As will be shown below, the FM nature of the austenite phase enables a proper resolution of the magnetic and non-magnetic components, which indeed, is used to study the contribution of defects to the MT. Later on, the study is extended to $Ni_{50}Mn_{37}Sn_{13}$ sample, and comparatively studied with a Co-doped $Ni_{45}Co_5Mn_{37}Sn_{13}$ alloy. Both ternary and quaternary samples exhibit the MT, which in the case of $Ni_{45}Co_5Mn_{37}Sn_{13}$ sample, it allows to study how the presence of microstructural defects affect the MCE linked with the MT.

A polycrystalline ingot of $Ni_{50}Mn_{35}Sn_{15}$ has been synthesized from high purity elements by the arc melting method[24]. The obtained alloy was homogenized under a protective Ar atmosphere at 1173 K during 24 h and at 1273 K during 4 h (in order to avoid dendritic structures[82]). The composition was checked by EDX in a JSM-5610LV Scanning Electron Microscope. With the aim of inducing defects, the alloy has been mechanically milled in an agate mortar until reaching a steady state in the spectra revealed by ^{119}Sn-MS ($\approx$ 20 min). The particle mean size measured by SEM has been around 10 μm.

Then, in order to analyze the microstructural evolution upon post-milling, several

[24]For more details see Sec. 2.1.1.

milled powdered samples are taken and separately annealed at 573 K, 673 K, 773 K and 873 K during 5 minutes (at each temperature). The samples are labeled as Milled, AN573, AN673, AN773 and AN873 respectively). DSC measurements have been carried out at a heating/cooling rate of 10 K/min. The temperature dependence of the magnetization under different fields from (0.01 T to 6 T) and the field dependence of the magnetization at low temperature have been measured in a Quantum Design MPMS XL-7 SQUID magnetometer. Microstructural evolution is characterized by XRD measurements recorded at room temperature in a D5000 Siemens Diffractometer operating with Cu Kα radiation. Additionally, the magnetostructural characterization is complemented with PND measurements, carried out at D2B instrument (λ = 1.59 Å) in the Institute Laue-Langevin in Grenoble (France)[161]. Both XRD and PND data have been analyzed using FullProf package programs[139].

Mössbauer spectra have been obtained using a $Ba^{119m}SnO_3$ source in a transmission geometry at 270 K and (at ferromagnetic cubic austenite phase) equipped with a triangle-wave generator at speed of 8, 12 and 16 mm/s. Spectra have been fitted using the NORMOS[103] program.

4.2 Effect of Strains and Stresses in $Ni_{50}Mn_{35}Sn_{15}$ Alloy

4.2.1 Effect of Internal Stresses in DSC and Magnetic Measurements

Fig. 4.1 shows the temperature dependence of the magnetization measured under 0.01 T (upper-left corner) and 6 T (upper-right corner) fields, for both Milled and AN673 samples. As shown in the low field thermomagnetization curves, annealing does not affect neither the T_c nor the T_{MT}, and the only effect that annealing produces on the Milled sample is the magnetization increase. This fact is also revealed by high-field measurements shown in the upper right-corner of Fig. 4.1, in which both characteristic temperatures remain also unaltered. Furthermore, as it will be discussed further in Sec. 4.2.4, the different approach to saturation of the normalized $M(H)$ curves (see lower-left corner of Fig. 4.1) points out a possible different AF contribution to the magnetic moment between the Milled and AN673 samples. The $M(H)$ curves have been measured at 270 K (FM austenite phase).

The lack of variation of T_c and T_{MT} can be also inferred from the DSC measurements shown in the lower-right corner of Fig. 4.1 and Fig. 4.2. In turn, the DSC of AN673 sample shows a narrower temperature range of the MT than the Milled sample, indicating a decrease in the elastic energy term as a result of annealing[61]. The lack of T_{MT} and T_c variation upon annealing is also observed for the rest of samples. Fig. 4.2 shows the cooling-heating calorimetric measurements carried out for all samples around the T_{MT}. The exothermic and endothermic peaks observed on the cooling and heating ramps reveal the occurrence of the MT, while the λ-type

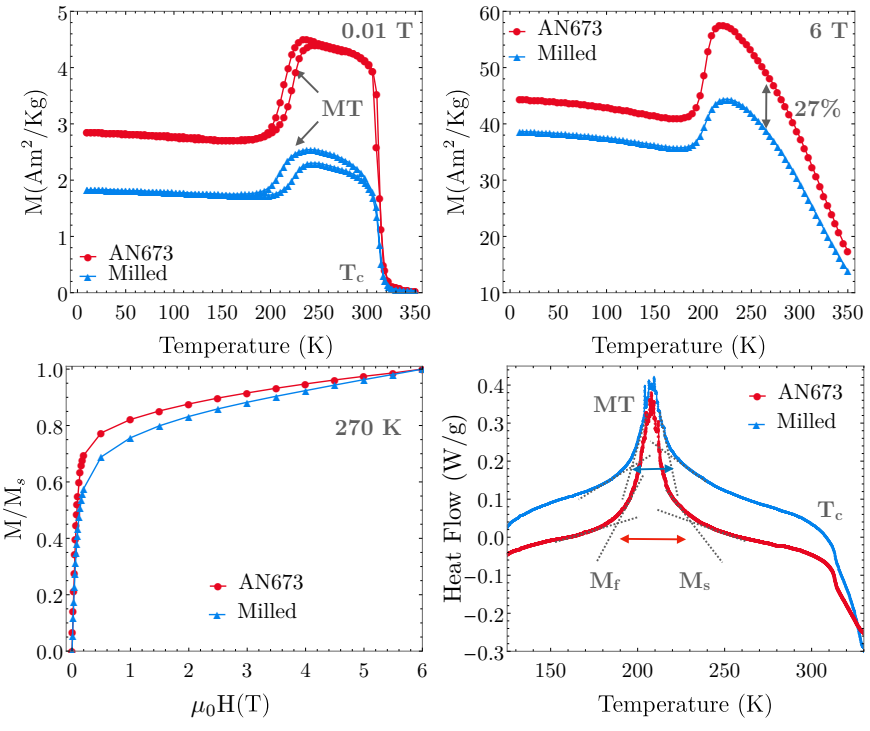

Figure 4.1: $M(T)$ for the Milled and AN673 samples recorded at 0.01 T (upper-left corner) and at 6T (upper-right corner). The normalized $M(H)$ cycles of both Milled and AN673 samples are recorded at 270 K, in ferromagnetic austenite phase (lower-left corner). The picture in the lower-right corner comparatively shows the DSC curves of Milled and AN673 sample, in which a reduction in the width of the MT is observed.

shoulder observed around 325 K is related to the magnetic ordering temperature at T_c. The structural and magnetic transformation temperatures obtained from DSC measurements are summarized in Table 4.1. The latent heat linked to the MT, ΔH, is estimated as the average value of the integrated area of the MT peaks between the cooling and heating ramps. Additionally, the entropy change at the MT is calculated by means of $\Delta S = \Delta H/T_p$, where T_p is the temperature of the corresponding peak. The similar values of the characteristic transition temperatures gathered in Table 4.1, confirm that the annealing does not affect the characteristic temperatures. The only effect that the annealing brought is that the peak height and the sharpness of the MT accentuate.

In this connection, the temperature range where the transformation spreads, ΔT, becomes gradually reduced with annealing, diminishing from 92 K to 70 K (see Table 4.1). Such transformation interval has been determined by the average value of the difference between the starting and finishing transformation temperatures for the forward MT (M_s and M_f, respectively) and for the reverse MT (temperatures

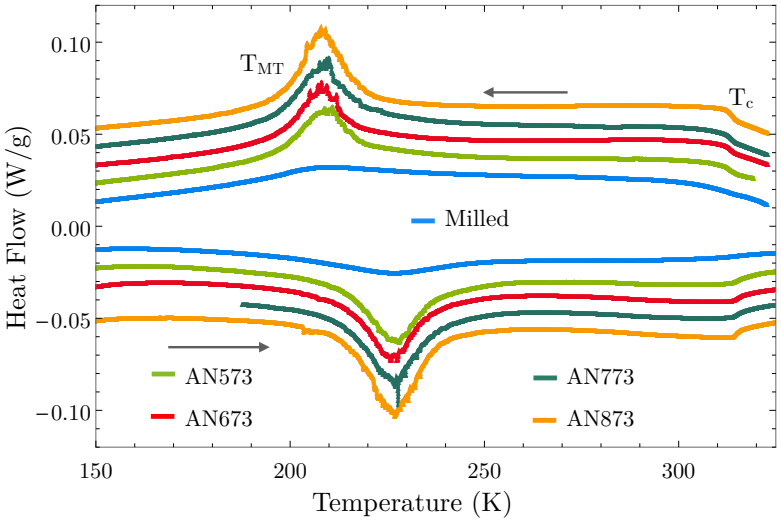

Figure 4.2: DSC curves of the full series of samples (Milled and after different annealing treatments).

A_s and A_f, respectively). Thus, although the temperatures of the magnetoestructural transitions T_{MT} and T_c do not change with the post-milling, the reduction of ΔT indicates that the dynamics of the transformation is strongly affected by the microstructural evolution taking place during the heat treatments. The effect of annealing on the studied sample is an increase in the saturation magnetization and a narrowing of the calorimetric MT peak. Taking into account that both T_c and the T_{MT} are highly sensitive to atomic order[162], the lack of variation in these transition temperatures seems to indicate a null effect of annealing on the atomic order[63].

Sample	M_p (K)	A_p (K)	T_c(K)	Hys (K)	ΔT (K)
Milled	208(1)	228(1)	317(1)	19(2)	92(2)
AN573	209(1)	228(1)	322(1)	18(2)	85(2)
AN673	208(1)	226(1)	321(1)	18(2)	83(2)
AN773	209(1)	227(1)	322(1)	19(2)	75(2)
AN873	208(1)	227(1)	322(1)	20(2)	70(2)

Table 4.1: Temperature of the DSC peaks related to forward MT (M_p) and reverse MT (A_p), values of Curie's temperature T_c, MT hysteresis width (Hys) and the transformation temperature interval ΔT for the set of samples.

4.2.2 Microstructural Evolution Upon Annealing

In order to correlate the microstructure with the annealing treatments, XRD measurements have been carried out in austenitic phase at room temperature. Fig. 4.3

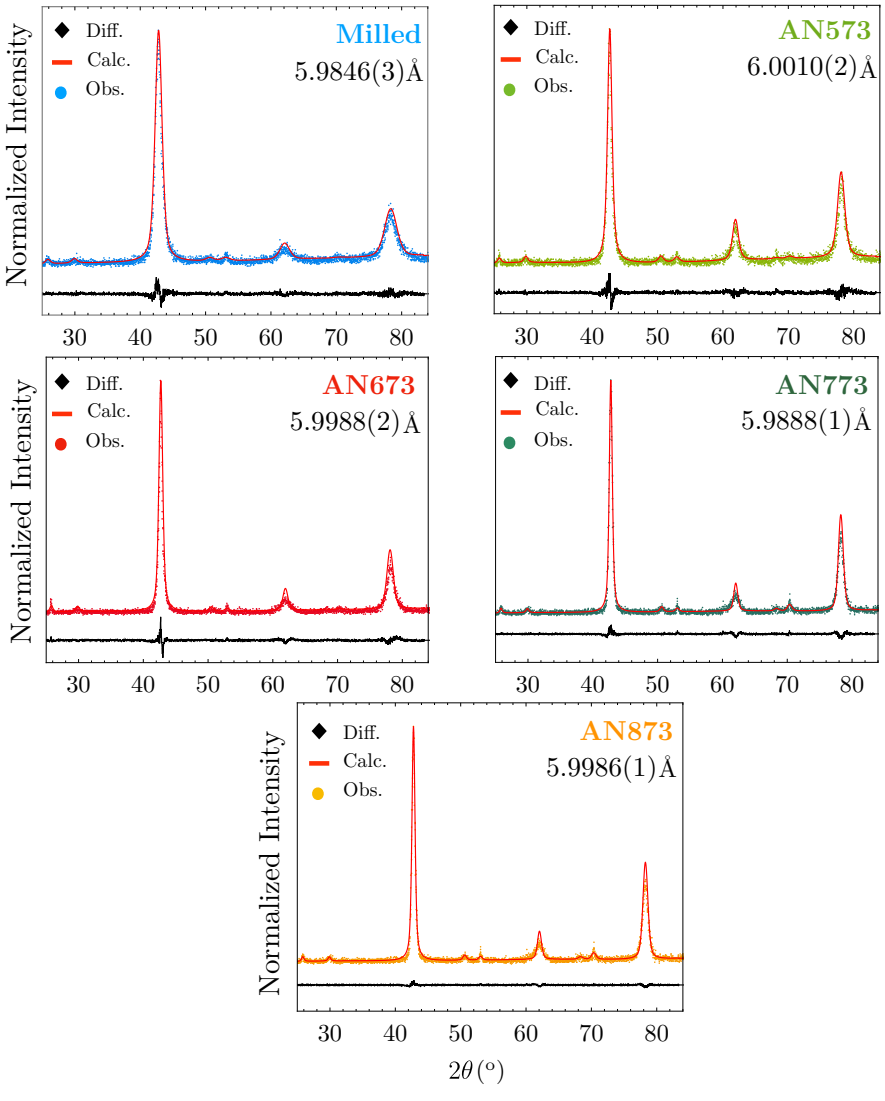

Figure 4.3: Room temperature XRD patterns and the corresponding calculated lattice parameters for Milled, AN573, AN673, AN773 and AN873 samples. The dots are the observations, the red line the calculated pattern and the black line the difference between observed and calculated intensity.

shows the XRD patterns obtained for the different samples. All of them display the characteristic [220], [400] and [422] peaks corresponding to the well-known Heusler $L2_1$ cubic structure, ($Fm\bar{3}m$) space group[63]. The reflection peaks lay at the same angles in all cases, indicating an almost null change of the cell parameter. These values of the cell parameters are displayed in the upper-right corner of each diffraction

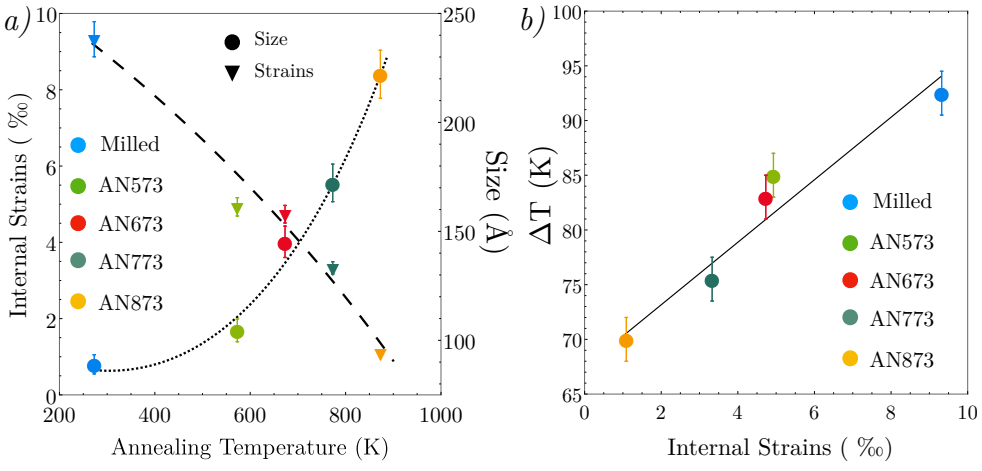

Figure 4.4: (a) Evolution of grain size and strains as a function of annealing temperature. b) Martensitic transformation temperature interval ΔT as a function of internal strains.

pattern in Fig. 4.3, which indeed confirm their constant value. Nevertheless, as happened in the DSC measurements, the XRD peaks become narrower as the annealing temperature increases, which, as expected, suggests a variation on microstructural state.

Fig. 4.4(a) displays the evolution of internal strains and grain size, determined from the Lebail analysis[163] of the diffraction patterns along the series of samples. The internal strains decrease and the grain size increases with the increasing annealing temperature, evolving from small grain size with high percentage of strains (88.98 ± 0.02Å and 9.32 ± 0.03 ‰, respectively, on the Milled sample) to bigger grains and lower strains (222.08 ± 0.06 Å and 1.09 ± 0.03 ‰, respectively, in AN873). The microstructural evolution upon annealing is followed by the removal of strains induced during the milling, so the width of the MT also evolves accordingly. Fig. 4.4(b) shows the MT temperature range (width of MT, ΔT) as a function of internal strains. ΔT increases almost linearly with the microstrains, which is in agreement with an increase of the elastic energy. The direct relationship between the evolution of ΔT and the internal strains confirms the microstructural origin of the evolution that ΔT exhibits upon annealing.

It is well known that due to the presence of elastic and frictional terms in the energy balance at the MT, the transformation takes place in a finite temperature range which also exhibit a hysteretic behavior[61, 164]. Additionally, at $T < T_0$ a local equilibrium is achieved during the forward MT at the transformation front,

$$-\Delta G_{ch}^{a\to m} + E_{el}^{a\to m} + E_{fr}^{a\to m} = 0 \tag{4.1}$$

where $\Delta G_{ch}^{a\to m}$ is the free energy difference between martensite and austenite, and $E_{el}^{a\to m}$ and $E_{fr}^{a\to m}$ are the stored elastic and dissipated frictional energy during

forward MT, respectively. On a further cooling, the chemical term acts as the driving force to overcome the elastic and frictional terms, which impede the development of the transformation[61, 164]. As a result, the recovery of defects during thermal annealing reduces the non-chemical terms and hence the MT becomes sharper. Thus, the evolution of ΔT is directly related to the annealing of defects.

Due to the magnetostructural coupling these alloys exhibit, the observed structural changes are often accompanied by magnetic changes. In this regard, PND experiments add a valuable information of both magnetic and structural state. Thus, the crystallographic structure and long-range atomic order of the studied samples have been also analyzed by means of PND measurements.

Fig. 4.5 shows the experimental and fitted diffractograms obtained for the Milled and AN673 samples at 270 K. As will be shown further in Sec. 4.2.3, the 270 K temperature has been selected for the sake of maximizing the resolution between the magnetic and non-magnetic components of ^{119}Sn-MS spectra. This temperature corresponds to the lowest temperature at which $Ni_{50}Mn_{35}Sn_{15}$ remains at austenitic ferromagnetic phase, just before to M_s temperature. Both Milled and AN673 samples show the cubic $L2_1$ ($Fm\bar{3}m$) structure with the same lattice parameters (6.004(1) Å for the Milled sample and 6.003(1) Å for the AN673), which are compatible with values obtained from XRD measurements shwon in Fig. 4.2. The magnetic and structural parameters for $4a$ and $4b$ positions, obtained after Rietveld refinement, are shown in Table 4.2, revealing identical occupancies for both, Milled and AN673 samples. As illustrated in Fig. 4.6, in stoichiometric conditions, $4a$ positions are occupied by Mn atoms whereas $4b$ positions are occupied by Sn atoms[16]. However, in off-stoichiometric conditions, the exceed Mn atoms tend to occupy the natural

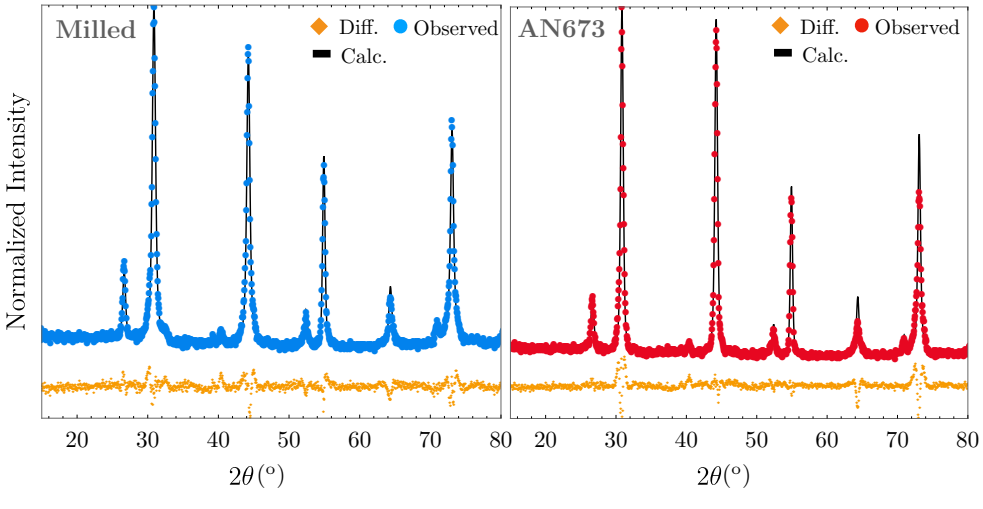

Figure 4.5: Rietveld refinement of diffraction patterns for the Milled and AN673 samples recorded at 270 K.

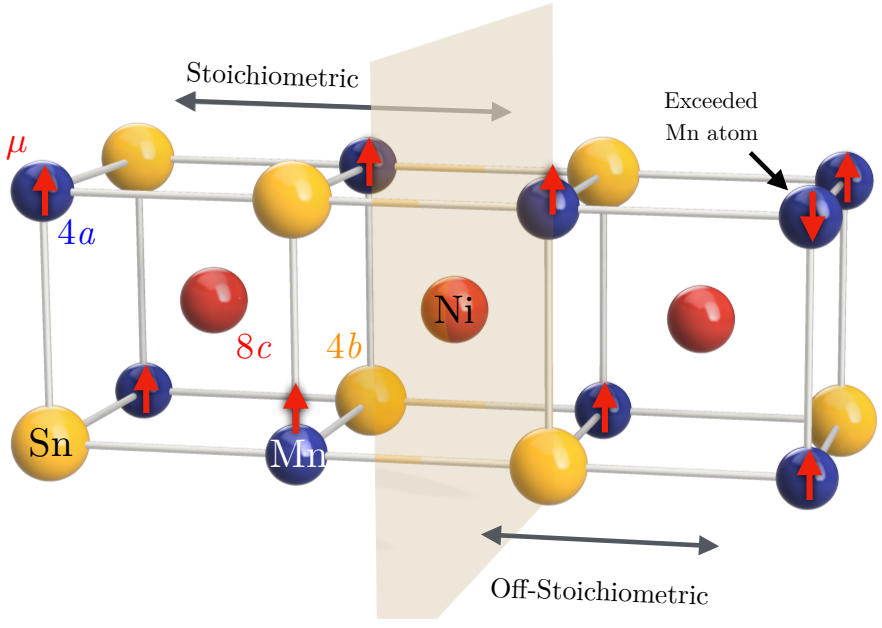

Figure 4.6: Preferred positions of Ni, Mn and Sn atoms in stoichiometric and off-stoichiometric samples. The exceeded Mn atoms tend to occupy the natural Sn position, 4*b*. As a result, due to the reduced Mn-Mn distance, the magnetic moments couple AF.

position of Sn (4*b*), and as a result, the occupation of 4*b* position is distributed between Mn and Sn atoms. The fact that occupancies of Milled and AN673 samples for 4*a*, 4*b* and 8*c* sites are identical, implies that the degree of $L2_1$ atomic order is the same in both samples.

Therefore, in agreement with the observed absence of variation in transition temperatures, from PND data it can be concluded that no atomic order variation is brought by annealing. Interestingly, as shown in Table 4.2, the magnetic coupling between Mn atoms in 4*a* and 4*b* positions drastically evolves upon annealing from AF to FM. In particular, the magnetic moment linked with 4*b* position evolves from a negative value of -0.45μ_B to a positive 0.37μ_B value. The change from AF to FM coupling of Mn atoms is indeed in line with the observed increase in the high-field magnetization.

However, PND and XRD data reveal that neither atomic order nor lattice parameter evolves upon annealing. In this connection, it is worth noting that the only effect of the annealing in XRD and PND data is that reflection peaks are clearly broader in the Milled sample. This effect points out a microstructural evolution during the annealing which would imply a higher crystallite size and lower microstrains in the annealed sample, which in turn, could be behind the observed magnetic evolution. In fact, the magnetic evolution that PND data reveals regarding the Mn-Mn coupling may be on the origin of the observed changes in the width of the MT. The variation

of the magnetic driving force during the MT seems to affect the dynamics of the MT. Thus, an atomic scale characterization of the magnetism may shed light on the macroscopic behavior of both, magnetic properties and the evolution of the MT.

	Site 4*a*		Site 4*b*		Site 8*c*
	Occupancy	$\mu(\mu_B)$	Occupancy	$\mu(\mu_B)$	Occupancy
Milled	Mn 0.95(4) Ni 0.05(4) Sn (—)	1.26(6)	Mn 0.41(4) Ni 0.02(0) Sn 0.57(4)	-0.45(6)	Mn 0.08(1) Ni 0.92(1) Sn (—)
AN673	Mn 0.94(3) Ni 0.06(3) Sn (—)	2.58(2)	Mn 0.43(3) Ni 0.05(0) Sn 0.52(3)	0.37(2)	Mn (—) Ni 1(-) Sn (—)

Table 4.2: Occupancies and magnetic moment values (μ) for 4*a*, 4*b* and 8*c* positions obtained from the Rietveld refinement for Milled and AN673 samples. For 8*c* position $\mu = 0$ is considered.

4.2.3 ^{119}Sn Mössbauer Spectroscopy

In order to ascertain the nature of the effect that annealing and the recovery of the defects have on the magnetic properties of $Ni_{50}Mn_{35}Sn_{15}$, the atomic level magnetism has been investigated by means of ^{119}Sn-MS. Fig. 4.7 shows experimental and fitted ^{119}Sn-MS spectra for all the investigated samples.

On the one hand, the spectrum of the Milled sample is mainly composed by a non-magnetic singlet with a non-resolved magnetic component as a minor contribution. However, in the annealed samples, the relative intensity of both components changes gradually with annealing temperature increase, being the magnetic subspectrum practically the only contribution to the spectrum of the AN873 sample. All spectra have been satisfactorily fitted exclusively with these two discrete contributions.

The values obtained from the fitting of Mössbauer spectra are listed in Table 4.3. The main common feature is the decrease that the singlet component (I_s) exhibit (and therefore the increase that B_{hf} magnetic hyperfine exhibit) with increasing the annealing temperature. Similar values of the δ isomer shift of both components have been obtained for all the samples, indicating that the chemical order in the surrounding of Sn atoms remains the same independently of the annealing process[165]. However, the line-width parameter Γ listed in Table 4.3 decreases as the annealing temperature increases. As the Γ parameter is sensitive to slight distortions of the local environment of the Mössbauer probe atoms[166], its decrease indicates a microstructural recovery on the very close environment of Sn atoms. Indded, this result is in line with the results obtained from PND measurements.

In summary, PND, ^{119}Sn-MS and magnetic measurements show similar long-range atomic order degree between Milled and all annealed samples. However, the decrease

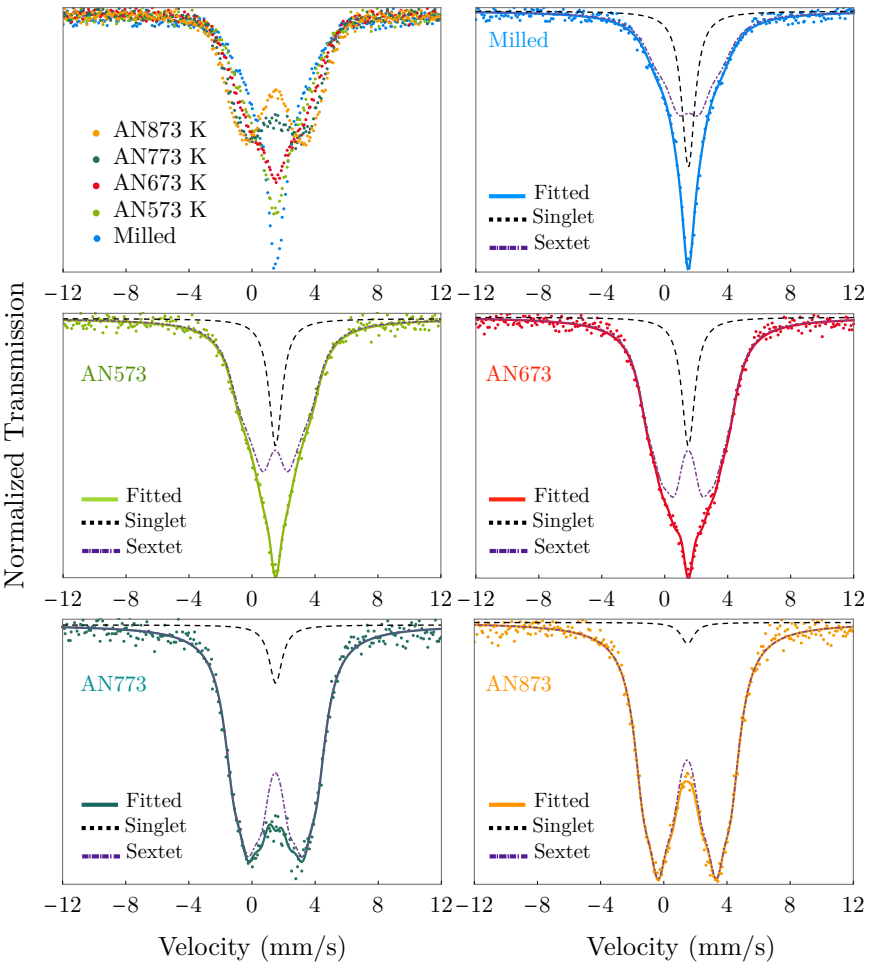

Figure 4.7: Raw (upper-left) and fitted ^{119}Sn-MS spectra of the Milled, AN573, AN673, AN773 and AN873 samples (from left to right and from top to bottom). Spectra are taken at 270 K, at ferromagnetic $Fm\bar{3}m$ phase.

of Γ parameter and the narrowing of the PND peaks with annealing temperature increase, suggest an evolution in the microstructural parameters. Thereby, the observed changes on the magnetic properties and in the width of the MT may rely on different internal stress state and the presence of defects created during milling.

As previously reported in some Heusler alloys, during mechanical treatments (i. e. cold working), several local distortions such as dislocations and defects can be created even without inducing any atomic disorder[167, 168]. Specifically, the presence of superlattice dislocations in cold worked Heusler alloys are accompanied by anti-phase boundaries (APB)[169, 170]. Besides, the exchange interaction between

Sample	Singlet	Sextet		Constrained Parameters	
	I_s	B_{hf} (T)	I_{hf} (%)	$\delta(mm/s)$	$\Gamma(mm/s)$
Milled	%31(3)	4.1(1)	%31(3)	1.53(1)	1.96(1)
AN573	%18(1)	4.6(2)	%18(1)	1.48(1)	1.67(7)
AN673	%15(1)	5.2(1)	%15(1)	1.48(1)	1.54(5)
AN773	%6(1)	5.3(1)	%6(1)	1.48(1)	1.51(4)
AN873	%1(1)	5.6(1)	%1(1)	1.48(1)	1.50(2)

Table 4.3: Hyperfine parameters obtained from the fitting procedure of all the studied samples. B_{hf} hyperfine field of the sextet component and I_s intensity of the singlet component, along with δ isomer shift and Γ line-width parameter. δ and Γ have been constrained to be the same for both subspectra.

the second nearest neighbor (SNN) Mn atoms located across the APB can become AF in an otherwise FM material[171, 172]. Fig. 4.8 depicts a schematic representation of APB, where the Mn atoms are colored in red. In a perfect lattice Mn atoms couple FM, while in the vicinity of an APB Mn atoms may couple AF due to the reduced interatomic distance. As the coupling between Mn atoms is dictated by RKKY exchange interactions, the change in the interatomic distance through an APB is enough to change the coupling between the natural ($4a$) and antisite ($4b$) Mn atoms.

Although the SNN of Mn are Sn atoms at $4b$ positions, in off-stoichiometric conditions the excess Mn occupy $4b$ positions, see Fig. 4.6. As listed in Table 4.2, the coupling of $4a$ and $4b$ positions is mostly AF in the Milled sample. However, when the samples are annealed, the FM coupling is recovered. Taking into account that the number of AF coupled Mn atoms is proportional to the dislocation density[169], the annihilation of dislocations results in a decrease of the density of the APB present in the sample. Thus, the number of AF coupled Mn atoms decreases and the FM coupling is reinforced. Hence, the magnetization is greater in the AN673 sample than in the Milled sample. Additionally, as shown in the $M(H)$ curves in Fig. 4.1 the magnetization of the AN673 sample approaches better the saturation than the Milled sample.

The annihilation of dislocations also explains the reduction of Γ parameter and the narrowing of PND peaks after the annealing[172]. The release of local stresses associated to dislocations homogenizes the surrounding environment of Sn atoms and, as a consequence, the value of Γ decreases. As shown in Table 4.3, the major recovery of Γ occurs in the first two annealing steps, at 573 K and 673 K. The annihilation of dislocations at these temperatures has been previously reported in other Heusler alloys[167, 170]. However, as ^{119}Sn-MS measurements shows in Fig. 4.5, the recovery process continues above 673 K without a significant change on Γ. In this region, the recovery would be mediated by the elimination of point defects, such as vacancies[79].

Despite Sn atoms do not carry intrinsic magnetic moment, a transferred hyperfine field can be induced from the neighbor magnetic ions (Mn ions in the case of Ni-Mn-

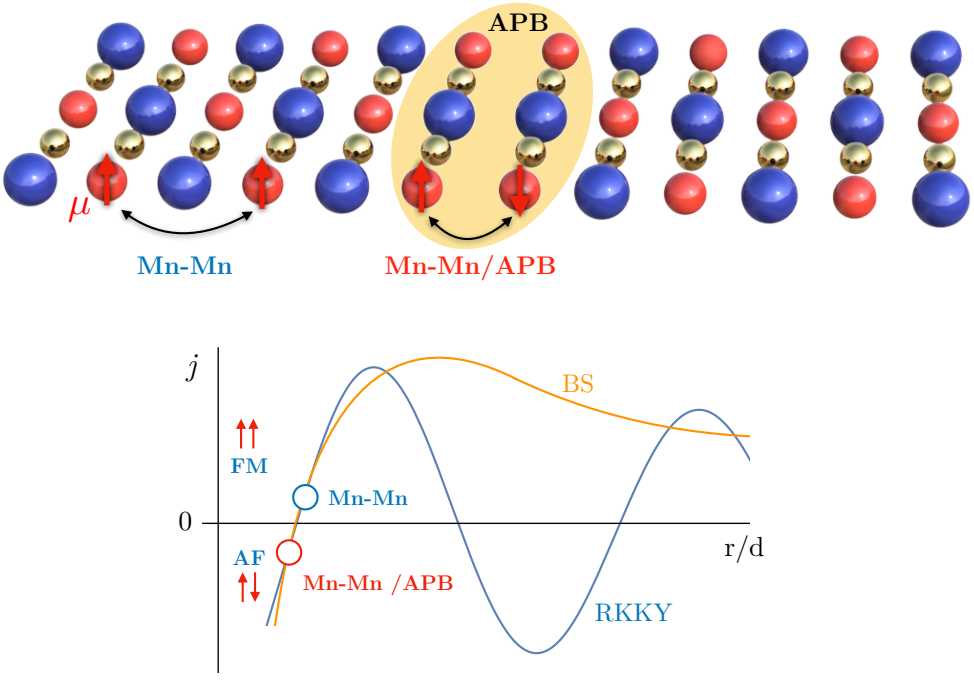

Figure 4.8: Schematic representation of an APB where the Mn atoms across the APB couple AF (adapted from [173]). Below, the schematic diagram of Bethe-Slater (BS) and RKKY exchange interaction (j) curves show the different types of magnetic coupling as a function of Mn-Mn distance (adapted from Lazpita *et. al* [174]).

Sn)[95], by which ^{119}Sn-MS can reflect the local magnetic field felt by Sn atoms. The singlet component observed by ^{119}Sn-MS of Fig. 4.5, related to stressed regions caused by dislocations and APB, indicates the absence of hyperfine magnetic field. Thus, this component points out that the ferromagnetic order is altered in the region of influence of the APB, in such a way that the total transferred dipolar field at Sn sites is zero. I_s decreases as soon as the density of dislocations and APB decreases with annealing at higher temperatures. On the contrary, the B_{hf} at 4b positions increases (see Table 4.3). In fact, B_{hf} is $\approx 27\%$ higher in AN673 than in the Milled sample, that is exactly the same difference observed in $M(T)$ curves recorded at 270 K (see Fig. 4.1). The increase of B_{hf} implies a reinforcement of the hyperfine magnetic field related to the annealing of defects and the recovery of the FM coupling. As a result, this effect affects directly the macroscopic magnetism.

4.2.4 Magnetic Characterization

Magnetic measurements at low temperature have been carried out in order to determine the evolution of the magnetic properties of the martensite during the mi-

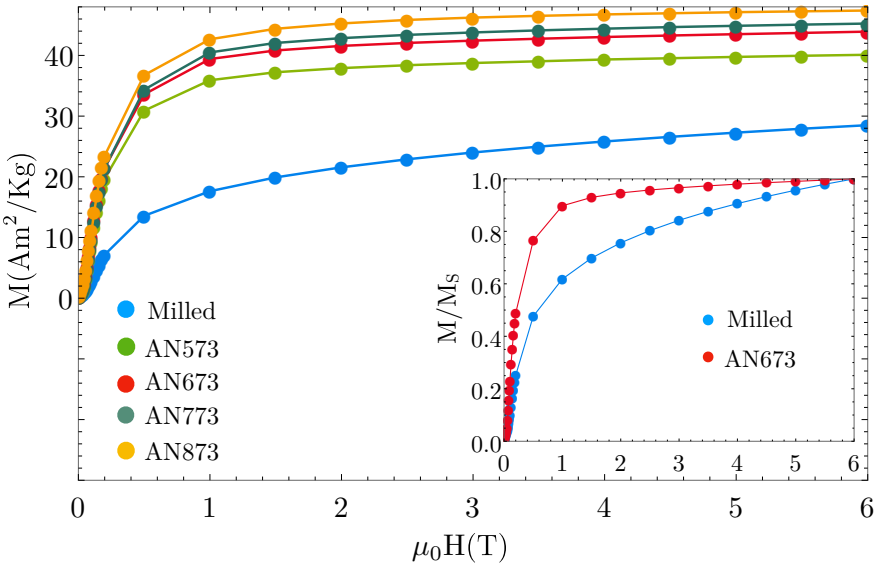

Figure 4.9: Magnetic field dependence of magnetization of the set of samples in martensite phase, recorded at 10 K. For a better visualization of the different approach towards saturation, the inset shows the normalized M/M$_s$ of the Milled and the AN873 samples.

crostructural recovery induced by the thermal treatments. Fig. 4.9 shows the magnetic field dependent magnetization of the different samples measured at 10 K. It is worth noting that the saturation magnetization (M_s) increases, as well as the shape of the curve evolves with the increasing annealing temperature. Additionally, the inset in Fig. 4.9 shows the normalized $M(H)$ curves of the Milled and AN673 samples, recorded at 10 K. By comparing both curves, a different approach to saturation is clearly observed. This different approach to saturation and the increase of the M_s on annealing can be ascribed to a different AF contribution to the magnetic moment between the Milled and AN673 samples, which is also supported by PND results gathered in Table 4.2. The decrease of the AF coupling between Mn atoms can be explained by the reduction that APB experience while dislocations annihilate[155]. Indeed, dislocations in atomic ordered structures appear as super-dislocations; a pair of dislocations separated by an APB where the atomic order. Consequently the FM coupling is modified while the density of dislocations decreases upon annealing.

The magnetization curves of Fig. 4.9 have been fitted to the classical law of approach to saturation, which can be expressed as[175, 176]:

$$M = M_s \left(1 - \frac{\alpha}{H} - \frac{\beta}{H^2}\right) + \chi H \tag{4.2}$$

where $\mu_0 H$ is the applied field, M_s the saturation magnetization, χ the field independent susceptibility and α and β coefficients related to magnetic and structural properties of the sample. In particular, the α parameter depends on the stress field

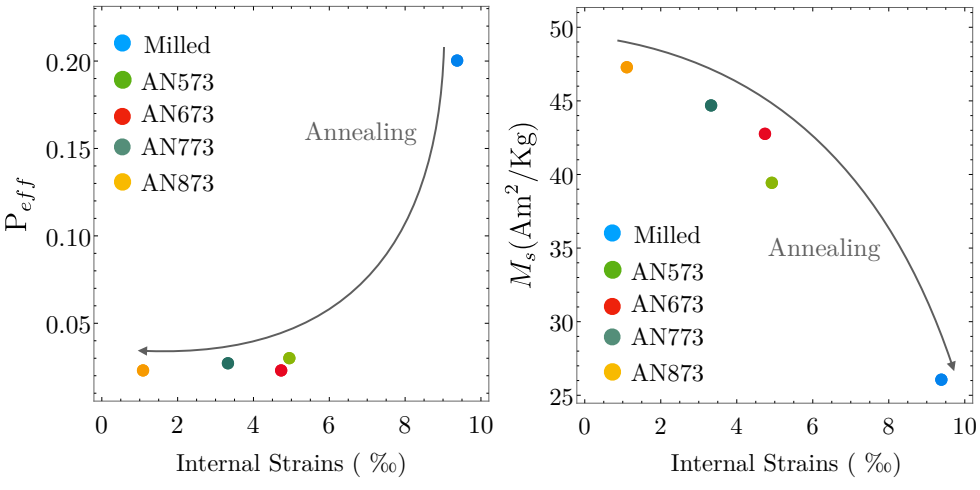

Figure 4.10: The evolution of the fraction of non-magnetic inclusions P_{eff} and of the saturation magnetization M_s as a function of internal strains.

created by dislocations and non-magnetic inclusions[177]. It can be approximated to $a \approx 4\pi\rho M_s P_{eff}$, where ρ is the density of the material and P_{eff} the effective fraction of porosity and non-magnetic inclusions. The values of P_{eff} and M_s obtained from the fitting are plotted in Fig. 4.10 as a function of the internal strains.

The high value of the effective fraction of non-magnetic inclusions of the Milled sample $P_{eff} = 0.2$ could be related, among other defects, to the high density of dislocations, where the FM coupling is lost by the local atomic disordering in their vicinity. The weakness of the magnetic coupling is also reflected in the low value of saturation magnetization, $M_s \approx 26$ Am^2/Kg. The initial recovery of the microstructure, when the internal strains undergo a decrease of 50%, drastically reduces the density of defects ($P_{eff} = 0.02$) and therefore increases M_s (up to values close to 40 Am^2/Kg). The slight variations of P_{eff} and M_s during the subsequent reduction of internal strains indicate that the macroscopic magnetism evolves mainly during the first stage of the microstructural recovery.

The recovery of the magnetism at atomic scale affects directly the macroscopic magnetism and also the MT. In fact, the DSC measurements of Fig. 4.1 show that the dynamics of MT (evolution of the width of the MT, ΔT) evolves upon annealing. This evolution may be related to the magnetostructural recovery revealed by ^{119}Sn-MS at atomic scale. Thus, in principle, the evolution of the atomic scale magnetism may add valuable information about the recovery of the MT.

4.2.5 Relation Between Martensitic Transformation and Singlet Component

As observed in the latter section, the recovery of the atomic scale magnetism goes in line with the observed recovery of the macroscopic magnetism. Thus, it is reasonable to think that the recovery of local stresses and strains mediates the recovery that the MT exhibit upon annealing. The evolution of the equilibrium temperature T_0 and the width of the MT as a function of annealing temperature is shown in Fig. 4.11.

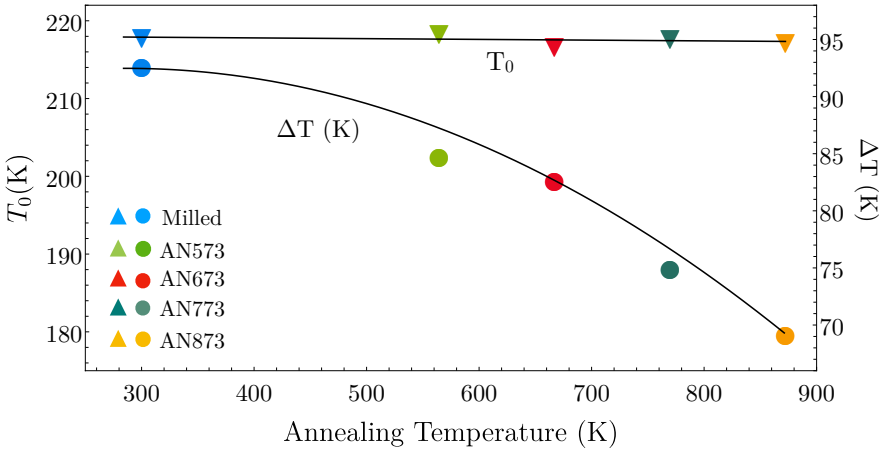

Figure 4.11: Evolution of T_0 parameter (triangles) and ΔT (full dots) as a function of the annealing temperature.

On the one hand, T_0 temperature, that is, the equilibrium temperature between the austenite and martensite phases, remains constant. The value of T_0 can be calculated by taking the characteristic temperatures of the forward and the reverse MT and by evaluating the following expression;

$$T_0 = \frac{(M_s - M_f) - (A_s - A_f)}{2}. \tag{4.3}$$

As shown in Fig. 4.11, it is noteworthy to mention that the recovery of the atomic scale magnetism and the annihilation of dislocations and defects does not affect the equilibrium temperature between the austenite and martensite phase. T_0 remains constant irrespectively of the annealing temperature. T_0 is highly sensitive to the atomic order[15] and its constant value reiterates the lack of differences in the long-range atomic order throughout the studied samples.

However, as shown in Fig. 4.11, the temperature range in which the MT is extended, ΔT, decreases from 92.5 K down to 70 K between the Milled and AN873 samples. As the annealing temperature increases, the non-magnetic regions close to the dislocations decrease. As a result, the intensity of the non-magnetic component revealed by ^{119}Sn-MS, I_s, decreases as well. The singlet component of ^{119}Sn-MS is

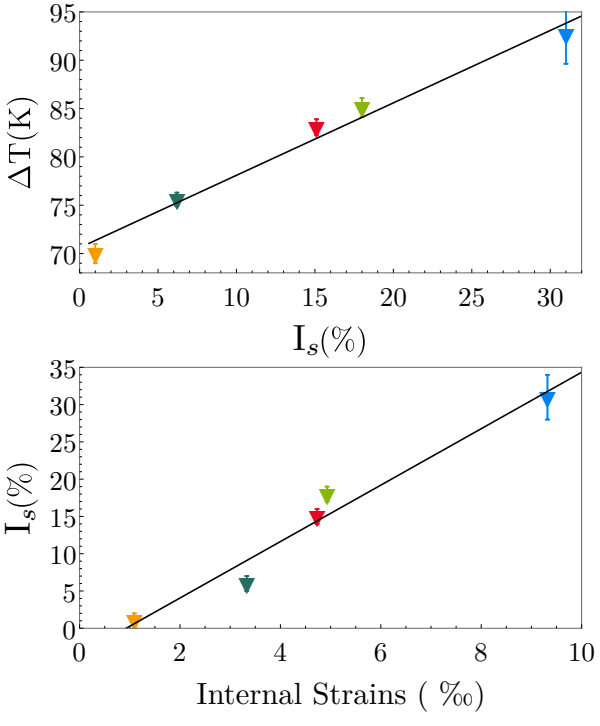

Figure 4.12: Upper figure; evolution of the width of the MT (ΔT), as a function of the area of the singlet component I_s (%). The figure below shows the evolution of the singlet component I_s as a function of internal strains.

then directly related to the internal stress state and the distorted regions that ultimately affect the MT. Therefore, the influence of the microstructural recovery on the MT is directly linked with the non-magnetic component revealed by ^{119}Sn-MS.

Fig. 4.12 shows the width of the temperature range in which the MT is extended as a function of the singlet contribution I_s, evincing their direct relationship. Additionally, Fig. 4.12 shows how the intensity of the singlet component I_s of the ^{119}Sn-MS varies as a function of internal strains. The two graphs of Fig. 4.12 clearly indicate that I_s is directly related to the internal strain state and to the distorted regions present in the sample. Due to the fact that all spectra are fitted using these two discrete components, the reduction of I_s implies a reinforcement of B_{hf} (and vice versa), which explains the recovery of the macroscopic magnetism shown in Fig. 4.1. As soon as the non-magnetic regions decrease due to annealing, B_{hf} is recovered and ΔT does behave in the same way. Therefore, the influence of the microstructural recovery on the MT can be directly tracked by the singlet component measured by ^{119}Sn-MS.

4.3 Effect of Co Addition on $Ni_{50}Mn_{37}Sn_{13}$: A Comparative Study

The study performed in Sec. 4.2 for the ternary $Ni_{50}Mn_{35}Sn_{15}$ alloy demonstrates that the non-magnetic component (i. e., singlet component) revealed by ^{119}Sn-MS is directly related to the stressed regions. Moreover, the decrease of the singlet component goes in hand with the narrowing of the MT. It is noteworthy to mention that ^{119}Sn-MS spectra of $Ni_{50}Mn_{35}Sn_{15}$ alloy have been collected at 270 K, just before the occurrence of the MT. This temperature has been chosen to match the lowest possible temperature of the austenite phase, thus enabling a better resolution of the magnetic component. As a result, the sextet and singlet component are well differentiated, enabling the tracking of the evolution of the singlet as a function of the annealing temperature. Indeed, it is reasonable to assess that the approach mentioned above can only be performed on alloys in which the non-magnetic component related to the stressed regions is clearly differentiated from the magnetic one. For instance, in other Ni-Mn-Sn compounds with a lower B_{hf}, the magnetic and non-magnetic component may overlap, thus hindering a clear differentiation between the magnetic and non-magnetic components.

In this connection, Co-doping can be used to increase the magnetism of the austenite phase, while the magnetism of the martensite phase is notoriously diminished. In both Ni-Mn-In and Ni-Mn-Sn alloys, Co doping decreases the MT temperature while the Curie's temperature T_c is considerably increased[48]. As a result, the magnetization discrepancy (ΔM) between the austenite and martensite phases increases, which in the endeavour of exploiting the multifunctional properties of the Ni-Mn based Heusler alloys, acquires a key relevance. Large ΔM values give rise to additional multifunctional properties like the magnetic-field induced shape memory effect[43] and the inverse magnetocaloric effect[22, 23]. This effect is especially notorious in Ni-Mn-In-Co alloys, in which an almost PM martensite phase is obtained. As a result, Co-doped samples show enhanced magnetocaloric properties[27]. In Ni-Mn-Sn alloys, although ΔM is also enhanced, the obtained metamagnetic character is in general smaller compared to In-based ones. However, the $L2_1$ crystal structure of Ni-Mn-Sn alloys is highly stable against thermal treatments, becoming a good candidate for thermal-cycling involving applications[63].

In order to test the suitability of the approach developed in Sec. 4.2, the composition of the investigated alloy is extended to $Ni_{50}Mn_{37}Sn_{13}$ and $Ni_{45}Co_5Mn_{37}Sn_{13}$ alloys[25]. The initial magnetic characterization reveals similar values of T_c and T_{MT} $\approx$ 320 K for $Ni_{50}Mn_{37}Sn_{13}$, while for $Ni_{45}Co_5Mn_{37}Sn_{13}$ these values are T_{MT} = 160 K and T_c = 390 K, both in good agreement with previous reports[178, 179]. In this section, instead of only focusing on the austenite phase as carried out in the

[25]The details of the experiments carried out for $Ni_{50}Mn_{37}Sn_{13}$ and $Ni_{45}Co_5Mn_{37}Sn_{13}$ are identical to those described in Sec. 4.1.

$Ni_{50}Mn_{35}Sn_{15}$ sample, the ^{119}Sn-MS characterization is extended to the martensite phase.

Following the approach employed in $Ni_{50}Mn_{35}Sn_{15}$ sample, and with the aim of inducing stresses and checking the evolution of the non-magnetic component revealed by ^{119}Sn-MS, the two ingots have been mechanically crushed and hand milled using an agate mortar. The samples have been milled until a steady state has been reached in ^{119}Sn-MS spectra. From each milled sample, some powder is taken apart and annealed at 873 K during 5 minutes in order to analyze the lower and upper bound of the singlet component upon post-milling anneal. The samples are labeled as Sn13M, Sn13AN, Sn13CoM and Sn13CoAN, where Sn13 and Sn13Co refer to the composition and M and AN labels indicate the milled and annealed state of samples, respectively. In order to cover different structural and magnetic states, both samples have been measured at at 295 K, 200 K and 77 K.

4.3.1 ^{119}Sn-MS in $Ni_{50}Mn_{37}Sn_{13}$ and in $Ni_{45}Co_5Mn_{37}Sn_{13}$ Samples

Fig. 4.13 shows the experimental and fitted ^{119}Sn-MS spectra recorded for milled and annealed $Ni_{50}Mn_{37}Sn_{13}$ and $Ni_{45}Co_5Mn_{37}Sn_{13}$ samples. Spectra have been recorded at 295 K, 200 K and 77 K. It is noteworthy that the MT temperature of the ternary $Ni_{50}Mn_{37}Sn_{13}$ sample is $\approx$ 320 K. Thus, the three spectra recorded in the ternary alloy have been measured on the martensite phase (and below T_c). Regarding the Co doped $Ni_{45}Co_5Mn_{37}Sn_{13}$ counterpart, the transition from the austenite to martensite phase takes place at 160 K. As a result, spectra of SnCo samples recorded at 295 K and at 200 K are measured at FM austenite phase, whereas the spectra collected at 77 K is measured in the martensite phase.

On the one hand, the spectra of Sn13M and Sn13AN samples taken at 295 K do not exhibit clear magnetic features. However, a slight magnetic component lying almost in the background can be distinguished. This magnetic contribution increases at lower temperatures, as observed in the spectra measured at 200 K.

In contrary to what is observed in the case of the ternary $Ni_{50}Mn_{35}Sn_{15}$ alloy, the effect of annealing on the Mössbauer spectra is rather subtle (or non-existent in the case of the Sn13 spectra measured at 295 K). Indeed, the evolution of the singlet component linked with the annealing of the stressed regions is not well resolved in the $Ni_{50}Mn_{37}Sn_{13}$ alloy. A definitive evolution from singlet-like spectra towards magnetic features is only seen in the ^{119}Sn-MS spectra measured at 77 K, Fig. 4.13.

The low resolution between the sextet and the singlet component in $Ni_{50}Mn_{37}Sn_{13}$ is a consequence of two factors. On the one hand, the low T_c of $Ni_{50}Mn_{37}Sn_{13}$, which is slightly above room temperature, implies that the magnetic features only emerge at very relatively low temperatures. Due to the metamagnetic character of Ni-Mn-Sn alloys, the magnetism of the martensite phase is lower than the austenite phase. As a result, the value of $\langle B_{hf} \rangle$[26] measured by ^{119}Sn-MS is much lower compared with the magnetic splitting observed in $Ni_{50}Mn_{35}Sn_{15}$ sample (see Fig. 4.7), thus hindering

[26]The magnetic component of both milled and annealed samples have been modeled considering an hyperfine field distribution. Thus, the value of average hyperfine field is represented as $\langle B_{hf} \rangle$.

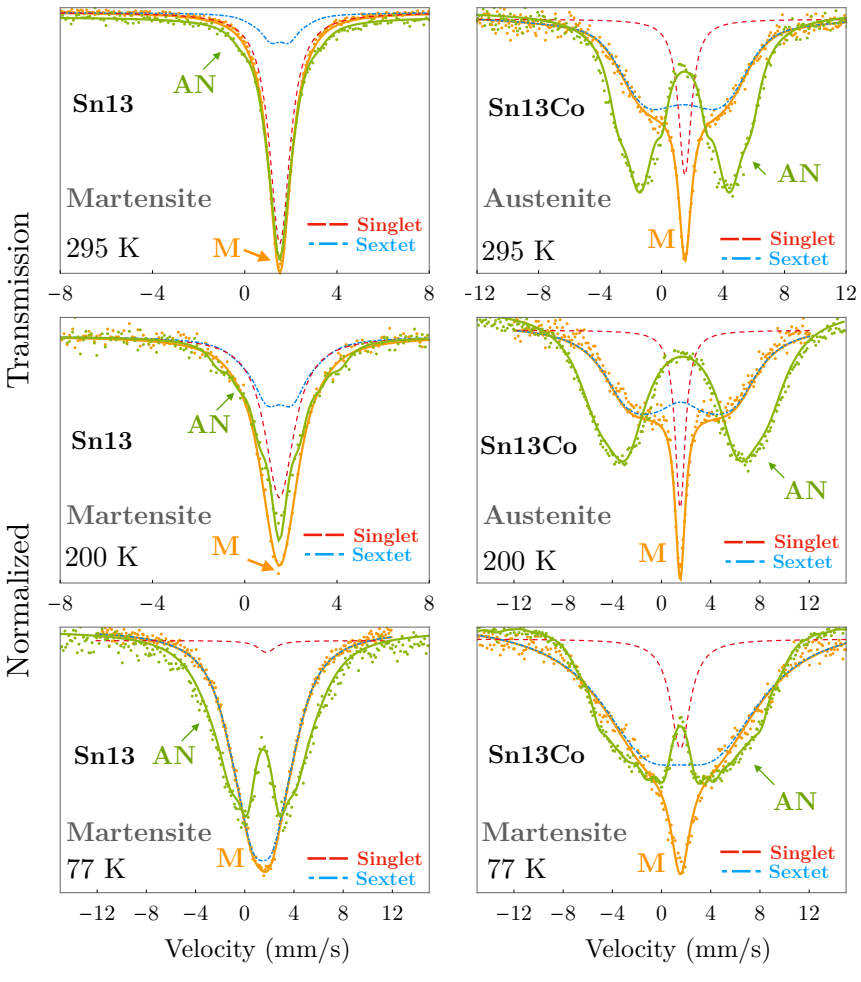

Figure 4.13: ^{119}Sn-MS spectra for the annealed (at 873 K during 5 minutes) and milled Sn13AN-Sn13M and Sn13CoAN-Sn13CoM samples recorded at 295 K, 200 K and 77 K. For a better visualization, subspectra obtained from the fitting are only displayed for the hand-milled samples.

the resolution between singlet and sextet components.

However, in the Co-doped alloy $\langle B_{hf} \rangle$ increases considerably with respect to the ternary alloy. As shown in Fig. 4.13, all spectra exhibit clear magnetic features. Regarding the spectra of Sn13CoM sample collected at 295 K and 200 K (Fig. 4.13), the singlet component related to the stressed regions can be clearly identified. When samples are annealed, the contribution of the singlet vanishes, which in turn, reinforces the magnetic component. Thus, by comparing Sn13CoM and Sn13CoAN sample, the reduction of the singlet component related to the stressed regions is clearly identified in the $Ni_{45}Co_5Mn_{37}Sn_{13}$ alloy. Even in the martensite phase, the

reduction of the singlet component is clearly observed, which is turn, is in line with the evolution of the ^{119}Sn-MS spectra observed for the ternary $Ni_{50}Mn_{35}Sn_{15}$ alloy (see Sec. 4.2.3). Thsee results demonstrates the capability of the ^{119}Sn-MS for tracking the evolution of the singlet component related to the stressed regions in Co doped Ni-Mn-Sn systems.

Even though the expected metamagnetic character that Co-doped Ni-Mn-Sn alloys exhibit, the magnetic splitting observed in Fig. 4.13 for the Sn13CoAN sample does not decrease substantially between the austenite phase (measured at 200 K) and the martensite phase (measured at 77 K). The magnetic nature of the martensite phase is expected to exhibit lower magnetism than the austenite phase (due to the magnetization discrepancy ΔM between two phases). However, ^{119}Sn-MS reveals a similar magnetic splitting for both austenite and martensite phases in the $Ni_{45}Co_5Mn_{37}Sn_{13}$ sample.

4.3.2 Magnetic and Neutron Diffraction Characterization

In order to evaluate the magnetization discrepancy between the austenite and martensite phases in $Ni_{45}Co_5Mn_{37}Sn_{13}$ sample, magnetic measurements have been carried out for both Sn13CoM and Sn13CoAN samples. Fig. 4.14 (left) shows the $M(T)$ thermomagnetization curves measured at 6 T. The upper part of the $M(H)$ cycles measured at austenite (225 K) and martensite (10 K) phases are shown in Fig. 4.14 (right).

The $M(T)$ evolution of Sn13CoM and Sn13CoAN samples shown in Fig. 4.14 con-

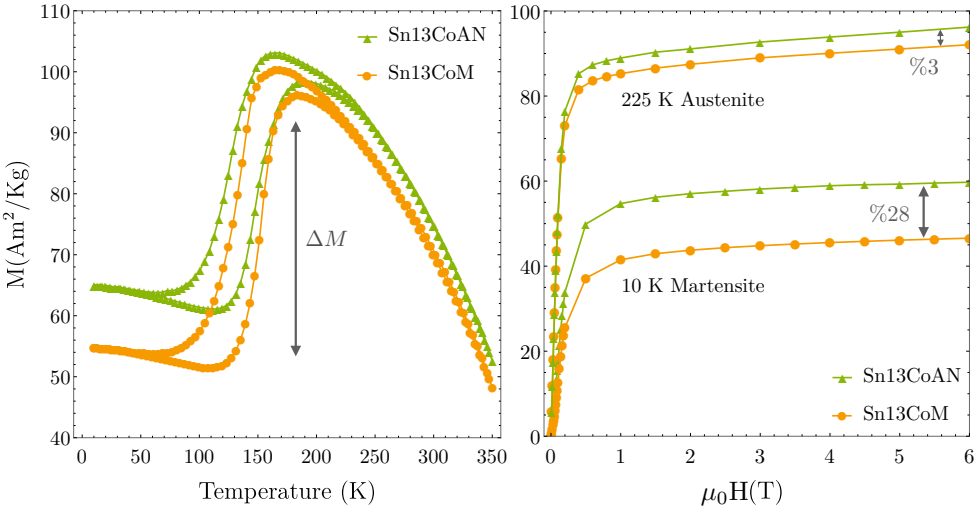

Figure 4.14: For both Sn13CoM and Sn13CoAN samples, $M(T)$ (FC-FH) thermomagnetization curves measured at 6 T (left) and the upper part of the $M(H)$ cycles (right) collected at 225 K (austenite) and 10 K (martensite) temperatures.

firms the enhanced metamagnetic character of the $Ni_{45}Co_5Mn_{37}Sn_{13}$ alloy. In fact, the magnetization of the martensite decreases significatively after the MT. The occurrence of the MT is evinced with the hysteresis that FC-FH curves show around 150 K. However, by comparing the magnetization jump between Sn13CoM and Sn13CoAN samples of Fig. 4.14 (left), the obtained ΔM in the milled sample is larger than the one obtained in the annealed sample. This behavior is opposite to what it is observed in the ternary $Ni_{50}Mn_{35}Sn_{15}$ alloy (see $M(T)$ curves measured at 6 T in Fig. 4.1).

The $M(H)$ curves shown in Fig. 4.14 (right) are in line with the previous description. The increase of M_s between Sn13CoM and Sn13CoAN samples is larger in the martensite phase than in the austenite phase. Indeed $\Delta M_s^{\text{aus}}/M_s^{\text{aus}} \approx \%3$, whereas $\Delta M_s^{\text{mart}}/M_s^{\text{mart}} \approx \%28$. Contrary to what happens in the ternary alloy of Sec. 4.2, the metamagnetic character is enhanced in the disordered $Ni_{45}Co_5Mn_{37}Sn_{13}$ alloy. Taking into account what was discussed in Sec. 4.2, a different magnetic moment coupling of Mn atoms could be the origin of the observed enhancement of ΔM in the Sn13CoM sample. In order to figure out the magnetic coupling in the quaternary alloy, PND measurements have been performed. The experimental PND spectra are gathered in Fig. 4.15.

The magnetic moment values obtained from the Rietveld refinement of the PND data are summarized in Table 4.4. On the one hand, in both, austenite and martensite phases the magnetic moment that contributes more is the one related to the Mn atoms, at $4a$ and $1a$, $1h$, $2n$, $2m$ positions respectively. However, by comparing the values of the magnetic moments obtained for the natural Sn position ($4b$ and $1b$, $1g$, $2m'$, $2n'$) in the ternary $Ni_{50}Mn_{35}Sn_{15}$ and quaternary $Ni_{45}Co_5Mn_{37}Sn_{13}$ alloys, an astonishing difference is observed.

Phase	Sample	$\mu_{4a}(\mu_B)$	$\mu_{4b}(\mu_B)$	$\mu_{8c}(\mu_B)$
$Fm\bar{3}m$	SnCo13M	3.119	1.145	0.56
Austenite	SnCo13AN	3.114	1.19	0.56
		$\mu_*(\mu_B)$	$\mu_\ddagger(\mu_B)$	$\mu_\dagger(\mu_B)$
P2/m	SnCo13M	2.47	-0.91	0.296
Martensite	SnCo13AN	2.505	-0.56	0.28

* $1a$, $1h$, $2n$, $2m$ ‡ $1b$, $1g$, $2m'$, $2n'$ † $2j$, $2k$, $4o$, $4o'$

Table 4.4: Magnetic moment values obtained from the Rietveld refinement of the PND data measured in Sn13CoM and Sn13CoAN samples.

In the case of the Milled $Ni_{50}Mn_{35}Sn_{15}$ sample (see Table. 4.2), the magnetic coupling between $4a$ and $4b$ positions in austenite phase is AF ($-0.45\mu_B$), while upon annealing, the magnetic coupling between $4a$ and $4b$ positions becomes FM ($0.37\mu_B$). However, in the quaternary alloy (see Table. 4.4), and even under the presence of strains, defects and stresses induced by milling, the magnetic coupling between the natural Sn and Mn positions is FM ($1.145\mu_B$). Moreover, upon annealing, the mag-

netic moment linked to the 4*b* positions in $Ni_{45}Co_5Mn_{37}Sn_{13}$ sample remains FM ($1.19\mu_B$). In fact, the value of the magnetic moment linked to 4*b* position do not evolve through annealing in the quaternary alloy. This fact explains the low recovery that M_s shows in the austenite phase between Sn13CoM and Sn13CoAN samples (see $M(H)$ curves of Fig. 4.14).

On the contrary, as shown in Table 4.4, the magnetic moment obtained for the natural Sn position of the martensite phase is negative for both the milled and annealed $Ni_{45}Co_5Mn_{37}Sn_{13}$ sample. However, the magnetic moment value linked

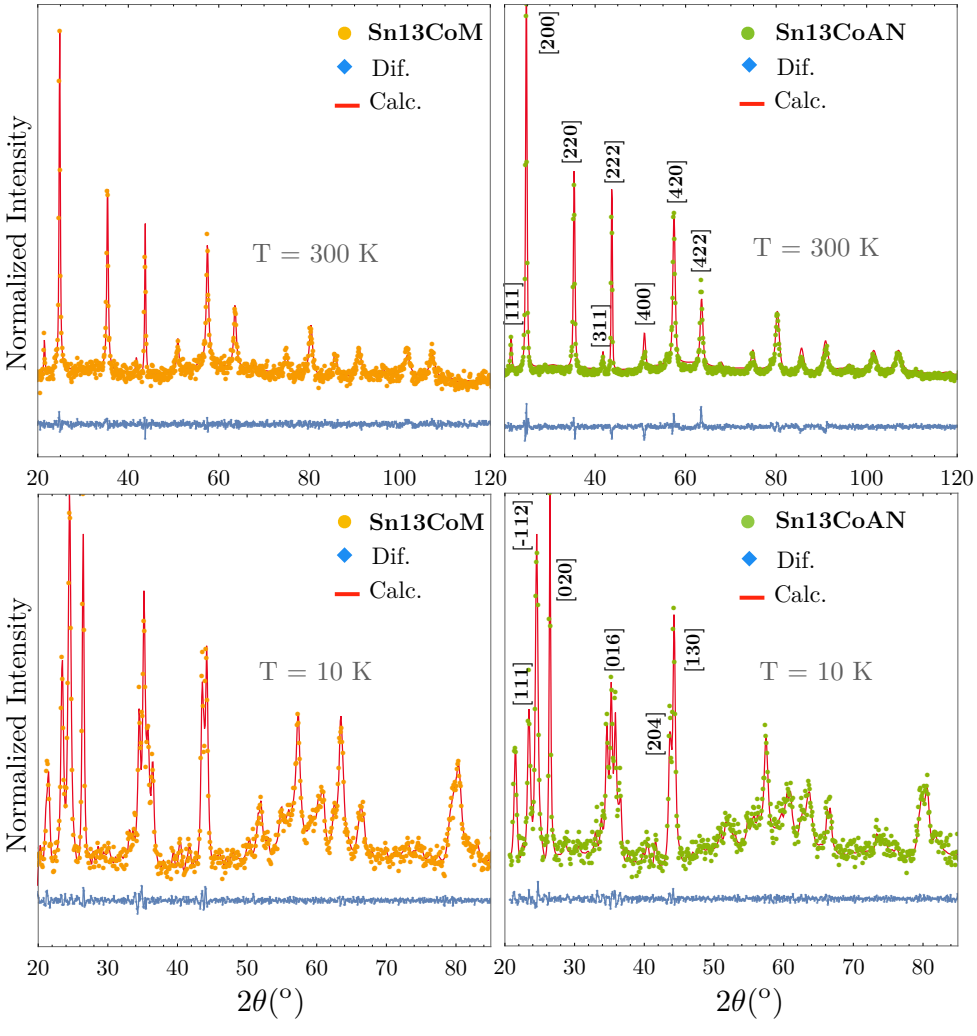

Figure 4.15: Neutron Diffraction Spectra for milled and annealed $Ni_{45}Co_5Mn_{37}Sn_{13}$ samples measured in the austenite (300 K) and martensite (10 K) phases.

to the Sn sites evolve from -0.91μ_B to -0.56μ_B upon annealing. In a nutshell, in the $Ni_{45}Co_5Mn_{37}Sn_{13}$ alloy, the local and overall magnetic moments of the austenite phase remain unaltered regardless of the annealing, whereas in the martensite phase a significant variation of the atomic moments is observed. As shown by the $M(T)$ curves of Fig. 4.14, the variation of the saturation magnetization M_s in the martensite phase is larger than the one corresponding to the austenite phase.

In line with the results of $Ni_{50}Mn_{35}Sn_{15}$ alloy, PND results confirm that neither the crystallographic structure nor lattice parameters nor long-range atomic order evolve upon annealing in the Co-doped quaternary alloy. Thus, according to the observed phenomena in Sec. 4.2, the evolution of the saturation magnetization and the magnetic moments in the martensite phase of $Ni_{45}Co_5Mn_{37}Sn_{13}$ sample, must be purely attributable to microstructural relaxations[64]. In the austenitic phase of the quaternary alloy, in turn, the presence of Co on the Ni sites, irrespectively of the presence of APB, makes the Mn atoms at the 4*a* and 4*b* sites to couple FM. As a result, the almost null evolution of the saturation magnetization in the austenite phase can be understood as a direct consequence of the ferromagnetic coupling between Mn atoms.

With respect to the martensitic phase, the change in the interatomic distances upon the MT makes the Mn atoms in the martensitic structure to couple antiferromagnetically or ferromagnetically depending on whether they are nearest or next-nearest neighbors, respectively. Therefore, the change on Mn-Mn distances associated to the presence of defects (or even to internal stresses) may explain the lower AF contribution in the Sn13CoAN sample, where the amount of defects is presumably lower than in the Sn13CoM sample.

4.3.3 MCE Evaluation in Ni-Mn-Sn-Co Samples

The magnetic measurements depicted in Fig. 4.14 indicate that the magnetic properties of the Sn13CoM and Sn13CoAN samples evolve in a different way in the martensite and austenite phases. The enhanced ΔM value that Sn13CoM sample shows compared with its annealed counterpart, may imply, in principle, a better MCE. Thus, in order to confirm the latter hypothesis, the MCE for Sn13CoM and Sn13CoAN samples has been evaluated following the approach described in Sec. 3.6.

According to the *Clausius-Clapeyron* equation the application of a magnetic field at temperatures close to MT may result in the induction of the MT, and therefore, in a magnetically induced entropy change i. e., a MCE. According to Eq. (3.11), the entropy change in isothermal conditions has been calculated by a numerical integration of $(\partial M/\partial T)$ from a set of magnetization versus temperature curves. The obtained MCE values for both Sn13CoM and Sn13CoAN samples are shown in Fig. 4.16.

The maximum value obtained under a magnetic applied field of 6 T are $\Delta S^{\mathrm{M}}_{\mathrm{iso}} = 8$ J/KgK and $\Delta S^{\mathrm{M}}_{\mathrm{iso}} = 6$ J/KgK for Sn13CoM and Sn13CoAN samples, respectively. This result suggest that the presence of defects, far from worsening, may be beneficial for MCE in metamagnetic Heusler alloys. Indeed, the higher entropy change in isothermal conditions obtained in the Sn13CoM sample must be a consequence of

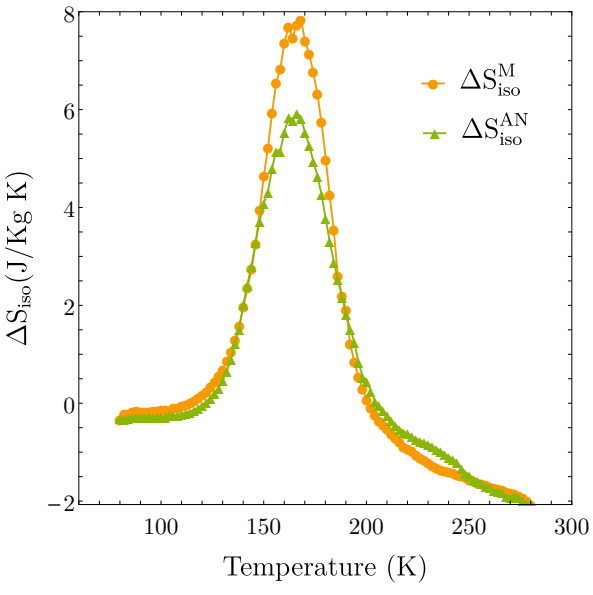

Figure 4.16: Isothermal magnetically-induced entropy change under 6 T applied magnetic field as a function of temperature for Sn13CoM and Sn13CoAN samples.

its higher intrinsic entropy change related to the occurrence of the MT. Due to the diffusionless character of the MT, the configuration contributions to the entropy change are absent in the fase transformation. Then, it is customary to consider that ΔS has three main contributions[180]:

$$\Delta S = \Delta S_{vib} + \Delta S_M + \Delta S_E \tag{4.4}$$

where ΔS_{vib} is the vibrational contribution, ΔS_M the magnetic contribution and ΔS_E the contribution of the conduction electrons. The electronic term is usually neglected, even more if the composition of the alloy is not modified[181]. Thus, the increase in ΔS can be ascribed to ΔS_{vib} and ΔS_M terms.

For the martensite to austenite transformation in metamagnetic shape memory alloys (in which $\Delta M > 0$), the vibrational and the magnetic contributions are positive and negative, respectively, being the vibrational one necessarily higher. Since ΔS_M is directly related to ΔM, and it is higher in the Sn13CoM sample, a higher magnetic contribution opposing the vibrational one, and therefore a lower ΔS, should be expected for the Sn13CoM sample. In this sense, the fact that ΔS is actually higher in the Sn13CoM sample results quite surprising. ΔS typically increases as a result of microstructural recovery brought by annealing in similar alloys[156]. Furthermore, it implies that ΔS_{vib} must be considerably higher in the Sn13CoM sample than in the Sn13CoAN. Taking into account that the crystallographic structures are exactly the same in both samples, and that just small differences related to microstructural defects are inferred from diffraction measurements, the obtained difference in ΔS_{vib}

points out a significant influence of such defects on the vibrational entropy of these alloys. All in all, the increase of the vibrational entropy change is a consequence of the much stronger influence of the induced defects on the vibrational entropy of the austenite than on the vibrational entropy of the martensite.

Finally, given the difficulty to modify the atomic order in the Ni-Mn-Sn system by means of conventional thermal treatments, the results in the ternary and quaternary alloys evince that, once the composition is fixed, the induction of microstructural defects can be an effective way to enhance the multifunctional properties of these alloys.

4.4 eMS Measurements in Ni-Mn-Z (Z = In, Sn)

The results of the previous sections confirm the important role that microstructural defects play on the tuning of the multifunctional properties in Sn containing Ni-Mn-based Heusler alloys. By tracking the non-magnetic component revealed by ^{119}Sn-MS, it is possible to quantify the whole contribution of defects and local stresses on the width of the MT. However, due to the fact that ^{119}Sn is the only Mössbauer active element in Ni-Mn-Z (Z = In, Sn) systems, the approach detailed in previous Sec. 4.2 and Sec. 4.3 could not be conducted in Ni-Mn-In ternary systems. With the aim of extending the Mössbauer study to Ni-Mn-In system, eMS measurements have been carried out at ISOLDE (CERN), where the investigated samples have been previously implanted with radioactive ions. The experimental work has been carried out under the IS578 project: *Atomic Scale Properties of Magnetic Mn-based Alloys Probed by Emission Mössbauer Spectroscopy*.

This technique consists in implanting specific radioactive ions in the sample, which act as the source in the emission Mössbauer experiments (the absorber is the detector). In the present case, the implanted ions are ^{57}Mn and ^{119}In radioactive ions. When the ions enter the solid, they are thermalized within few picoseconds. Regarding ^{57}Mn, the radioactive ions adopt the lattice location of Mn during their lifetime of 1.42 min[101]. Afterwards, they eventually decay to ^{57}Fe by β^- decay, which is the excited state of ^{57}Fe atom (Mössbuaer state). In the case of ^{119}In ion, a similar process takes place. With a half-life of 2.4 min, ^{119}In decays to the $3/2^+$ Mössbauer state of the ^{119}Sn (see Fig. 2.18).

The radioactive implantation of ^{57}Mn and ^{119}In ions, enables the characterization of the hyperfine parameters of Mn and In sites. Combining the implantation and eMS, it is possible to study dilute impurities (down to 10^{-4} at. %), which has obvious applications in the study of intrinsic properties of materials. In some cases one can also make use of the recoil of the daughter nucleus to study interstitial defects. When parent atoms are implanted, the low implantation fluence (dose $\propto 10^{12}$ ions/cm^2) ensures that segregation and/or precipitation is avoided.

4.4.1 eMS Measurements Followed by ^{57}Mn and ^{119}In Implantation

The radioactive ^{57}Mn and ^{119}In beams are produced at ISOLDE facility at CERN by proton-induced fission in a UC_2 target[27]. After the selective laser ionization stage, the ions are accelerated up to 50-60 keV, which enables obtaining a pure beam of about 10^8 ions/s. The implantation of radioactive ions takes place in a Mössbauer chamber. The radioactive beam incides at 30° from the sample surface normal and the detector is place at 60°. Regarding the velocity scale for ^{57}Fe-eMS and ^{119}Sn-eMS measurements, the values are given relative to α-Fe and $BaSnO_3$, respectively. The spectra have been fitted using VINDA program[104].

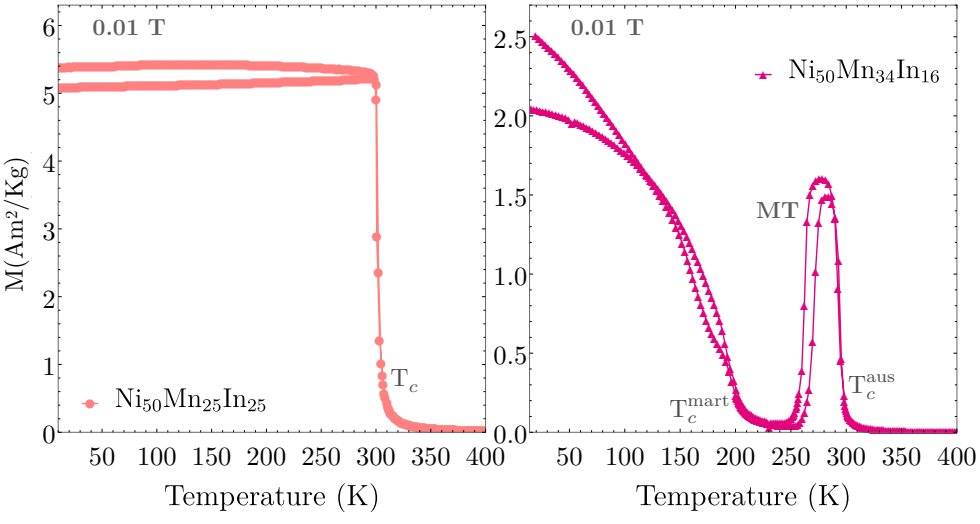

Figure 4.17: $M(T)$ curves (FC/FH) of $Ni_{50}Mn_{25}In_{25}$ (left) and $Ni_{50}Mn_{34}In_{16}$ samples (right).

Initially, with the aim of gaining insight about the influence of ^{57}Mn and ^{119}In ion implantation, eMS measurements have been conducted in the stoichiometric $Ni_{50}Mn_{25}In_{25}$ alloy, which is intended to use as a reference sample. As confirmed by the thermomagnetization curve shown in Fig. 4.17 (left), this sample do not exhibit the MT, and the sudden drop of the magnetization observed at 320 K is related to the magnetic transition taking place at T_c. In order to evaluate the effect of the implantation on the magnetic properties of the studied alloys, eMS experiments have been carried out above and below T_c.

The experimental and fitted ^{57}Fe and ^{119}Sn eMS spectra for $Ni_{50}Mn_{25}In_{25}$ are shown in Fig. 4.18. A successful fitting of the spectra has been obtained using a single broad non-magnetic (singlet) component. One of the most striking features is the resemblance that all spectra present regardless of the measurement temperature (above and below T_c). On the one hand, in accordance with what is expected for a PM austenite, the ^{57}Mn implanted $Ni_{50}Mn_{25}In_{25}$ sample exhibits a single emission

[27] A thorough description of the experiments is detailed in Sec. 2.4.4.

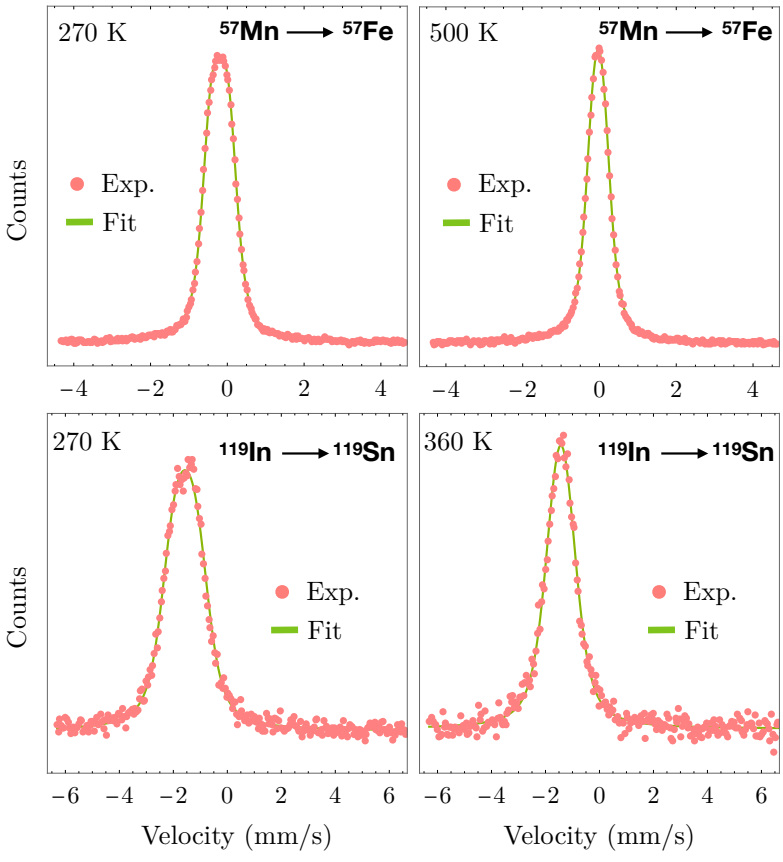

Figure 4.18: ^{57}Fe and ^{119}Sn eMS measurements in $Ni_{50}Mn_{25}In_{25}$ sample after ^{57}Mn (top row) and ^{119}In (bottom row) implantation.

line resembling to a singlet component (upper-right corner of Fig. 4.18). However, when the measurement is taken at 270 K, which is below T_c, the shape of the spectra remains the same. Apart from a slight variation on δ isomer shift, and on the width of the emission line, the spectrum taken at 270 K (upper-left corner of Fig. 4.18) does not show any magnetic features. Due to the strong FM nature of the $Ni_{50}Mn_{25}In_{25}$ sample, the eMS measurements should reveal substantial differences between the measurements taken above and below T_c.

On the other hand, as shown in the bottom row of Fig. 4.18, the temperature dependence of ^{119}In implanted $Ni_{50}Mn_{25}In_{25}$ sample follows the same trend. Again, the spectra recorded above and below T_c are identical, and theyt do not show any magnetic features. In this regard, and according to the Mössbauer result gathered in Sec. 4.2.3, one would expect to see a strong magnetic contribution in the ^{119}Sn-eMS experiments carried out in Ni-Mn-In systems.

In addition to the stoichiometric sample, a $Ni_{50}Mn_{34}In_{16}$ sample has been also investigated. As shown in Fig. 4.17 (right), this sample exhibits both MT and magnetic transition but structural and magnetic transition are overlapped. Below $T_c^{aus} = 300$ K, the magnetization starts decreasing along with the occurrence of the MT. Due to the metamagnetic nature of $Ni_{50}Mn_{34}In_{16}$ sample, the magnetization of the martensite decreases respect to the magnetization of the austenite phase. In further cooling, and below the magnetic transition of the martensite phase $T_c^{mart} = 200$ K, the magnetization increases. As a result, the sample brings the unique opportunity to study the magnetism of the martensite phases probed at both Mn and In sites.

The results of eMS following ^{57}Mn ion implantation in $Ni_{50}Mn_{34}In_{16}$ sample

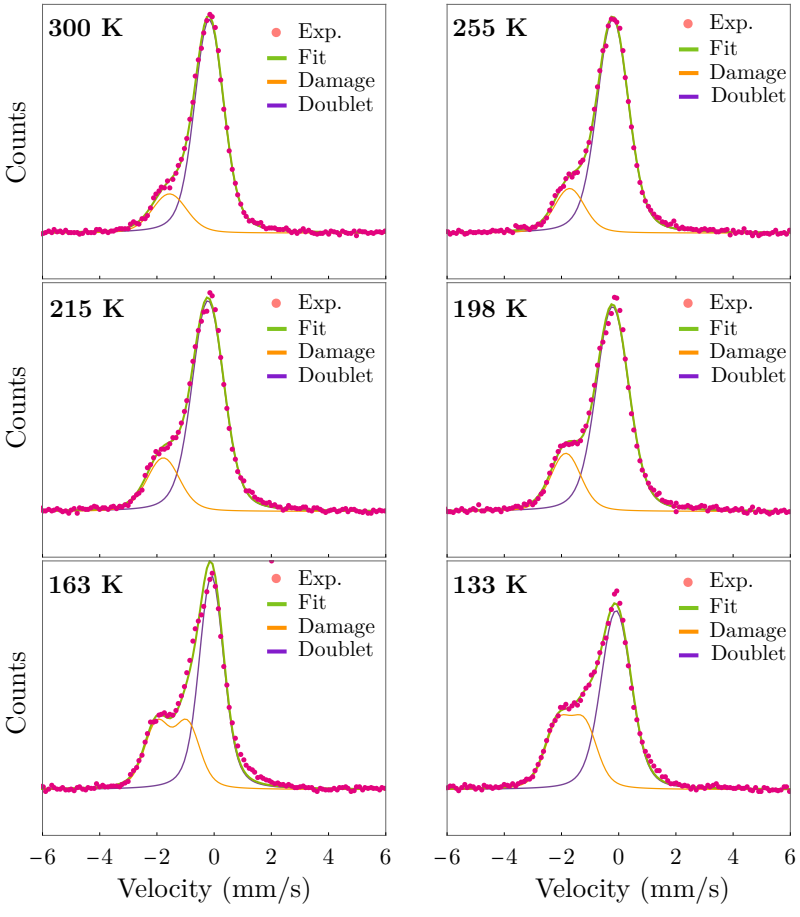

Figure 4.19: ^{57}Fe-eMS spectra for $Ni_{50}Mn_{34}In_{16}$ sample measured within the 133 - 300 K temperature range. The damage component is already visible at room temperature, which is better resolved while the temperature decreases.

are gathered in Fig. 4.19[28]. At room temperature, the spectrum exhibits a central emission line with a small shoulder at negative velocities around -2 mm/s. Although the eMS spectra show a clear evolution, none of them present clear magnetic features. Again, taking into account the magnetization curve of Fig. 4.17, one should expect to see substantial magnetic components throughout the covered temperature range.

In summary, the ^{57}Fe-eM and ^{119}Sn-eMS spectra obtained in $Ni_{50}Mn_{25}In_{25}$ and in $Ni_{50}Mn_{34}In_{16}$ samples do not exhibit any magnetic feature. These results may point out that ^{57}Fe and ^{119}Sn probe atoms are located in non-magnetic sites. In this connection, Khovaylo *et. al*[182] reported that when Fe atoms located at the natural Mn and In positions, Mössbauer spectra exhibit sextet-like features due to the hyperfine field that Fe atoms experience. Rayar *et. al*[183] also demonstrated the same effect when Fe is located at Ni sites. As a result, it is reasonable to asses that ^{57}Fe and ^{119}Sn probe atoms do not end up in substitutional sites.

In this connection, it has to be taken into account that the probe atoms may be located at interstitial sites. The interstitial atoms can be created because the direct implantation of the ion onto these sites, or more likely as a result of the following β^- decay that both ^{57}Mn and ^{119}In radioactive ions undergo. For instance, during the decay of ^{57}Mn, the daughter ^{57}Fe nucleus experience an average recoil of 40 eV, and may end up in interstitial sites.

On the other hand, the absence of magnetic features can be also explained by the damage that the implantation induces in the sample, giving rise to an amorphous-like region that surrounds the probe atom. The lattice may have not enough time or energy to recrystallize the distorted region induced during the implantation. As a result, the probe atom experience a disordered surrounding environment which ultimately explains the eMS spectra of Figs. 4.18 and 4.19. The contribution of the damage component to the eMS spectra have been studied in detail in previous works[98, 101].

The damage component exhibits a strong temperature-dependent annealing and is strongly reduced in spectra obtained at increasing temperatures. Previous investigations show that the probe atoms located at amorphous regions contribute as an asymmetric doublet. This component arises due to an average probing of different amorphous regions with somewhat different isomer shifts and quadrupole splittings[98]. Indeed, the shoulder that $Ni_{50}Mn_{34}In_{16}$ sample shows at -2 mm/s velocities can be attributed to the damage component, which in turn, leads to a good fitting of the experimental data (see Fig. 4.19). As expected, the intensity of the damage component increases while lowering the temperature. At lower temperatures, the lattice may have not enough time or energy to recover the damaged local structure, and the contribution of the damage component increases from 17 % at 300 K up to 40 % at 133 K. It is important to notice that the damage component is present even at room temperature, meaning that the implantation has to be performed at higher temperatures in order to enable a fast crystallization of the amorphous region.

The critical impact that the implantation has on the magnetic properties of the

[28]The eMS spectra of ^{119}In implanted $Ni_{50}Mn_{34}In_{16}$ sample exhibits similar features. Thus, the discussion have been focused on samples implanted with ^{57}Mn.

studied alloys is evinced in Fig. 4.20, where the transmission and emission Mössbauer measurements are comparatively displayed. Regarding the transmission ^{119}Sn-MS measurements in $Ni_{50}Mn_{25}Sn_{25}$ sample, a well defined sextet splitting can be observed at 77 K, which is in agreement with the FM nature of the austenite phase. However, in the ^{119}In implanted sample, the obtained eMS spectrum is drastically different. The eMS spectrum resembles more to a broad singlet spectrum rather than to a sextet. Regarding to $Ni_{50}Mn_{30}Sn_{20}$ sample, the same fact is observed. The magnetic contribution revealed by transmission ^{119}Sn-MS measurements is absent in the ^{119}Sn-eMS measurements.

The shape and features that eMS spectra show in the implanted samples can be understood considering the results obtained in Sec. 4.2.3. From the ^{119}Sn-MS

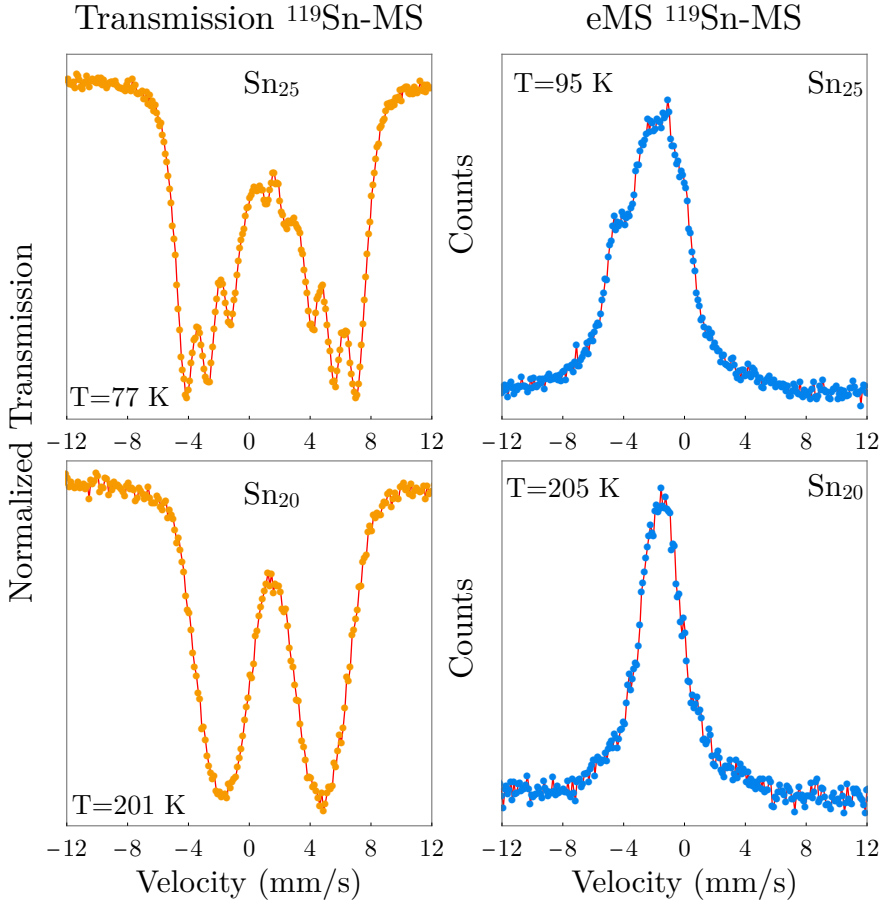

Figure 4.20: Comparison between the eMS measurements and transmission ^{119}Sn-MS experiments performed in $Ni_{50}Mn_{25}Sn_{25}$ and $Ni_{50}Mn_{30}Sn_{20}$ samples. As it is evinced, the damage induced by the implantation has a great impact on the structural and magnetic properties of these alloys.

measurements carried out in a ternary Ni-Mn-Sn sample, it has been demonstrated that the atomic scale magnetism is very sensitive to the microstructural defects, local stresses and strains. In the disordered samples, the Mössbauer spectra exhibit singlet-like features and the singlet component revealed by ^{119}Sn-MS is directly related to the stressed regions. In analog to milling process carried out in Sec. 4.2.3, the damage induced by the implantation acts in the same way. The stresses and strains field induced during the implantation affect the magnetic ordering surrounding the probe atom. As a result, the ^{57}Fe and ^{119}Sn eMS exhibit singlet-like features related to the distorted regions.

4.4.2 Future Works

In line with the conclusions of Sec. 4.2.3, the eMS results show that the implantation induces highly stressed regions which destroys the atomic scale magnetism. As a result, the implanted samples have to be subjected to annealing treatments in order to remove the implantation damage. Post-implantation annealing treatments will enable the probe atom to experience a well ordered surrounding lattice, which ultimately will enable a proper structural and magnetic characterization at atomic scale level. This fact is actually supported by preliminary quenching experiments (to liquid nitrogen) that have been performed after high temperature implantation. In fact, in quenched $Ni_{50}Mn_{25}Sn_{25}$ samples an enhancement of the magnetic component has been observed compared with the non-quenched samples. As the high temperature implantation enables an ultra-fast recovery of the lattice, it is assumed that the damage is instantaneously recovered. However, due to the limited lifetime of the parent nuclei, the obtained statistics were not enough to obtain definitive results. In this connection, the post-implantation annealing treatments are not feasible either. The half-life of ^{57}Mn and ^{119}In ions are 1.42 and 2.4 min respectively, which implies that in a matter of 1 h the sample can be considered as non-radioactive.

This handicap can be overcome by using long lived isotopes such as ^{119m}Sn and ^{57}Co, with a half-life of 293 days and 271 days respectively. Due to the long lifetime of these parent isotopes, annealing treatments can be performed without compromising the activity of the implanted samples. The preliminary tests that have been performed in ^{119m}Sn-implanted Ni-Mn-Sn samples confirm the suitability of this approach for eMS study on implanted Ni-based Heusler alloys.

5 Vacancy Defects in Ni-Mn-Z and Ni-Fe-Ga Alloys

The characteristic temperatures (T_{MT} and T_c) of the Ni-based Heusler alloys are dictated by the degree of the long-range atomic order. As discussed in Sec. 1.4.1, the variation of the $L2_1$ atomic order brought by quenching and by subsequent annealing enables shifts of T_{MT} up to 100 K. The observed evolution that T_{MT} and T_c exhibit upon annealing, is driven through the recovery of the long-range atomic order in some Ni-based Heusler alloys [49]. In contrast to the MT, which is a displacive phase transformation, the ordering process is mediated by atomic diffusion. In this connection, the most probable diffusion mechanism is the one which is mediated by vacancies [184]. As vacancies assist the diffusion, their evolution also dictates the ordering process, which ultimately affects the characteristic temperatures.

Several works have already suggested the potential role that vacancies may play on the MT and the magnetic properties of Ni-based Heusler alloys. Zhang *et al.* [185] suggest that the observed magnetic entropy change in Ni-Mn-Sn ribbons may be a consequence of the enhancement of the atomic order which may be due to the annealing of vacancies. Moreover, Zhou *et al.* [186] and Kustov *et al.* [187, 188] point out the potential role that vacancy defects could have on the pinning of the MT, whereas

Sánchez-Alarcos *et al.* [76] and Santamarta *et al.* [189] suggest different vacancy dynamics as responsible for the changes observed on the Curie's temperature T_c and T_{MT} in Ni-Mn-Ga and Ni-Fe-Ga alloys, respectively. In a recent work Hedayati *et al.* [190] claim that Sn vacancies in Ni-Mn-Sn systems can be used to obtain shifts on T_{MT} up to 80 K. However, none of the previous works contribute any experimental evidence on vacancies.

Thus far, the vast majority of works focused on the effect of vacancies in MT and magnetic properties of Ni-based Heusler alloys have been conducted within a the theoretical framework. For instance, from first principles calculations, Bai *et al.* [191, 192, 193] and Kulkova *et al.* [194, 195] calculated the formation energy of possible anti-site and vacancy defects on several Ni-based Heusler compounds. In recent works, by first principles calculations and Monte Carlo simulations, Kosogor *et al.* [196] and Wang *et al.* [197], respectively, link the vacancy concentration (C_v) with the ordering process and their effect on the shift of the T_{MT}. In this context, Tehrani *et al.* [198], by means of molecular dynamics simulations also suggest the potential effect that vacancies may have on T_{MT}. Despite the number of investigations suggesting the non-trivial role that vacancies may play in the MT, experimental works have been scarcely reported, the elusive nature of the vacancies' effect being the reason this is less investigated compared with other physical factors.

One of the most thorough studies has been performed by Merida *et al.* [79, 80]. By Positron Annihilation Lifetime Spectroscopy (PALS) they experimentally measure the C_v present in Ni-Mn-Ga single crystals and polycrystals. Depending on the composition, they report different equilibrium vacancy concentration, as well as different migration and formation energies of vacancies. Additionally, they show that with proper annealing treatments [79], C_v can be tuned from ≈2000 ppm down to 10 ppm. These works demonstrate the capability of PALS for the study of vacancy dynamics in Ni-based Heusler alloys. In fact, this technique has been widely used over decades and it is a powerful tool for defect characterization in metals [105]. As the positron lifetime is directly related to the electronic density of the material, crystal imperfections such as vacancy defects, alter significantly the surrounding electronic density. Thus, when positrons are trapped in such defects the positron lifetime varies, enabling a direct detection of vacancies.

In this chapter, vacancy-type defects are systematically investigated by PALS in Ni-Mn-In, Ni-Mn-Sn and in Ni-Mn-Ga systems. Additionally, the mutual dependence of the evolution of T_{MT} and C_v in a $Ni_{55}Fe_{17}Ga_{28}$ sample is additionally investigated. All the experimental measurements are complemented with Density Functional Theory (DFT) calculations of the positron lifetime. In order to establish the parametrization of the enhancement factor, which best suits the experimental PALS results in Ni-Mn based Heusler alloys and in Ni-Fe-Ga systems, five different widely used parametrizations have been also comparatively studied.

As will be seen, the results show that the Boronski-Nieminen parametrization gives the most accurate values for positron lifetimes, which, in turn, enables the identification of the Ni vacancy (V_{Ni}) as the vacancy type present in the Ni-Mn-Sn, Ni-Mn-In and Ni-Fe-Ga systems. Taking advantage of the existing PALS results in

Ni-Mn-Ga [79, 80], theoretical calculations have been carried out in Ni-Mn-Ga to test the agreement between calculations and experimental results. On the one hand, and contrary to what happens in Ni-Mn-Ga systems, results in Ni-Mn-Sn and in Ni-Mn-In systems show that the irreducible high C_v presents a handicap for its control by means of standard heat treatments. However, in the case of Ni-Fe-Ga systems, the direct relationship between vacancies and ΔT_{MT} is experimentally demonstrated. By means of quenching and annealing procedures, the transformation temperature is shifted up to 50 K, which is linked with the evolution of C_v. Additionally, it is also proven that the different evolution of the T_{MT} exhibited by samples quenched from $L2_1$ or B2 phases is linked with a different vacancy dynamics, evincing the capability of vacancies to control the atomic ordering process and ultimately, the fine tuning of the T_{MT} in these alloys.

5.1 Theoretical Calculations: Electron-Positron DFT Theory

In order to interpret the experimental PALS results, complementary theoretical positron lifetime calculations have been also performed. As electron-positron calculations are rooted in the DFT theory, in the following Section the basic method, principles and foundations of the DFT theory are briefly summarized.

5.1.1 Variational Method

The variational principle consists in employing a trial parametrized function, which maximizes or minimizes a certain relevant magnitude describing the studied system. In the quantum mechanic framework, the eigenstates and the corresponding eigenvalues of the ground state of a system can be calculated by means of variational methods. Starting from a plausible parametrized wave function (trial function), the value of the parameters are modified throughout a mathematical operation for the sake of minimizing the expectation values of a quantum mechanical system.

Let us assume that due to a non-trivial Hamiltonian $\hat{\mathcal{H}}$ it is not possible to obtain an analytical solution of its ground state energy and wave-functions. However, a physically representative parametrization of the ground state wave-function can be defined $|\widehat{0}(\lambda_1, \ldots, \lambda_n)\rangle$, where $\lambda_1, \ldots, \lambda_n$ represent the unknown parameters of the wave-function. Then, the main task of the variational principle consists in minimizing the

$$\overline{E} = \langle \widehat{0}(\lambda_1, \ldots, \lambda_n) | \hat{\mathcal{H}} | \widehat{0}(\lambda_1, \ldots, \lambda_n) \rangle \tag{5.1}$$

expression respect to $\lambda_1, \ldots, \lambda_n$ parameters, so

$$\frac{\partial \overline{E}}{\partial \lambda_1} = \frac{\partial \overline{E}}{\partial \lambda_2} = \cdots = 0. \tag{5.2}$$

The wave-function corresponding to the ground state of the systems is obtained by introducing the calculated values of $\lambda_1, \ldots, \lambda_n$[29]. It is important to notice that the energy of the ground state obtained from the variational method will be always, at least, equal or greater that the actual energy of the ground state. By definition, for a system defined by $\hat{\mathcal{H}}$, its ground state is the state with the lower possible energy

$$\hat{\mathcal{H}} |0\rangle = E_0 |0\rangle \tag{5.3}$$

while the possible excited states posses a higher energy

$$\hat{\mathcal{H}} |n\rangle = E_n |n\rangle \qquad E_n > E_0. \tag{5.4}$$

Due to the fact that the initial trial function $|\widehat{0}\rangle$ is in general distinct to the real wave function $|0\rangle$, the trial function can be expressed as a linear combination of the eigenstates of the $\hat{\mathcal{H}}$ Hamiltonian,

$$|\widehat{0}\rangle = \sum_{n=0}^{\infty} |n\rangle \langle n|\widehat{0}\rangle = \sum_{n=0}^{\infty} c_n |n\rangle. \tag{5.5}$$

In a hypothetical case in which the trial wave-functions results in the actual wave-function properly describing the ground state of the system, all $c_n = 0$ whereas $c_0 = 1$. The expectation value of the energy then:

$$\langle \widehat{0}|\hat{H}|\widehat{0}\rangle = |c_0|^2 E_0 + \sum_{n\neq 0} |c_n|^2 E_n \geq E_0. \tag{5.6}$$

Thus, the value of the energy cannot be underestimated and it is not possible to obtain a value of the energy, which is lower than the actual E_0 of the system.

5.1.2 Density Functional Theory DFT

Density Functional Theory (DFT) is an approach to compute the electronic structure of matter that is rooted in the variational method explained above. However, in DFT, the energy of the ground state of multielectronic atoms, compounds and molecules are obtained by minimizing the energy functional respect to the electronic density. In DFT, the characteristic magnitudes defining a systems are determined by functionals (functions that in turn, depend on other functions). Specifically, the implicit function that is used is the electronic density $n(\mathbf{r})$. The DFT theory is based in two theorems of Hohenberg-Kohn [199].

Theorem 5.1. (I. Hohenberg-Kohn Theorem) *For any system of interacting particles in an external potential $V_{ext}(\mathbf{r})$, the $n(\mathbf{r})$ electron density is uniquely determined. In other words, the external potential is a unique functional of the density.*

[29] The better the initial guess for the wave function, the more accurate the obtained result.

Theorem 5.2. (II. Hohenberg-Kohn Theorem) *A universal functional for the energy $E[n]$ can be defined in terms of $n(\mathbf{r})$. The exact ground state is the global minimum value of this functional.*

On the one hand, *I. Hohenberg-Kohn Theorem* dictates that if two systems are characterized by the same $n(\mathbf{r})$, then the potential of the two system only can differ in a constant. Additionally, *II. Hohenberg-Kohn Theorem* states that the energy of the ground state is a functional of the electron density.

In DFT, for a given electron density, the minimum energy is minimized relative to the parameters of the initial trial functions. Afterwards, taking into account that the electron density of the ground state is the one which minimizes the energy, $E_v[\widetilde{n}(\mathbf{r})]$ (the energy corresponding to the initial trial function) is minimized respect to $n(\mathbf{r})$. In this task is where DFT exploits its potential. Whereas in the conventional method, such as the Hartree-Fock method, the minimization has to be carried out in a $3N$ dimensional system, in DFT the ground state is obtained by minimizing $E_v[\widetilde{n}(\mathbf{r})]$.

5.1.3 Self-Consistent Kohn-Sham Equations

By means of the Kohn-Sham formalism [200], the real potential that takes into account all interaction terms, is replaced by an ideal system in which the electrons do not interact with each other and it is assumed that they all evolve under the presence of idealized $V_{ks}(\mathbf{r})$ potential. In the Hartree-Fock Formalism (not developed here), the $V_H(\mathbf{r})$ also comprehends the electron-electron interaction and as a result, it can be considered that all electrons move freely under the influence of $V_H(\mathbf{r})$ potential. The approach behind DFT is the same as the Hartree-Fock Formalism. For such a system characterized by $V(\mathbf{r})$ potential, the variational principle adopts the following form:

$$E_v[\widetilde{n}(\mathbf{r})] = \int V(\mathbf{r})\widetilde{n}(\mathbf{r})\mathrm{d}\mathbf{r} + T_s[\widetilde{n}(\mathbf{r})] \geq E_0 \tag{5.7}$$

where, $\widetilde{n}(\mathbf{r})$ and $T_s[\widetilde{n}(\mathbf{r})]$ are the electron density and the kinetic energy of the ground state (respectively) for noninteracting electron system. According to the *II. Hohenberg-Kohn Theorem*, the energy of the ground state is obtained by minimizing the energy functional. This minimization can be performed by applying the Lagrange multipliers method [201],

$$\delta E_v[\widetilde{n}] = \int \delta\widetilde{n}(\mathbf{r}) \left(V(\mathbf{r}) + \frac{\delta}{\delta\widetilde{n}(\mathbf{r})} T_s[\widetilde{n}(\mathbf{r})]|_{\widetilde{n}=n} - \epsilon \right) d\mathbf{r} = 0 \tag{5.8}$$

where ϵ is the Lagrange multiplier constant which ensures the conservation of the number of electrons N. Due to the fact that electrons move freely under the presence of a $V(\mathbf{r})$ potential, the ground state is obtained by solving the corresponding Schrödinger equation,

$$\left[-\frac{1}{2}\nabla^2 + V(\mathbf{r}) \right] |\Phi_i(r)\rangle = \epsilon_i |\Phi_i(r)\rangle . \tag{5.9}$$

However, this potential does not take into account the interaction energy. In the Kohn-Sham formalism, the interaction energy of the electrons is added as another functional within the $F[\widetilde{n}(\mathbf{r})]$ term. As a results, the later term is redefined as

$$F[n(r)] = T_s[\widetilde{n}(\mathbf{r})] + \frac{1}{2}\int \frac{\widetilde{n}(\mathbf{r}')\widetilde{n}(\mathbf{r})}{|\mathbf{r}'-\mathbf{r}|}\mathrm{d}\mathbf{r}\mathrm{d}\mathbf{r}' + E_{xc}[\widetilde{n}(\mathbf{r})] \tag{5.10}$$

The first term represents the kinetic energy of the independent electrons and the second term is the expression for $\hat{U}$ within the classical (or mean-field) approximation [201]. This term is the classical electrostatic energy (Hartree) and the last one, is the exchange-correlation functional. $E_{xc}[\widetilde{n}(\mathbf{r})]$ functional takes into account all the interactions that have been discarded when the real potential $V(\mathbf{r})$ has been substituted for the $V_{ks}(\mathbf{r})$ potential within the Kohn-Sham formalism. Apart form the Kinetic energy of the system, $E_{xc}[\widetilde{n}(\mathbf{r})]$ comprehends additional non-classical contribution of electron-electron interaction, such as the exchange-correlation energy. It is important to notice that if $E_{xc}[\widetilde{n}(\mathbf{r})]$ would be known in advance, DFT would predict the exact result of the systems. As a result, the modeling of this functional acquires the key relevance in DFT. Taking into account the definition of Eq. (5.10), Eq. (5.7) adopts the following form:

$$\begin{aligned} E_v[\widetilde{n}(\mathbf{r})] &= \int V(\mathbf{r})\widetilde{n}(\mathbf{r})\mathrm{d}\mathbf{r} + T_s[\widetilde{n}(\mathbf{r})] + \frac{1}{2}\int \frac{\widetilde{n}(\mathbf{r}')\widetilde{n}(\mathbf{r})}{|\mathbf{r}'-\mathbf{r}|}\mathrm{d}\mathbf{r}\mathrm{d}\mathbf{r}' \\ &+ E_{xc}[\widetilde{n}(\mathbf{r})] \geq E_0. \end{aligned} \tag{5.11}$$

In this case, the corresponding Euler-Lagrange equations for a given total number of electrons has the form [201],

$$\delta E_v[\widetilde{n}] = \int \delta\widetilde{n}(\mathbf{r}) \left(V_{ks}(\mathbf{r}) + \frac{\delta}{\delta\widetilde{n}(\mathbf{r})} T_s[\widetilde{n}(\mathbf{r})]|_{\widetilde{n}(\mathbf{r})=n(\mathbf{r})} - \epsilon \right) d\mathbf{r} = 0 \tag{5.12}$$

where the $V_{ks}(\mathbf{r})$ can be defined as,

$$V_{ks}(\mathbf{r}) = V(\mathbf{r}) + \int \frac{n(\mathbf{r}')}{|\mathbf{r}'-\mathbf{r}|}\mathrm{d}\mathbf{r}' + V_{xc}(\mathbf{r}) \qquad \text{where} \tag{5.13}$$

$$V_{xc}(\mathbf{r}) = \frac{\delta}{\delta\widetilde{n}(\mathbf{r})} E_{xc}[\widetilde{n}(\mathbf{r})]|_{\widetilde{n}(\mathbf{r})=n(\mathbf{r})}. \tag{5.14}$$

As a result, $V_{ks}(\mathbf{r})$ represent the effective potential in which the electrons move freely. In this connection, it is noteworthy to mention that Eq. (5.8) and Eq. (5.12) are mathematically identical, and in the Kohn-Sham formalism electrons move freely in $V_{ks}(\mathbf{r})$ potentials instead of moving in a real potential $V(\mathbf{r})$. The electronic density of the system can be calculated by solving the Schrödinger equation,

$$\left[-\frac{1}{2}\nabla^2 + V_{ks}(\mathbf{r}) \right] |\Phi_i(\mathbf{r})\rangle = \epsilon_i |\Phi_i(\mathbf{r})\rangle \tag{5.15}$$

where

$$n(\mathbf{r}) = \sum_{i=1}^{N} |\,|\Phi_i(\mathbf{r})\rangle\,|^2 \quad \text{and} \quad V_{ks}(\mathbf{r}) = V(\mathbf{r}) + \int \frac{n(\mathbf{r}')}{|\mathbf{r}-\mathbf{r}'|}\mathrm{d}\mathbf{r}' + V_{xc}(\mathbf{r}). \tag{5.16}$$

Finally, combining the theorems of Hohenberg-Kohn and the Kohn-Sham formalism, the energy of the ground state can be obtained by means of

$$E_0 = \sum_i \epsilon_i + E_{xc}[n(\mathbf{r})] - \int V_{xc}(\mathbf{r})n(\mathbf{r})\mathrm{d}\mathbf{r} - \frac{1}{2}\int \frac{n(\mathbf{r})n(\mathbf{r}')}{|\mathbf{r}-\mathbf{r}'|}\mathrm{d}\mathbf{r}\mathrm{d}\mathbf{r}'. \tag{5.17}$$

Eq. (5.15), Eq. (5.16) and Eq. (5.17) are know as the Self-Consistent Kohn-Sham Equations.

5.1.4 Approximations of $E_{xc}[n(\mathbf{r})]$

The success of the DFT calculations rely on the employed approximation for $E_{xc}[n(\mathbf{r})]$. Depending on the physical system, several specific approximation can be found. However, the most widely used expression adopts the quasi-local form that reads

$$E_{xc}[n(\mathbf{r})] = \int e_{xc}\left(\mathbf{r}; [\widetilde{n}(\mathbf{r})]\right) n(\mathbf{r})\mathrm{d}\mathbf{r}, \tag{5.18}$$

where $e_{xc}\left(\mathbf{r}; [\widetilde{n}(\mathbf{r})]\right)$ represents the exchange-correlation energy. This term is in turn defined as a functional of $\widetilde{n}(\mathbf{r})$, which depends on the density at $\widetilde{r}$ position near r.

- **Local Density Approximation (LDA):** The idea behind the LDA model is to take the known result of an uniform electron gas system and apply it locally to a non-homogeneous system. In such approximation Eq. (5.18) turns into:

$$E_{xc}^{LDA} = \int e_{xc}[n(\mathbf{r})]n(\mathbf{r})\mathrm{d}\mathbf{r} = -\frac{3q^2}{4}\left(\frac{3}{\pi}\right)^{1/3}\int n(\mathbf{r})^{4/3}\mathrm{d}\mathbf{r} \tag{5.19}$$

  Although no explicit expression is known for the correlation potential, LDA provides accurate results in systems whith smooth variation of the electron density. In addition, highly accurate numerical Quantum Monte-Carlo simulations of the homogeneous electron gas are available for its modelization [202]. However, LDA fails in systems where the electron-electron interaction becomes strong, such as in heavy fermionic systems.

- **Generalized Gradient Approximation (GGA):** Due to the fact that in several systems, such as molecules, the electron density can vary rapidly over small regions of space, in the GGA model, the effects of the non-local uniform

electron density are taken into account. In GGA the $E_{xc}[n(\mathbf{r})]$ functional depends on both the density and the gradient of the density and in general is described as

$$E_{xc}^{GGA} = \int f(n(\mathbf{r}), \nabla n(\mathbf{r}))\mathrm{d}\mathbf{r} \tag{5.20}$$

The most popular parametrizations of GGA are the ones developed by Perdew, Burke and Ernzerhof [203] and Becke, Lee, Yan and Parr [204].

- In the present thesis, the theoretical calculations of the positron lifetime have been performed within the LDA and GGA approximations. However, additional approximations such as the Gradient Expansion Approximation (GEA), Meta-GGA, Exact Exchange (EXX) and Hybrid Functionals are also widely employed.

5.1.5 Positron Annihilation Lifetime Calculations

In order to complement the experimental PALS results, theoretical calculations of the positron lifetimes have been conducted using a two component density functional theory (TCDFT) [205, 206]. TCDFT is an extension of previously developed Kohn-Sham formalism where the total energy of the system is written now as a functional of both electron $n_-(\mathbf{r})$ and positron density $n_+(\mathbf{r})$. As a result, the kinetic energy, potential and the exchange-correlation functionals depend not only in $n_-(\mathbf{r})$ but also in $n_+(\mathbf{r})$. Thus, an additional term named electron-positron correlation functional is introduced. In TCDFT the total energy of the system can be written as a functional of the electron $\widetilde{n}_-(\mathbf{r})$ and positron $\widetilde{n}_+(\mathbf{r})$ density, and Eq.(5.11) turns into,

$$\begin{aligned}
E_v[\widetilde{n}_-(\mathbf{r}), \widetilde{n}_+(\mathbf{r})] &= \int V_{ks}(\mathbf{r})[\widetilde{n}_-(\mathbf{r}) - \widetilde{n}_+(\mathbf{r})]\mathrm{d}\mathbf{r} - \int \frac{\widetilde{n}_-(\mathbf{r}')\widetilde{n}_+(\mathbf{r})}{|\mathbf{r}' - \mathbf{r}|}\mathrm{d}\mathbf{r}\mathrm{d}\mathbf{r}' \\
&+ \frac{1}{2}\int \frac{\widetilde{n}_-(\mathbf{r}')\widetilde{n}_-(\mathbf{r})}{|\mathbf{r}' - \mathbf{r}|}\mathrm{d}\mathbf{r}\mathrm{d}\mathbf{r}' + \frac{1}{2}\int \frac{\widetilde{n}_+(\mathbf{r}')\widetilde{n}_+(\mathbf{r})}{|\mathbf{r}' - \mathbf{r}|}\mathrm{d}\mathbf{r}\mathrm{d}\mathbf{r}' \\
&+ E_{xc}[\widetilde{n}_-(\mathbf{r})] + E_{xc}[\widetilde{n}_+(\mathbf{r})] + E_{xc}^{-+}[\widetilde{n}(\mathbf{r})] \qquad (5.21) \\
&+ T_s[\widetilde{n}_-(\mathbf{r})] + T_s[\widetilde{n}_+(\mathbf{r})] \qquad (5.22)
\end{aligned}$$

where $E_{xc}^{-+}[\widetilde{n}(\mathbf{r})]$ is the electron-positron correlation energy functional. Applying the variational method, the equation is iteratively resolved and the wavefunctions and eigenvalues are obtained. Regarding the calculation of the positron lifetime, the annihilation rate λ, (i.e., the inverse of the τ positron lifetime) is evaluated by overlapping the positron density $n_+(\mathbf{r})$ and the electron density of the solid $n_-(\mathbf{r})$ as

$$\lambda = \tau^{-1} = \pi c r_o^2 \int n_+(\mathbf{r}) n_-(\mathbf{r}) \gamma(\mathbf{r})\mathrm{d}\mathbf{r} \tag{5.23}$$

where c is the speed of light in vacuum, r_0 the classical electron radius and $\gamma(\mathbf{r})$ the so-called enhancement factor that comprises the enhanced electron density due to the Coulombic attraction exerted by e^+. The positron lifetime for the perfect (i. e., bulk lifetime) and defected lattice has been calculated with the Atomic Superposition Approximation Method (AT-SUP) [207], which provides values in good agreement with the experimental positron lifetimes values in metals and in semiconductors [123, 208, 209, 210]. The electron density $\mathrm{n}_-(\mathbf{r})$ of the crystal and the crystalline Coulomb potential $V_c(\mathbf{r})$ are constructed by adding individual atomic charges $n_-^{at}(|\mathbf{r}-\mathbf{R}_i|)$ and $V^{at}(|\mathbf{r}-\mathbf{R}_i|)$ potentials over the $\mathbf{R}_i$ occupied atomic sites. Finally, the potential felt by the positron $V_+(\mathbf{r})$ is evaluated by adding the positron-electron correlation potential $V_{corr}[n_-(\mathbf{r})]$ to the Coulombic potential, so that

$$V_+(\mathbf{r}) = V_c(\mathbf{r}) + V_{corr}\left[n_-(\mathbf{r})\right] \tag{5.24}$$

$$= \sum_i V^{at}\left(|\mathbf{r}-\mathbf{R}_i|\right) + V_{corr}\left[\sum_i n_-^{at}(|\mathbf{r}-\mathbf{R}_i|)\right]. \tag{5.25}$$

The enhancement factor of Eq. (5.23) and the correlation potential of Eq. (5.25) have been taken into account within the (*i*) local density approximation (LDA) and (*ii*) Generalized Gradient Approximation (GGA) frameworks.

Within the LDA approximation, the $V_{corr}[n_-(\mathbf{r})]$ has been modeled using the interpolation formula proposed by Boronski and Nieminen [211], which is based on the results of Arponen and Pajanne [212]. For modeling $\gamma(\mathbf{r})$, three different parametrizations have been used. The first is the expression proposed by Boronski and Nieminen [211], which is based on the many-body calculations by Lantto [213] (labeled as LDA-BN),

$$\gamma(\mathbf{r})^{\mathrm{BN}}_{\mathrm{LDA}} = 1 + 1.23r_s + 0.8295r_s^{3/2} - 1.26r_s^2 + 0.3286r_s^{5/2} + \frac{1}{6}r_s^3 \tag{5.26}$$

where $r_s = (3/4\pi n_-)^{1/3}$. The other two expressions suggested by Barbiellini *et al.* [214] are based on results of Arponen and Pajanne [212] and labeled as LDA-AP1

$$\gamma(\mathbf{r})^{\mathrm{AP1}}_{\mathrm{LDA}} = 1 + 1.23r_s - 0.0742r_s^2 + \frac{1}{6}r_s^3 \tag{5.27}$$

and LDA-AP2

$$\gamma(\mathbf{r})^{\mathrm{AP2}}_{\mathrm{LDA}} = 1 + 1.23r_s - 0.91657r_s^{3/2} + 1.0564r_s^2 - 0.3455r_s^{5/2} + \frac{1}{6}r_s^3. \tag{5.28}$$

Within the GGA approximation, both correlation potential and the enhancement factor have been taken into account using the expression employed by Barbiellini *et al.* [209, 214] (based on results of Arponen and Pajanne [212]). Regarding $\gamma(\mathbf{r})_{\mathrm{GGA}}$, it is deduced from the enhancement factor obtained within LDA. Within

GGA, the effects of the non-uniform electron density are modeled by a parameter $\epsilon = |\Delta \ln n_-|^2 / q_{TF}^2$ which describes the reduction of the screening cloud close to the positron, q_{TF} being the local Thomas-Fermi screening length. Finally, an adjustable parameter α is also introduced, so the corrected enhancement factor then reads,

$$\gamma(\mathbf{r})_{\mathrm{GGA}} = 1 + (\gamma(\mathbf{r})_{\mathrm{LDA}} - 1)\, e^{-\alpha\epsilon}. \tag{5.29}$$

The value of α is set to be $\alpha = 0.22$, which has been proven to give lifetimes for different types of metals and semiconductors in good agreement with experimental results [214]. For GGA calculations, two parametrizations for the $\gamma(\mathbf{r})_{\mathrm{GGA}}$ of Eq. (5.29) have been used: (*i*) the expression of Eq. (5.27) (labeled as $\gamma(\mathbf{r})^{\mathrm{AP1}}_{\mathrm{GGA}}$) and (*ii*) the expression of Eq. (5.28) (labeled as $\gamma(\mathbf{r})^{\mathrm{AP2}}_{\mathrm{GGA}}$). It is noteworthy to mention that when $\alpha \to 0$ the Eq. (5.29) turns into $\gamma(\mathbf{r})_{\mathrm{GGA}} = \gamma(\mathbf{r})_{\mathrm{LDA}}$.

5.2 PALS in Ni-Mn-Ga, Ni-Mn-In and Ni-Mn-Sn Alloys

5.2.1 Experimental Procedure

$Ni_{50}Mn_{50-x}Sn_x$ (x = 25, 20, 15, 13, 10) and $Ni_{50}Mn_{50-x}In_x$ (x = 25, 20, 16, 13) (Sn_x and In_x respectively) polycrystalline ingots have been synthesized from high purity elements by the arc melting method under a protective argon atmosphere (see Sec. 2.1.1). Each initial ingot is remelted up to eight times to ensure the homogeneity. Afterwards, Sn_x and In_x samples are homogenized at 1173 K during 24 h. Regarding Sn_x samples, a further annealing of 4 h at 1273 K is performed to avoid dendritic structures [82]. Bulk pieces for the initial characterization are obtained from the center of each ingot by cutting small pieces using a low speed diamond saw. The initial characterization consists in EDX analysis and differential scanning calorimetric measurements (DSC) carried out in a TA Q100 DSC, by which the composition and the characteristic T_{MT} and Curie's T_c temperatures are determined. The results of the initial characterization are gathered in Table 2.2, which are consistent with previous experimental reports [44, 16].

Subsequently, Sn_x and In_x samples are quenched from 1173 K into iced water (AQ state). In order to ensure thermal equilibrium, samples are kept at 1173 K during 30 min before quenching. The study of the microstructural evolution of vacancy defects upon post quenching has been performed using the approach employed in Ref. [79]. In essence, the samples are subjected to the so-called isochronal annealing cycles. Quenched samples are heated up at a constant rate of 10 K/min to a maximum temperature (T_i), which in turn is successively increased from 473 K to 873 K in 50 K steps. Afterwards, the sample is cooled down to the initial temperature at the same rate.

After each isochronal annealing cycle, PALS measurements are carried out at room temperature using a fast-fast timing coincidence spectrometer of 250 ps resolution at FWHM. H1949-50 Hamamatsu photomultiplier tubes are equipped with BC-442 plastic scintillators in a collinear geometry. A 20μCi ^{22}NaCl positron source covered in Kapton© is sandwiched by a pair of identical samples. All spectra have been collected with more than 3×10^6 counts and analyzed with the POSITRONFIT [118] code. The analysis has been performed subtracting the source contribution, which consists of two components. The first is a component with a lifetime $\approx$ 1500 ps [121, 122] and a measured average intensity of 2.5 %. The second component, with an intensity of $\approx$ 13 %, is related to the positron annihilation in the 7.5 μm thick Kapton© foil that wraps the ^{22}NaCl positron source. The characteristic positron lifetime in Kapton© has a very well-known value of 382 ps [119, 120]. The obtained χ^2 values have been kept below 1.2 in all fittings.

5.2.2 Experimental Results

Fig. 5.1 and Fig. 5.2 show the experimental positron average lifetime ($\overline{\tau}$) values measured for both Sn_x and In_x series (respectively) as a function of T_i. The first point of PALS measurements corresponds to the AQ $\overline{\tau}$ value. In both set of samples, the AQ state ranges between 181 - 187 ps. The quenching procedure has been repeated more than three times resulting in identical results. In order to study the dynamics of vacancies induced during the quenching procedure, AQ samples have been subjected to isochronal annealing cycles. In both Sn_x and In_x systems, apart from slight fluctuations of 2 - 3 ps, $\overline{\tau}$ remains almost constant regardless of the T_i. Only In_{16} and Sn_{15} samples show a significant drop of $\overline{\tau}$. This drop takes place at 773 K and 573 K temperatures respectively, approaching the $\approx$ 178 ps value. However, this drop is rapidly recovered during the next isochronal annealing cycle and finally, $\overline{\tau}$ increases back to its initial AQ's value. The observed moderate evolution of $\overline{\tau}$ can be understood by the physics governing the positron trapping at defects.

When a positron enters a solid, it thermalizes and diffuses through the lattice, until eventually the positron gets annihilated with a surrounding electron. In a defect-free lattice, the positron annihilates from the delocalized state (i. e., Bloch state) at an average λ_b rate, or with a characteristic τ_b lifetime (bulk lifetime). However, when open volume defects are present they may act as positron trapping centers. Actually, in the specific case of vacancy defects they act as deep traps for positrons due to the lack of the positive ion. The trapping occurs when a positron turns from the Bloch state into a localized state within a vacancy (i.e., the positron wave function becomes localized at the vacancy). The lack of the ion, leaves behind an open volume that in turn, is characterized by a lower electron density compared with the perfect lattice.

As shown in Eq. (5.23), the lower the electron density is, the lower is λ. Thus, positrons trapped at vacancies annihilate from a localized state at an average rate $\lambda_v < \lambda_b$, thus exhibiting a longer vacancy-related positron lifetime τ_v, where $\tau_v > \tau_b$. As a result, the moderate variation of $\overline{\tau}$ shown in Fig. 5.1 and Fig. 5.2 can be explained considering two different scenarios. On the one hand, the lack of open-

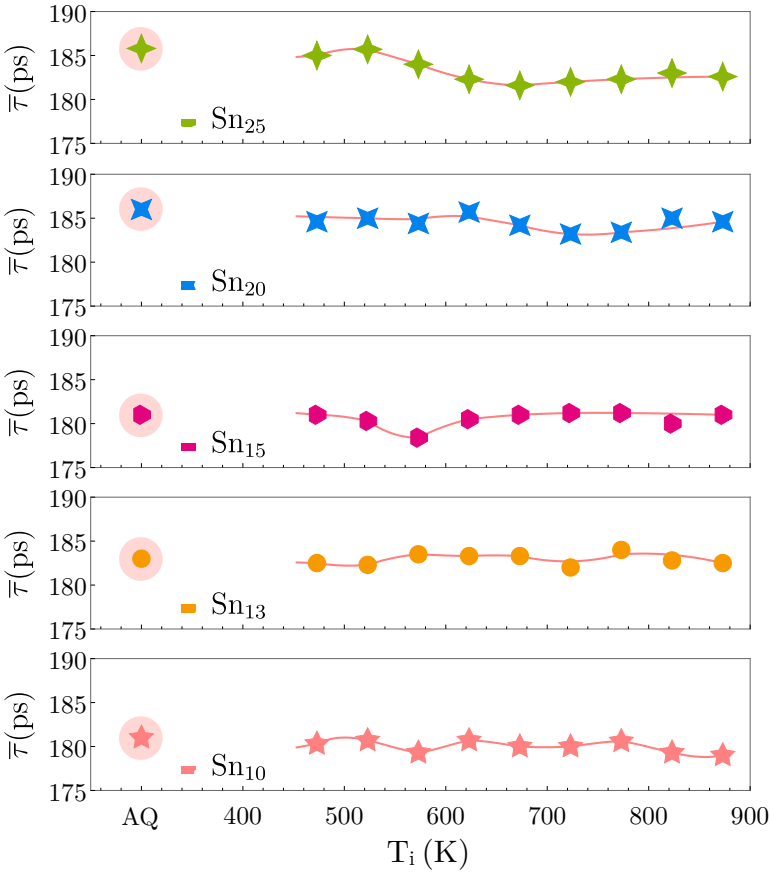

Figure 5.1: Experimental average positron lifetime $\overline{\tau}$ values for Sn_x set of samples. The red shaded points correspond to $\overline{\tau}$ value measured in the as-quenched state. The remaining points correspond to $\overline{\tau}$ values as a function of T_i of isochronal annealing cycles. The joint line is a guide for the eye. Experimental errors lie within the markers size.

volume defects (e. g., vacancies) would imply that all positrons only annihilate from the delocalized state or bulk state. Then, the measured lifetime would reflect the lifetime related to the bulk lifetime, τ_b. On the other hand, due to a high C_v retained during quenching, the contribution of the positrons annihilated from vacancies could become the one dominating $\overline{\tau}$, overcoming the contribution of positrons annihilated from the delocalized state (i. e., bulk). In such scenario, the measured lifetime would reflect the characteristic positron lifetime τ_v related to the present vacancy defect.

Even though the decomposition of the spectra would provide valuable information about different contributions of $\overline{\tau}$, unfortunately the spectra could not be decomposed in none of the Sn_x and In_x samples. As will be discussed further below, the saturation-trapping regime of vacancies hinder the decomposition of the decay spec-

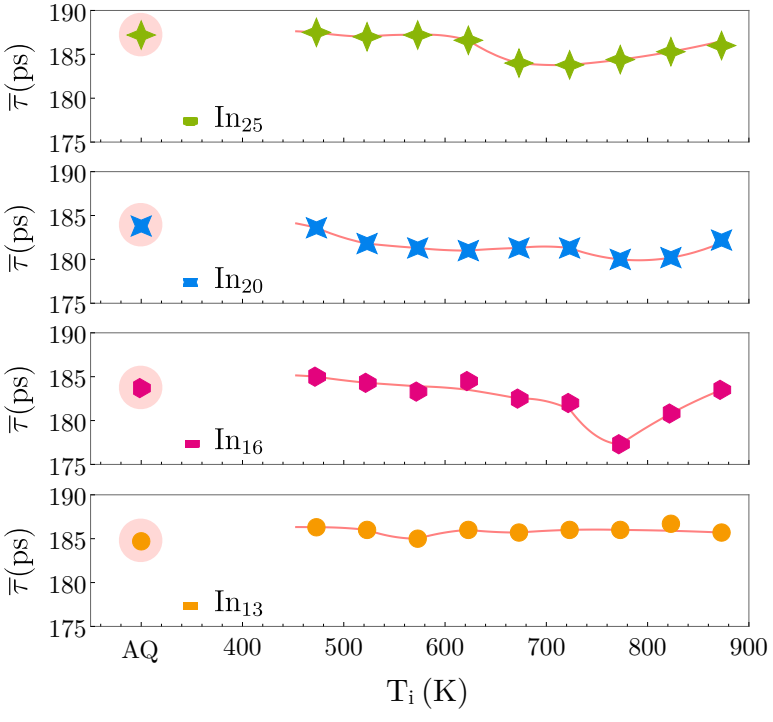

Figure 5.2: Experimental average positron lifetime $\overline{\tau}$ values for In_x set of samples. The red shaded points correspond to $\overline{\tau}$ values measured in the as-quenched state. The remaining points correspond to $\overline{\tau}$ values as a function of T_i of isochronal annealing cycles. The joint line is a guide for the eye. Experimental errors lie within the markers size.

trum of positrons. However, $\overline{\tau}$ is the statistically most accurate parameter in PALS experiments, and along with theoretical calculations, it provides information for data interpretation in cases where the experimental data cannot be decomposed [215]. In order to find out whether the measured lifetime is related to the bulk lifetime or with the presence of vacancy defects, experimental results have been complemented with theoretical DFT electron-positron calculations.

5.2.3 DFT Electron-Positron Results in Ni-Mn-In and Ni-Mn-Sn Alloys

Positron lifetime calculations have been conducted for all Sn_x and In_x samples. Even though the sample $Ni_{50}Mn_{40}In_{10}$ has not been synthesized and experimentally measured by PALS, this composition has been added to the calculations in order to complete the theoretical study. The crystallographic data used in the calculations are shown in Table 5.1. The simulated structure for each sample has been chosen according to the proper phase at room temperature. Samples without MT and samples with T_{MT} < room temperature (Sn_{25}, Sn_{20}, In_{25}, In_{20} and Sn_{15}, In_{16}) have

Crystallographic Data			
Label	Lattice Parameters (Å)	Simulated Phase	Ref.
Sn_{25}	$a = b = c = 6.046$	$Fm\overline{3}m$	[16]
Sn_{20}	$a = b = c = 6.024$	$Fm\overline{3}m$	[16]
Sn_{15}	$a = b = c = 5.995$	$Fm\overline{3}m$	[16]
Sn_{13}	$a = 4.317\ b = 5.621\ c = 4.361$	Pmma	[45]
Sn_{10}	$a = 4.333\ b = 5.570\ c = 4.281$	P2/m	[16]
In_{25}	$a = b = c = 6.071$	$Fm\overline{3}m$	[44]
In_{20}	$a = b = c = 6.031$	$Fm\overline{3}m$	[44]
In_{16}	$a = b = c = 6.004$	$Fm\overline{3}m$	[44]
In_{13}	$a = 4.391\ b = 5.620\ c = 4.331$	P2/m	[46]
In_{10}	$a = 4.284\ b = 5.811\ c = 4.301$	P2/m	[44, 46]

Table 5.1: Crystallographic data employed in AT-SUP calculations of the studied $Ni_{50}Mn_{50-x}Sn_x$ ($x = 25, 20, 15, 13, 10$) and $Ni_{50}Mn_{50-x}In_x$ ($x = 25, 20, 16, 13, 10$) samples.

been simulated by using the cubic $L2_1$ austenite structure. Regarding the calculations of the martensite phase, most previous works indicate a monoclinic martensite with different degrees of modulation [16, 44, 45, 46]. For the sake of simplicity (specially for vacancy calculations), the martensite phase has been modeled considering a non-modulated orthorhombic martensite (using the lattice parameters of the monoclinic structure and fixing $\beta = 90^{\circ}$), which has been proven to give identical results compared to those obtained considering a monoclinic structure.

The annihilation rate λ of Eq. (5.23) is evaluated at both the Γ and L points in the Brillouin zone, as well as calculating the mean value of the wave functions from the Γ and L points. The simulations are performed using the supercell approach. The supercells corresponding to off-stoichiometric samples have been built starting from a stoichiometric lattice and by substituting Sn/In atoms by Mn atoms until matching the proper composition of each sample. The corresponding supercell is increased in size until a convergence of 0.1 ps is reached in bulk lifetime calculations. Afterwards, in order to overcome the artificial defect-defect interactions caused by periodic boundary conditions, the supercell containing vacancy defects is built with increasing size in order to ensure the convergence of 0.1 ps in lifetime calculations, and 0.01 eV in positron binding energies.

The maximum number of atoms used in the vacancy calculations is 500 atoms for the austenite phase and 512 atoms for the martensite phase using $5 \times 5 \times 5$ and $4 \times 4 \times 4$ expansions of the primitive unit cell, respectively. A mesh size of 160^3 points has been used for both phases. Finally, taking into account the potential felt by the positron $V_+(\mathbf{r})$ of Eq. (5.25) and the enhancement factor $\gamma(\mathbf{r})$, the Schrödinger equation is solved iteratively at the mesh points of the supercell using a numerical relaxation method [216]. The positron wave functions and their energy eigenvalues

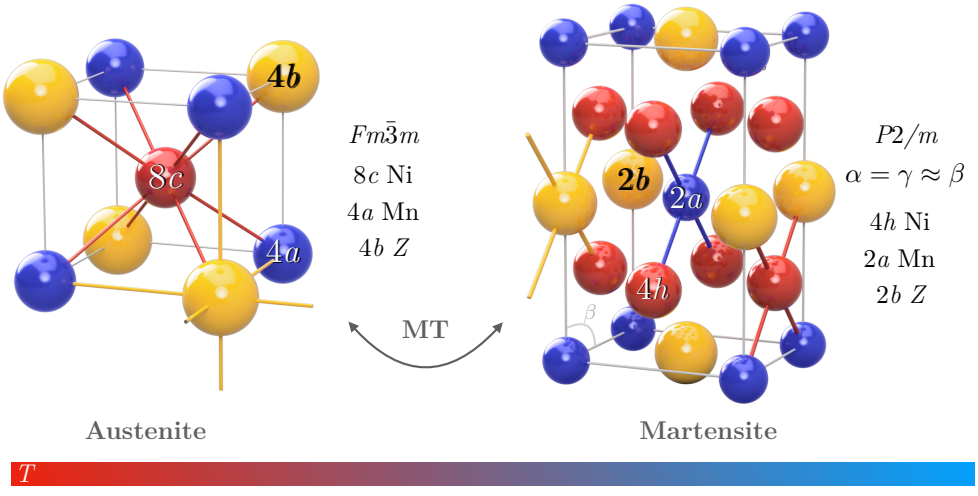

Figure 5.3: Schematic representation of stoichiometric austenite phase and martensite phase. In the austenite phase Ni atoms are bound to 4 Mn and 4 Sn/In atoms, whereas Z and Mn atoms are always surrounded by 8 Ni atoms. In the martensite phase, due to the lack of cubic symmetry, Z and Mn atoms are bound to 4 Ni atoms, whereas Ni atoms are bound to 2 Mn and 2 Z atoms. In off-stoichiometric conditions, Mn atoms tend to occupy $4b$ and $2b$ positions.

are obtained to evaluate the λ annihilation rate of Eq. (5.23).

Theoretical calculations for the bulk and defected lattice for Sn_x and In_x systems have been performed using the AT-SUP method. Besides, calculations for the defected lattice have been taken into account considering several type of posible vacancy defects.

Fig. 5.3 illustrates the austenite and martensite structures, as well as the nearest neighbors (NN) of each type of atoms. In the stoichiometric $Fm\bar{3}m$ phase (austenite), Ni atoms occupy $8c$ positions, Mn atoms $4a$ positions and Z atoms (Ga/Sn/In - Z) $4b$ positions. However, as the Mn content increases on detriment of Z atoms, the exceeded Mn atoms tend to occupy $4b$ positions [16, 44]. As a result, in off-stoichiometric samples two types of non-equivalent Mn atoms are present.

In the studied samples the Ni content has been fixed to 50% and the Mn/Z ratio is the one which is modified throughout the studied samples. It is noteworthy to mention that regardless of the composition, the nearest neighbors of both Mn and In/Sn atoms (positions $4a$ and $4b$) are always Ni in both Sn_x and In_x systems. Regarding the Ni atom, while in stoichiometric conditions the nearest neighbors of Ni are 4 Mn atoms and 4 Z atoms, as soon as the Mn content increases, the probability of Ni atoms to be coordinated with more Mn atoms than Z atoms also does. With respect to the possible vacancy types present in the studied samples, apart from Ni, Mn and Z vacancies (V_{Ni}, V_{Mn} and V_Z respectively), additional possible vacancies have been also taken into account in off-stoichiometric calculations: V^{as}_{Mn}, which refers to the vacancy of the antisite Mn atom located at $4b$ positions, and V^{i}_{Ni}, which refers

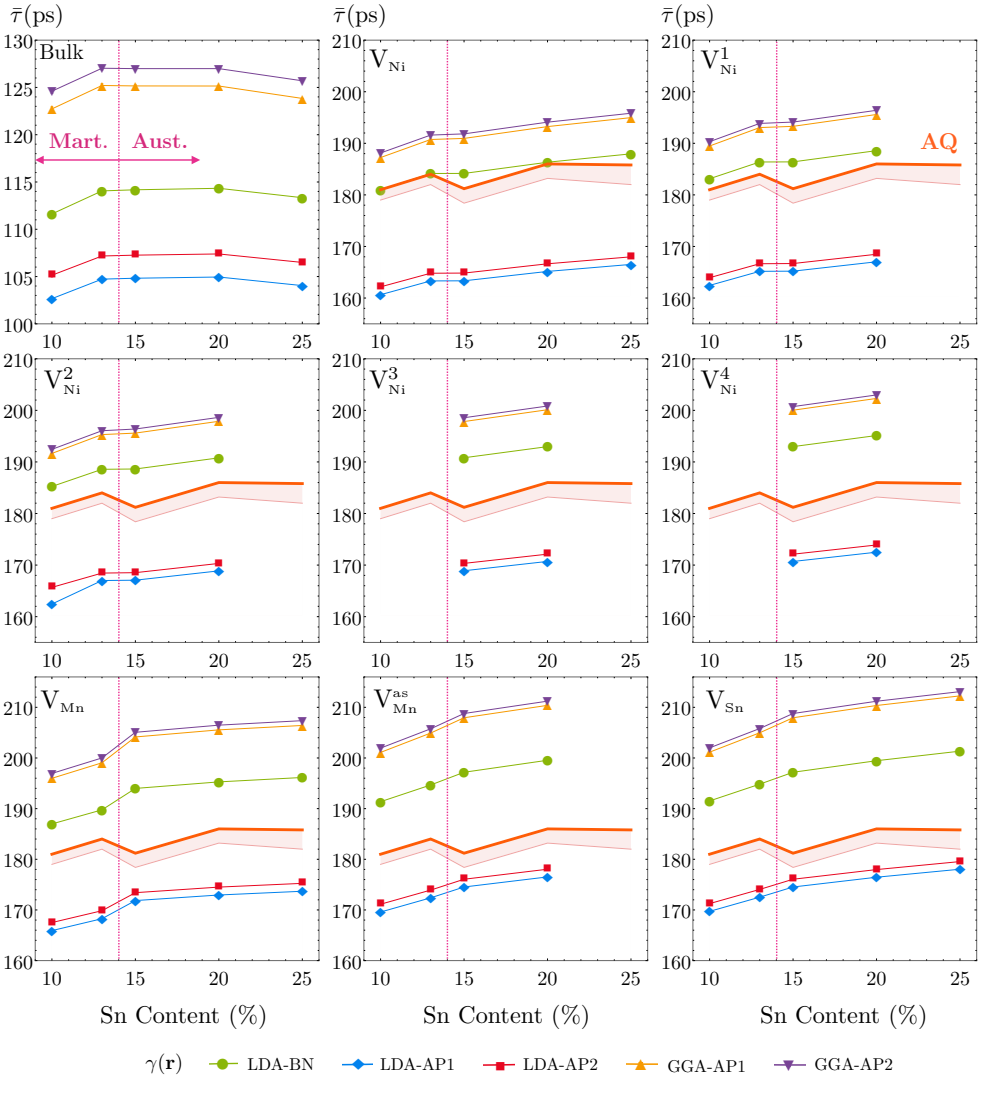

Figure 5.4: Theoretical positron lifetimes for $Ni_{50}Mn_{50-x}Sn_x$ ($x = 25, 20, 15, 13, 10$) alloys, calculated for the perfect lattice (bulk) and for each vacancy type defect. The red shaded area represents the range of the maximum and the minimum experimental $\overline{\tau}$ values measured after isochronal annealing cycles. The upper thick line of the shaded area represents the $\overline{\tau}$ values of samples measured in the AQ state.

to the Ni atoms surrounded for different Mn/Z atoms.

The previous description can be extended to the martensite structure. However, due to the cell-contraction caused by the MT, the nearest neighbors of Ni atoms change. As illustrated in Fig. 5.3, in the martensite structure, contrary to the cubic structure, Ni atoms are not bound to 8 atoms but to 4 atoms (i. e., two Mn and two

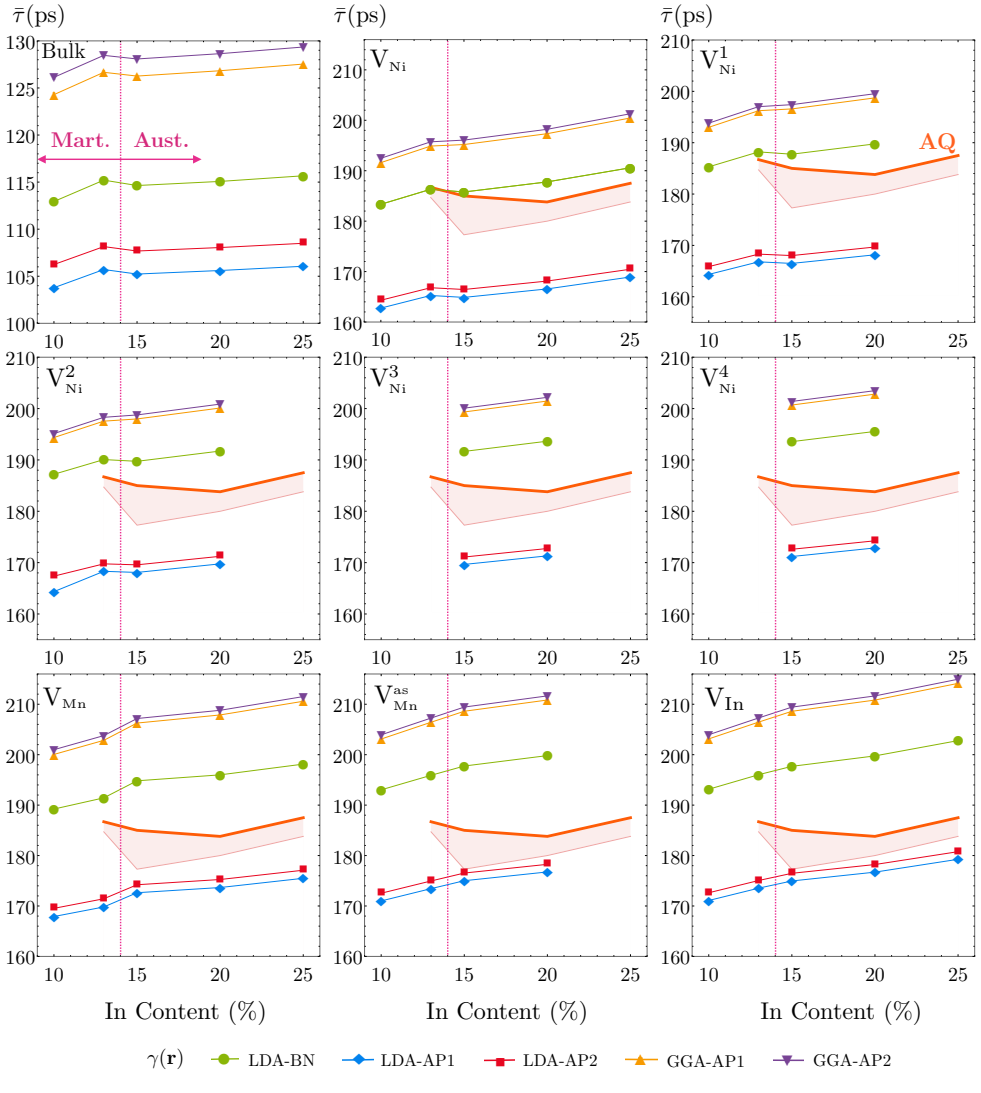

Figure 5.5: Theoretical positron lifetimes for $Ni_{50}Mn_{50-x}In_x$ ($x = 25, 20, 16, 13, 10$) alloys calculated for the perfect lattice (bulk) and for each vacancy defect type. The red shaded area represents the range of the maximum and the minimum experimental $\overline{\tau}$ values measured after isochronal annealing cycles. The upper thick line of the shaded area represents $\overline{\tau}$ values of samples measured in the AQ state.

Z atoms). As previously pointed out, the exceeded Mn atoms occupy $2b$ positions and the probability of a Ni atom to be bound to more Mn atoms than to Z atoms is non-negligible in samples far away from stoichiometry (i. e., Sn_{13}, Sn_{10}, In_{13} and In_{13}).

In summary, for stoichiometric Sn_{25} and In_{25} samples, three different types of

possible vacancy defects have been considered: V_{Ni}, V_{Mn} and V_Z. Regarding the off-stoichiometric samples, additional V^{as}_{Mn}, V^1_{Ni}, V^2_{Ni}, V^3_{Ni} and V^4_{Ni} vacancies have been also introduced in the calculations. The Ni vacancy surrounded by 4 Mn and 4 Z atoms has been labeled as V_{Ni}, while V^1_{Ni} refers to the Ni vacancy surrounded by an antisite Mn atom, which results in a Ni vacancy defect with 5 Mn atoms and 3 Z at nearest neighbor. Using the same scheme, the remaining type of Ni vacancies are labeled accordingly, and finally, V^4_{Ni} is assigned to the vacancy of a Ni atom surrounded by 8 Mn atoms. For the martensite phase, V^1_{Ni} and V^2_{Ni} labels have been used to refer to the Ni vacancies with 3 and 4 Mn atoms at nearest neighbor, respectively.

The results of the calculations are shown in Fig. 5.4 for Sn_x and in Fig. 5.5 for In_x. Each figure gathers the calculated positron lifetime (τ) values for perfect and defected lattices. The different outcomes of the five different parametrizations employed for modeling $\gamma(\mathbf{r})$ (described in Sec. 5.1.5) are plotted comparatively as a function of composition. Additionally, the range of experimental $\overline{\tau}$ is also plotted by a red shaded area.

On the one hand, the lifetime values calculated within the GGA are higher than the LDA ones. Although $\overline{\tau}$ values predicted by AP1 and AP2 parametrizations are very similar, the absolute values predicted by these two parametrizations within the GGA and LDA approximations are significantly different. Indeed, they differ by ≈ 30 ps offset value. Otherwise, $\gamma(\mathbf{r})^{BN}_{LDA}$ parametrization gives intermediate values of the positron lifetimes compared with the rest of parametrizations.

In order to explain the evolution shown by $\overline{\tau}$ as a function of T_i (see Fig. 5.1), in Sec. 5.2.2 two possible scenarios have been proposed. The first scenario, in which due to a lack of open volume defects all positrons are annihilated from the delocalized state at a constant rate $\lambda_b = \tau_b^{-1}$, would imply that the $\overline{\tau} \approx \tau_b$. As shown in Fig. 5.4 and Fig. 5.5, the calculated bulk lifetime for both systems range between 100 - 130 ps. However, experimental $\overline{\tau}$ values range between 177 - 190 ps. Taking into account that the dispersion of theoretical results between the different parametrizations $\gamma(\mathbf{r})$ is ≈ 30 ps, experimental $\overline{\tau}$ values are significantly above the calculated bulk lifetimes.

In a second scenario, it is posed that the behavior of $\overline{\tau}$ may be related to the presence of vacancies. Due to a high C_v retained during quenching, the contribution of the positrons annihilated from vacancies may become the one dominating $\overline{\tau}$, which would overcome the bulk's contribution. In such scenario, $\overline{\tau}$ would approach τ_v. In this connection, theoretically calculated vacancy-related positron lifetimes are more compatible with the experimental results, lying between 170 and 210 ps.

Additionally, the calculated density plots shown in Fig. 5.6 indicate that the positron density is highly localized within vacancies (i. e., the probability density of the positron is maximum at the vacancy). For the undefected solid the highest position probability density is found at interstitial regions, whereas $|\Psi_+|^2$ vanishes close to atomic nuclei. DFT calculations reveal that regardless of the vacancy type, structure and composition, the binding energies of positrons to vacancies range between 2-3 eV. Therefore, positron lifetime calculations reveal that the studied vacancies act as effective positron traps. Taking into account that $\overline{\tau}$ values ≈ 180 ps reported in

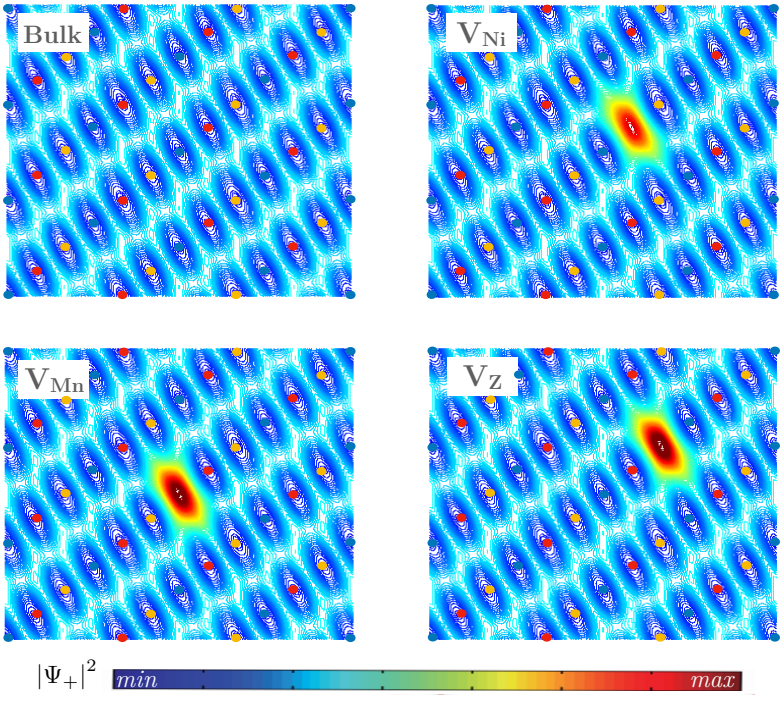

Figure 5.6: From left to right, the calculated positron density for a perfect lattice (bulk), and for a defected lattice with V_{Ni}, V_{Mn}, and V_Z, respectively, plane (110). The trapping features exhibited by all samples are identical. The plot is represented in a non-orthogonal symmetric set of primitive vectors for the face-centered cubic lattice [217].

Ni-Mn-Ga alloys were ascribed to the presence of vacancies [79, 80], it is reasonable to assess that vacancies are present in the studied Sn_x and In_x samples. As a result, the measured $\overline{\tau}$ comprehends two different contributions.

Let us define η_1 as the percentage of total positrons annihilated from the delocalized state with a characteristic lifetime τ_b. Considering the presence of a single vacancy acting as a positron trap (or an effective vacancy type accounting for the contribution of several vacancy defects with similar τ_v [79]), the rest of the positrons (η_2) get trapped at the vacancy and they annihilate from the localized state with a characteristic lifetime τ_v related to the defect. As a result, the experimentally measured $\overline{\tau}$ comprehend these two contributions, so that, $\overline{\tau} = \eta_1\tau_b + \eta_2\tau_v$. Thus, a larger C_v implies a higher probability of positrons annihilated from vacancies. In such scenario, the relation between C_v and $\overline{\tau}$ is given by the so-called *one-trap model* of Eq. (2.40):

$$\kappa_v = \mu_v C_v = \frac{1}{\tau_b}\frac{\overline{\tau}-\tau_b}{\tau_v-\overline{\tau}} \quad \rightarrow \quad C_v = \frac{1}{\tau_b\mu_v}\frac{\overline{\tau}-\tau_b}{\tau_v-\overline{\tau}} \tag{5.30}$$

where κ_v is the so-called trapping rate [116]. The parameter μ_v is the specific

trapping coefficient of the vacancy and it depends on the type of defect and also on the surrounding lattice [117]. The trapping rate κ_v describes how effective is a certain type of defect trapping positrons. As shown in Eq. (5.30) a high value of μ_v or C_v would result in a $\overline{\tau}$ value close to τ_v. In metals, unlike in semiconductors, the specific trapping rate μ_v is constant and it does not depend on temperature [117]. In the present work a constant $\mu_v = 1.5 \times 10^{14}$ s^{-1} value has been used, which is widely employed for Ni [218, 219].

The lack of variation of experimental $\overline{\tau}$ values reflect that the vacancy contribution to $\overline{\tau}$ remains almost unaltered as a function of the isochronal annealing cycles. Additionally $\overline{\tau}$ values are significantly higher than theoretical τ_b values, and indeed, $\overline{\tau}$ values are closer to the calculated vacancy-related lifetimes. All in all, and taking into account the fact that spectra could not be decomposed, the behavior exhibited by $\overline{\tau}$ as a function of T_i indicates that it lies in a so-called saturation-trapping regime. In such regime, $|\overline{\tau} - \tau_v| < 10$ ps [215], due to a high C_v, the contribution of positrons trapped at vacancies dominates $\overline{\tau}$, in such a way that the decomposition becomes unfeasible. According to the *one-trap model*, the decay spectrum $D(t)$ of positrons is given by,

$$D(t) = I_1 e^{-t/\tau_1} + I_2 e^{-t/\tau_2}. \tag{5.31}$$

where

$$\tau_1 = \frac{1}{\lambda_b + \kappa_v}, \quad \tau_2 = \frac{1}{\lambda_v}, \quad I_2 = \frac{\kappa_v}{\lambda_b - \lambda_v + \kappa_v} \quad I_1 = 1 - I_2. \tag{5.32}$$

τ_1 is often called reduced bulk lifetime. When C_v is very large, the vast majority of positrons are trapped at vacancies and annihilated from them. As a result, $\lim_{\kappa_v \to \infty} C_v = \infty$ and $\lim_{\kappa_v \to \infty} I_2 = 1$. According to the $I_1 = 1 - I_2$ constrain, the intensity of the first component of Eq. (5.31) vanishes for high C_v values (i. e., $I_1 \to 0$). Moreover, it is noteworthy to mention that when $\lim_{\kappa_v \to \infty} \tau_1 = 0$, as well. τ_1 is one of the lifetime components (along with τ_2 according to the *one-trap model*) that comprises the decay spectrum of positrons, see Eq. (5.31). Thus, when the sample is characterized by a large C_v, most of positrons are annihilated at defects, and τ_1 and $I_1 \to 0$. As a result, the decay spectrum of positron lifetime is mainly composed by a single component $\tau_2 = \lambda_v^{-1} = \tau_v$, which in turn, is the characteristic lifetime related to the present vacancy. Due to that, it is not possible to obtain the τ_1 value, because its contribution to the experimental decay spectrum is negligible. As a result, in PALS spectra only $\overline{\tau}$ can be extracted, which in turn, $\overline{\tau} \approx \tau_v$. Thereby, the $\overline{\tau}$ values corresponding to the AQ states are the ones that approach best the characteristic vacancy-related lifetime.

Fig. 5.4 and Fig. 5.5 show the overlap betwen theoretical and experimental $\overline{\tau}$ results (red shaded area). On the one hand, in both Sn_x and In_x systems, regardless of the calculated type of defect, GGA seems to overestimate the positron lifetime. Indeed, in the case of V_{In} and V_{Sn} the predicted lifetimes lie above 210 ps, 20 ps higher than the experimental $\overline{\tau}$ values, which range between 178 - 190 ps. However, it is noteworthy to mention that this fact alone, does not imply that $\gamma(\mathbf{r})_{GGA}$ results are

not compatible with the experimental results. In principle, according to Eq. (2.40), a non-saturated regime of vacancies with a higher characteristic lifetime than the measured $\overline{\tau}$ could reproduce a $\tau_v > \overline{\tau} > \tau_b$. However, if the values predicted by $\gamma(\mathbf{r})_{\mathrm{GGA}}$ were accurate, $\overline{\tau}$ would not be in a saturated trapping regime, which would enable the spectra decomposition. As previously pointed out the decomposition is not feasible in any of the studied samples, which implies that $\gamma(\mathbf{r})_{\mathrm{GGA}}$ gives overestimated values.

On the other hand, within the LDA framework, both $\gamma(\mathbf{r})^{\mathrm{AP1}}_{\mathrm{LDA}}$ and $\gamma(\mathbf{r})^{\mathrm{AP2}}_{\mathrm{LDA}}$ systematically underestimate the positron lifetime. Because $\overline{\tau}$ must be always $\overline{\tau} \leq \tau_v$ ($\lim_{\kappa_v \to \infty} \overline{\tau} = \tau_v$), the positron lifetime values predicted by $\gamma(\mathbf{r})^{\mathrm{AP1}}_{\mathrm{LDA}}$ and $\gamma(\mathbf{r})^{\mathrm{AP2}}_{\mathrm{LDA}}$ cannot reproduce the experimental $\overline{\tau}$ values. As shown in Fig. 5.5, only in the case of the In_{15} sample, the characteristic lifetimes calculated by using $\gamma(\mathbf{r})^{\mathrm{AP1}}_{\mathrm{LDA}}$ and $\gamma(\mathbf{r})^{\mathrm{AP2}}_{\mathrm{LDA}}$ for $V^{\mathrm{as}}_{\mathrm{Mn}}$ and V_{In} vacancies approach the experimental lifetimes. However, the calculated $\overline{\tau}$ values do not approach the AQ experimental values (ideally, the defect related characteristic positron lifetimes), but the lower bound of experimental $\overline{\tau}$ values. The lower bound of $\overline{\tau}$ does not directly reflect the characteristic lifetime of the involved vacancy defect, since these $\overline{\tau}$ values comprehend the weighted contributions of positrons annihilated from the delocalized state and from vacancies. As a result, it can be concluded that $\gamma(\mathbf{r})^{\mathrm{AP1}}_{\mathrm{LDA}}$ and $\gamma(\mathbf{r})^{\mathrm{AP2}}_{\mathrm{LDA}}$do not predict the appropriate value either.

Regarding the positron lifetime values calculated by using the $\gamma(\mathbf{r})^{\mathrm{BN}}_{\mathrm{LDA}}$ parametrization, they lie between those predicted within the GGA, and the lifetimes predicted by using $\gamma(\mathbf{r})^{\mathrm{AP1}}_{\mathrm{LDA}}$ and $\gamma(\mathbf{r})^{\mathrm{AP2}}_{\mathrm{LDA}}$. In fact, as shown in Fig. 5.4 and Fig. 5.5, it seems that the most accurate values comparing the experimental results are given by the $\gamma(\mathbf{r})^{\mathrm{BN}}_{\mathrm{LDA}}$ parametrization.

5.2.4 Theoretical calculations on Ni_2MnGa

For the sake of validating the accuracy of $\gamma(\mathbf{r})^{\mathrm{BN}}_{\mathrm{LDA}}$ parametrization in Sn_x and In_x systems, positron lifetime calculations have been performed on the Ni_2MnGa sample. Taking advantage of the existing PALS results in the literature on Ni_2MnGa [79, 80], the calculated values have been compared with the available experimental results. The crystallographic details, along with the results of theoretical positron calculations on Ni_2MnGa, are gathered in Table 5.2. Calculations have been carried out for both austenite ($Fm\overline{3}m$) [220] and tetragonal martensite ($I4/mmm$) [221] following the methodology described in Sec. 5.1.5.

The vacancy-related positron lifetime values calculated using $\gamma(\mathbf{r})^{\mathrm{BN}}_{\mathrm{LDA}}$ for the austenite Ni_2MnGa phase, range between 178 - 185 ps, while the lifetime values calculated for the martensite phase are $\approx$ 3-4 ps lower than those calculated for the austenite phase. Here, as observed in Sn_x and In_x systems, the calculated vacancy-related positron lifetime of V_{Mn} and V_{Ga} are higher than the one of V_{Ni}. Moreover, either for vacancy-related positron lifetimes and for bulk lifetimes, the range of the calculated values for Ni_2MnGa matches those calculated for Sn_x and In_x.

The experimental values measured by Merida *et al.* for AQ Ni_2MnGa sample

Phase	Cell parameters		τ
	Atom	Site	$\gamma(\mathbf{r})^{\mathrm{BN}}_{\mathrm{LDA}}$
Austenite Ref. [220]	Ni	8*c* (1/4,1/4,1/4)	182 ps
$Fm\overline{3}m$, 225	Mn	4*a* (0,0,0)	185 ps
$a = 5.8229$Å	Ga	4*b* (1/2,1/2,1/2)	185 ps
	Bulk		108 ps
Martensite Ref. [221]	Ni	4*d* (0,1/2,1/4)	178 ps
$I4/mmm$, 139	Mn	2*b* (0,0,1/2)	182 ps
$a = b = 3.865$Å	Ga	2*a* (0,0,0)	181 ps
$c = 6.596$Å	Bulk		106 ps

Table 5.2: The structural parameters used for theoretical positron lifetime calculations fin Ni_2MnGa alloy using the $\gamma(\mathbf{r})^{\mathrm{BN}}_{\mathrm{LDA}}$ parametrization. The last column gathers the theoretical vacancy-related positron lifetimes for the corresponding atom, along with τ_b bulk lifetime.

are 181 ps [222] and 182 ps [223]. The positron lifetime value related to V_{Ni} in the austenite phase (see Table 5.2) is the one that approaches best the experimental lifetimes measured for the AQ Ni_2MnGa samples. It is important to notice that these experimental values correspond to $\overline{\tau}$ values measured in the austenite phase (T_{MT} of Ni_2MnGa is ≈ 200 K). The $\overline{\tau}$ value measured in the AQ Ni_2MnGa samples was attributed to the presence of an effective vacancy defect which its concentration ranged between 1000 - 2000 ppm. In a nutshell, the present theoretical calculations are in good agreement with the experimental $\overline{\tau}$ values measured for Ni_2MnGa. This results confirms the validity of the $\gamma(\mathbf{r})^{\mathrm{BN}}_{\mathrm{LDA}}$ parametrization. Moreover, the best agreement between experimental $\overline{\tau}$ values and calculated defect-related lifetimes in Sn_x and In_x systems is achieved by using the $\gamma(\mathbf{r})^{\mathrm{BN}}_{\mathrm{LDA}}$ parametrization. Thereby, from now on, only the results obtained by means of $\gamma(\mathbf{r})^{\mathrm{BN}}_{\mathrm{LDA}}$ will be discussed.

5.2.5 Vacancy Concentration and Vacancy-Type Determination

Theoretical positron lifetimes calculated by using $\gamma(\mathbf{r})^{\mathrm{BN}}_{\mathrm{LDA}}$ parametrization for Sn_x and In_x systems are listed in Table 5.3. On the one hand, the calculations reveal that both $V^{\mathrm{as}}_{\mathrm{Mn}}$ and V_Z have the same defect-related positron lifetime. As illustrated in Fig. 5.2, the exceeded Mn atoms tend to occupy the natural positions of Z. Then, Z atoms and antisite Mn atoms are surrounded by the same environment (that is 8 Ni atoms), which results in an identical defect-related positron lifetime. In addition, the calculated τ values related to V_{Sn} and V_{In} are the largest among the simulated defects, exceeding 200 ps in some In_x samples. The calculated characteristic lifetimes related to V_{Mn} and $V^{\mathrm{as}}_{\mathrm{Mn}}$ are the next largest, still significantly above from the measured $\overline{\tau}$.

For each composition of both Sn_x and In_x alloys, the lowest calculated lifetimes values are related to V_{Ni}. Besides, this value decreases with decreasing of the stoi-

Z_x	τ_b	V_{Ni}					V_{Mn}		V_Z
		V_{Ni}	V^1_{Ni}	V^2_{Ni}	V^3_{Ni}	V^4_{Ni}	V_{Mn}	V^{as}_{Mn}	
Sn_{25}	113	187	(–)	(–)	(–)	(–)	196	(–)	201
Sn_{20}	114	186	189	191	193	195	195	200	200
Sn_{15}	114	184	186	189	191	193	194	197	197
Sn_{13}	114	184	186	189	(–)	(–)	190	195	195
Sn_{10}	111	181	183	185	(–)	(–)	187	191	191
In_{25}	116	191	(–)	(–)	(–)	(–)	198	(–)	203
In_{20}	115	188	190	192	194	196	196	200	200
In_{16}	114	186	188	190	192	194	195	198	198
In_{13}	115	186	188	190	(–)	(–)	191	196	196
In_{10}	113	183	185	187	(–)	(–)	189	193	193

Table 5.3: Results of the calculated positron lifetime (in ps) for the perfect lattice, calculated by means of $\gamma(\mathbf{r})^{BN}_{LDA}$ parametrization, for several types of vacancy defects in Sn_x and In_x systems

chiometry of the samples, from $\approx$ 190 ps down to 181 ps. Regarding the lifetimes related to V^i_{Ni}, for a fixed composition, calculations show that as soon as the exceeded Mn atom occupies the 4*b* positions, the characteristic lifetime related to V^i_{Ni} increases on average $\approx$ 2 ps, see Table 5.3. Due to the fact that Sn and In carry more electrons (valence and core) than Mn atoms, when an exceeded Mn atom occupies a 4*b* position, the electronic density surrounding V^i_{Ni} decreases. According to Eq. (5.23), a lower electronic density involves a lower annihilation rate λ_v and therefore, a higher defect-related τ_v lifetime.

Finally, as Fig. 5.3 and Fig. 5.4 show, the calculated τ values for V_{Ni} are the ones that present the best agreement with AQ $\overline{\tau}$ values, illustrated in the upper-part of the red shaded area. In the Sn_x set, for Sn_{25}, Sn_{20}, Sn_{13} and Sn_{10}, the measured $\overline{\tau}$ value and the predicted values match perfectly, while for Sn_{15} the deviation is $\approx$ 1 ps. The calculated τ values related to the rest of the vacancies are all 4 ps above. In the case of In_x alloys, again, the best accordance between the measured and calculated lifetime is observed for the V_{Ni} defect. In the specific case of In_{16} and In_{13} the calculated lifetime matches with the $\overline{\tau}$ experimental value, and for In_{20} and In_{25}, the deviation is about 2 ps. Thus, in light of the experimental and theoretical results for Sn_x and In_x systems, along with the good agreement between $\gamma(\mathbf{r})^{BN}_{LDA}$ outcomes and experimental PALS results in the Ni_2MnGa system, it is concluded that V_{Ni} is the vacancy type trapping positrons in Ni-Mn-Sn and Ni-Mn-In alloys.

This experimental result is in agreement with previous theoretical predictions. Recently Wang *et al.* [197] have shown that the most favorable type of defect in Ni-Mn-Ga samples is V_{Ni}. Regarding Ni-Mn-Sn and Ni-Mn-In samples, previous theoretical works also point out to V_{Ni} as the most favorable defect. Reports of Kulkova *et al.* [194, 195] show that the formation energy E_f of V_{Ni} is the smallest

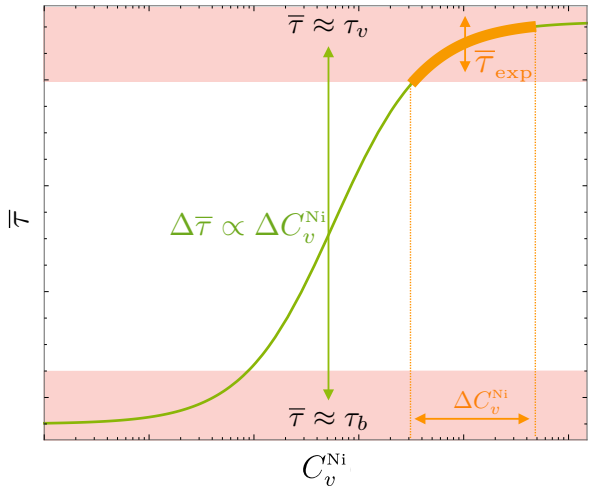

Figure 5.7: Positron-lifetime sensitivity to the vacancy concentration calculated by Eq. (2.40). The upper and lower red shaded areas correspond to the saturated and diluted vacancy regimes, respectively.

in both the Ni_2MnSn and Ni_2MnIn systems, with $E_f = 0.4$ eV and $E_f = 0.7$ eV values, respectively. The formation energy of V_{Mn} and V_Z are 1.04 eV and 2.59 eV in Ni_2MnSn, and 1.58 eV and 2.29 eV in Ni_2MnIn. Bai *et al.* [191, 192, 193] also suggest V_{Ni} as the most favorable type of defect with $E_f = 0.59$ eV for the Ni_2MnIn alloy. Thus, taking into account the theoretical predictions, and the experimental and theoretical PALS results of the present work, it is concluded that the actual type of vacancy in Ni-Mn-Ga, Ni-Mn-Sn, and Ni-Mn-In systems is V_{Ni}.

The V_{Ni} concentration (C_v^{Ni}) can be estimated by means of Eq. (5.30). Usually, τ_v and τ_b values can be obtained after decomposing $\overline{\tau}$. However, as discussed before, $\overline{\tau}$ could not be decomposed in any of the samples of Sn_x or of In_x. As an alternative way, and taking into account the good agreement between PALS experiments and DFT calculations, the theoretically calculated τ_v and τ_b values of Table 5.3 have been used to evaluate Eq. (2.40). Fig. 5.7 shows the generic relation between C_v and $\overline{\tau}$, according to Eq. (2.40). In the dilute regime of defects, $\overline{\tau}$ lies close to τ_b, and in this range the variation of C_v does not influence significantly $\overline{\tau}$. However, in the midrange, the sensitivity of PALS is maximum, with a linear dependence between C_v and $\overline{\tau}$. Afterwards, in the saturation-trapping regime, the sensitivity decreases again and $\overline{\tau}$ approaches τ_v. As it is illustrated by the thick red line in Fig. 5.7, PALS measurements on Sn_x and In_x lie in the saturated regime.

Fig. 5.8 gathers the estimated C_v^{Ni} for Sn_x and In_x systems, respectively. The markers that delimit the thick line in each curve indicate the maximum and the minimum experimentally obtained $\overline{\tau}$ values (and their corresponding C_v^{Ni}). In both, Sn_x and In_x systems the lowest value of experimentally measured vacancy concentration is ≈ 500 ppm. The highest C_v^{Ni} value, on the other hand, may go beyond 10^4 ppm. Particularly, in the case of Sn_x the predicted high C_v^{Ni} is a consequence

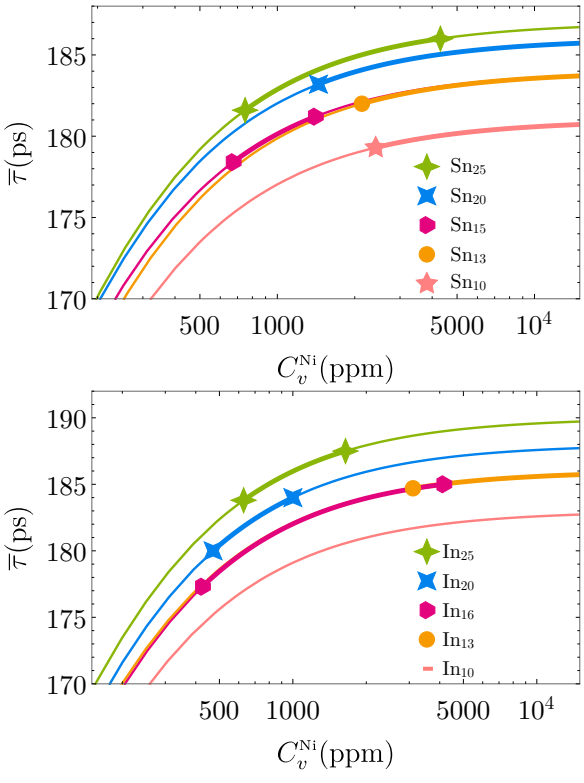

Figure 5.8: From top to bottom, the calculated evolution of C_v ($\overline{\tau}$) for $Ni_{50}Mn_{50-x}Sn_x$ ($x = 25, 20, 15, 13, 10$) and $Ni_{50}Mn_{50-x}In_x$ ($x = 25, 20, 16, 13, 10$) systems. C_v^{Ni} has been calculated after evaluating Eq. (5.30) with the theoretical τ_b and τ_v values predicted by $\gamma(\mathbf{r})^{\mathrm{BN}}_{\mathrm{LDA}}$ (see Table 5.3). The markers delimiting the thick lines represent the C_v^{Ni} range calculated from experimental $\overline{\tau}$ values.

of the lack of sensitivity of the PALS technique in the saturation-trapping regime. However, the lower bound of the calculated C_v^{Ni} lies around hundreds of ppm, a high value compared with those reported in some Ni-Mn-Ga systems [79, 80] (around 10 - 50 ppm). Regardless of the composition, all samples show saturated trapping features. This result indicates that contrary to what is observed for Ni-Mn-Ga systems, Ni-Mn-Z (Z = In, Sn) present a high irreducible C_v, which hinders their control by conventional heat treatments.

These results contrast with the ones obtained by Hedayati *et al.* [190]. They claim to be able to tune the T_{MT} as a function of V_{Sn} concentration. It is noteworthy to mention that they do not report any experimental evidence of Sn vacancies. On the one hand, the combination of theoretical and experimental PALS results show that the actual vacancy present in Ni-Mn-Sn systems is V_{Ni}. Additionally, it is demonstrated that Ni-Mn-Sn systems are characterized with a high C_v and that

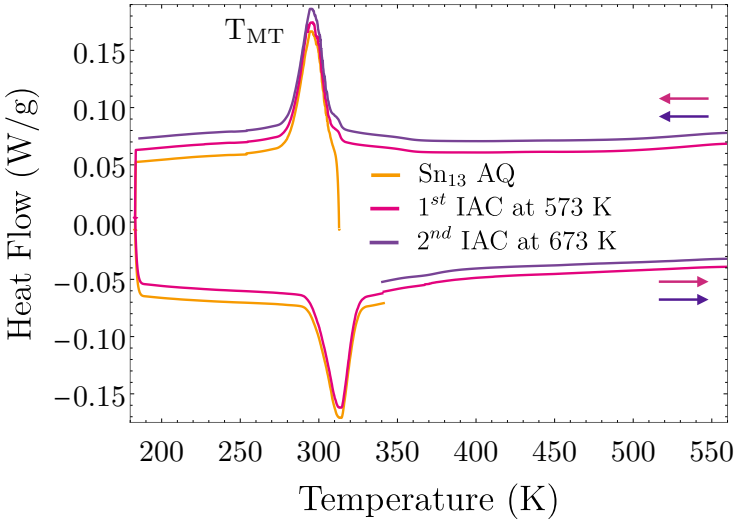

Figure 5.9: DSC curves of the AQ Sn_{13} sample, and after two isochronal annealing cycles with T_i = 573 K. The T_{MT} remains unchanged even though C_v^{Ni} is different (as revealed by PALS results). For a better visualization, an offset value have been intentionally added to DSC curves of each isochronal annealing cycles.

their tuning and control by conventional heat-treatments is not straightforward at all.

Indeed, as shown in Fig. 5.9, the variation of C_v^{Ni} observed in the present work does not produce any T_{MT} shift in the $Ni_{50}Mn_{37}Sn_{13}$ sample, which is one of the samples investigated by Hedayati *et al.* The lack of T_{MT} variation is in agreement with the well-known fact that Ni-Mn-Sn systems exhibit a high stability of the $L2_1$ structure, which precludes the variation of the long-range atomic order and its consequent change on T_{MT} [63]. In light of the present results, the capability of V_{Sn} as a parameter to optimize the T_{MT} seems to be unfeasible in Ni-Mn-Sn systems.

5.3 PALS in a Ni-Fe-Ga Alloy

In contrast to what it is observed in Ni-Mn-Ga alloys, the results of the previous chapter evidence that Ni-Mn-Sn and Ni-Mn-In alloys present a high irreducible vacancy concentration. Moreover, in the studied alloys the vacancy concentration never decreases below 500 ppm, which is a significantly high C_v value compared with 10 - 50 ppm values obtained in Ni-Mn-Ga alloys. As a result, the determination of the effect that vacancies may have on the MT in Ni-Mn-Sn and Ni-Mn-In samples could

not be undertaken.

In Ni-Fe-Ga Heusler systems, T_{MT} exhibits a strong annealing temperature dependence. Indeed, the degree of long-range atomic order is found to affect strongly both T_c and T_{MT}. In this connection, Ni-Fe-Ga systems are increasingly attracting a great interest due to their mechanical properties and its consequent enhanced deformation behavior [31, 32, 33]. The improved ductility performance in bulky off-stoichiometric samples, makes Ni-Fe-Ga system a promising alternative to the classic Ni-Mn-Ga systems [35]. Recently, a giant reversible elastocaloric effect has been reported in Ni-Fe-Ga alloys near room temperature [34]. Moreover, in the Ni-Fe-Ga system the composition can be tuned to get a T_{MT} near room temperature [30]. Additionally, as occurs in Ni-Mn-Z (Z = Ga, In, Sn), the microstructure plays a key role in the MT characteristics in Ni-Fe-Ga systems [224]. The magnetism of Ni-Fe-Ga atoms is mainly confined to the Fe sites and the variation of Fe-Fe distances affects strongly the exchange coupling [38, 39].

Regarding the effect that vacancies may have on the MT of quenched Ni-Fe-Ga systems, Santamarta *et al.*, Font *et al.* and Oikawa *et al.* suggest a different vacancy concentration between $L2_1$ and B2 phases as the responsible of the observed changes on T_{MT} [225, 189, 226]. As vacancies mediate the ordering process, a different C_v could in principle explain the observed changes in T_{MT}, which would have its origin on the different long-range atomic order achieved in the samples quenched above or below the $T_{L2_1\text{-}B2}$ transition. In this connection, Hsu *et al.* [227] suggest that vacancies may drive the $L2_1$-B2 order-disorder transition. However, none of the above suggestions have been experimentally proven, being the elusive nature of vacancies, which has made it less experimentally investigated in comparison with other physical factors. Proof of vacancies assisting the aforementioned processes are scarcely reported or non-existent in the literature.

Then, by combining PALS and DSC measurements the relationship between vacancies and ΔT_{MT} is investigated in a $Ni_{55}Fe_{17}Ga_{28}$ alloy. The evolution of the T_{MT} exhibited by samples quenched from $L2_1$ or B2 phases is also addressed. Moreover, PALS measurements are complemented with DFT electron-positron calculations, enabling the identiffication of V_{Ni} as the most probable vacancy defect in the $Ni_{55}Fe_{17}Ga_{28}$ alloy. This investigation shows the potential of vacancies for the fine tuning of T_{MT}, which enable shifts in T_{MT} up to 50 K. The present results open the way for defect engineering in tuning T_{MT} and the related multifunctional properties of Ni-Fe-Ga alloys.

Starting from high purity elements Ni, Fe and Ga, a polycrystalline ingot has been cast by induction melting method under protective Ar atmosphere. The ingot has been remelted several times to ensure homogeneity. After encapsulating the ingot in a quartz ampoule it has been homogenized during 24 h at 1423 K in Ar atmosphere, followed by slow cooling within the furnace. By means of EDX and DSC the composition and the characteristic temperatures T_c and T_{MT} have been measured, resulting in a $Ni_{55}Fe_{17}Ga_{28}$ sample with $T_c \approx T_{MT} \approx 300$ K [42]. The studied samples have been quenched into iced water from 673 K up to 1173 K in 100 K steps. Samples are labeled according to their quenching temperature T_q as Q673,

Q773, Q873, Q973 Q1073 and Q1173. The detail of PALS measurements, DSC measurements and the computational procedure related to $Ni_{55}Fe_{17}Ga_{28}$ measurements and simulations are identical to those described in the experimental part in Sec. 5.2.1 and in the computational part in Sec. 5.1.5.

5.3.1 Influence of Quenching Temperature on T_{MT}

The influence of the quenching temperature on T_{MT} has been evaluated by DSC measurements. As shown in Fig. 5.10, for samples quenched from $T_q < 900$ K, T_{MT} increases with growing T_q. However, for samples with $T_q > 900$ K, T_{MT} decreases as T_q increases. In Ni-Mn based Heusler alloys and in Ni-Fe-Ga alloys, T_{MT} is highly sensitive to the atomic order [77, 15, 63, 189]. Indeed, as opposed to other Ni-Mn alloys [78], a less ordered $L2_1$ phase results in a higher T_{MT} [189, 228] in Ni-Fe-Ga alloys. Thus, the observed increment of T_{MT} for the samples quenched from $T_q < 900$ K indicates that for higher T_q, the retained $L2_1$ order degree is lower. However, for samples quenched from $T_q > 900$ K, T_{MT} decreases with the increase of T_q, denoting a higher degree of $L2_1$ order retained during quenching.

The different dependencies of T_{MT} on T_q shown by the AQ samples matches the occurrence of a second neighbor ordering transition at 930 K ($T_{L2_1\text{-}B2}$), see Fig. 5.10. Thereby, it implies that while Q673, Q773 and Q873 samples have been quenched within the same structure (from $L2_1$ to $L2_1$), samples Q973, Q1073 and Q1173 have been quenched from B2 phase to $L2_1$ one. As previosly said, the T_{MT} decreases while the atomic order degree increases. Then, by proper annealing treatments the disorder retained during quenching can be gradually diminished, which allow to track the evolution of T_{MT}. The quenched samples have been subjected to several isochronal

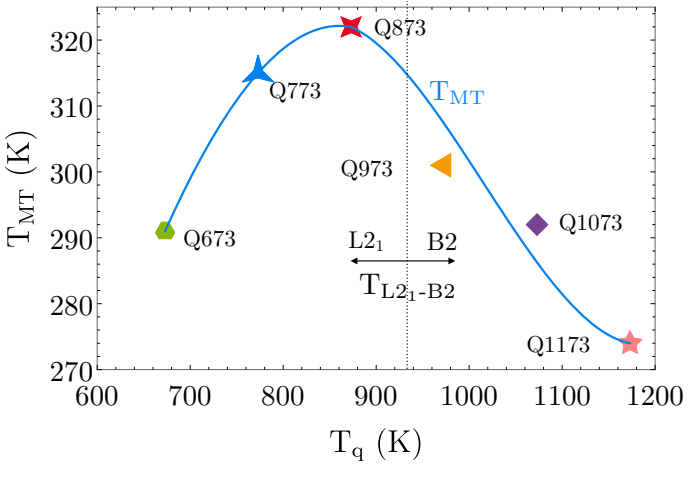

Figure 5.10: Direct T_{MT} versus T_q for Q673, Q773, Q873, Q973, Q1073 and Q1173 $Ni_{55}Fe_{17}Ga_{28}$ samples. The T_{MT} increases as T_q does until the quenching temperature exceeds the $T_{L2_1\text{-}B2}$. Afterwards, for higher quenching temperatures the T_{MT} of the quenched samples decreases.

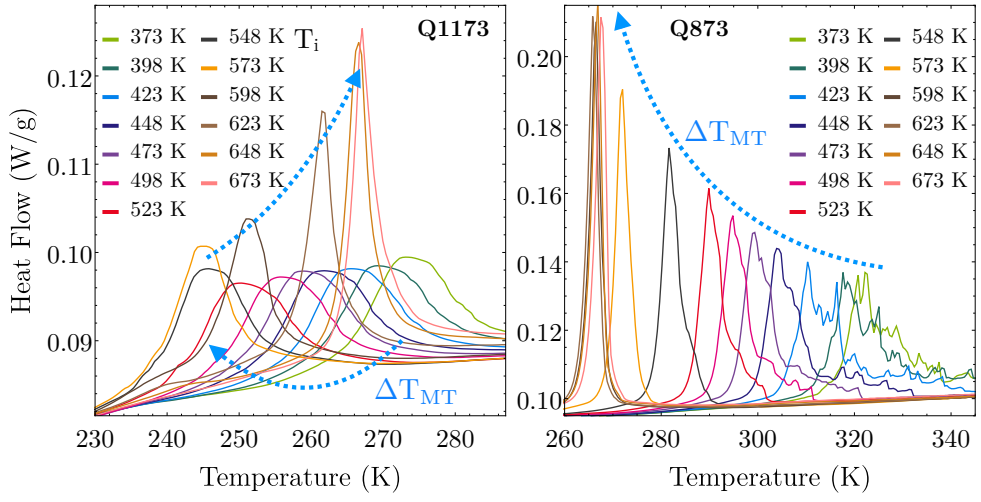

Figure 5.11: Direct DSC curves for the Q873 sample and Q1173 samples for each isochronal annealing cycle. As expected, for higher T_i the T_{MT} decreases in both samples. However, in the Q1173 sample, for $T_i > 573$ K, T_{MT} increases.

annealing cycles in a DSC, where T_i have been increased from 398 K up to 698 K every 25 K.

Fig. 5.11 shows a detailed shape of the DSC thermogram peaks for samples Q1173 and Q873. The exothermic peak observed in the DSC corresponds to the forward martensitic transition, which in turn, indicates the T_{MT}.

In sample Q873 T_{MT} decreases monotonically with increasing T_i. However, T_{MT} for Q1173 sample initially decreases with T_i increase, but above $T_i \approx 570$ K, T_{MT} increases along with T_i. Although all the DSC curves are not shown here the same behavior is reproduced for all the samples with $T_q < T_{L2_1\text{-}B2}$ and $T_q > T_{L2_1\text{-}B2}$. Fig. 5.12 shows the shift of T_{MT} as a function of T_i for all the samples quenched between 673 K and 1173 K.

As it happened in the case of Q873 and Q1173, the remaining quenched samples also show a different behavior depending on whether the sample is quenched above or below the $T_{L2_1\text{-}B2}$ temperature. On the other hand, the T_{MT} of the samples quenched below $T_{L2_1\text{-}B2}$ are higher than T_{MT} of the samples quenched above $T_{L2_1\text{-}B2}$. In line with the previous reasoning, this fact implies that the samples quenched above the second-order neighbour transition retain less disorder than the rest of samples quenched below $T_{L2_1\text{-}B2}$. In this connection, Santamarta *et al.* [189, 229] and Oikawa *et al.* [226] ascribe the dependency that the evolution of T_{MT} has on T_q, to different vacancy dynamics for the $L2_1$ and B2 phases, which would promote different long-range atomic order retained during quenching. Moreover, previous works on Fe-Ni systems also show the dependence of T_{MT} on T_q, which has been also ascribed to the presence of quenched-in vacancies [227]. However, as previously pointed out, none of the previous works contribute any experimental evidence supporting their claims.

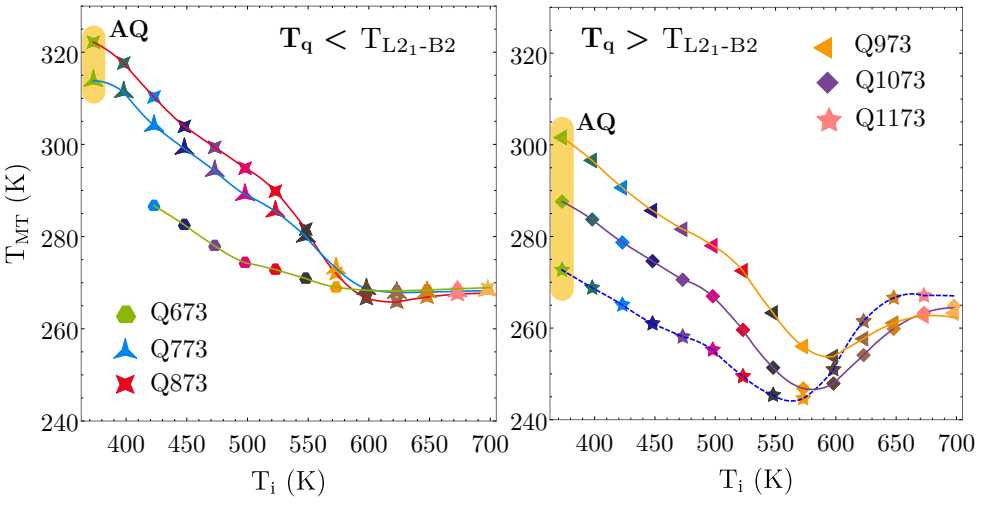

Figure 5.12: The evolution of T_{MT} for all the studied samples as a function of T_i.

As vacancies mediate the ordering process via diffusion [80], a different C_v could explain the observed phenomena. In this context, the powerful combination of PALS and DFT theory have been proven to be one of the most accurate techniques for the advanced characterization of vacancy defects in metals and semiconductors [105, 230]. Thus, in order to ascertain the potential role of vacancies on the T_{MT} shift, PALS experiments, along with theoretical positron lifetime calculations have been conducted on $Ni_{55}Fe_{17}Ga_{28}$ samples.

5.3.2 Experimental PALS results in $Ni_{55}Fe_{17}Ga_{28}$ alloy

In order to study the vacancy dynamics in samples quenched above and below the $T_{L2_1\text{-}B2}$, AQ samples have been subjected to isochronal annealing cycles (described in Sec. 5.2.1). For the sake of comparison, the isochronal annealing cycles have been performed using the same heating-cooling rate of 10 K/min employed in the DSC measurements. Moreover, $Ni_{55}Fe_{17}Ga_{28}$ samples have been heated from room temperature to a maximum temperature T_i ranging between 398 K - 698 K every 25 K.

Fig. 5.13 shows the evolution of $\overline{\tau}$ as a function of T_i for samples Q873 and Q1173. Although there is a significant variation of $\overline{\tau}$ as a function of T_i, spectra could not be decomposed because $\overline{\tau}$ is in a saturation-trapping regime [215]. Anywise, for a given defect (one positron trap), $\overline{\tau}$ only depends on C_v, and the relation between $\overline{\tau}$ and C_v is given by the so-called *one-trap model* defined previously in Eq. (5.30).

$$C_v = \frac{1}{\tau_b \mu_v} \frac{\overline{\tau} - \tau_b}{\tau_v - \overline{\tau}} \tag{5.33}$$

In line with the choice of the specific trapping rate acquired for Ni-Mn-Sn and

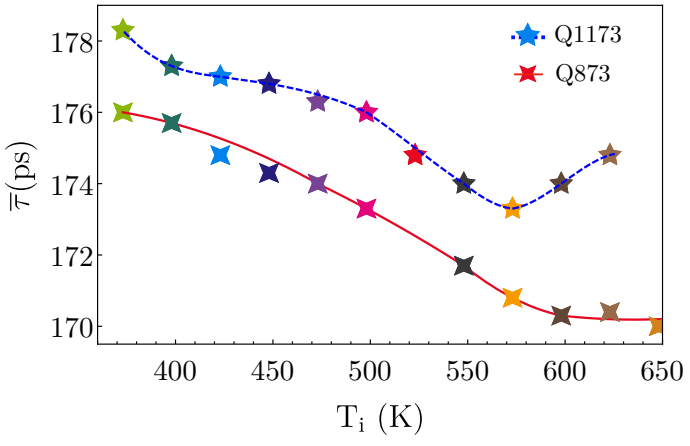

Figure 5.13: PALS measurements of the samples quenched above (Q1173), and below (Q873) $T_{L2_1\text{-}B2}$. The picture shows the measured $\overline{\tau}$ as a function of T_i. As it happens on DSC measurements, the evolution of Q1173 and Q873 sample differs at $T_i > 573$ K.

Ni-Mn-In samples, $\mu_v = 1.5 \times 10^{14} s^{-1}$ [219, 218, 79, 80] is selected for $Ni_{55}Fe_{17}Ga_{28}$. As it is inferred from the *one-trap model*, and evinced in Fig. 5.7, a larger $\overline{\tau}$ implies a larger C_v. Thus, according to Eq. (5.33), the vacancy concentration corresponding to the experimentally measured $\overline{\tau}$ can be obtained as long as τ_b and τ_v are known. These two lifetimes are often obtained from the decomposition of $\overline{\tau}$. However, due to the fact that the decomposition is not feasible, τ_b and τ_v cannot be obtained directly. Thus, in order to complement the experimental PALS results, DFT calculations of the positron lifetime in $Ni_{55}Fe_{17}Ga_{28}$ alloy have been performed using the Atomic Superposition method [207].

As described in Sec. 5.1.5, positron lifetime calculations are performed by overlapping the $n_+(\mathbf{r})$ positron density and $n_-(\mathbf{r})$ electron densities of the $Ni_{55}Fe_{17}Ga_{28}$, as defined in Eq. (5.23). The annihilation rate has been evaluated at both Γ and L points of the Brillouin zone, as well as calculating the average of the wave functions from Γ and L points. Regarding the calculation of vacancy-related characteristic positron lifetimes, and in order to overcome the artificial defect-defect interactions caused by the periodic boundary condition, a supercell approach has been used for positron lifetime calculations of the defected lattices.

The supercell has been built with increasing size in order to ensure convergence (0.1 ps lifetime values and < 0.01 eV in positron binding energies). For the austenite phase a $5 \times 5 \times 5$ supercell expansion of the primitive unit cell [231] has been created containing 500 atoms, whereas for the martensite phase a $3 \times 3 \times 3$ supercell expansion of the primitive unit cell [231] has been used with 108 total atoms. A mesh size of 160^3 has been used in the austenite and martensite supercells. Finally, the Schrödinger equation is discretized, and the positron wave function and its energy eigenvalue are solved iteratively at the mesh points of the supercell, using a numerical relaxation

method [216].

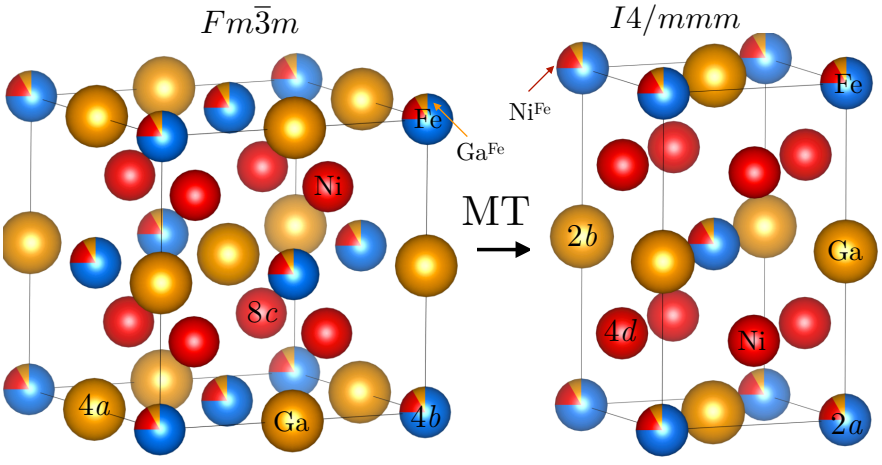

Figure 5.14: Illustration of the austenite and martensite phases of Ni-Fe-Ga. In the Ni-Fe-Ga systems, the excess of Ni and Ga atoms occupy the natural Fe positions.

In off-stoichiometric conditions, the excess Ni and Ga occupy Fe sites [231], thus leading to two non-equivalent positions of both Ni and Ga, and a single Fe position. This is illustrated in Fig. 5.14. Then, the supercell corresponding to $Ni_{55}Fe_{17}Ga_{28}$ have been built Starting from a stoichiometric Ni_2FeGa lattice and by substituting Fe atoms by Ni and Ga atoms until matching the proper composition of the sample. As a consequence, five types of vacancy defects are possible; V_{Ni}, V_{Fe} and V_{Ga}, and vacancies of antisite atoms V_{Ni}^{Fe} and V_{Ga}^{Fe}. The last vacancies refer to vacancies of antisite Ga and Ni excess atoms occupaying natural Fe positions. Calculations have been carried out for both, austenite ($Fm\bar{3}m$) and martensite ($I4/mmm$) phases. Table 5.4 gathers the crystallographic data of the structures used in the calculations.

The enhancement factor $\gamma(\mathbf{r})$ of Eq. (5.23) has been modeled within LDA and GGA approximations using five different parametrizations, labeled $\gamma(\mathbf{r})^{\mathrm{BN}}_{\mathrm{LDA}}$, $\gamma(\mathbf{r})^{\mathrm{AP1}}_{\mathrm{LDA}}$, $\gamma(\mathbf{r})^{\mathrm{AP2}}_{\mathrm{LDA}}$, $\gamma(\mathbf{r})^{\mathrm{AP1}}_{\mathrm{GGA}}$ and $\gamma(\mathbf{r})^{\mathrm{AP2}}_{\mathrm{GGA}}$ as defined in Section 5.1.5). Results of the calculated defect-related positron lifetimes are illustrated in Fig. 5.15. The area shaded in red indicates the range of experimental $\overline{\tau}$ values of Fig. 5.13. Calculated bulk lifetimes are not explicitly shown since in all cases τ_b ranges between 100 - 130 ps. Thus, in line with the results obtained in Ni-Mn-Sn and Ni-Mn-In samples, the presence of vacancy-type defects must be considered in order to explain the behavior of $\overline{\tau}$.

Regardless of the phase and the parametrization used, the calculated lifetime of V_{Ni} is slightly lower compared to the other ones. Depending on the $\gamma(\mathbf{r})$ parametrization, a clear dispersion is observed. On the one hand, by comparing the shaded area in Fig. 5.15 and the theoretical calculations, it is concluded that $\gamma(\mathbf{r})^{\mathrm{AP1}}_{\mathrm{LDA}}$ and $\gamma(\mathbf{r})^{\mathrm{AP2}}_{\mathrm{LDA}}$ underestimate the positron lifetime. These characteristic lifetimes cannot reproduce the experimental values because of the $\overline{\tau} \leq \tau_v$ constraint. On the other hand, $\gamma(\mathbf{r})^{\mathrm{AP1}}_{\mathrm{GGA}}$

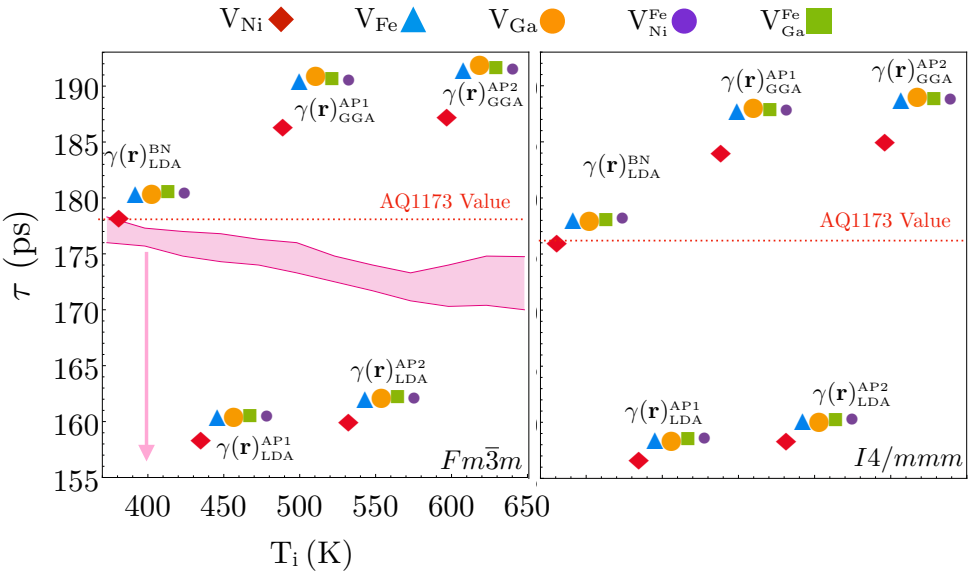

Figure 5.15: The calculated defect-related characteristic lifetimes for several possible type of vacancies, as well as for five different parametrization of $\gamma(\mathbf{r})$ for $Fm\bar{3}m$ phase (austenite), and for $I4/mmm$ phase (martensite). The red-dashed lines indicate experimental AQ $\overline{\tau}$ values. The red shaded area illustrates the experimentally measured $\overline{\tau}$ range in the austenite phase.

and $\gamma(\mathbf{r})^{\mathrm{AP2}}_{\mathrm{GGA}}$ yield values up to $\approx$ 12 ps higher than the experimental ones. These results are in line with those obtained for Ni-Mn-Z alloys.

As previously commented, the evolution of the experimental $\overline{\tau}$ is in the saturation-trapping regime. In this regime, the contribution of the saturated defect overcomes the bulk contribution and $\overline{\tau}$ reflects the characteristic lifetime that the defect present, $\overline{\tau} \approx \tau_v$ [215]. Along with it, the highest value that has been reached by quenching has always been around 178 ps. Therefore, as happened in Ni-Mn-Z (Z = Ga, In, Sn) systems, the $\gamma(\mathbf{r})^{\mathrm{BN}}_{\mathrm{LDA}}$ parametrization is the one that predicts best the experimental results in Ni-Fe-Ga systems, too.

The inset of Fig. 5.16 shows $\overline{\tau}$ values of AQ Q1173 (AQ1173) and AQ Q873 (AQ873) samples measured in both austenite ($Fm\bar{3}m$, yellow region) and martensite ($I4/mmm$, blue region) phases. As indicated by the area shaded in red, the $\overline{\tau}$ value of sample AQ1173 measured in the $Fm\bar{3}m$ phase is higher than the one of AQ873. The same trend is observed for samples AQ1173 and AQ873 measured in the $I4/mmm$ phase, indicating that the B2 phase is characterized by a higher C_v than the $L2_1$ phase. A larger C_v results in larger supply of vacancies, which assist more effectively the ordering process during quenching. This fact gives rise to an enhanced degree of $L2_1$ order in sample AQ1173, which explains the lower T_{MT} that AQ1173 exhibit compared to sample AQ873.

The last column of Table 5.4 gathers the calculated positron lifetimes using

Phase Ref. [220]	Cell parameters			τ_v
	Vacancy	Site	Occupancy	$\gamma(\mathbf{r})^{\mathrm{BN}}_{\mathrm{LDA}}$
Austenite $Fm\bar{3}m$, 225 $a = 5.774$Å	V_{Ni}	8*c* (1/4,1/4,1/4)	1.00	178 ps
	V^{Fe}_{Ni}	4*a* (0,0,0)	0.16	180 ps
	V_{Ga}	4*b* (1/2,1/2,1/2)	1.00	181 ps
	V^{Fe}_{Ga}	4*a* (0,0,0)	0.08	180 ps
	V_{Fe}	4*a* (0,0,0)	0.76	181 ps
	Bulk	(—)	(—)	106 ps
Martensite $I4/mmm$, 139 $a = b = 5.818$Å $c = 6.49600$	V_{Ni}	4*d* (0,1/2,1/4)	1.00	176 ps
	V^{Fe}_{Ni}	2*a* (0,0,0)	0.16	178 ps
	V_{Ga}	2*b* (0,0,1/2)	1.00	178 ps
	V^{Fe}_{Ga}	2*a* (0,0,0)	0.08	178 ps
	V_{Fe}	2*a* (0,0,0)	0.76	178 ps
	Bulk	(—)	(—)	104 ps

Table 5.4: Structural parameters used in theoretical calculations. The last column gathers the theoretical defect-related positron lifetime values calculated by $\gamma(\mathbf{r})^{\mathrm{BN}}_{\mathrm{LDA}}$ parametrization.

$\gamma(\mathbf{r})^{\mathrm{BN}}_{\mathrm{LDA}}$. It is worth mentioning that PALS measurements of samples Q1173 and Q873 during isochronal annealing cycles have been taken at 350 K ($Fm\bar{3}m$ phase). The calculated positron lifetime value of V_{Ni} is the one that best matches the experimental $\overline{\tau}$ value for sample AQ1173 (178 ps). Additionally, prior to isochronal annealing cycles, both quenched samples have been also measured in $I4/mmm$ phase at 273 K, showing a value of 176 ps for AQ1173 and 174 ps for AQ873 (see inset in Fig. 5.16, blue shaded area). As shown in Fig. 5.16, the 176 ps value matches with the calculated value of V_{Ni} in $I4/mmm$ phase (see inset Fig. 5.16). As a result, the vacancy concentration for AQ1173 is higher than the one for AQ873 in both phases, as AQ873 shows values below 178 ps in the $Fm\bar{3}m$ phase, and 176 ps in the $I4/mmm$ phase. The identification of V_{Ni} as the most probable vacancy present in $Ni_{55}Fe_{17}Ga_{28}$ is in good agreement with most predictions of vacancy formation energies in Ni-based Heusler alloys [197, 191, 192, 193, 195], which indicate that Ni is the vacancy that presents the lowest formation energy, ranging between 0.4 - 0.7 eV. Therefore, it can be concluded that V_{Ni} is the most probable vacancy type defect assisting the observed shift in T_{MT}. This result is again in line with the results obtained in Ni-Mn-Z (Z = Ga, In, Sn) systems. In fact, in both cases the parametrization that best predicts the experimental PALS data is $\gamma(\mathbf{r})^{\mathrm{BN}}_{\mathrm{LDA}}$, too.

At this point, and considering the good agreement between DFT calculation and PALS data, the C_v^{Ni}can be estimated from the corresponding $\overline{\tau}$ experimental data of Fig. 5.13. C_v^{Ni} can be calculated by means of Eq. (5.33) using the theoretical calculation corresponding to bulk and V_{Ni}, where $\tau_b = 106$ ps and $\tau_v = 178$ ps. The evolution of C_v^{Ni} as a function of isochronal annealing temperature is shown in Fig. 5.16

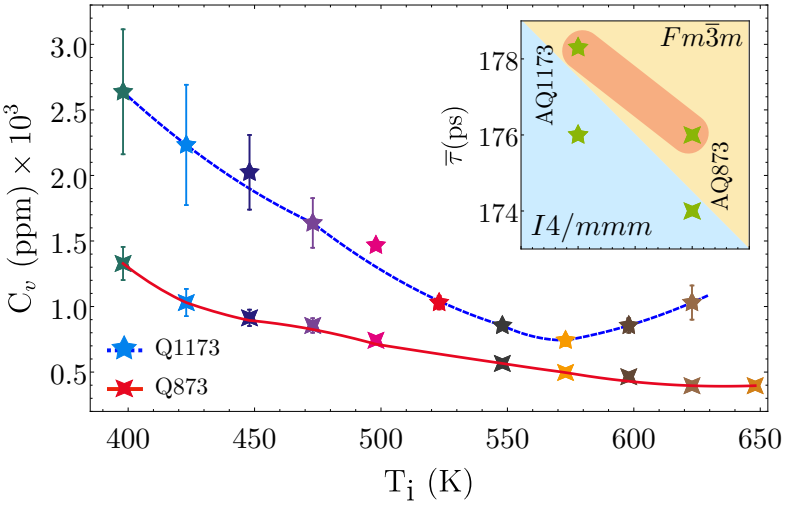

Figure 5.16: C_v^{Ni} calculated by means of Eq. (5.33), using $\tau_b = 106$ ps and $\tau_v = 178$ ps. The inset shows the experimental $\overline{\tau}$ values for samples AQ1173 and AQ873 measured in both austenite ($Fm\bar{3}m$, yellow region, measured at 350 K) and martensite (I4/mmm, blue region, measured at 273 K) phases.

It is important to notice that the evolution of C_v^{Ni} inherits the same evolution that $\overline{\tau}$ shows as a function of $\mathrm{T_i}$. By comparing the studied samples, the most outstanding fact is the different behavior of $\overline{\tau}$ (and C_v^{Ni}) for Q1173 and Q873 in respect to $\mathrm{T_i}$. For sample Q873 C_v^{Ni} decreases monotonically with $\mathrm{T_i}$ increase, while for sample Q1173 C_v^{Ni} decreases until $\mathrm{T_i} \approx 570$ K. Then, from that temperature on, C_v^{Ni} increases as $\mathrm{T_i}$ does, indicating different vacancy dynamics for samples quenched above and below $\mathrm{T_{L2_1\text{-}B2}}$. Additionally, the evolution of C_v^{Ni} in respect to $\mathrm{T_i}$ matches with the evolution of $\mathrm{T_{MT}}$ in respect to $\mathrm{T_i}$, which suggests that different vacancy dynamics may play a role on the dependency that the shift of $\mathrm{T_{MT}}$ shows on $\mathrm{T_q}$(see Fig. 5.8 and Fig. 5.9).

5.4 Relation Between Vacancy Concentration and the Shift of $\mathrm{T_{MT}}$

Up to now, the results obtained in $\mathrm{Ni_{55}Fe_{17}Ga_{28}}$ alloy are in line with those obtained in Ni-Mn-Z (Z = Ga, In, Sn) systems. In both cases, the parametrization that best predicts the experimental PALS results is $\gamma(\mathbf{r})^{\mathrm{BN}}_{\mathrm{LDA}}$. This parametrization also enables the identification of $\mathrm{V_{Ni}}$ as the vacancy present in $\mathrm{Ni_{55}Fe_{17}Ga_{28}}$ and Ni-Mn-Z (Z = Ga, In, Sn) systems. However, contrary to what happens in Ni-Mn-Sn and Ni-

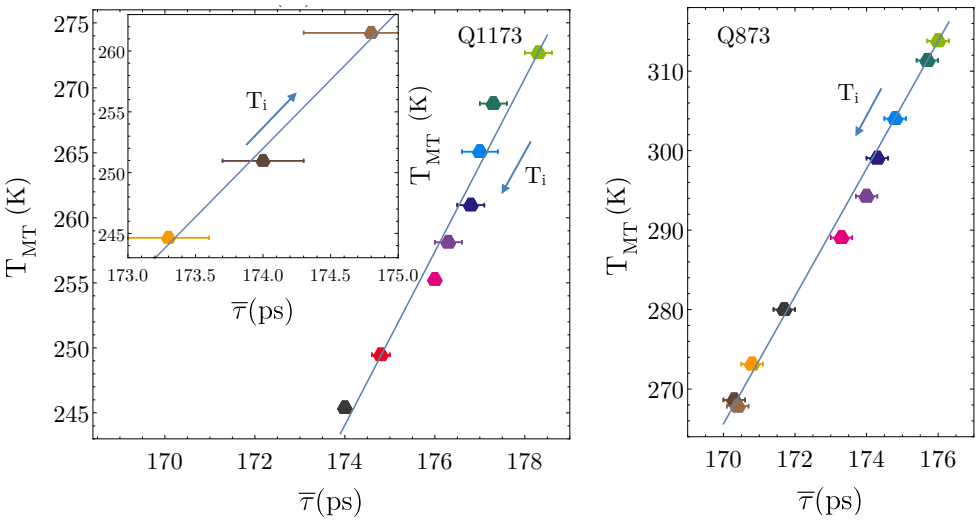

Figure 5.17: Mutual relationship between the evolution of T_{MT} and $\overline{\tau}$ in Q1173 and Q873 samples. For a better display, the range in which T_{MT} and $\overline{\tau}$ increase are shown in the inset. Both curves manifest the mutual dependence between $\overline{\tau}$ and T_{MT}.

Mn-In alloys, $Ni_{55}Fe_{17}Ga_{28}$ shows a clear evolution of $\overline{\tau}$, C_v^{Ni} and T_{MT} as a function of T_i. As vacancies assist the ordering process, the reduction of C_v^{Ni} may enhance the long-range atomic order degree, which would explain the observed evolution on T_{MT}.

Fig. 5.17 evinces the mutual dependence of the evolution of T_{MT} versus $\overline{\tau}$. In sample Q1173, the ordering process during subsequent isochronal annealing cycles is accomplished by a reduction of $\overline{\tau}$, which in turn, matches the T_{MT} decrease (see Fig. 5.12). It is important to notice that the reduction of $\overline{\tau}$ directly reflects a reduction in C_v^{Ni}. During the diffusion and annihilation of vacancies the sample is ordered, it implies that $L2_1$ order-degree is enhanced, and as a consequence, T_{MT} decreases. Additionally, as shown in the inset of Fig. 5.17, between 550 - 600 K, T_{MT} increases with $\overline{\tau}$ increase, which takes place at the same temperature. Indeed, the increase of $C_v^{Ni}$and the increase of T_{MT} take place at the same temperature and the inset shows their correlated evolution, see Fig. 5.18. In this process, thermally activated vacancies contribute to increase the disorder (lower $L2_1$ degree), which results in a T_{MT} increase. Regarding sample AQ873, Fig. 5.17 confirms, again, the mutual relationship between the evolution of T_{MT} and $\overline{\tau}$. As previously mentioned, the evolution of C_v^{Ni} inherits the dependence that $\overline{\tau}$ exhibit in respect to T_i. During the isochronal annealing cycles, T_{MT} decreases monotonically rather than showing a minimum value as the T_{MT} of Q1173 sample does. Even so, the evolution of $\overline{\tau}$ and C_v^{Ni} of Q873 sample follows the same trend of T_{MT}.

The different evolution of C_v^{Ni} that samples Q1173 and Q873 show as a function of the isochronal annealing temperature, evince a different vacancy dynamics in the

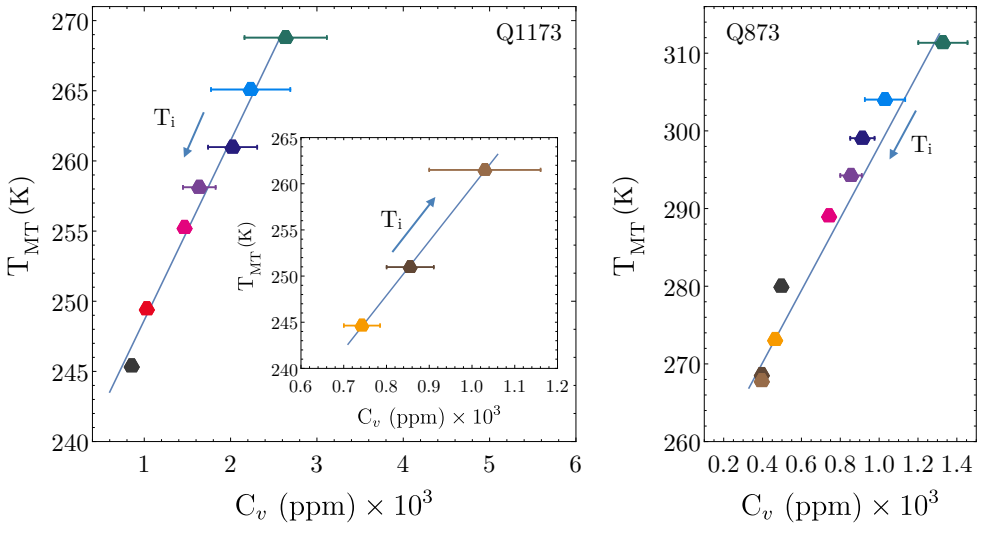

Figure 5.18: Mutual relationship between the evolution of T_{MT} and C_v^{Ni} in Q1173 and Q873 samples. For a better display, the range in which T_{MT} and C_v^{Ni} increase are shown in the inset. Both curves manifest the mutual dependence between vacancies and ΔT_{MT}.

samples quenched above or below $T_{L2_1\text{-}B2}$. This different evolution results, in turn, in a different evolution of T_{MT}. Moreover, the mutual dependence of C_v^{Ni} and T_{MT} exhibited by both samples does confirm that vacancies play a fundamental role in the evolution of T_{MT}. It is important to notice that the variation of T_{MT} (the recovery of the $L2_1$ order-degree assisted by vacancies) is relative to the retained $L2_1$ order-degree of the AQ samples. The underlaying mechanism by which vacancies drive the Δ T_{MT} may be related to the interaction of vacancies with partial dislocations [227], or vacancies acting as pinning centers [232, 198] among others. In particular, Ren and Otsuka [233, 234] demonstrate that for the short-range order adaptation between phases the aging of samples is needed, which opens a time lag for vacancies to accomodate. The diffusion of point defects to match the new symmetry may be a plausible mechanism by which the MT characteristics are altered. Anyway, as shown in Fig. 5.18, the present results clearly prove that vacancies play a fundamental role on ΔT_{MT} in Ni-Fe-Ga alloys.

6 Conclusions

The present thesis deals with the effect that microstructural defects have on the magnetic properties and on the MT of Ni-Mn-Z (Z = Ga, In, Sn) and Ni-Fe-Ga alloys. For this purpose, along with the standard characterization techniques, two additional specific nuclear techniques have been employed; ^{119}Sn Mössbauer Spectroscopy and PALS. In this connection, and for the consecution of this thesis, a PALS spectrometer has been designed, built and optimized. The setup has been tested in a Bi_2Se_3 sample (see Ref. [125]). Regarding Mössbauer spectroscopy, an offline eMS spectrometer has been built for measuring the ion implanted samples. Finally, a high temperature annealing furnace has been designed to carry out the annealing of powder samples under controllable atmosphere.

The main conclusion of this thesis are:

- Regarding the effect that mechanically induced defects have on the properties of Ni-Mn-In ball-milled alloys, it has been shown that long ball-milling times (≈ 40 h) induce the disappearance of the long-range atomic order and the subsequent occurrence of the MT. This approach leads to a frustrated magnetic system. The obtained amorphous state is compatible with a canonical spin glass state in the ball-milled $Ni_{50}Mn_{34}In_{16}$ powders.

- The crystallization dynamics of the ball-milled micro and nano samples, reveals that the recovery takes place at two-stage crystallization processes. On heating, an abrupt crystallization process occurs around 500 K, leading to a cubic B2 structure, which, in turn, does not show martensitic transformation. On further heating, a relaxation process takes place above 700 K concurrently with a B2-$L2_1$ atomic ordering, giving rise to an anomalous two-step thermal expansion. This fact demonstrates, that by a proper combination of ball-milling and annealing procedures, the high-temperature B2 phase can be obtained at much lower temperatures. On the other hand, the annealed micro and nano particles display a large relative cooling power linked to the magnetocaloric effect at the martensitic transformation. This results confirms the suitability of ball-milled samples for practical applications of magnetic refrigeration at nanoscale.

- In $Ni_{50}Mn_{35}Sn_{15}$ alloy, several microstructural states have been induced by means of soft-milling, where high internal strains, small grain sizes and a high density of defects are induced. The temperature range of the transformation is considerably affected by the mechanically induced local stresses, which in turn does not affect the equilibrium temperature between the austenite and martensite phases. Moreover, ^{119}Sn-MS results confirm its suitability to link the MT with the microstructural state. The recovery brought by annealing in the martensitic transformation is directly related to the intensity of the non-magnetic component revealed by ^{119}Sn-MS. Due to the high stability that Ni-Mn-Sn systems show against the atomic disorder, this result opens an additional way to properly tune the multifunctional properties in the Ni-Mn-Sn systems. From a technological point of view, once the transition temperature has been fixed by composition, the characteristics and therefore the properties linked to the martensitic transformation can be modified by thermomechanical treatments.

- The effect of internal stresses and strains on the MT has been extended to other compositions. In the $Ni_{45}Co_5Mn_{37}Sn_{13}$ sample it is found that the mechanically-induced defects, far for worsening, improve the magnetocaloric response. The different exchange coupling between nearest-neighbors Mn atoms in the austenite and in the martensite structures, makes the magnetization change at the martensitic transformation to be increased as a result of the presence of APB linked to dislocations.

- In $Ni_{50}Mn_{50-x}Sn_x$ (x = 25, 20, 15, 13, 10) and $Ni_{50}Mn_{50-x}In_x$ (x = 25, 20, 16, 13) alloys a thorough experimental and theoretical PALS study has been performed. The obtained experimental PALS results support that $\gamma(\mathbf{r})^{\mathrm{BN}}_{\mathrm{LDA}}$ parameterization is the one that best predicts PALS values in the studied systems. This work proves that V_{Ni} is the type of vacancy trapping positrons in these alloys, whith a characteristic V_{Ni}-related positron lifetime ranging between 181 - 191 ps. Different vacancy concentrations have been obtained as a function of heat treatments, as well.

- The PALS study has been extended to $Ni_{55}Fe_{17}Ga_{28}$ alloy. Together with theoretical electron-positron calculations, V_{Ni} is identified as the actual vacancy type present in these samples, too. The longstanding question whether the different T_{MT} evolution of samples quenched above or below $T_{L2_1\text{-}B2}$ rely on different vacancy dynamics, is answered. In $Ni_{55}Fe_{17}Ga_{28}$ alloy, vacancy evolution of and T_{MT} evolve hand by hand, an their mutual relationship is experimentally confirmed. The investigation carried out in $Ni_{55}Fe_{17}Ga_{28}$ evinces the potential of vacancies for the fine tuning of T_{MT}, which enables shifts up to $\approx$ 50 K.

Bibliography

Certainly the plagiarism, and dealing with the fallout of it, was the most difficult thing I've ever faced since I started writing.
-Nora Roberts

[1] P. Vilarinho, *"Functional Materials: Properties, Processing and Applications",* in *Scanning Probe Microscopy: Characterization, Nanofabrication and Device Application of Functional Materials*, P. M. Vilarinho, Y. Rosenwaks, and A. Kingon, eds., pp. 3–33. Springer Netherlands, Dordrecht, 2005.

[2] Y. Xu, *Ferroelectric Materials and Their Application.* North Holland, 1991.

[3] B. Jaffe, *Piezoelectric Ceramics.* Academic Press, London & New York, 1971.

[4] K. H. J. Buschow and F. R. de Boer, *Magnetostrictive Materials*, pp. 171–175. Springer US, Boston, MA, 2003. https://doi.org/10.1007/0-306-48408-0_16.

[5] T. Graf, C. Felser, and S. S. Parkin, *"Simple Rules for the Understanding of Heusler Compounds",* Progress in Solid State Chemistry **39**, 1 - 50 (2011).

[6] T. Graf, F. Casper, J. Winterlik, B. Balke, G. H. Fecher, and C. Felser, *"Crystal Structure of New Heusler Compounds",* Zeitschrift Für Anorganische und Allgemeine Chemie **635**, 976-981 .

[7] R. A. de Groot, F. M. Mueller, P. G. v. Engen, and K. H. J. Buschow, *"New Class of Materials: Half-Metallic Ferromagnets"*, Physical Review Letters **50**, 2024–2027 (1983).

[8] K. Ullakko, J. K. Huang, C. Kantner, R. C. O. Handley, and V. V. Kokorin, *"Large Magnetic-Field-Induced Strains in Ni_2MnGa Single Crystals"*, Applied Physics Letters **69**, 1966-1968 (1996).

[9] G.-H. Yu, Y.-L. Xu, Z.-H. Liu, H.-M. Qiu, Z.-Y. Zhu, X.-P. Huang, and L.-Q. Pan, *"Recent progress in Heusler-type Magnetic Shape Memory Alloys"*, Rare Metals **34**, 527–539 (2015).

[10] F. Heusler, *"Über Magnetische Manganlegierungen"*, Verhandlungen der Deutschen Physikalischen Gesellschaft **5**, 219 (1903).

[11] P. J. Webster, *"Heusler Alloys"*, Contemporary Physics **10**, 559-577 (1969).

[12] J. W. Christian, G. B. Olson, and M. Cohen, *"Classification of Displacive Transformations: What is a Martensitic Transformation?"*, J. Phys. IV France **05**, C8-3-C8-10 (1995).

[13] C. P. Opeil, B. Mihaila, R. K. Schulze, L. Mañosa, A. Planes, W. L. Hults, R. A. Fisher, P. S. Riseborough, P. B. Littlewood, J. L. Smith, and J. C. Lashley, *"Combined Experimental and Theoretical Investigation of the Premartensitic Transition in Ni_2MnGa"*, Physial Review Letters **100**, 165703 (2008).

[14] M. Ye, A. Kimura, Y. Miura, M. Shirai, Y. T. Cui, K. Shimada, H. Namatame, M. Taniguchi, S. Ueda, K. Kobayashi, R. Kainuma, T. Shishido, K. Fukushima, and T. Kanomata, *"Role of Electronic Structure in the Martensitic Phase Transition of $Ni_2Mn_{1+x}Sn_{1-x}$ Studied by Hard-X-Ray Photoelectron Spectroscopy and Ab Initio Calculation"*, Physial Review Letters **104**, 176401 (2010).

[15] V. Sánchez-Alarcos, V. Recarte, J. Pérez-Landazábal, C. Gómez-Polo, and J. Rodríguez-Velamazán, *"Role of magnetism on the martensitic transformation in Ni-Mn-based magnetic shape memory alloys"*, Acta Materialia **60**, 459 - 468 (2012).

[16] T. Krenke, M. Acet, E. F. Wassermann, X. Moya, L. Mañosa, and A. Planes, *"Martensitic transitions and the nature of ferromagnetism in the austenitic and martensitic states of Ni-Mn-Sn alloys"*, Physical Review B **72**, 014412 (2005).

[17] M. Chmielus, X. X. Zhang, C. Witherspoon, D. C. Dunand, and P. Mullner, *"Giant Magnetic-Field-induced Strains in Polycrystalline Ni-Mn-Ga Foams"*, Nature Materials **8**, 863–866 (2009).

[18] S. Y. Yu, Z. H. Liu, G. D. Liu, J. L. Chen, Z. X. Cao, G. H. Wu, B. Zhang, and X. X. Zhang, *"Large Magnetoresistance in Single-Crystalline $Ni_{50}Mn_{50-x}In_x$ Alloys ($x = 14 - 16$) Upon Martensitic Transformation"*, Applied Physics Letters **89**, 162503 (2006).

[19] W. Ito, K. Ito, R. Y. Umetsu, R. Kainuma, K. Koyama, K. Watanabe, A. Fujita, K. Oikawa, K. Ishida, and T. Kanomata, *"Kinetic Arrest of Martensitic Transformation in the NiCoMnIn Metamagnetic Shape Memory Alloy"*, Applied Physics Letters **92**, 021908 (2008).

[20] A. Planes, L. Mañosa, and M. Acet, *"Magnetocaloric Effect and Its Relation to Shape-Memory Properties in Ferromagnetic Heusler Alloys"*, Journal of Physics: Condensed Matter **21**, 233201 (2009).

[21] L. Mañosa, D. González-Alonso, A. Planes, E. Bonnot, M. Barrio, J.-L. Tamarit, S. Aksoy, and M. Acet, *"Giant Solid-State Barocaloric Effect in the Ni-Mn-In Magnetic Shape-Memory Alloy"*, Nature Materials **9**, 478–481 (2010).

[22] Z. D. Han, D. H. Wang, C. L. Zhang, H. C. Xuan, B. X. Gu, and Y. W. Du, *"Low-Field Inverse Magnetocaloric Effect in $Ni_{50-x}Mn_{39-x}Sn_{11}$"*, Applied Physics Letters **90**, 042507 (2007).

[23] T. Krenke, E. Duman, M. Acet, E. F. Wassermann, X. Moya, L. Manosa, and A. Planes, *"Inverse Magnetocaloric Effect in Ferromagnetic Ni-Mn-Sn Alloys"*, Nature Materials **4**, 450–454 (2005).

[24] M. Khan, I. Dubenko, S. Stadler, and N. Ali, *"Magnetostructural Phase Transitions in $Ni_{50}Mn_{25+x}Sb_{25-x}$ Heusler Alloys"*, Journal of Physis: Condensed Matter **20**, 235204 (2008).

[25] Y. B. Yang, X. B. Ma, X. G. Chen, J. Z. Wei, R. Wu, J. Z. Han, H. L. Du, C. S. Wang, S. Q. Liu, Y. C. Yang, Y. Zhang, and J. B. Yang, *"Structure and Exchange Bias of $Ni_{50}Mn_{37}Sn_{13}$ Ribbons"*, Journal of Applied Physics **111**, 07A916 (2012).

[26] Y. Sutou, Y. Imano, N. Koeda, T. Omori, R. Kainuma, K. Ishida, and K. Oikawa, *"Magnetic and Martensitic Transformations of Ni-Mn-X (X = In, Sn, Sb) Ferromagnetic Shape Memory Alloys"*, Applied Physics Letters **85**, 4358-4360 (2004).

[27] J. Liu, T. Gottschall, K. P. Skokov, J. D. Moore, and O. Gutfleisch, *"Giant Magnetocaloric Effect Driven by Structural Transitions"*, Nature Materials **11**, 620–626 (2012).

[28] R. Hamilton, H. Sehitoglu, C. Efstathiou, and H. Maier, *"Inter-Martensitic Transitions in Ni-Fe-Ga Single Crystals"*, Acta Materialia **55**, 4867 - 4876 (2007).

[29] A. Sozinov, N. Lanska, A. Soroka, and W. Zou, *"12% Magnetic Field-Induced Strain in Ni-Mn-Ga-Based Non-Modulated Martensite"*, Applied Physics Letters **102**, 021902 (2013).

[30] K. Oikawa, T. Ota, T. Ohmori, Y. Tanaka, H. Morito, A. Fujita, R. Kainuma, K. Fukamichi, and K. Ishida, *"Magnetic and Martensitic Phase Transitions in Ferromagnetic Ni-Ga-Fe Shape Memory Alloys"*, Applied Physics Letters **81**, 5201-5203 (2002).

[31] P. Álvarez-Alonso, C. Aguilar-Ortiz, E. Villa, A. Nespoli, H. Flores-Zúñiga, and V. Chernenko, *"Conventional and Inverse Elastocaloric Effect in Ni-Fe-Ga and Ni-Mn-Sn Ribbons"*, Scripta Materialia **128**, 36 - 40 (2017).

[32] Y. Xu, B. Lu, W. Sun, A. Yan, and J. Liu, *"Large and Reversible Elastocaloric Effect in Dual-Phase $Ni_{54}Fe_{19}Ga_{27}$ Superelastic Alloys"*, Applied Physics Letters **106**, 201903 (2015).

[33] S. Chabungbam, P. Borgohain, S. Ghosh, N. Singh, and M. B. Sahariah, *"Martensitic Transformation and Magnetism in Ni and Fe-rich Compositions of Ni-Fe-Ga Shape Memory Alloys"*, Journal of Alloys and Compounds **689**, 199 - 207 (2016).

[34] Y. Li, D. Zhao, and J. Liu, *"Giant and Reversible Room-Temperature Elastocaloric Effect in a Single-Crystalline Ni-Fe-Ga Magnetic Shape Memory Alloy"*, Scientific Reports **6**, 25500 EP - (2016).

[35] J. Pons, E. Cesari, C. Seguí, F. Masdeu, and R. Santamarta, *"Ferromagnetic Shape Memory Alloys: Alternatives to Ni-Mn-Ga"*, Materials Science and Engineering: A **481-482**, 57 - 65 (2008). Proceedings of the 7th European Symposium on Martensitic Transformations, ESOMAT 2006.

[36] R. C. O'Handley, *"Model for Strain and Magnetization in Magnetic Shape-Memory Alloys"*, Journal of Applied Physics **83**, 3263-3270 (1998).

[37] Z. H. Liu, M. Zhang, Y. T. Cui, Y. Q. Zhou, W. H. Wang, G. H. Wu, X. X. Zhang, and G. Xiao, *"Martensitic Transformation and Shape Memory Effect in Ferromagnetic Heusler alloy Ni_2FeGa"*, Applied Physics Letters **82**, 424-426 (2003).

[38] Z. H. Liu, H. N. Hu, G. D. Liu, Y. T. Cui, M. Zhang, J. L. Chen, G. H. Wu, and G. Xiao, *"Electronic Structure and Ferromagnetism in the Martensitic Transformation Material Ni_2FeGa"*, Physical Review B **69**, 134415 (2004).

[39] Y. Qawasmeh and B. Hamad, *"Investigation of the Structural, Electronic, and Magnetic Properties of Ni-based Heusler Alloys From First Principles"*, Journal of Applied Physics **111**, 033905 (2012).

[40] H. Karaca, I. Karaman, B. Basaran, Y. Chumlyakov, and H. Maier, *"Magnetic Field and Stress Induced Martensite Reorientation in NiMnGa Ferromagnetic Shape Memory Alloy Single Crystals"*, Acta Materialia **54**, 233 - 245 (2006).

[41] J. hoon Kim, T. Fukuda, and T. Kakeshita, *"A New Phase Induced in Ni_2MnGa by Uniaxial Stress"*, Scripta Materialia **54**, 585 - 588 (2006).

[42] J. M. Barandiarán, V. A. Chernenko, P. Lázpita, J. Gutiérrez, and J. Feuchtwanger, *"Effect of Martensitic Transformation and Magnetic Field on Transport Properties of Ni-Mn-Ga and Ni-Fe-Ga Heusler Alloys"*, Physical Review B **80**, 104404 (2009).

[43] R. Kainuma, Y. Imano, W. Ito, Y. Sutou, H. Morito, S. Okamoto, O. Kitakami, K. Oikawa, A. Fujita, T. Kanomata, and K. Ishida, *"Magnetic-Field-Induced Shape Recovery by Reverse Phase Transformation"*, Nature **439**, 957–960 (2006).

[44] T. Krenke, M. Acet, E. F. Wassermann, X. Moya, L. Mañosa, and A. Planes, *"Ferromagnetism in the Austenitic and Martensitic States of Ni-Mn-In Alloys"*, Physical Review B **73**, 174413 (2006).

[45] P. J. Brown, A. P. Gandy, K. Ishida, R. Kainuma, T. Kanomata, K.-U. Neumann, K. Oikawa, B. Ouladdiaf, and K. R. A. Ziebeck, *"The Magnetic and Structural Properties of the Magnetic Shape Memory Compound $Ni_2Mn_{1.44}Sn_{0.56}$"*, Journal of Physics: Condensed Matter **18**, 2249 (2006).

[46] H. Yan, Y. Zhang, N. Xu, A. Senyshyn, H.-G. Brokmeier, C. Esling, X. Zhao, and L. Zuo, *"Crystal Structure Determination of Incommensurate Modulated Martensite in Ni-Mn-In Heusler alloys"*, Acta Materialia **88**, 375 - 388 (2015).

[47] V. K. Sharma, M. K. Chattopadhyay, and S. B. Roy, *"Large Inverse Magnetocaloric Effect in $Ni_{50}Mn_{34}In_{16}$"*, Journal of Physics D: Applied Physics **40**, 1869 (2007).

[48] H. Liu, C. Zhang, Z. Han, H. Xuan, D. Wang, and Y. Du, *"The Effect of Co Doping on the Magnetic Entropy Changes in $Ni_{44-x}Co_xMn_{45}Sn_{11}$ Alloys"*, Journal of Alloys and Compounds **467**, 27 - 30 (2009).

[49] V. Recarte, J. Pérez-Landazábal, V. Sánchez-Alarcos, and J. Rodríguez-Velamazán, *"Dependence of the Martensitic Transformation and Magnetic Transition on the Atomic Order in Ni-Mn-In Metamagnetic shape memory alloys"*, Acta Materialia **60**, 1937 - 1945 (2012).

[50] J. L. S. Llamazares, H. Flores-Zúñiga, D. Ríos-Jara, C. F. Sánchez-Valdes, T. García-Fernández, C. A. Ross, and C. García, *"Structural and Magnetic Characterization of the Intermartensitic Ihase Transition in Ni-Mn-Sn Heusler Alloy Ribbons"*, Journal of Applied Physics **113**, 17A948 (2013).

[51] M. Acet, *"Magnetic Shape Memory: Magnetoelastic Sponges"*, Nature Materials **8**, 854–855 (2009).

[52] R. Niemann, O. Heczko, L. Schultz, and S. Fähler, *"Metamagnetic Transitions and Magnetocaloric Effect in Epitaxial Ni-Co-Mn-In films"*, Applied Physics Letters **97**, 222507 (2010).

[53] J. Feuchtwanger, M. L. Richard, Y. J. Tang, A. E. Berkowitz, R. C. O'Handley, and S. M. Allen, *"Large Energy Absorption in Ni-Mn-Ga/Polymer Composites"*, Journal of Applied Physics **97**, 10M319 (2005).

[54] J. Liu, N. Scheerbaum, S. Kauffmann-Weiss, and O. Gutfleisch, *"Ni-Mn-Based Alloys and Composites for Magnetically Controlled Dampers and Actuators"*, Advanced Engineering Materials **14**, 653–667 (2012).

[55] M. Schmitt, A. Backen, S. Fähler, and M. Kohl, *"Freely Movable Ferromagnetic Shape Memory Nanostructures for Actuation"*, Microelectronic Engineering **98**, 536 - 539 (2012).

[56] M. Kohn, D. Brugger, M. Ohtsuka, and T. Takagi, *"A Novel Actuation Mechanism on the Basis of Ferromagnetic SMA Thin Films"*, Sensors and Actuators A: Physical **114**, 445 - 450 (2004). Selected papers from Transducers 03.

[57] C. Biffi and A. Tuissi, *"Micro-Processing of Ni-Mn-Ga Shape Memory Alloy by Using a Nanosecond Fiber Laser"*, Optics & Laser Technology **78, Part B**, 42 - 49 (2016).

[58] S. V. Kumar, R. Singh, M. M. Raja, A. Kumar, S. Bysakh, and M. Mahendran, *"Microstructure and Nanomechanical Properties of Mn-rich Ni-Mn-Ga Thin Films"*, Intermetallics **71**, 57 - 64 (2016).

[59] Z. Zhang, X. Ding, J. Sun, T. Suzuki, T. Lookman, K. Otsuka, and X. Ren, *"Nonhysteretic Superelasticity of Shape Memory Alloys at the Nanoscale"*, Physical Review Letters **111**, 145701 (2013).

[60] K. V. Peruman, S. Vinodh Kumar, K. Pushpanathan, and M. Mahendran, *"Structural and Martensitic Transformation of Bulk, Disordered and Nanocrystalline Ni_2MnGa Alloys"*, Funct. Mater. Lett. **04**, 415-418 (2011).

[61] J. Ortín and A. Planes, *"Thermodynamic Analysis of Thermal Measurements in Thermoelastic Martensitic Transformations"*, Acta Metallurgica **36**, 1873 - 1889 (1988).

[62] A. Roytburd, T. Kim, Q. Su, J. Slutsker, and M. Wuttig, *"Martensitic Transformation in Constrained Films"*, Acta Materialia **46**, 5095 - 5107 (1998).

[63] V. Sánchez-Alarcos, J. Pérez-Landazábal, V. Recarte, I. Lucía, J. Vélez, and J. Rodríguez-Velamazán, *"Effect of High-Temperature Quenching on the Magnetostructural Transformations and the Long-Range Atomic Order of Ni-Mn-Sn and Ni-Mn-Sb metamagnetic shape memory alloys"*, Acta Materialia **61**, 4676 - 4682 (2013).

[64] V. Sánchez-Alarcos, J. López-García, I. Unzueta, J. Pérez-Landazábal, V. Recarte, J. Beato-López, J. García, F. Plazaola, and J. Rodríguez-Velamazán, *"Magnetocaloric Effect Enhancement Driven by Intrinsic Defects in a $Ni_{45}Co_5Mn_{35}Sn_{15}$ Alloy"*, Journal of Alloys and Compounds **774**, 586 - 592 (2019).

[65] V. Sánchez-Alarcos, V. Recarte, J. Pérez-Landazábal, S. Larumbe, R. Caballero-Flores, I. Unzueta, J. García, F. Plazaola, and J. Rodríguez-Velamazán, *"Mechanically Induced Disorder and Crystallization Process in Ni-Mn-In Ball-Milled Alloys"*, Journal of Alloys and Compounds **689**, 983 - 991 (2016).

[66] S. Aksoy, *"Synthesis and Characterization of Ni-Mn-In Nanoparticles"*, Journal of Magnetism and Magnetic Materials **373**, 236 - 239 (2015). Recent Advances in Nanomagnetism and Spintronics.

[67] Y. D. Wang, Y. Ren, Z. H. Nie, D. M. Liu, L. Zuo, H. Choo, H. Li, P. K. Liaw, J. Q. Yan, R. J. McQueeney, J. W. Richardson, and A. Huq, *"Structural Transition of Ferromagnetic Ni_2MnGa Nanoparticles"*, Journal of Applied Physics **101**, 063530 (2007).

[68] B. Tian, F. Chen, Y. Liu, and Y. Zheng, *"Structural Transition and Atomic Ordering of $Ni_{49.8}Mn_{28.5}Ga_{21.7}$ Ferromagnetic Shape Memory Alloy Powders Prepared by Ball Milling"*, Materials Letters **62**, 2851 - 2854 (2008).

[69] R. Das, A. Perumal, and A. Srinivasan, *"Effect of Particle Size on the Magneto-Caloric Properties of $Ni_{51}Mn_{34}In_{14}Si_1$ alloy"*, Journal of Alloys and Compounds **572**, 192 - 198 (2013).

[70] K. V. Peruman, M. Mahendran, S. Seenithurai, R. Chokkalingam, R. Singh, and V. Chandrasekaran, *"Internal Stress Dependent Structural Transition in Ferromagnetic Ni-Mn-Ga Nanoparticles Prepared by Ball Milling"*, Journal of Physics and Chemistry of Solids **71**, 1540 - 1544 (2010).

[71] A. A. Prasanna and S. Ram, *"Local Strains, Calorimetry, and Magnetoresistance in Adaptive Martensite Transition in Multiple Nanostrips of $Ni_{39+x}Mn_{50}Sn_{11-x}$ ($x \leq 2$) alloys"*, Science and Technology of Advanced Materials **14**, 015004 (2013).

[72] H. Scherngell and A. Kneissl, *"Generation, Development and Degradation of the Intrinsic Two-way Shape Memory Effect in Different Alloy Systems"*, Acta Materialia **50**, 327 - 341 (2002).

[73] G. Rao, J. Wang, E. Han, and W. Ke, *"Study of Residual Stress Accumulation in Ti-Ni Shape Memory Alloy During Fatigue Using EBSD Technique"*, Mater. Lett. **60**, 779 - 782 (2006).

[74] A. Ghotbi Varzaneh, P. Kameli, V. R. Zahedi, F. Karimzadeh, and H. Salamati, *"Effect of Heat Treatment on Martensitic Transformation of $Ni_{47}Mn_{40}Sn_{13}$ Ferromagnetic Shape Memory Alloy Prepared by Mechanical Alloying"*, Met. Mater. Int **21**, 758–764 (2015).

[75] A. L. Alves, E. C. Passamani, V. P. Nascimento, A. Y. Takeuchi, and C. Larica, *"Influence of Grain Refinement and Induced Crystal Defects on the Magnetic Properties of $Ni_{50}Mn_{36}Sn_{14}$ Heusler Alloy"*, Journal of Physics D: Applied Physics **43**, 345001 (2010).

[76] V. Sánchez-Alarcos, V. Recarte, J. Pérez-Landazábal, and G. Cuello, *"Correlation Between Atomic Order and the Characteristics of the Structural and Magnetic*

Transformations in Ni-Mn-Ga Shape Memory Alloys", Acta Materialia **55**, 3883 - 3889 (2007).

[77] V. Sánchez-Alarcos, J. I. Pérez-Landazábal, V. Recarte, J. A. Rodríguez-Velamazán, and V. A. Chernenko, *"Effect of Atomic Order on the Martensitic and Magnetic Transformations in Ni-Mn-Ga Ferromagnetic Shape Memory Alloys"*, Journal of Physics: Condensed Matter **22**, 166001 (2010).

[78] V. Sánchez-Alarcos, J. Pérez-Landazábal, C. Gómez-Polo, and V. Recarte, *"Influence of the Atomic Order on the Magnetic Characteristics of a Ni-Mn-Ga Ferromagnetic Shape Memory Alloy"*, Journal of Magnetism and Magnetic Materials **320**, e160 - e163 (2008).

[79] D. Merida, J. A. García, V. Sánchez-Alarcos, J. I. Pérez-Landazábal, V. Recarte, and F. Plazaola, *"Vacancy Dynamic in Ni-Mn-Ga Ferromagnetic Shape Memory Alloys"*, Applied Physics Letters **104**, 231905 (2014).

[80] D. Merida, J. García, V. Sánchez-Alarcos, J. Pérez-Landazábal, V. Recarte, and F. Plazaola, *"Characterisation and Modelling of Vacancy Dynamics in Ni-Mn-Ga Ferromagnetic Shape Memory Alloys"*, Journal of Alloys and Compounds **639**, 180 - 186 (2015).

[81] G. D. Liu, X. F. Dai, H. Z. Luo, H. Y. Liu, F. B. Meng, Y. Li, X. Yu, J. L. Chen, and G. H. Wu, *"The Effect of Internal and External Stress on Two-Way Shape-Memory Behaviour in $Co_{49}Ni_{21.6}Ga_{29.4}$ single crystals"*, J. Phys. D: Appl. Phys. **44**, 045002 (2011).

[82] D. Schlagel, R. McCallum, and T. Lograsso, *"Influence of Solidification Microstructure on the Magnetic Properties of Ni-Mn-Sn Heusler Alloys"*, Journal of Alloys and Compounds **463**, 38 - 46 (2008).

[83] L. de Broglie, *"Rayonnement Noir Et Quanta de Lumière"*, Journal de Physique **3**, 422 (1922).

[84] B. D. Josephson, *"The Discovery of Tunnelling Supercurrents"*, Review of Modern Physics **46**, 251–254 (1974).

[85] F. Simon, *"Versatile and Sensitive Vibrating Sample Magnetometer"*, Review of Scientific Instruments **30**, 548-557 (1959).

[86] G. W. Van Oosterhout, *"A Rapid Method for Measuring Coercive Force and Other Ferromagnetic Properties of Very Small Samples"*, Applied Scientific Research, Section B **6**, 101–104 (1957).

[87] B. D. Cullity and S. R. Stock, *Elements of X-Ray Diffraction.* 3rd Edition, Prentice Hall, (2001).

[88] H. M. Rietveld, *"Line Profiles of Neutron Powder-Diffraction Peaks for Structure Refinement"*, Acta Crystallographica **22**, 151–152 (1967).

[89] H. M. Rietveld, *"A Profile Refinement Method for Nuclear and Magnetic Structures"*, Journal of Applied Crystallography **2**, 65–71 (1969).

[90] R. L. Mössbauer, *"Kernresonanzfluoreszenz von Gammastrahlung in ^{191}Ir"*, Zeitschrift für Physik **151**, 124–143 (1958).

[91] Y. L. Chen and D. P. Yang, *Mössbauer Effect in Lattice Dynamics.* Wiley-VCH, 2007.

[92] D. L. Williamson, L. Niesen, G. Weyer, R. Sielemann, and G. Langouche, *Hyperfine Interaction of Defects in Semiconductors*. Elsevier, Netherlands, 1992.

[93] P. Gütlich, E. Bill, and A. X. Trautwein, *Mössbauer Spectroscopy and Transition Metal Chemistry*. Springer-Verlag, 2011.

[94] W. K. Gunther, *Mössbauer Effect: Principles and Applications*. Academic Press, New York and London, 1964.

[95] P. K. Michael Kalvius, *The Rudolf Mössbauer Story*. Springer-Verlag Berlin Heidelberg, 2012.

[96] Live Chart of Nuclides IAEA NDS.

[97] I. Nowik, I. Felner, Z. Ren, G. H. Cao, and Z. A. Xu, *"Coexistence of Ferromagnetism and Superconductivity: Magnetization and Mösbauer Studies of $EuFe_2(As_{1-x}P_x)_2$"*, Journal of Physics: Condensed Matter **23**, 065701 (2011).

[98] T. E. M. lt, *Paramagnetism in Ion-Implanted Oxides*. PhD thesis, Faculty of Physical Science, University of Iceland, 2012.

[99] V. Fedoseyev, K. Bätzner, R. Catherall, A. Evensen, D. Forkel-Wirth, O. Jonsson, E. Kugler, J. Lettry, V. Mishin, H. Ravn, and G. Weyer, *"Chemically Zelective Laser ion Source of Manganese"*, Nuclear Instruments and Methods in Physics Research Section B: Beam Interactions with Materials and Atoms **126**, 88 - 91 (1997). International Conference on Electromagnetic Isotope Separators and Techniques Related to Their Applications.

[100] M. Deicher, G. Weyer, T. Wichert, and the ISOLDE Collaboration, *"Solid state physics at ISOLDE"*, Hyperfine Interactions **151**, 105–123 (2003).

[101] H. Masenda, *Are Fe and Co implanted ZnO and III-Nitride Semiconductors Magnetic?* PhD thesis, Faculty of Science, University of Witwatersrand, Johannesburg, 2014.

[102] F. Paschen, *"Ueber die zum Funkenübergang in Luft, Wasserstoff und Kohlensäure bei Verschiedenen Drucken Erforderliche Potentialdifferenz"*, Annalen der Physik **273**, 69-96 (1889).

[103] Brand RA (1998) NORMOS-98 Mössbauer Fitting Program Package.

[104] H. P. Gunnlaugsson, *"Spreadsheet based analysis of Mössbauer spectra"*, Hyperfine Interactions **237**, 79 (2016).

[105] P. Hautöjarvi, *Positrons in Solids. Topics in Current Physics*, volume 12. Springer, Heidelberg, 1979.

[106] H. L. R. Krause-Rehberg, *Positron Annihilation in Semiconductors. Defect Studies*, volume 27. Springer-Verlag, Berlin, 1999.

[107] L. Sodickson, W. Bowman, J. Stephenson, and R. Weinstein, *"Single-Quantum Annihilation of Positrons"*, Physical Review **124**, 1851–1861 (1961).

[108] W. Brandt and R. Paulin, *"Positron Implantation-Profile Effects in Solids"*, Physical Review B **15**, 2511–2518 (1977).

[109] A. Perkins and J. P. Carbotte, *"Effect of the Positron-Phonon Interaction on Positron Motion"*, Physical Review B **1**, 101–107 (1970).

[110] J. Oliva, *"Inelastic Positron Scattering in an Electron Gas"*, Physical Review B **21**, 4909–4917 (1980).

[111] J. Bardeen and W. Shockley, *"Scattering of Electrons in Crystals in the Presence of Large Electric Fields"*, Physical Review **80**, 69–71 (1950).

[112] E. Soininen, H. Huomo, P. A. Huttunen, J. Mäkinen, A. Vehanen, and P. Hautojärvi, *"Temperature Dependence of Positron Diffusion in Cubic Metals"*, Physical Review B **41**, 6227–6233 (1990).

[113] E. Soininen, J. Mäkinen, D. Beyer, and P. Hautojärvi, *"High-Temperature Positron Diffusion in Si, GaAs, and Ge"*, Physical Review B **46**, 13104–13118 (1992).

[114] P. J. Schultz and K. G. Lynn, *"Interaction of Positron Beams with Surfaces, Thin Films, and Interfaces"*, Review of Modern Physics **60**, 701–779 (1988).

[115] F. Tuomisto, *Defect Characterization in Semiconductors with Positron Annihilation Spectroscopy*, pp. 1551–1579. Springer Berlin Heidelberg, Berlin, Heidelberg, 2010. https://doi.org/10.1007/978-3-540-74761-1_46.

[116] W. Brandt and R. Paulin, *"Positron Diffusion in Solids"*, Physical Review B **5**, 2430–2435 (1972).

[117] M. Puska and R. Nieminen, *"Theory of Positrons in Solids and on Solid Surfaces"*, Review of Modern Physics **66**, 841–897 (1994).

[118] P. Kirkegaard and M. Eldrup, *"Positronfit extended: A New Version of a Program for Analysing Position Lifetime Spectra"*, Computer Physics Communications **7**, 401 - 409 (1974).

[119] K. Plotkowski, T. J. Panek, and J. Kansy, *"Positron Implantation Profile in Kapton"*, Il Nuovo Cimento D **10**, 933–940 (1988).

[120] I. K. MacKenzie and J. Fabian, *"Temperature Dependence of the Source Component in Positron Annihilation Measurements"*, Il Nuovo Cimento B (1971-1996) **58**, 162–168 (1980).

[121] M. Bertolaccini and L. Zappa, *"Source-Supporting Foil Effect on the Shape of Positron Time Annihilation Spectra"*, Il Nuovo Cimento B (1965-1970) **52**, 487–494 (1967).

[122] B. Somieski, T. Staab, and R. Krause-Rehberg, *"The Data Treatment Influence on the Spectra Decomposition in Positron Lifetime Spectroscopy Part 1: On the Interpretation of Multi-Component Analysis Studied by Monte Carlo Simulated Model Spectra"*, Nuclear Instruments and Methods in Physics Research Section A: Accelerators, Spectrometers, Detectors and Associated Equipment **381**, 128 - 140 (1996).

[123] J. M. C. Robles, E. Ogando, and F. Plazaola, *"Positron Lifetime Calculation for the Elements of the Periodic Table"*, Journal of Physics: Condensed Matter **19**, 176222 (2007).

[124] I. Unzueta, *"Desarrollo y Optimización de un Espectrómetro de Tiempos de Vida de Aniquilación de Positrones: Aplicación al Aislante Topológico Bi_2Se_3"*, Master's thesis, Euskal Herriko Unibertsitatea (UPV/EHU), Fisika Aplikatua II, Zientzia eta Teknologia Fakultatea, 2013.

[125] I. Unzueta, N. Zabala, V. Marín-Borrás, V. Muñoz Sanjosé, J. A. García, and F. Plazaola, *"Observation of a Charge Delocalization from Se Vacancies in* Bi_2Se_3*: A Positron Annihilation Study of Native Defects"*, Physical Review B **94**, 014117 (2016).

[126] P. Gorria, P. Álvarez, J. S. Marcos, J. L. S. Llamazares, M. J. Pérez, and J. A. Blanco, *"Crystal structure, Magnetocaloric Effect and Magnetovolume Anomalies in Nanostructured Pr_2Fe_17"*, Acta Materialia **57**, 1724 - 1733 (2009).

[127] W. Dagula, O. Tegus, X. W. Li, L. Song, E. Brück, D. T. Cam Thanh, F. R. de Boer, and K. H. J. Buschow, *"Magnetic Properties and Magnetic-Entropy Change of $MnFeP_{0.5}As_{0.5-x}Si_x$ $(x = 0 - 0.3)$ Compounds"*, Journal of Applied Physics **99**, 08Q105 (2006).

[128] A. G. Varzaneh, P. Kameli, F. Karimzadeh, B. Aslibeiki, G. Varvaro, and H. Salamati, *"Magnetocaloric Effect in $Ni_{47}Mn_{40}Sn_{13}$ Alloy Prepared by Mechanical Alloying"*, Journal of Alloys and Compounds **598**, 6 - 10 (2014).

[129] D. M. Liu, Z. H. Nie, Y. Ren, Y. D. Wang, J. Pearson, P. K. Liaw, and D. E. Brown, *"Structural Transitions and Magnetic Properties of $Ni_{50}Mn_{36.7}In_{13.3}$ Particles with Amorphous-Like Phase"*, Metallurgical and Materials Transactions A **42**, 3062 (2011).

[130] X. P. Fei, W. Li, J. Liu, F. Xu, G. D. Tang, W. S. Tan, and S. D. Li, *"Phase Transition of Ball-Milled $Ni_{50-x}Mn_{37}In_{13}Co_x$ $(x = 0, 5)$ Alloy Powders"*, in *2014 China Functional Materials Technology and Industry Forum*, volume 809 of *Materials Science Forum*, pp. 377–383. Trans Tech Publications, 2015.

[131] B. Aslibeiki, P. Kameli, H. Salamati, M. Eshraghi, and T. Tahmasebi, *"Superspin glass state in $MnFe_2O_4$ nanoparticles"*, Journal of Magnetism and Magnetic Materials **322**, 2929 - 2934 (2010).

[132] S. N. Jammalamadaka, S. S. Rao, J. Vanacken, A. Stesmans, S. V. Bhat, and V. V. Moshchalkov, *"Martensite-like Transition and Spin-Glass Behavior in Nanocrystalline $Pr_{0.5}Ca_{0.5}MnO_3$"*, AIP Advances 042151 (2011).

[133] S. Mukherjee, R. Ranganathan, P. S. Anilkumar, and P. A. Joy, *"Static and Dynamic Response of Cluster Glass in $La_{0.5}Sr_{0.5}CoO_3$"*, Physical Review B **54**, 9267–9274 (1996).

[134] A. Kumar, R. P. Tandon, and V. P. S. Awana, *"Study of Spin Glass and Cluster Ferromagnetism in $RuSr_2Eu_{1.4}Ce_{0.6}Cu_2O_{10-\delta}$ Magneto Superconductor"*, Journal of Applied Physics **110**, 043926 (2011).

[135] J. López, H.-D. Pfannes, R. Paniago, J. Sinnecker, and M. Novak, *"Investigation of the Static and Dynamic Magnetic Properties of $CoFe_2O_4$ Nanoparticles"*, Journal of Magnetism and Magnetic Materials **320**, e327 - e330 (2008).

[136] L. Ma, W. H. Wang, J. B. Lu, J. Q. Li, C. M. Zhen, D. L. Hou, and G. H. Wu, *"Coexistence of Reentrant-Spin-Glass and Ferromagnetic Martensitic Phases in the $Mn_2Ni_{1.6}Sn_{0.4}$ Heusler Alloy"*, Applied Physics Letters **99**, 182507 (2011).

[137] D. Aurongzeb, M. Holtz, and L. Menon, *"Diffusion Process and Formation of Super-Spin-Glass State in Soft Magnetic Fe/Pt System"*, Applied Physics Letters **89**, 092501 (2006).

[138] Fernández Barquín, L., Gómez Sal, J. C., Gorria, P., Garitaonandia, J. S., and Barandiarán, J. M., *"Dynamic Susceptibility of Reentrant Fe-Rich Inhomogeneous Amorphous Alloys"*, European Physics Journal B **35**, 3-12 (2003).

[139] J. Rodríguez-Carvajal, *"Recent Advances in Magnetic Structure Determination by Neutron Powder Diffraction"*, Physica B **192**, 55 - 69 (1993).

[140] M. Lee, D. Bae, W. Kim, and D. Kim, *"Ni-Based Refractory Bulk Amorphous Alloys with High Thermal Stability"*, Materials Transactions **44**, 2084-2087 (2003).

[141] L. Zhang, E. Brück, O. Tegus, K. Buschow, and F. de Boer, *"The Crystallization of Amorphous Fe_2MnGe Powder Prepared by Ball Milling"*, Journal of Alloys and Compounds **352**, 99 - 102 (2003).

[142] H. E. Kissinger, *"Reaction Kinetics in Differential Thermal Analysis"*, Analytical Chemistry **29**, 1702–1706 (1957).

[143] C. A. Cardoso, F. M. Araujo-Moreira, V. P. S. Awana, E. Takayama-Muromachi, O. F. de Lima, H. Yamauchi, and M. Karppinen, *"Spin Glass Behavior in $RuSr_2Gd_{1.5}Ce_{0.5}Cu_2O_{10-\delta}$"*, Physical Review B **67**, 020407 (2003).

[144] O. F. de Lima, J. A. H. Coaquira, R. L. de Almeida, and S. K. Malik, *"Magnetic Phase Separation and Cluster-Spin-Glass Behavior in $LaMn_{1-x}Fe_xO_{3+y}$"*, Journal of Applied Physics **107**, 09E107 (2010).

[145] J. R. L. de Almeida and D. J. Thouless, *"Stability of the Sherrington-Kirkpatrick solution of a Spin Glass Model"*, Journal of Physics A: Mathematical and General **11**, 983 (1978).

[146] H. P. Klug and L. E. Alexander, *X-ray Diffraction Procedures: For Polycristalline and Amorphous Materials*. John Wiley & Sons, New York, 1974.

[147] A. Arrott and J. E. Noakes, *"Approximate Equation of State For Nickel Near its Critical Temperature"*, Physical Review Letters **19**, 786–789 (1967).

[148] H. Stanley, *Introduction to Phase Transitions and Critical Phenomena*. London Oxford University Press, London, 1971.

[149] J. S. Kouvel and M. E. Fisher, *"Detailed Magnetic Behavior of Nickel Near its Curie Point"*, Physical Review **136**, A1626–A1632 (1964).

[150] L. Tocado, E. Palacios, and R. Burriel, *"Entropy Determinations and Magnetocaloric Parameters in Systems with First-Order Transitions: Study of MnAs"*, Journal of Applied Physics **105**, 093918 (2009).

[151] T. Krenke, E. Duman, M. Acet, E. F. Wassermann, X. Moya, L. Mañosa, A. Planes, E. Suard, and B. Ouladdiaf, *"Magnetic Superelasticity and Inverse Magnetocaloric Effect in Ni-Mn-In"*, Physical Review B **75**, 104414 (2007).

[152] K. A. Gschneidner and V. K. Pecharsky, *"Magnetocaloric Materials"*, Annual Review of Materials Science **30**, 387-429 (2000).

[153] N. M. Bruno, C. Yegin, I. Karaman, J.-H. Chen, J. H. Ross, J. Liu, and J. Li, *"The Effect of Heat Treatments on $Ni_{43}Mn_{42}Co_4Sn_{11}$ Metamagnetic Shape Memory Alloys for Magnetic Refrigeration"*, Acta Materialia **74**, 66 - 84 (2014).

[154] T. Gottschall, A. Gràcia-Condal, M. Fries, A. Taubel, L. Pfeuffer, L. Mañosa, A. Planes, K. P. Skokov, and O. Gutfleisch, *"A Multicaloric Cooling Cycle that Exploits Thermal Hysteresis"*, Nature Materials **17**, 929–934 (2018).

[155] I. Unzueta, J. López-García, V. Sánchez-Alarcos, V. Recarte, J. I. Pérez-Landazábal, J. A. Rodríguez-Velamazán, J. S. Garitaonandia, J. A. García, and F. Plazaola, *"^{119}Sn Mössbauer Spectroscopy for Assessing the Local Stress and Defect State Towards the Tuning of Ni-Mn-Sn Alloys"*, Applied Physics Letters **110**, 181908 (2017).

[156] J. López-García, I. Unzueta, V. Sánchez-Alarcos, V. Recarte, J. Pérez-Landazábal, J. Rodríguez-Velamazán, J. García, and F. Plazaola, *"Correlation Between Defects and Magneto-Structural Properties in Ni-Mn-Sn Metamagnetic Shape Memory Alloys"*, Intermetallics **94**, 133 - 137 (2018).

[157] E. C. Passamani, C. Córdova, A. L. Alves, P. S. Moscon, C. Larica, A. Y. Takeuchi, and A. Biondo, *"Magnetic Studies of Fe-Doped Martensitic $Ni_2Mn_{1.44}Sn_{0.56}$-type Heusler alloy"*, J. Phys. D: Appl. Phys. **42**, 215006 (2009).

[158] R. Y. Umetsu, R. Kainuma, Y. Amako, Y. Taniguchi, T. Kanomata, K. Fukushima, A. Fujita, K. Oikawa, and K. Ishida, *"Mössbauer Study on Martensite Phase in $Ni_{50}Mn_{36.5}Fe_{0.557}Sn_{13}$ Metamagnetic Shape Memory Alloy"*, Applied Physics Letters **93**, 042509 (2008).

[159] R. Y. Umetsu, K. Sano, K. Fukushima, T. Kanomata, Y. Taniguchi, Y. Amako, and R. Kainuma, *"Mössbauer Spectroscopy Studies on Magnetic Properties for ^{57}Fe-substituted Ni-Mn-Sn Metamagnetic Shape Memory Alloys"*, Metals **3**, 225–236 (2013).

[160] E. Passamani, V. Nascimento, C. Larica, A. Takeuchi, A. Alves, J. Proveti, M. Pereira, and J. Fabris, *"The Influence of Chemical Disorder Enhancement on the Martensitic Transformation of the $Ni_{50}Mn_{36}Sn_{14}$ Heusler-type Alloy"*, Journal of Alloys and Compounds **509**, 7826 - 7832 (2011).

[161] J. López-García, J. I. Pérez-Landazábal, V. Recarte, J. A. Rodríguez-Velamazán, V. Sánchez-Alarcos, and I. Unzueta Institut Laue-Langevin (ILL) (2016).

[162] V. V. Sokolovskiy, V. D. Buchelnikov, M. A. Zagrebin, P. Entel, S. Sahoo, and M. Ogura, *"First-principles Investigation of Chemical and Structural Disorder in Magnetic $Ni_2Mn_{1+x}Sn_{1-x}$ Heusler Alloys"*, Physical Review B **86**, 134418 (2012).

[163] A. Le Bail, *"Whole Powder Pattern Decomposition Methods and Applications: A Retrospection"*, Powder Diffraction **20**, 316-326 (2005).

[164] J. Ortín and A. Planes, *"Thermodynamics of Thermoelastic Martensitic Transformations"*, Acta Metallurgica **37**, 1433 - 1441 (1989).

[165] O. C. Kistner and A. W. Sunyar, *"Evidence for Quadrupole Interaction of* Fe^{57m}*, and Influence of Chemical Binding on Nuclear Gamma-Ray Energy"*, Physical Review Letters **4**, 412–415 (1960).

[166] F. J. B. Dominic P. E. Dickson, *Mössbauer Spectroscopy*. Cambridge University press, Berlin, 1986.

[167] J. Schaf, K. L. Dang, P. Veillet, and I. A. Campbell, *"Extended and Local Effects of Cold Work in Heusler Alloys"*, J. Phys. F: Metal Physics **13**, 1311 (1983).

[168] T. Shinohara, K. Sasaki, H. Yamauchi, H. Watanabe, H. Sekizawa, and T. Okada, *"On the Reduction in Magnetization by Clod Working on the Ferromagnetic Heusler Alloy Pd_2MnSn"*, J. Phys. Soc. Jpn. **50**, 2904-2908 (1981).

[169] K. Ikeda and S. Takahashi, *"Cold-working Effect on Magnetic Properties in the Heusler Alloys"*, Physical Review B **30**, 3808–3814 (1984).

[170] S. Takahashi and T. Shinohara, *"Magnetic Moment Distribution in Deformed Heusler Alloy Pd_2MnSn"*, J. Phys. F: Metal Physics **12**, 3115 (1982).

[171] A. P. Young and J. P. Jakubovics, *"The effect of Planar Sefects on Exchange Interactions in Ferromagnetic Metals"*, J. Phys. F: Metal Physics **5**, 1866 (1975).

[172] T. Kamiyama, T. Shinohara, S. Tomiyoshi, Y. Minonishi, H. Yamamoto, H. Asano, and N. Watanabe, *"Effect of Deformation on Pd_2MnSn Heusler Alloy Studied with Transmission Electron Microscopy, Profile Analysis of Neutron Powder Diffraction Pattern, and Magnetization Measurement"*, Journal of Applied Physics **68**, 4741-4750 (1990).

[173] K. Niitsu, K. Minakuchi, X. Xu, M. Nagasako, I. Ohnuma, T. Tanigaki, Y. Murakami, D. Shindo, and R. Kainuma, *"Atomic-Resolution Evaluation of Microsegregation and Degree of Atomic Order at Antiphase Boundaries in $Ni_{50}Mn_{20}In_{30}$ Heusler alloy"*, Acta Materialia **122**, 166 - 177 (2017).

[174] P. Lázpita, J. M. Barandiará, J. Gutiérrez, J. Feuchtwanger, V. A. Chernenko, and M. L. Richard, *"Magnetic Moment and Chemical Order in Off-Stoichiometric Ni-Mn-Ga Ferromagnetic Shape Memory Alloy"*, New Journal of Physics **13**, 033039 (2011).

[175] E. Schlömann, *"Properties of Magnetic Materials with a Nonuniform Saturation Magnetization. I. General Theory and Calculation of the Static Magnetization"*, Journal of Applied Physics **38**, 5027-5034 (1967).

[176] H. Zhang, D. Zeng, and Z. Liu, *"The Law of Approach to Saturation in Ferromagnets Originating from the Magnetocrystalline Anisotropy"*, Journal of Magnetism and Magnetic Materials **322**, 2375 - 2380 (2010).

[177] G. F. Dionne, J. A. Weiss, and G. A. Allen, *"Hysteresis Loops Modeled From Coercivity, Anisotropy, and Microstructure Parameters"*, Journal of Applied Physics **61**, 3862-3864 (1987).

[178] R. Caballero-Flores, L. González-Legarreta, W. Rosa, T. Sánchez, V. Prida, L. Escoda, J. Suñol, A. Batdalov, A. Aliev, V. Koledov, V. Shavrov, and B. Hernando, *"Magnetocaloric effect, Magnetostructural and Magnetic Phase Transformations in $Ni_{50.3}Mn_{36.5}Sn_{13.2}$ Heusler Alloy Ribbons"*, Journal of Alloys and Compounds **629**, 332 - 342 (2015).

[179] S. Ma, Q. Cao, H. Xuan, C. Zhang, L. Shen, D. Wang, and Y. Du, *"Magnetic and Magnetocaloric Properties in Melt-Spun and Annealed $Ni_{42.7}Mn_{40.8}Co_{5.2}Sn_{11.3}$ Ribbons"*, Journal of Alloys and Compounds **509**, 1111 - 1114 (2011).

[180] V. V. Khovailo, K. Oikawa, T. Abe, and T. Takagi, *"Entropy Change at the Martensitic Transformation in Ferromagnetic Shape Memory Alloys $Ni_{2+x}Mn_{1-x}Ga$"*, Journal of Applied Physics **93**, 8483-8485 (2003).

[181] G. Fraga, D. B. ao, and J. Sereni, *"Specific Heat of X_2MnSn (X = Co, Ni, Pd, Cu), X_2MnIn (X = Ni, Pd) and Ni_2MnSb Heusler Compounds"*, Journal of Magnetism and Magnetic Materials **102**, 199 - 207 (1991).

[182] V. V. Khovaylo, T. Kanomata, T. Tanaka, M. Nakashima, Y. Amako, R. Kainuma, R. Y. Umetsu, H. Morito, and H. Miki, *"Magnetic properties of $Ni_{50}Mn_{34.8}In_{15.2}$ Probed by Mössbauer spectroscopy"*, Physical Review B **80**, 144409 (2009).

[183] J. Ray, G. Chandra, and C. Bansal, *"Distribution of ^{57}Fe Hyperfine Fields in Ni-Mn Alloys: A Mössbauer Effect Study"*, Journal of Physics F: Metal Physics **6**, 265 (1976).

[184] G. Erdélyi, H. Mehrer, A. Imre, T. Lograsso, and D. Schlagel, *"Self-Diffusion in Ni_2MnGa"*, Intermetallics **15**, 1078 - 1083 (2007).

[185] Y. Zhang, L. Zhang, Q. Zheng, X. Zheng, M. Li, J. Du, and A. Yan, *"Enhanced Magnetic Refrigeration Properties in Mn-rich Ni-Mn-Sn Ribbons by Optimal Annealing"*, Scientific Reports **5**, 11010 EP - (2015).

[186] Z. ni Zhou, L. Yang, J. ge Wang, T. Jin, Y. Huang, J. Li, Q. Hu, and J. guo Li, *"Internal Friction Behaviors of Ni-Mn-In Magnetic Shape Memory Alloy with Two-Step Structural Transformation"*, Progress in Natural Science: Materials International **27**, 356 - 361 (2017).

[187] S. Kustov, J. Pons, E. Cesari, and J. V. Humbeeck, *"Pinning-Induced Stabilization of Martensite: Part I. Stabilization Due to Static Pinning of Interfaces"*, Acta Materialia **52**, 3075 - 3081 (2004).

[188] S. Kustov, J. Pons, E. Cesari, and J. V. Humbeeck, *"Pinning-Induced Stabilization of Martensite: Part II. Kinetic Stabilization in Cu-Zn-Al Alloy Due to Pinning of Moving Interfaces"*, Acta Materialia **52**, 3083 - 3096 (2004).

[189] R. Santamarta, E. Cesari, J. Font, J. Muntasell, J. Pons, and J. Dutkiewicz, *"Effect of Atomic Order on the Martensitic Transformation of Ni-Fe-Ga Alloys"*, Scripta Materialia **54**, 1985 - 1989 (2006).

[190] H. Hedayati, P. Kameli, A. G. Varzaneh, S. Jannati, and H. Salamati, *"Effects of Sn Vacancy and Excess Sn Doping on Structural, Magnetic and Electrical Properties of $Ni_{47}Mn_{40}Sn_{13}$ Ferromagnetic Shape Memory Alloy"*, Intermetallics **82**, 14 - 19 (2017).

[191] J. Bai, J. M. Raulot, Y. D. Zhang, C. Esling, X. Zhao, and L. Zuo, *"Defect Formation Energy and Magnetic Structure of Shape Memory Alloys Ni-X-Ga (X = Mn, Fe, Co) by First Principle Calculation"*, Journal of Applied Physics **108**, 064904 (2010).

[192] J. Bai, N. Xu, J.-M. Raulot, Y. D. Zhang, C. Esling, X. Zhao, and L. Zuo, *"Defect Formation Energy and Magnetic Properties of Off-Stoichiometric Ni-Mn-In Alloys by First-Principles Calculations"*, Journal of Applied Physics **113**, 174901 (2013).

[193] J. Bai, N. Xu, J. M. Raulot, C. Esling, X. Zhao, and L. Zuo, *"First-Principles Investigation of Magnetic Property and Defect Formation Energy in Ni-Mn-Ga Ferromagnetic Shape Memory Alloy"*, International Journal of Quantum Chemistry **113**, 847-851 .

[194] S. Kulkova, S. Eremeev, S. Kulkov, and V. Skripnyak, *"Ab Initio Investigations of Magnetic Properties of Thin Film Heusler Alloys"*, Materials Science and Engineering: A **481-482**, 209 - 213 (2008). Proceedings of the 7th European Symposium on Martensitic Transformations, ESOMAT 2006.

[195] S. Kulkova, S. Eremeev, Q. Hu, C. Li, and R. Yang, *"The Influence of Defects and Composition on the Electronic Structure and Magnetic Properties of Shape Memory Heusler Alloys"*, in *ESOMAT 2009 (Czech Republic, September 7-11, 2009)*, no. 02017. EDP Sciences, Les Ulis,France, 2009.

[196] A. Kosogor, V. V. Sokolovskiy, V. A. L'vov, and V. V. Khovaylo, *"Martensitic Transformation in Shape Memory Crystal with Defects: Monte Carlo Simulations and Landau Theory"*, Physica Status Solidi (B) **252**, 2309-2316 (2015).

[197] Y. Wang, D. Salas, B. Medasani, P. Entel, I. Karaman, R. Arróyave, and T. C. Duong, *"First-Principles Characterization of Equilibrium Vacancy Concentration in*

Metamagnetic Shape Memory Alloys: An Example of Ni_2MnGa", Physica Status Solidi (B) **255**, 1700523 (2018).

[198] A. Mansouri Tehrani, H. Shahrokhshahi, N. Parvin, and J. Brgoch, *"Influencing the Martensitic Phase Transformation in Ni-Ti Through Point Defects",* Journal of Applied Physics **118**, 014901 (2015).

[199] P. Hohenberg and W. Kohn, *"Inhomogeneous Electron Gas",* Physical Review **136**, B864–B871 (1964).

[200] W. Kohn and L. J. Sham, *"Self-Consistent Equations Including Exchange and Correlation Effects",* Physical Review **140**, A1133–A1138 (1965).

[201] W. Kohn, *"Nobel Lecture: Electronic Structure of Matter - Wave Functions and Density Functionals",* Rev. Mod. Phys. **71**, 1253–1266 (1999).

[202] D. M. Ceperley and B. J. Alder, *"Ground State of the Electron Gas by a Stochastic Method",* Physical Review Letters **45**, 566–569 (1980).

[203] J. P. Perdew, K. Burke, and M. Ernzerhof, *"Generalized Gradient Approximation Made Simple",* Physical Review Letters **77**, 3865–3868 (1996).

[204] C. Lee, W. Yang, and R. G. Parr, *"Development of the Colle-Salvetti Correlation-Energy Formula into a Functional of the Electron Density",* Physical Review B **37**, 785–789 (1988).

[205] R. M. Nieminen, E. Boronski, and L. J. Lantto, *"Two-component Density-Functional Theory: Application to Positron States",* Physical Review B **32**, 1377–1379 (1985).

[206] E. Boroński and R. M. Nieminen, *"Electron-Positron Density-Functional Theory",* Physical Review B **34**, 3820–3831 (1986).

[207] M. J. Puska and R. M. Nieminen, *"Defect Spectroscopy with Positrons: A General Calculational Method",* Journal of Physics F: Metal Physics **13**, 333 (1983).

[208] K. O. Jensen, *"Local Density Calculation of Positron Annihilation in Metals",* Journal of Physics: Condensed Matter **1**, 10595 (1989).

[209] B. Barbiellini, M. J. Puska, T. Korhonen, A. Harju, T. Torsti, and R. M. Nieminen, *"Calculation of Positron States and Annihilation in Solids: A Density-Gradient-Correction Scheme",* Physical Review B **53**, 16201–16213 (1996).

[210] T. Korhonen, M. J. Puska, and R. M. Nieminen, *"First-Principles Calculation of Positron Annihilation Characteristics at Metal Vacancies",* Physical Review B **54**, 15016–15024 (1996).

[211] E. Boroński and R. M. Nieminen, *"Electron-Positron Density-Functional Theory",* Physical Review B **34**, 3820–3831 (1986).

[212] J. Arponen and E. Pajanne, *"Electron Liquid in Collective Description. III. Positron Annihilation",* Annals of Physics **121**, 343 - 389 (1979).

[213] L. J. Lantto, *"Variational Theory of Multicomponent Quantum Fluids: An Application to Positron-Electron Plasmas at T=0",* Physical Review B **36**, 5160–5170 (1987).

[214] B. Barbiellini, M. J. Puska, T. Torsti, and R. M. Nieminen, *"Gradient Correction for Positron States in Solids",* Physical Review B **51**, 7341–7344 (1995).

[215] F. Tuomisto and I. Makkonen, *"Defect Identification in Semiconductors with Positron Annihilation: Experiment and Theory"*, Review of Modern Physics **85**, 1583–1631 (2013).

[216] G. E. Kimball and G. H. Shortley, *"The Numerical Solution of Schödinger's Equation"*, Physical Review **45**, 815–820 (1934).

[217] N. W. ashcroft and N. D. Mermin, *Solid State Physics*. Thomson Learning Inc, 1976.

[218] H.-E. Schaefer, *"Investigation of Thermal Equilibrium Vacancies in Metals by Positron Annihilation"*, Physica Status Solidi (A) **102**, 47-65 .

[219] T. E. M. Staab, R. Krause-Rehberg, B. Vetter, and B. Kieback, *"The Influence of Microstructure on the Sintering Process in Crystalline Metal Powders Investigated by Positron Lifetime Spectroscopy: III. Nickel Reduction Powder"*, Journal of Physics: Condensed Matter **11**, 1807 (1999).

[220] P. J. Brown, J. Crangle, T. Kanomata, M. Matsumoto, K.-U. Neumann, B. Ouladdiaf, and K. R. A. Ziebeck, *"The Crystal Structure and Phase Transitions of the Magnetic Shape Memory Compound Ni_2MnGa"*, Journal of Physics: Condensed Matter **14**, 10159 (2002).

[221] D. Y. Cong, P. Zetterström, Y. D. Wang, R. Delaplane, R. L. Peng, X. Zhao, and L. Zuo, *"Crystal Structure and Phase Transformation in $Ni_{53}Mn_{25}Ga_{22}$ Shape Memory Alloy from 20 K to 473 K"*, Applied Physics Letters **87**, 111906 (2005).

[222] D. Merida, J. A. García, E. A. naniz, F. Plazaola, V. Sánchez-Alarcos, J. I. Pérez-Landazábal, and V. Recarte, *"Positron Annihilation Spectroscopy Study of Ni-Mn-Ga Ferromagnetic Shape Memory Alloys"*, Physics Procedia **35**, 57 - 62 (2012). Positron Studies of Defects 2011.

[223] D. Merida, *Caracterización de la Dinámica de Vacantes en Aleaciones Ferromagnéticas con Memoria de Forma del Sistema NiMnGa*. PhD thesis, University of the Basque Country, The address of the publisher, 2016. `https://addi.ehu.es/handle/10810/19740`. An optional note.

[224] H. R. Zhang, C. Ma, H. F. Tian, G. H. Wu, and J. Q. Li, *"Martensitic Transformation of Ni_2FeGa Ferromagnetic Shape-Memory Alloy Studied via Transmission Electron Microscopy and Electron Energy-Loss Spectroscopy"*, Physical Review B **77**, 214106 (2008).

[225] J. Font, J. Muntasell, R. Santamarta, J. Pons, E. Cesari, V. Recarte, J. Pérez-Landazábal, C. Gómez-Polo, and J. Dutkiewicz, *"Thermal Stability and Ordering Effects in Ni-Fe-Ga Ferromagnetic Shape Memory Alloys"*, Materials Science and Engineering: A **481-482**, 262 - 265 (2008). Proceedings of the 7th European Symposium on Martensitic Transformations, ESOMAT 2006.

[226] K. Oikawa, T. Omori, Y. Sutou, H. Morito, R. Kainuma, and K. Ishida, *"Phase Equilibria and Phase Transition of the Ni-Fe-Ga Ferromagnetic Shape Memory Alloy System"*, Metallurgical and Materials Transactions: A **38**, 767–776 (2007).

[227] T. Y. Hsu and Y. Linfah, *"The Effect of Quenched-in Vacancies on the Martensitic Transformation"*, Journal of Material Science **18**, 3213–3218 (1983).

[228] C. Picornell, J. Pons, E. Cesari, and J. Dutkiewicz, *"Thermal Characteristics of Ni-Fe-Ga-Mn and Ni-Fe-Ga-Co Ferromagnetic Shape Memory Alloys"*, Intermetallics **16**, 751 - 757 (2008).

[229] R. Santamarta, J. Font, J. Muntasell, F. Masdeu, J. Pons, E. Cesari, and J. Dutkiewicz, *"Effect of Ageing on the Martensitic Transformation of Ni-Fe-Ga Alloys"*, Scripta Materialia **54**, 1105 - 1109 (2006). Viewpoint set no. 40: Grain boundary engineering.

[230] B. Barbiellini, *New Directions in Antimatter Chemistry and Physics*. Kluwer Academic Publishers, 2001.

[231] P. J. Brown, A. P. Gandy, K. Ishida, R. Kainuma, T. Kanomata, H. Morito, K.-U. Neumann, K. Oikawa, and K. R. A. Ziebeck, *"Crystal Structures and Magnetization Distributions in the Field Dependent Ferromagnetic Shape Memory Alloy* $Ni_{54}Fe_{19}Ga_{27}$*"*, Journal of Physics: Condensed Matter **19**, 016201 (2007).

[232] S. Kustov, J. Pons, E. Cesari, and J. V. Humbeeck, *"Pinning-Induced Stabilization of Martensite: Part II. Kinetic Stabilization in Cu-Zn-Al Alloy due to Pinning of Moving Interfaces"*, Acta Materialia **52**, 3083 - 3096 (2004).

[233] X. Ren and K. Otsuka, *"Universal Symmetry Property of Point Defects in Crystals"*, Physical Review Letters **85**, 1016–1019 (2000).

[234] X. Ren and K. Otsuka, *"Origin of Rubber-Like Behaviour in Metal Alloys"*, Nature **389**, 579 EP - (1997).